

ADAPTIVE CONTROL OF RENEWABLE ENERGY RESOURCES FOR
IMPROVING THE DISPATCHABILITY AND OPERATIONAL STABILITY OF
RENEWABLE ENERGY INTEGRATED POWER SYSTEM

by

Rojan Bhattarai

A dissertation submitted to the faculty of
The University of North Carolina at Charlotte
in partial fulfillment of the requirements
for the degree of Doctor of Philosophy in
Electrical Engineering

Charlotte

2018

Approved by:

Dr. Sukumar Kamalasan

Dr. Yogendra Kakad

Dr. Abasifreke Ebong

Dr. David Young

ABSTRACT

ROJAN BHATTARAI. Adaptive control of renewable energy resources for improving the dispatchability and operational stability of renewable energy integrated power system. (Under the direction of DR. SUKUMAR KAMALASADAN)

This dissertation presents a measurement based adaptive control framework for renewable energy resources (RER) in order to improve the dispatch-ability and operational stability of renewable energy integrated bulk power grid. The proposed technique identifies a system model in real-time based on the input and output data which is then utilized to design a control framework. This approach is utilized as it provides control based on a dynamically changing linear model of the system at various operating points as opposed to the conventional control design technique based on a static model at a single operating point. In this work, recursive least squares (RLS) technique is utilized for the system identification and minimum variance control (MVC) is used to minimize the variance of the system output from its reference set-point. The work focuses both on local control of RER as well as utilization of RER to support the bulk power grid. Also, it has been demonstrated that the proposed technique enhances the reliability of RER, as the dependency of the RER control on multiple sensors is minimized. It has also been demonstrated that proposed identification based technique can lead to better damping of system oscillations as it updates the linear model of the power system based on the changing operating point as opposed to conventional damping control techniques. The design technique is discussed, and the performance analysis is studied on various test systems using dynamic simulations in order to validate the merits of the proposed control technique. As the proposed technique is dynamically adjusting online, the results show better performance when compared to the conventional control technique for RER.

ACKNOWLEDGEMENTS

I would like to express my sincere gratitude to my advisor, Dr. Sukumar Kamalasan who provided me with an opportunity to be a part of his research team and honed my skills as a researcher and an individual. I would also like to appreciate the time and support provided by the advising committee of Dr. Yogendra Kakad, Dr. Abasifreke Ebong, and Dr. David Young.

I am grateful for all of my teachers throughout my life, without whom I would have never come this far. I would like to thank UNCC, ECE Department of UNCC, graduate school at EPIC for providing the suitable environment to perform research, grow and learn. I am also grateful for the getting the chance to work along with inspiring people in my lab like: Niroj Gurung, Muhammad Ahmed, Reza Yousefian, Amirreza Sahami, Sheikh Jakir Hossain, Abilash Thakallapelli, Rabindra Maharjan, Bikash Poudel, Sudipta Ghosh and many others. I am certain that this bonding continues for rest of our professional life. Special thanks to my friends during this journey Rajan Puri, Bilkis Hossain and Susma Gurung, your support throughout is much appreciated. I appreciate feedback and support from Dr. Junjian Qi, who was my advisor during my brief internship in Argonne National Lab.

I cannot thank enough to my family members, who have always been my inspiration and motivation throughout this journey: My grandmother, who has always blessed me and motivated me to work towards my goal, My parents, who were always supportive and helped me persevere throughout these years, My sister and brother in law, who always helped me look at the bright side of things and finally my brother who has always been supportive and encouraging. Thank you all for being there for me, motivating me, supporting my ambitions and reminding me to be grateful for what I already have in my life.

DEDICATION

To my beloved family:

My grandmother: Dhanmaya Bhattarai

My parents: Chudamani Bhattarai, Hema Bhattarai

My Siblings: Roshni, Sujan, Ranjita

My brother in law: Ashok and my sister in law: Aasha

My niece: Aashni (most precious of all)

TABLE OF CONTENTS

LIST OF FIGURES	xii
LIST OF TABLES	xxv
LIST OF ABBREVIATIONS	xxvii
CHAPTER 1: INTRODUCTION	1
1.1. Wind Power: Worldwide and US scenario	1
1.2. Wind Energy Conversion Systems	4
1.2.1. Horizontal and Vertical Axis Wind Turbines	5
1.2.2. Drag and Lift Powered Motion	5
1.2.3. Number of Blades	5
1.2.4. Betz Limit	6
1.3. Components in a Wind Turbine	7
1.4. Wind Turbine Generator Concepts	8
1.4.1. Type 1 Wind Turbine Generators	9
1.4.2. Type 2 Wind Turbine Generators	9
1.4.3. Type 3 Wind Turbine Generators	11
1.4.4. Type 4 Wind Turbine Generators	11
1.5. Dissertation Objectives, Motivation and Contribution	12
1.5.1. Objectives	12
1.5.2. Motivation	13
1.5.3. Contribution	14
1.5.4. Intellectual Merit and Broader Impact	15

	vii
1.5.5. Dissertation Organization	16
CHAPTER 2: LITERATURE REVIEW: CONTROL TECHNIQUES FOR DFIG BASED WECS	17
2.1. Control Techniques for DFIG	18
2.1.1. Vector Control (VC) of DFIG	18
2.1.2. Direct Torque Control (DTC) of DFIG	20
2.1.3. Direct Power Control (DPC) of DFIG	25
2.1.4. Rotor Flux Magnitude and Angle Control of DFIG	26
2.1.5. Rotor Resistance Control of DFIG	28
2.1.6. State Feedback Control (SFC) of DFIG	29
2.1.7. Control of GSC	30
2.1.8. Pitch Control of DFIG	32
2.1.9. Maximum Power Point Tracking (MPPT) Control	33
2.2. Speed Sensorless Control of DFIG	34
CHAPTER 3: MODEL BASED APPROACH: ROTOR CURRENT SENSORLESS STATE ESTIMATORS BASED STATE FEEDBACK CONTROL OF DFIG	38
3.1. State Feedback Control (SFC) for DFIG	39
3.2. Simulation Results for State Feedback Control (SFC)	47
3.2.1. Response Comparison for Step Changes in Input	47
3.2.2. Response to Grid Voltage Sag	47
3.2.3. Dynamic Analysis with Real Wind Speed Profile	48
3.3. Design of State Estimators	51
3.4. State Feedback with State Observers	55

3.5. Simulation Results using 3-Bus System	57
3.5.1. Analysis of the Observer Based Controller with Dynamic Wind Conditions	57
3.5.2. Analysis of Observer Based Controller for Changes in DFIG Rotor Resistance	63
3.5.3. Analysis of the Observer Based Controller During Grid Voltage Sag	66
3.5.4. Simulation Results for Mutual Inductance Variation	66
3.6. Simulation Results on a Modified IEEE 39 Bus System	67
3.6.1. Comparison Between State Observer Based Feedback Controllers	68
3.6.2. Analysis of the State Observer Based State Feedback Control (SFC) for Dynamic Wind Conditions	71
3.6.3. Analysis of the Observer Based Vector Control(VC) For System Fault	72
3.7. Hardware-in-the-Loop (HIL) Simulation Results	75
3.7.1. Analysis of the State Observer based Controller for Dynamic Changes in Stator Power References	76
3.8. Chapter Summary	78
CHAPTER 4: MEASUREMENT BASED APPROACH: PARAMETRICALLY ROBUST DYNAMIC SPEED ESTIMATION BASED CONTROL FOR DFIG	80
4.1. Speed Observer for DFIG	81
4.2. Main Contributions: Dynamic Speed Estimation for DFIG	83
4.2.1. Small Signal Model of Proposed Estimator	83
4.2.2. Machine Parameter Sensitivity	86
4.2.3. Minimum Variance Controller	88

4.2.4.	Closed Loop Response of Proposed Speed Estimator	90
4.2.5.	Asymptotic Properties of MVC with RLS Identification	91
4.2.6.	Estimation of Mutual Inductance of DFIG	91
4.3.	Experimental Results	94
4.3.1.	Comparison with the Conventional MRAS based Speed Estimation Technique	94
4.3.2.	Real Time Simulation results for Speed Estimation	97
4.3.3.	Hardware in the Loop (HIL) Simulation Results	110
4.4.	Chapter Summary	112
CHAPTER 5: MEASUREMENT BASED APPROACH: SYSTEM IDENTIFICATION BASED CONTROL APPROACH FOR DFIG		115
5.1.	Adaptive Minimum Variance Controller for Grid Connected DFIG in Synchronously Rotating DQ Reference Frame	115
5.1.1.	Model of DFIG for Adaptive Control Design	115
5.1.2.	Adaptive Control of DFIG	117
5.1.3.	Simulation Results for MVC for DFIG	120
5.2.	Adaptive Minimum Variance Control of Grid Connected Three Phase Inverters in Synchronously Rotating DQ Reference Frame	126
5.2.1.	Model of Grid Connected Inverter	127
5.2.2.	MVC control of GCI	129
5.2.3.	Closed loop system bandwidth	131
5.2.4.	Simulation Results	132
5.2.5.	HIL Experimental Results	137

5.3. System Identification based Sensorless Control Approach for DFIG	139
5.3.1. Simulation Results	142
5.4. Chapter Summary	152
CHAPTER 6: CONTROL OF LARGE SCALE DFIG TO PROVIDE REACTIVE POWER SUPPORT TO BULK POWER GRID	153
6.1. Analysis of Dynamic Reactive Power Estimation Based Coordinated Reactive Power Support from Grid Integrated DFIG	156
6.1.1. Reactive Power Capability Limits of DFIG	156
6.1.2. Co-ordination Control Strategies for Extended Reactive Power Support	164
6.1.3. Proposed Controller Augmentation for RSC and GSC	168
6.1.4. Proposed Pitch Control Augmentation	170
6.1.5. Implementation Test on Interconnected Power Grid	171
6.2. Chapter Summary	182
CHAPTER 7: CONTROL OF LARGE SCALE DFIG TO PROVIDE ACTIVE POWER SUPPORT TO BULK POWER GRID	183
7.1. Impact Study of Wind Farm penetration on a test power grid	184
7.1.1. Case 1: Wind Generator in Area 1	185
7.1.2. Case 2: Wind Generator in Area 2	188
7.1.3. Changes in the Operating Condition causing Change in Tie-line Power Flows	189
7.2. System Modeling	199

7.3. Augmentation of DER Local Controller with Proposed WAC Technique	203
7.3.1. System Identification based Damping Controller Design	205
7.4. Simulation Results and Discussion	206
7.4.1. Fault in Middle of Transmission Line	206
7.4.2. Comparison with the Existing WADC architecture for DER	210
7.4.3. Comparison with the Existing system identification based Adaptive WADC architecture	211
7.4.4. Performance of the Proposed DER damping controller on System without PSS	211
7.4.5. Effect of Time Delay on Proposed DER damping controller	212
7.5. Chapter Summary	212
CHAPTER 8: CONCLUSIONS AND FUTURE WORKS	214
REFERENCES	219
APPENDIX A: MATHEMATICAL MODELING OF DOUBLY FED INDUCTION MACHINE	230
APPENDIX B: MATHEMATICAL MODELING OF A GRID CONNECTED INVERTER	232
APPENDIX C: RECURSIVE LEAST SQUARES BASED SYSTEM IDENTIFICATION	234
APPENDIX D: MACHINE PARAMETERS	238
APPENDIX E: GAIN COMPUTATION FOR SFC	239
APPENDIX F: SIMULATION MODELS AND SOURCE CODES	241

LIST OF FIGURES

FIGURE 1.1: Global Cumulative Installed Wind Capacity from 2001 to 2016 [1].	2
FIGURE 1.2: Nation-wise Cumulative Installed Wind Capacity as of December 2016 [1].	3
FIGURE 1.3: Major Components in a Modern Wind Turbine Generator System [2].	7
FIGURE 1.4: Schematic Diagram of Type 1 Wind Turbine Generator.	10
FIGURE 1.5: Schematic Diagram of Type 2 Wind Turbine Generator.	10
FIGURE 1.6: Schematic Diagram of Type 3 Wind Turbine Generator.	11
FIGURE 1.7: Schematic Diagram of Type 4 Wind Turbine Generator.	12
FIGURE 2.1: Schematic Diagram Representation of Conventional Vector Control of DFIG.	20
FIGURE 2.2: Vector Diagram Showing Principle of Direct Torque Control Technique of DFIG.	21
FIGURE 2.3: Schematic Diagram Showing Direct Torque Control Technique of DFIG.	22
FIGURE 2.4: Schematic Diagram Showing DPC Technique of DFIG.	25
FIGURE 2.5: Vector Diagram Representation of DFIG Operating Conditions.	27
FIGURE 2.6: Schematic Diagram of the Rotor Flux and Magnitude Control of DFIG.	27
FIGURE 2.7: Schematic Diagram of the OptiSlip Control of DFIG.	29
FIGURE 2.8: Classification of Different Control Techniques for DFIG.	31
FIGURE 2.9: Pitch Control Technique for a Wind Turbine System.	33
FIGURE 2.10: Typical Power Speed Curve for a Wind Turbine.	33

FIGURE 3.1: Phasor diagram showing the effect of neglecting the stator resistance in the position of voltage vector.	40
FIGURE 3.2: Schematic of Proposed State Feedback Control for DFIG.	45
FIGURE 3.3: Flowchart showing the Control Sequence for proposed State Feedback Controller.	46
FIGURE 3.4: One line Diagram of the Studied Test System.	47
FIGURE 3.5: Controller Performance Comparison for Step Change in Stator Power.	48
FIGURE 3.6: Comparison of the Controller Performance for Grid Voltage Sag.	48
FIGURE 3.7: Wind Velocity Profile used for Performance Assessment.	49
FIGURE 3.8: Stator Active Power Tracking Performance Comparison between SFC and VC for Dynamic Wind Conditions in 3.7.	49
FIGURE 3.9: DFIG Stator Terminal Voltage Regulation Comparison between SFC and VC for Dynamic Wind Conditions in 3.7.	50
FIGURE 3.10: DFIG DC link Voltage Regulation Comparison between SFC and VC for Dynamic Wind Conditions in 3.7.	50
FIGURE 3.11: q -axis Current Regulation Comparison between SFC and VC for Dynamic Wind Conditions in 3.7.	50
FIGURE 3.12: Schematic Diagram of the State Estimator based State Feedback Controller.	53
FIGURE 3.13: Augmented Vector Control Strategy for DFIG with State Observer.	54
FIGURE 3.14: Flowchart of the State Estimator based SFC.	58
FIGURE 3.15: Wind speed Profile used for Controller Performance Assessment.	59
FIGURE 3.16: Rotor Current Comparisons based on the State Observer.	59

FIGURE 3.17: Stator Active Power Tracking Performance Analysis with State Observer based State Feedback Control.	60
FIGURE 3.18: PCC Voltage Control with State Observer based State Feedback Control.	60
FIGURE 3.19: Stator Active Power Tracking Performance with State Observer based Vector Control.	61
FIGURE 3.20: PCC Voltage Control with State Observer based Vector Control.	62
FIGURE 3.21: Rotor Speed Oscillations with the two Proposed Controllers.	63
FIGURE 3.22: Rotor current Estimation Error during Rotor Resistance Variation.	63
FIGURE 3.23: Comparison of the Two Controllers during Grid Voltage Sag.	64
FIGURE 3.24: d -axis Rotor Current Estimation Comparison with 50% L_m Variation.	65
FIGURE 3.25: q -axis Rotor Current Estimation Comparison with 50% L_m Variation.	65
FIGURE 3.26: DFIG Terminal Voltage Control with State Observer based SFC with 50% L_m Variation.	65
FIGURE 3.27: Stator Active Power Tracking with Estimators with 1.5 L_m .	66
FIGURE 3.28: Wind integrated IEEE 39-bus System.	68
FIGURE 3.29: Real-Time Implementation Architecture.	69
FIGURE 3.30: Wind speed Profile used for Case A.	70
FIGURE 3.31: d - q axis Rotor Current Estimation during Steady State and Grid Fault Condition.	70
FIGURE 3.32: Stator Active Power Tracking Performance Comparisons in Steady State and Grid Fault Condition with the Two Controllers.	71

FIGURE 3.33: Voltage Profile Comparisons in Steady State and Grid Fault Condition with the Two Controllers.	71
FIGURE 3.34: Rotor Speed Comparisons in Steady State and Grid Fault Condition with the Two Controllers.	72
FIGURE 3.35: Wind speed Profile used for the Study.	72
FIGURE 3.36: Rotor Current Estimation for Dynamic Wind Conditions.	73
FIGURE 3.37: Stator Active Power Tracking Performance Comparisons.	73
FIGURE 3.38: Rotor Current Estimation Comparison during Grid Fault Conditions.	73
FIGURE 3.39: Voltage Profile Comparisons for Different Wind Farms.	74
FIGURE 3.40: Rotor Speed for Different Wind Farm.	74
FIGURE 3.41: Experimental Setup.	75
FIGURE 3.42: Comparison of Actual d -axis Rotor Current with the Estimated d -axis Rotor Current.	76
FIGURE 3.43: Comparison of Actual q -axis Rotor Current with the Estimated q -axis Rotor Current.	76
FIGURE 3.44: Stator Active Power Tracking Performance of the Proposed State Observer based SFC.	77
FIGURE 3.45: Stator Reactive Power Tracking Performance of the Proposed State Observer based SFC.	77
FIGURE 3.46: Instantaneous Stator Current.	78
FIGURE 4.1: Proposed Sensorless VC Scheme for a Grid Connected DFIG.	83
FIGURE 4.2: Small Signal Model of Proposed Speed Estimator.	84
FIGURE 4.3: Phasor Diagram showing the Effect of L_m Variation on Rotor Position Estimation.	88
FIGURE 4.4: Hardware Set-up Used.	93

FIGURE 4.5: Rotor Speed Estimation Comparison between the Proposed MRAS Technique and Conventional MRAS Technique.	94
FIGURE 4.6: Active Power Tracking Performance Comparison of DFIG with Speed Estimated using the Proposed MRAS technique and conventional MRAS Technique.	95
FIGURE 4.7: Reactive Power Tracking Performance Comparison of DFIG with Speed Estimated using the Proposed MRAS technique and conventional MRAS Technique.	95
FIGURE 4.8: Angle Performance Comparison of DFIG with Speed Estimated using the Conventional MRAS Technique.	96
FIGURE 4.9: Angle Performance Comparison of DFIG with Speed Estimated using the Proposed MRAS Technique.	96
FIGURE 4.10: Estimated Rotor Speed and Actual Rotor Speed for Step Changes in Wind Speed.	97
FIGURE 4.11: Speed Estimation Error for Rotor Speed Changes Case in Figure 4.10.	98
FIGURE 4.12: Angle Estimation Error for Rotor Speed Changes Case in Figure 4.10.	98
FIGURE 4.13: Mutual Inductance Estimation for Rotor Speed Changes Case in Figure 4.10.	100
FIGURE 4.14: Wind Speed Profile Used.	100
FIGURE 4.15: Rotor Speed Estimation Performance of Proposed Speed Estimator for Wind Conditions in Figure 4.14.	100
FIGURE 4.16: Active Power Generated by Sensorless Vector Controlled DFIG for Wind Conditions in Figure 4.14.	101
FIGURE 4.17: Stator Terminal Voltage Control by Sensorless Vector Controlled DFIG for Wind Conditions in Figure 4.14.	101
FIGURE 4.18: Mutual Inductance Estimation in a Sensorless Vector Controlled DFIG for Wind Conditions in Figure 4.14.	101

FIGURE 4.19: Rotor Position Estimation Error in a Sensorless Vector Controlled DFIG for Wind Conditions in Figure 4.14.	102
FIGURE 4.20: Angle Estimation Error for Changes in Machine Mutual Inductance with and without L_m Estimation.	102
FIGURE 4.21: Mutual Inductance Estimation Error for changes in Machine Mutual Inductance.	102
FIGURE 4.22: Voltage Control Performance when the Proposed Speed Estimation was used along with Conventional Vector Control.	103
FIGURE 4.23: Speed Estimation during PCC Voltage Variations.	104
FIGURE 4.24: Mutual Inductance Estimation for changes in PCC Voltage.	104
FIGURE 4.25: Rotor Position Estimation Error for Voltage Changes.	104
FIGURE 4.26: PCC Voltage Response for a Three Phase Short Circuit Fault.	105
FIGURE 4.27: Active Power Generation Response for a Three Phase Short Circuit Fault with Proposed Speed Estimation Technique used in Vector Control.	105
FIGURE 4.28: Mutual Inductance Estimation Performance for a Three phase Short Circuit Fault with Proposed L_m Estimation Technique.	106
FIGURE 4.29: Rotor Speed Estimation Performance for a Three phase Short Circuit Fault with Proposed Speed Estimation Technique.	106
FIGURE 4.30: Angle Estimation Error for a Three phase Short Circuit Fault with Proposed Speed Estimation Technique.	106
FIGURE 4.31: Stator Active Power Tracking Performance of Proposed Sensorless Control.	108
FIGURE 4.32: Estimated Speed and Actual Speed when the DFIG is used for Frequency Regulation Causing Rotor Oscillations.	109
FIGURE 4.33: Mutual Inductance Estimation Performance when DFIG is used for Frequency Regulation with Proposed L_m Estimation Technique.	109

FIGURE 4.34: Angle Estimation Error when DFIG is used for Frequency Regulation with the Proposed Rotor Position Estimation Technique.	109
FIGURE 4.35: Angle Estimation Error Comparison for Vector Control and Direct Power Control of DFIG with the Proposed Rotor Position Estimation Technique.	110
FIGURE 4.36: Speed Estimation Performance Comparison for Vector Control and Direct Power Control of DFIG with the Proposed Speed Estimation Technique.	111
FIGURE 4.37: Active Power Control Performance Comparison for Vector Control and Direct Power Control of DFIG with the Proposed Speed Estimation Technique.	111
FIGURE 4.38: Rotor Angle Estimation Comparison from Hardware Setup.	112
FIGURE 4.39: Rotor Speed Estimation Performance Comparison for Hardware Setup.	112
FIGURE 4.40: Speed Estimation Error for Hardware Setup.	113
FIGURE 4.41: Instantaneous Rotor Current as seen in Hardware Setup.	113
FIGURE 4.42: Stator Active and Reactive Power Profile in Hardware Setup.	113
FIGURE 5.1: Schematic Representation of an Adaptive Control System.	118
FIGURE 5.2: Proposed Adaptive Control Scheme for DFIG.	121
FIGURE 5.3: One Line Diagram of the Test System used to access Controller Performance.	121
FIGURE 5.4: Rotor Speed Profile used to access the Performance of Proposed Control.	121
FIGURE 5.5: Stator Active Power Tracking Performance with Proposed Control.	122
FIGURE 5.6: Stator Reactive Power Tracking Performance with Proposed Control.	123

FIGURE 5.7: $d - q$ axis Stator and Rotor Currents for Step Changes in Active and Reactive Power.	123
FIGURE 5.8: Wind Speed Profile used to assess Performance of the Controller.	124
FIGURE 5.9: Stator Active Power Tracking Performance Comparison of Vector Control and Proposed Adaptive Control.	124
FIGURE 5.10: Performance Comparison of Vector Control and Proposed Adaptive Control during Grid Voltage Sag.	125
FIGURE 5.11: Performance Comparison of Vector Control and Proposed Adaptive Control during Machine's L_m Variation.	125
FIGURE 5.12: Proposed Adaptive Control Scheme for GCI.	132
FIGURE 5.13: Closed loop System Bandwidth with Different Controllers Active Power Control Loop for Results shown in Figure 5.14.	133
FIGURE 5.14: Comparison of Active Power Tracking for Step Changes in the Reference Set-points.	135
FIGURE 5.15: Comparison of Reactive Power Tracking for Step Changes in the Reference.	135
FIGURE 5.16: Phase A Current Comparison.	136
FIGURE 5.17: Comparison of Output Current Harmonics Spectrum when operated in Grid Connected Mode.	136
FIGURE 5.18: Comparison of Active Power Tracking for Step Changes in the Reference and Changes in Coupling Inductance.	136
FIGURE 5.19: Comparison of Reactive Power Tracking for Step Changes in the Reference and Changes in Coupling Inductance.	137
FIGURE 5.20: Experimental Test-bed Used for testing the Proposed Control Architecture.	138
FIGURE 5.21: Comparison of Active Power Tracking on Experimental Test-bed.	138

FIGURE 5.22: Comparison of Reactive Power Tracking on Experimental Test-bed.	139
FIGURE 5.23: GCI $d - q$ -axis Current using the Proposed Controller during Active and Reactive Power Tracking.	139
FIGURE 5.24: Proposed system identification based control structure for DFIG.	142
FIGURE 5.25: System identification process data flow diagram.	143
FIGURE 5.26: System identification based adaptive control approach.	144
FIGURE 5.27: Case A: Wind Speed used to test the Performance of Proposed Controller.	145
FIGURE 5.28: Case A: DFIG Rotor Speed Estimation Comparison with Proposed Adaptive Speed Estimation Technique when using Vector Control and Proposed Identification Based Control.	145
FIGURE 5.29: Case A: Comparison between Total Power Generated from DFIG when using Vector Control and Proposed Identification Based Control for Wind Speed shown in Figure 5.27.	147
FIGURE 5.30: Case A: Comparison between Mechanical Power Input and Electrical Power Output when using Vector Control and Proposed Identification based Control for Wind Speed shown in Figure 5.27.	147
FIGURE 5.31: Case A: Comparison between PCC Voltage Regulation from DFIG when using Vector Control and Proposed Identification based Control for Wind Speed shown in Figure 5.27.	148
FIGURE 5.32: Case A: Comparison between DC link Voltage when using Vector Control and Proposed Identification based Control for Wind Speed shown in Figure 5.27.	148
FIGURE 5.33: Case A: Comparison between GSC Reactive Power Output when using Vector Control and Proposed Identification based Control for Wind Speed shown in Figure 5.27.	149
FIGURE 5.34: Case B: Comparison between DFIG Mechanical and Total Electrical Power Generated following a Rotor Current Sensor Failure with VC and proposed identification based Control	150

FIGURE 5.35: Case B: Comparison between DFIG Rotor Speed following a Rotor Current Sensor Failure with VC and Proposed Identification based Control	150
FIGURE 5.36: Case C: Comparison between PCC Voltage Regulation from DFIG when using Vector Control and Proposed Identification based Control following a Three phase to Ground Fault.	151
FIGURE 5.37: Comparison between Proposed Identification based Control and Vector Control for Step Changes in Stator Reactive Power after Changes in Machine Mutual Inductance	151
FIGURE 6.1: Vector diagram of (a) Angle deviation (b) Voltage deviation. V_g : Grid voltage, V_t : DFIG Stator Terminal Voltage, V_x : Line Voltage Drop, I_t : Current flowing through DFIG, δ Angle between Terminal and Grid Voltage, Superscript: 0: Initial Steady State Vectors, f : Transient Vectors (after the fault), * = Final Steady State Vectors.	155
FIGURE 6.2: Capability curve of DFIG considering Rotor Voltage Limit.	159
FIGURE 6.3: Capability curve of DFIG without Considering GSC's Reactive Power Capability Illustrating Individual Limits for Stator Current, Rotor Current and Rotor Voltage.	160
FIGURE 6.4: Active and reactive power variation of GSC as a function of active power generated from stator.	161
FIGURE 6.5: Overall Capability Curve of DFIG.	162
FIGURE 6.6: Block Diagram Representation of an Adaptive Controller.	165
FIGURE 6.7: Extended Reactive Power Capability using Droop Constant (GSC included).	170
FIGURE 6.8: Overall Controller Design Flowchart.	172
FIGURE 6.9: Kundur Two Area Four Machine Test System.	173
FIGURE 6.10: Wind Speed Profile Used .	174
FIGURE 6.11: PCC Voltage During Three phase Ground Fault.	174
FIGURE 6.12: PCC Voltage During Voltage Sag.	175

FIGURE 6.13: Reactive Power Support Using Proposed Technique During Voltage Sag.	175
FIGURE 6.14: One Line Diagram of the 68 Bus System [3].	176
FIGURE 6.15: Wind Speed (v_w) used for the Case Study.	176
FIGURE 6.16: PCC Voltage Recovery on 68 Bus System through use of DFIG based Windfarm.	177
FIGURE 6.17: PCC Frequency on Windfarm bus.	177
FIGURE 6.18: Rotor Speed of DFIG.	178
FIGURE 6.19: Active Power Support from DFIG.	178
FIGURE 6.20: Reactive Power Support from DFIG.	179
FIGURE 6.21: PQ plot of Individual WT of Windfarm for the above cases.	179
FIGURE 6.22: Rotor Voltage Dynamics.	180
FIGURE 6.23: Rotor Current Dynamics.	180
FIGURE 6.24: Stator Current Dynamics.	181
FIGURE 7.1: Five Generator Two Area Test System.	186
FIGURE 7.2: Locus of Inter-area mode and Local Mode at Different Penetration Level of Renewable Energy Resources.	186
FIGURE 7.3: Locus of Inter-area Mode with Different Penetration Level of Renewable Energy Resources in Area 1 with Different Loading Condition.	192
FIGURE 7.4: Locus of Inter-area Mode with Different Penetration Level of Renewable Energy Resources in Area 2 with Different Loading Condition.	192
FIGURE 7.5: Locus of Local Mode 1 with Different Penetration Level of Renewable Energy Resources in Area 1 with Different Loading Condition.	198

FIGURE 7.6: Locus of Local mode 2 with Different Penetration Level of Renewable Energy Resources in Area 1 with Different Loading Condition.	199
FIGURE 7.7: Locus of Local mode 1 with Different Penetration Level of Renewable Energy Resources in Area 2 with Different Loading Condition.	200
FIGURE 7.8: Locus of Local mode 2 with Different Penetration Level of Renewable Energy Resources in Area 2 with Different Loading Condition.	200
FIGURE 7.9: Inter-area Speed Oscillation for a Three Phase Fault for a Fixed Operating Point at Different Penetration of Wind Farm.	201
FIGURE 7.10: Proposed structure of damping controller based on system identification.	202
FIGURE 7.11: Augmentation of DER LC using Proposed WAC Signal.	203
FIGURE 7.12: Modified Classical Two-area Four-machine System with Integrated DER.	205
FIGURE 7.13: Comparison of Actual Inter-area Speed Deviation and Estimated Inter-area Speed Deviation.	207
FIGURE 7.14: Estimation Error of the Recursive Least Square Multi-channel Identification Routine.	207
FIGURE 7.15: Inter-area Speed Deviation Comparison with PSS and Proposed Technique with Multiple Combination of DER.	207
FIGURE 7.16: Tie-line Power Flow Transfer Comparison with PSS and Proposed Technique with Multiple Combination of DER.	208
FIGURE 7.17: DER Power Output Deviation from its Local Setpoint for WAC Contribution a)DER1 b)DER2.	208
FIGURE 7.18: Inter-area Speed Oscillation Damping Comparison for Different WAC Schemes.	209
FIGURE 7.19: Inter-area Speed Oscillation Damping Comparison between Proposed Adaptive WADC and WADC proposed in [4].	210

FIGURE 7.20: Inter-area Speed Oscillation Comparison without PSS but only with Proposed Damping Controller.	211
FIGURE 7.21: Inter-area Speed Oscillation Comparison with and without Delay Compensation for Proposed DER Damping Controller.	212
FIGURE A.1: Dynamic Electric Circuit Model of DFIG	231
FIGURE B.1: Arrangement of a bidirectional GCI.	233

LIST OF TABLES

TABLE 3.1: Location of Eigenvalues and controllability and observability for RSC control	43
TABLE 3.2: Location of Eigenvalues and controllability and observability for GSC control	43
TABLE 3.3: Rotor Current Estimation Error	62
TABLE 3.4: Case Studies on Large Scale System	69
TABLE 4.1: atan2 Approximations for Small Deviations	85
TABLE 4.2: Changes in Stator Terminal Voltage Reference	103
TABLE 5.1: Comparison of Response Time between Proposed Adaptive Controller and other Controllers	134
TABLE 5.2: Performance Comparison in Dynamic Wind Conditions	144
TABLE 5.3: Difference between Mechanical Power Input and Electrical Power Output with the Proposed Technique and Vector Control	146
TABLE 5.4: Sensor Configuration for Case B	149
TABLE 5.5: Response Characteristics for Case C	149
TABLE 5.6: Case D: Step Response Characteristics Comparison between Proposed Control and Vector Control for Parameter Variation	151
TABLE 6.1: Variation of Reactive Power Limits of DFIG with Various Slip and Loading Conditions	163
TABLE 6.2: Wind Farm Interconnected Grid Details (MW)	177
TABLE 6.3: Different Control Cases Considered	178
TABLE 6.4: Comparison of Performance of Proposed Control Technique with Conventional Voltage Control Technique.	179
TABLE 7.1: Inter-area Modes at different penetration level of Wind Farm	187
TABLE 7.2: Local Mode 1 at different penetration level of Wind Farm	187

TABLE 7.3: Local Mode 2 at different penetration level of Wind Farm	189
TABLE 7.4: Interarea Mode at different penetration level of Wind Farm on Area 1 and at different operating condition	190
TABLE 7.5: Interarea Mode at different penetration level of Wind Farm on Area 2 and at different operating condition	191
TABLE 7.6: Local Mode 1 at different penetration level of Wind Farm on Area 1 and at different operating condition	194
TABLE 7.7: Local Mode 2 at different penetration level of Wind Farm on Area 1 and at different operating condition	195
TABLE 7.8: Local Mode 1 at different penetration level of Wind Farm on Area 2 and at different operating condition	196
TABLE 7.9: Local Mode 2 at different penetration level of Wind Farm on Area 2 and at different operating condition	197

LIST OF ABBREVIATIONS

<i>d</i>	Direct Axis Component.
<i>q</i>	Quadrature Axis Component.
ABB	ASEA Brown Boveri
AC	Alternating Current.
ARMAX	Autoregressive Moving Average Exogenous.
ARX	Autoregressive Exogenous.
CARMA	Controlled Auto Regressive Moving Average.
CPP	Clean Power Plan.
DC	Direct Current.
DFIG	Doubly Fed Induction Generator.
DFIM	Doubly Fed Induction Machine.
DOE	Department of Energy.
EIA	Energy Information Administration.
EPA	Environmental Protection Agency.
FMAC	Flux Magnitude and Angle Control.
GCI	Grid Connected Inverter.
HAWT	Horizontal Axis Wind Turbine.
HIL	Hardware in the Loop.
ITC	Investment Tax Credit.

LQI	Linear Quadratic Integral.
LQR	Linear Quadratic Regulator.
MPPT	Maximum Power Point Tracking.
MRAS	Model Reference Adaptive System.
MVC	Minimum Variance Control.
PCC	Point of Common Coupling.
PID	Proportional Integral Derivative.
PMSG	Permanent Magnet Synchronous Generator.
PTC	Production Tax Credit.
RHP	Right Handside Plane.
RLS	Recursive Least Squares.
SCIG	Squirrel Cage Induction Generator.
SCIM	Squirrel Cage Induction Machine.
SFC	State Feedback Control.
SPGCI	Single Phase Grid Connected Inverter.
TPGCI	Three Phase Grid Connected Inverter.
VAWT	Vertical Axis Wind Turbine.
VC	Vector Control.
VSC	Voltage Source Converter.
WECS	Wind Energy Conversion System.

WRIG Wound Rotor Induction Generator.

WT Wind Turbine.

WTG Wind Turbine Generator.

CHAPTER 1: INTRODUCTION

1.1 Wind Power: Worldwide and US scenario

Wind energy has emerged as a promising source of renewable energy over the past decade. The global cumulative installed wind power capacity has grown to 486.79 GW in 2016 from about 23.9 GW in 2001 [1]. And, the trend shows an almost exponential growth in the power production from wind energy with rise of 12.5% in 2016 as compared to previous year. This phenomenal increment in the wind energy can be attributed to the rising concerns about the environmental issues, increasing cost of fossil fuels, and also research and development in the field of innovative cost reducing technology in power electronics and in wind turbines. Figure 1.1 shows the changing trends for wind power capacity from 2001 to recent years.

In 2015, the US wind industry installed 8,598 MW of new capacity across 20 states, which is 77% increase over 2014 and the third highest annual total in history. With the new installations, the total wind power capacity in the US rose upto 74,471 MW, enough to power 20 million average American homes. Wind energy has supplied 30% of all new power capacity additions in US over the last 5 years and in 2015 represented 41% of new capacity additions [1].

The key barriers to wind energy developments in the US are the long term policy instability and inadequacy of transmission systems. In August 2015, the Environmental Protection Agency (EPA) released the final rule of the Clean Power Plan (CPP). With the CPP rule the emission from most of the fossil generating units is expected to reduce and the total carbon emissions by this rule is estimated to be 32% of the 2005 levels by 2030. According to economic analysis from the US Energy Information Administration (EIA) of the CPP, wind energy can supply the majority of the

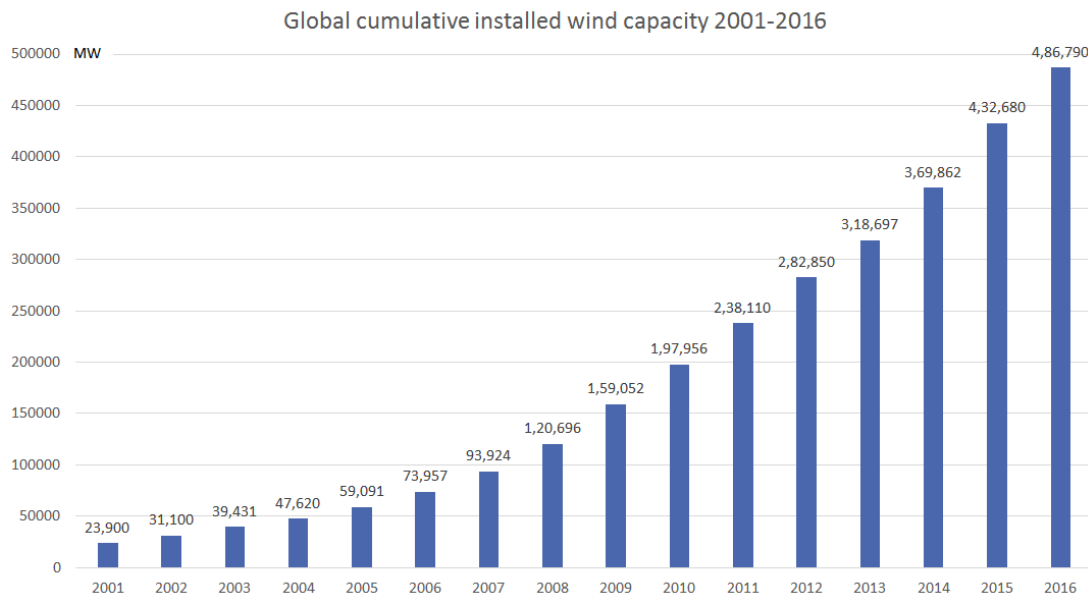


Figure 1.1: Global Cumulative Installed Wind Capacity from 2001 to 2016 [1].

lowest-cost CPP compliance mix [1].

The second major policy development occurred late in 2015 when congress passed a multi-year extension of the Production Tax Credit (PTC) and Investment Tax Credit (ITC), securing the predictable business environment needed to keep US factories open and further scale up American wind power. In 2003, when the PTC expired without being renewed, the new installations amounted to 389 MW in 2004, as compared to more than 2400 MW annually in each of the following years after the PTC was renewed in late 2004.

In 2015, the US Department of Energy (DOE) released its "Wind Vision: A New Era for Wind Power in the United States" report which shows that wind energy can supply the US with 10% of the country's electricity by 2020, 20% by 2030, and 35% by 2050 and provides a road map for how to get there. By providing 20% of the nation's electricity by 2030, wind energy would support 380,000 jobs, US \$650 million in annual lease payments to landowners, and nearly US \$1.8 billion a year in tax payments to communities [5].

Figure 1.2 shows the cumulative installed wind capacity on various nations around

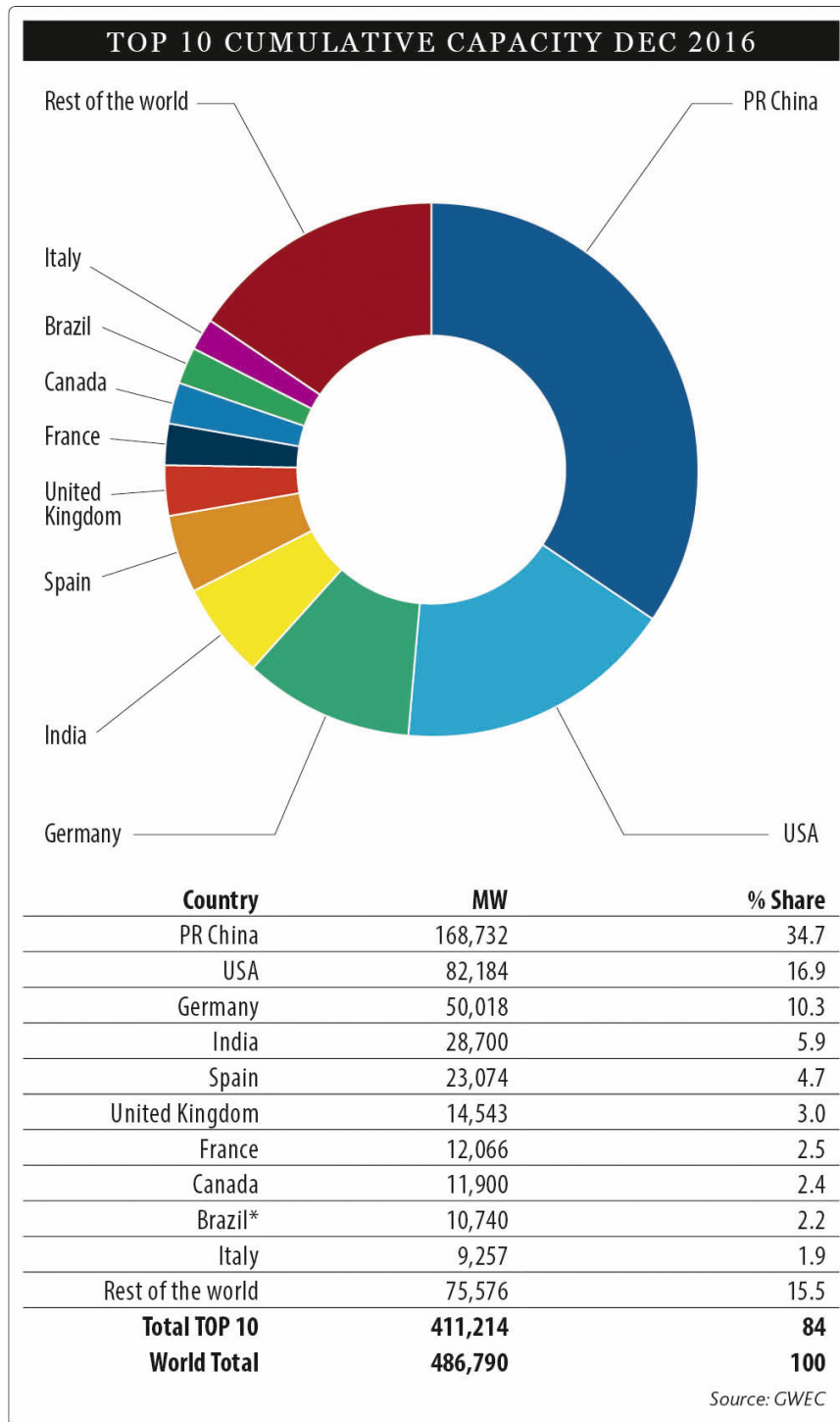


Figure 1.2: Nation-wise Cumulative Installed Wind Capacity as of December 2016 [1].

the world as of December 2016. It can be observed that US market covers a huge share of the overall cumulative installed wind capacity after PR China.

A typical modern wind turbine (WT) generates usable amount of power over 90% of time however, most of those time, it is at less than full capacity, which makes the capacity factor of wind power plants lower than the conventional power plants. Capacity factor is defined as the ratio of actual electricity production over the total production if the plant was running continuously at full capacity. The capacity factor of wind farms depends mainly location of and technology used in wind farms. For wind units, a capacity factor of 0.25-0.3 can be considered as reasonable and a capacity factor of 0.4 as very good [6].

1.2 Wind Energy Conversion Systems

The modern wind energy conversion system (WECS) includes turbine rotor, gearbox, generator, transformer and power electronics converters. The turbine rotor captures the wind energy by means of aerodynamically designed blades and converts it to rotating mechanical energy, which is eventually converted into electrical energy through the generator and is transferred to grid through transformers and transmission lines. The rotor blades rotate at a low speed but with high torque, which is converted to high speed using set of gearboxes. If multi-pole machines are to be used, gearbox may not be a necessity. It is important to control and regulate the converted mechanical power at higher wind speeds, as the power in the wind is proportional to the cube of the wind speed.

The mechanical power conversion control is done by using either stall control or pitch control [7]. Stall control techniques are of two types, in one of them, the position of the rotor blades is fixed but stall of wind turbine appears along the blade at higher wind speed, in other, also called active stall control, the rotor blade angles are adjusted to create stall along the blades. And, in pitch control, the blades are turned out of the wind at higher wind speed in order to limit the turbine speed as well as the power output of the WT.

1.2.1 Horizontal and Vertical Axis Wind Turbines

From the physical setup viewpoint, there are horizontal axis wind turbines (HAWT) and vertical axis wind turbines (VAWT). As the name suggests, HAWT have rotor blades that rotate about an axis that is parallel to the ground whereas, airflow and the rotor blades in VAWT rotate about an axis which is perpendicular to the ground. Common examples of HAWT are the old-style Dutch windmill and modern wind turbines and that of VAWT are the Darrieus (curved blades) and Savonius (scoop blades) [8].

Almost all of the modern day wind turbines are HAWT, especially because they are more suitable for harnessing the higher and smoother wind speed at higher altitude [8].

1.2.2 Drag and Lift Powered Motion

The rotation of both HAWT and VAWT can be powered predominantly by lift or drag force depending on the design of the blade. In drag design, the wind pushes the blade out of the way. The rotational speed is typically slower. Due to their high torque capabilities, drag powered turbines are suitable for pumping, sawing or grinding. The typical example of such design is the old style Dutch windmill. In lift design, the blade cross section has an airfoil shape so that when the wind passes by the blade, the pressure on the lower surface is higher and hence lifts the blade. The same principle allows airplanes and birds to fly. Lift powered turbines have much higher rotational speed than drag-powered turbine and are well suited for electricity generation . In general, lift machines are more efficient than their drag counterpart [9].

1.2.3 Number of Blades

In order to extract a maximum amount of wind power, each blade should interact as much as possible with the wind passing through the swept area. Swept area is the

total area covered by the WT rotor blades. Hence the lesser the blades the higher the rotational speed of the turbine, as the blades have to move faster to ‘fill up’ the swept area. In theory, the more blades a turbine has, the more efficient it should be. However for larger number of blades there is more interference and a blade is more likely to pass in the disturbed weaker flow of the previous blade. In practice, low-solidity turbines tend to have a higher efficiency [10]. Blade solidity is an important design parameter for the axial flow impeller and is defined as the ratio of blade chord length to pitch.

From a structural stability viewpoint, the number of blades of lift powered HAWT should be odd and greater or equal to 3, in which case the dynamic properties of the turbine rotor are similar to those of a disc. For an even number of blades, the structure is subject to more important bending forces because when a blade is in the uppermost position receiving most wind power, another blade is in the lowermost position in the shadow of the tower. The majority of commercialized modern wind turbines are two or three bladed [11]. Sometimes, even a single bladed design are used to save the cost of blades. However these turbines require more complex structural design to avoid heavy shocks (two-bladed turbines require a teetering hub, one bladed turbines require a counterweight on the hub) and are visually more intrusive due to their higher rotational speed as compared to three bladed turbines.

1.2.4 Betz Limit

An important operational characteristic of WTs is the Betz limit. It indicates the theoretical maximum amount of wind energy that can be extracted by a turbine. If turbines were 100% efficient all the airflow energy would be extracted and the flow speed after passing through the turbine would be zero, which is impossible. In 1928, Betz showed that under ideal assumptions (uniform rotor disk with infinite number of blades) the maximum efficiency of a turbine is $16/27$ (59.3%). In practice, this coefficient is less due to non-idealities (wake rotation behind the rotor, finite number of

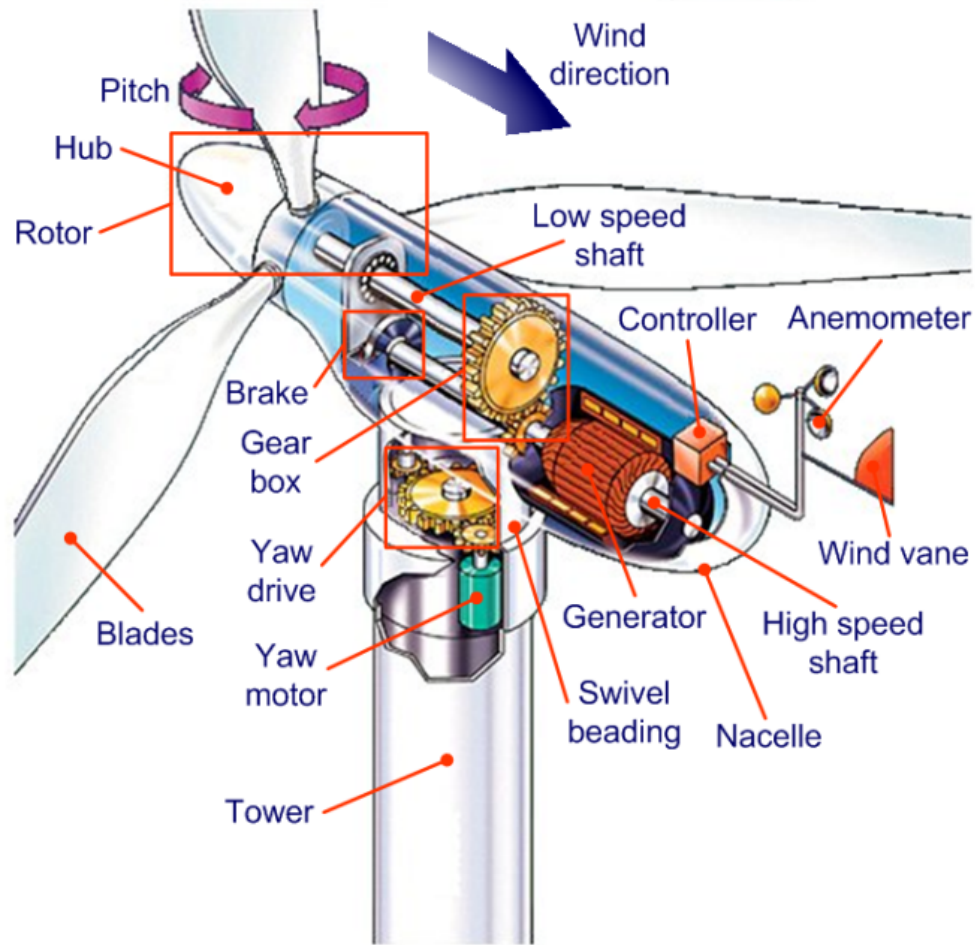


Figure 1.3: Major Components in a Modern Wind Turbine Generator System [2].

blades, blade-tip losses, frictional drag, etc). Present turbines have efficiency around 30-40% [10] .

1.3 Components in a Wind Turbine

The major components of a modern wind turbine generator (WTG) system is shown in Figure 1.3. The turbine is formed by the blades, the hub and the connecting components (bearings, pitching actuators). It transforms kinetic energy in wind into mechanical energy. For multi-megawatt turbines, dimensions are large with blade length ranging from 35-60 meters.

The drive train is formed by the turbine rotating mass, low-speed shaft, gearbox, high speed shaft and generator rotating mass. It transfers input power (turbine

mechanical power extracted by rotor blades from wind) to the point where useful power (generator mechanical power) is used. In most cases, a gearbox is required because the rotating speed of the turbine is much lower than that of the generator. For multi-MW units the gearbox ratio is about 50-100 as the typical speed range of the turbine is 10-20 rpm while for the generator it is about 1000-2000 rpm [2]. For smaller wind turbines, the turbine speed is higher, hence the gearbox ratio may be less than 50 [12].

The generator converts mechanical power into electrical power. For variable speed generators, an AC-DC-AC converter is required. Usually the generator produces power at 690 V and a transformer steps up this voltage to 33 kV for underground cable transmission [13]. The transformer may be placed at the bottom of the tower [14] or in the nacelle for losses consideration [15]. The power is then transmitted to the wind farm substation where a further voltage step-up may be done to 110 to 765 kV for long distance transmission [13].

Other components include the anemometer and vane which measure the wind speed and direction respectively. Wind speed measurement is used to start and stop the turbine. Wind direction measurement is used by the yaw-control mechanism. Devices such as electric fans and oil coolers are used to cool the gearbox and generator.

1.4 Wind Turbine Generator Concepts

The WTGs are most commonly sorted into two major categories based on the speed of rotational speed of the generator as ‘fixed speed turbines’ and ‘variable speed turbines’. From these two major categories, four WTG technologies are commercially prevalent and available for utility size applications. They are:

1. Fixed Speed WTGs with Squirrel Cage Induction Generators (SCIGs) - Type 1
2. WTGs with Wound Rotor Induction Generator (WRIG) and limited speed variation through an external resistor - Type 2

3. Doubly Fed Induction Generator (DFIG) with variable speed range - Type 3
4. Permanent Magnet Synchronous Generator (PMSG) or an induction machine (cage or wound rotor) with a full converter and variable speed range - Type 4

Of these most commonly used WTGs, type 3 or DFIG based WTG configuration is predominantly used and covers the largest market share [16]. This dissertation work will primarily focus on the control of DFIG based WTG and analysis of power grid with large penetration of type 3 WTGs.

1.4.1 Type 1 Wind Turbine Generators

The schematic of type 1 WTG is shown in Figure 1.4. In this type of WTG configuration, the induction generator is directly interconnected to the power grid. The speed of operation of the generator is determined by the gear box and the number of pole pairs of the induction generator. These are least expensive type of WTG, but also are highly rugged and reliable as there are no slip rings involved.

However, this configuration extracts sub-optimal amount of energy from the wind as they operate in a fixed speed. In addition, they require reactive power support from capacitor banks in order to not to draw magnetizing reactive current from the grid. Danish manufacturers tried to overcome the disadvantage of sub-optimal energy extraction by utilizing two generators of different ratings and pole pairs or using a single generator with two separate windings having different ratings and pole pairs [17]. This arrangement resulted in increased energy extraction and also reduced the magnetizing losses at low wind speeds, but the overall cost increases.

1.4.2 Type 2 Wind Turbine Generators

Type 2 WTGs typically include a WRIG with a variable speed external resistance connected in series with the rotor windings. A limited range of speed variation is achieved through the external resistor [17]. The torque speed characteristics of the machine can be manipulated by varying the external resistance. The rotor resistance

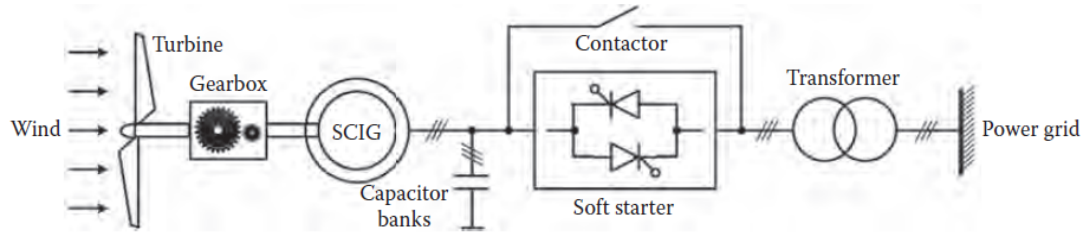


Figure 1.4: Schematic Diagram of Type 1 Wind Turbine Generator.

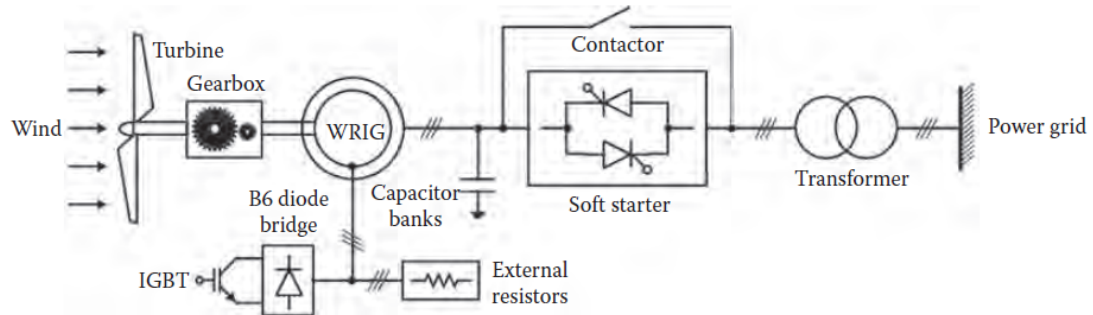


Figure 1.5: Schematic Diagram of Type 2 Wind Turbine Generator.

can be mounted on the rotor shaft and can be controlled using optical signals, which avoids the need of slip rings. The external resistor are pulsed using a DC chopper circuit with a variable duty cycle. This results in a variable resistance without any moving parts. This WTG allow the generator speed to vary within a 10% range so as to provide a constant power output even at changing wind conditions. The generator always operates at a variable slip above synchronous speed. This arrangement still lacks the ability to control the reactive power consumption independent of real power and an external capacitor bank is to be provided. In addition, the inclusion of the external resistance results in higher rotor losses, which increases with slip and limits the range of speed variation. However, there is a lesser amount of flicker associated with this WTG configuration as compared to type 1 mostly because of the flexibility of variable speed operation [17]. The schematic diagram of type 2 WTG is shown in Figure 1.5.

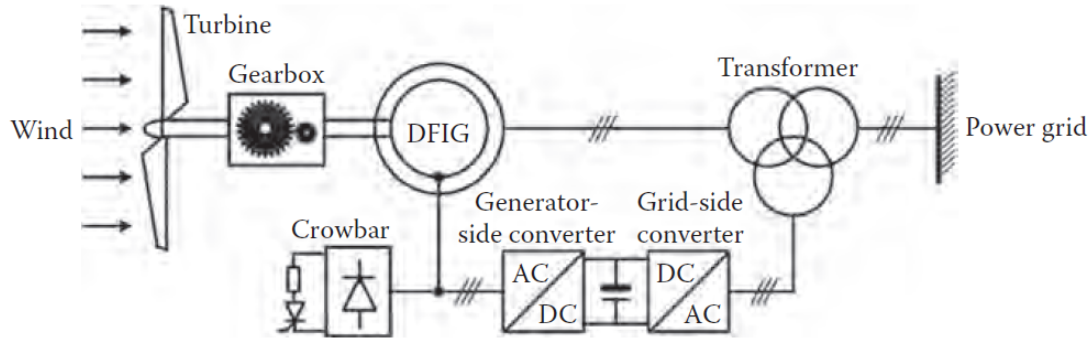


Figure 1.6: Schematic Diagram of Type 3 Wind Turbine Generator.

1.4.3 Type 3 Wind Turbine Generators

This WTG configuration consists of a wind turbine coupled with a WRIG whose rotor windings are fed with three phase converters and the stator windings are directly connected to the power grid. The turbine speed can be controlled by operating the rotor circuit at a variable frequency. The net power output of the machine is the sum total of the stator power output and the rotor power output. The rotor of DFIG consumes power from the grid when operating at a sub-synchronous speed and generates power when operating at a super-synchronous speed. And exactly at the synchronous speed, there is no power exchange between the rotor and the grid. The power electronic converters used in this WTG configuration are rated at 25% of the total system power and the rotor speed is allowed to vary $\pm 33\%$ of the synchronous speed[17]. The schematic diagram of type 3 WTG is shown in Figure 1.6.

1.4.4 Type 4 Wind Turbine Generators

This WTG configuration consists of variable speed machine equipped with a fully rated converter that interconnects the stator of the machine to the power grid. The generator could either be SCIG, WRIG or PMSG. This WTG configuration does not necessarily require gearboxes which greatly adds to the overall reliability of the WTG system and also have a wide speed range of operation. However, these WTGs are more expensive because of the fully rated power converters. This configuration

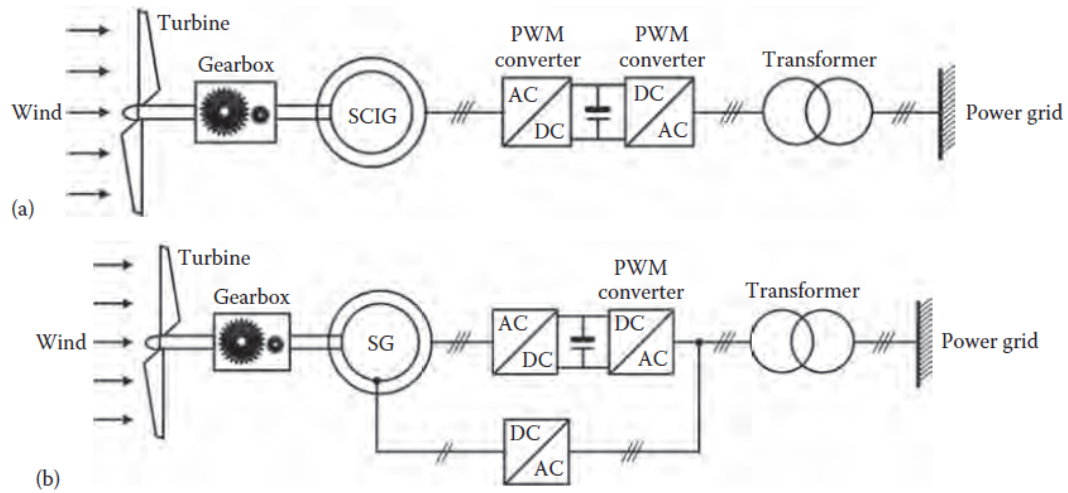


Figure 1.7: Schematic Diagram of Type 4 Wind Turbine Generator.

is rapidly growing and starting to take a large share of new wind turbine installed worldwide. The schematic diagram of type 4 WTG is shown in Figure 1.7.

1.5 Dissertation Objectives, Motivation and Contribution

1.5.1 Objectives

The objectives of this dissertation is to design a control technique that can enhance the operational reliability and stability of DFIG integrated power grid.

The research questions that will be attempted to answer in this work can be summarized as follows:

- *Sensorless Control of DFIG*: What are the techniques that enable reliable operation of DFIG? As currently installed DFIG in the grid ages, how can we enable their continued operation by augmenting their control topology? How can one augment existing control for DFIG to make DFIG control less parameter independent as possible?
- *Frequency and Voltage Support using DFIG*: How can one utilize the capability of DFIG based wind farms to provide voltage and frequency support to the power grid? How does DFIG interacts with the power grid and what impacts

it has on the small signal and transient stability of power grid? How can one utilize adaptive control framework for DFIG to enhance transient stability of the power grid?

1.5.2 Motivation

As penetration of renewable energy resources (RERs) in the power grid is continually increasing, it has become crucial to study and understand their effects on power grid along with ways to enhance their reliable operation. DFIG is the generator of choice for majority of WECS. As the first generation of DFIG based wind farms continue to age and the components used in them (especially sensors) deteriorate in performance, it has become essential to study ways to operate DFIG based wind farms without sensor so that the reliable operation of these wind farms can be maintained. In [18] the failure rate and downtimes associated with different components in WECS has been studied. It was shown that sensors and control system failure rate can contribute upto 15% of the total failures in the WECS and upto 7% of the downtime. In such a scenario, ways to increase the controller reliability and its dependency on large number of sensors should be reduced. This dissertation has attempted to solve this controller and sensor related issue of operation of WECS by designing controllers that can work with less number of sensors. Model based approach and output measurement based approach for control of DFIG based WECS has been studied and discussed in detail.

The other part of this research involves use of DFIG based wind farms for ancillary support to the power grid. As the numbers of these generators in the power grid is increasing, their use for grid support should be well studied. In this dissertation, novel control techniques considering the operational limit of DFIG based WECS has been proposed to provide active and reactive power support to bulk power grid, thus enhancing the transient stability of the renewable energy resources integrated bulk power grid.

1.5.3 Contribution

The major contributions of the dissertation can be summarized as follows:

- This dissertation discusses two novel approaches for DFIG control one is model based which assumes the proper knowledge of the DFIG model and its parameters and the other is measurement based control which doesn't require explicit knowledge of the system parameters.
- This dissertation discusses the design technique of the adaptive control for DFIG based WECS starting from the mathematical model of DFIG which provides insight for the order of system identification. Once the proper order of identified system is determined the design technique for minimum variance control is discussed in detail. The proposed system identification based adaptive control technique for DFIG is novel control technique for DFIG that minimizes the variance of system output from its reference set-point.
- The performance analysis of the proposed control techniques have been performed both in DFIG integrated in small scale power grid system and wind farms integrated large scale power grid system using real time simulators. Such tests validate the scalability of the proposed control technique for grid level applications. The dynamic models were developed and tested in various simulation platforms including MATLAB, PSCAD, PSS/E, RSCAD and Opal-RT's RTLAB.
- The proposed controller was also tested using Hardware in the Loop simulation testbed in laboratory which demonstrates the suitability of the proposed technique for industrial applications.

1.5.4 Intellectual Merit and Broader Impact

The intellectual merit of the work presented in this dissertation can be summarized as follows:

a. The proposed controller allows DFIG based WECS to operate without speed, position and current sensors. This has a significant impact on advances in the sensorless control approach for type 3 WECS. Studies conducted on existing WTG topologies has shown that around 20% of failures in the WTG is associated with the sensors and control techniques used in WTG control. Proposed sensorless operation with estimated speed and current quantities can help augment the operation of existing DFIG control as well as increase the share of DFIG based WECS in power grid.

b. The proposed controller technique is machine parameter independent and is solely based on the measurement feedback. As the WTG age, the machine parameter tends to deviate from nominal values which causes the performance of existing controller to degrade. With the proposed control technique, WTGs can be used for a longer period with controller recalibration as the controller adapts itself with the changes in machine parameters.

c. The proposed control technique can be used initially as a backup control topology along with the existing control topology in WTG and can eventually substitute the sensed control of WTG. The control technique presented thus increases overall reliability of DFIG based WECS. This might lead to paradigm shift in the way the future wind turbines will be controlled.

d. The power system oscillation damping control technique proposed in this research is not designed to damp a specific range of frequency, instead can damp any frequency of interest. This is especially crucial as with the increased penetration of renewable energy the system operating point is more dynamic and the modes of oscillation change rapidly over time. Thus, the proposed damping control scheme is crucial for next generation of power grid with large scale integration of renewable

energy resources.

The broader impact of the research work presented in this work can be summarized as follows:

a. The proposed control approach can be used in any type of renewable energy resources which are variable/ intermittent in nature. The adaptive nature of proposed control is well suited for applications with frequent changes in operating conditions.

b. The proposed control technique facilitates increased penetration of renewable energy, thus help achieving the goal of utilizing cleaner sources of energy to meet our energy needs and reduce the emission of green house gases and minimize global warming. Also any of the societal benefit that can be associated with increased penetration of wind energy can also be attributed to this research as the work performed here helps in at least maintaining if not enhancing the dispatchability of DFIG based WECS.

1.5.5 Dissertation Organization

Chapter 1 provides an introduction to wind energy conversion systems and various types of wind turbine generators. The objectives, motivation and contribution of the dissertation is presented in Chapter 1. Chapter 2 introduces various control topologies that has been reported in literature for DFIG control. Chapter 3 discusses the design of state observer and state feedback control technique for DFIG along with the test results. Chapter 4 discusses the design and operation of speed sensorless control of DFIG. Current sensorless control approach for DFIG is presented in chapter 5. Use of large scale DFIG based wind farms to provide reactive power support to bulk power grid along with reactive power support capability of DFIG is presented in chapter 6. Chapter 7 studies the impact on small signal stability of test power grid with different wind farm penetration and proposes a novel system identification based damping controller to damp the electromechanical modes of oscillation in the power grid. Conclusions and future works are discussed in chapter 8.

CHAPTER 2: LITERATURE REVIEW: CONTROL TECHNIQUES FOR DFIG BASED WECS

In the past, wind power production did not have much impact on the power system operation and control, but now as the wind energy penetration is increasing steadily, the impact of WECS in the grid are to be considered for stable operation of the grid[19]. This has demanded the development of WECS with higher efficiency and more controllability. Also, the recent grid codes require the WECS to operate in a way conventional synchronous generator operate. The technology used for wind energy harvesting has evolved from a SCIG to PMSG with full rated power electronic converters. The advances in power electronics have changed the basic characteristic of the wind turbines from being an energy source to an active power source [20].

It has been shown in [21], a fixed speed wind energy system, even though more simple and reliable, severely limits the energy output of a WT developing more fluctuations in the power output due to the fact that there is no torque control loop. In case of variable speed systems for a machine of similar rating such as DFIG, energy capture can be significantly enhanced. For example in DFIG, the rated torque can be maintained even at super-synchronous speeds whereas, in a fixed speed system with SCIG, field weakening control has to be employed beyond synchronous speed, leading to torque reduction. It has been concluded that a variable speed system using DFIG is superior because of higher energy output, lower rating of converters (hence, lower cost) and better generator utilization as compared to fixed speed wind generator systems [14].

DFIM also known as the wound rotor or slip ring induction machine, is an induction machine with windings on both stator and rotor [22, 23] . The DFIM is one of the

most popular system used in WECS. The reason behind the popularity of DFIMs in wind energy applications is that relatively small power converters are required to control the generator. For a typical DFIG, the power converters are connected to the rotor circuit and used for a restricted speed range, with ratings as a fraction (usually 30%) of the machine nominal power. Typically, slip rings are required in order to connect the RSC to the rotor. Because of the popularity of DFIGs for wind energy generation, control systems suitable for this application have been extensively investigated. The goal of this chapter is to present an overview on the recent advances in the field of DFIG control designs under various operational circumstances and at the same time discuss the field of research which can be pursued to enhance the performance of DFIG as generator of choice for WECS.

2.1 Control Techniques for DFIG

2.1.1 Vector Control (VC) of DFIG

The VC technique is widely used for control of induction machines [24] and has been extended to control of DFIGs [25]. In squirrel cage induction machine (SCIM), the VC is achieved by controlling the direct and quadrature ($d-q$) axis stator currents using an inverter and by aligning the $d-q$ rotating reference frame with the rotor flux. However, in case of DFIG, the rotor is fed through an inverter, and the rotor currents are controlled using a rotating reference frame aligned with the stator flux [25]. Some variations of VC is reported in literature where the rotating reference frame is aligned with the stator voltage vector instead of stator flux vector [14].

When using the stator flux oriented reference frame, the electrical torque is proportional to the q -axis rotor current, so q -axis rotor current can be regulated to control the torque of DFIG and hence the active power. Likewise, the d -axis rotor current can be used to regulate the reactive power flow of the machine. The machine equations for a DFIG in a synchronously rotating reference frame in p.u. assuming generator convention is given by set of equations (from [26]) presented in (A.1) and (A.2).

For VC of DFIG, it is important to know the position of the stator flux (θ_s) and position of rotor (θ_r). Knowing the position of the stator flux (θ_s) and rotor (θ_r), one can compute the slip angle (θ_{sl}), which is used to transform the rotor current and voltage into $d - q$ rotating reference frame. Mathematically,

$$\theta_{sl} = \theta_s - \theta_r \quad (2.1)$$

The position of the stator flux vector θ_s can be obtained from the stator flux $\alpha - \beta$ components as:

$$\theta_s = \tan^{-1} \left(\frac{\Psi_{\beta s}}{\Psi_{\alpha s}} \right) \quad (2.2)$$

where $\Psi_{\alpha s}$ and $\Psi_{\beta s}$ are the stator flux components in $\alpha - \beta$ reference frame.

Further the $\alpha - \beta$ components of the stator flux can be calculated from the stator voltages and currents as,

$$\begin{aligned} \Psi_{\alpha s} &= \int (v_{\alpha s} - R_s i_{\alpha s}) \\ \Psi_{\beta s} &= \int (v_{\beta s} - R_s i_{\beta s}) \end{aligned} \quad (2.3)$$

where, $v_{\alpha s}$ and $v_{\beta s}$ are the stator voltage components in $\alpha - \beta$ reference frame, $i_{\alpha s}$ and $i_{\beta s}$ are the stator current components in $\alpha - \beta$ reference frame and R_s is the stator resistance.

The expression in (2.3) requires an integrator, which in practical implementations are replaced by a low pass filter with a low cutoff frequency of 0.1 to 1 Hz. Because the stator voltages and currents are 60 Hz signals, the performance deterioration due to integral action is negligible [27].

The control strategy for a typical VC technique is shown in Figure 2.1. It can be seen that the active power from DFIG is controlled using q -axis rotor current and

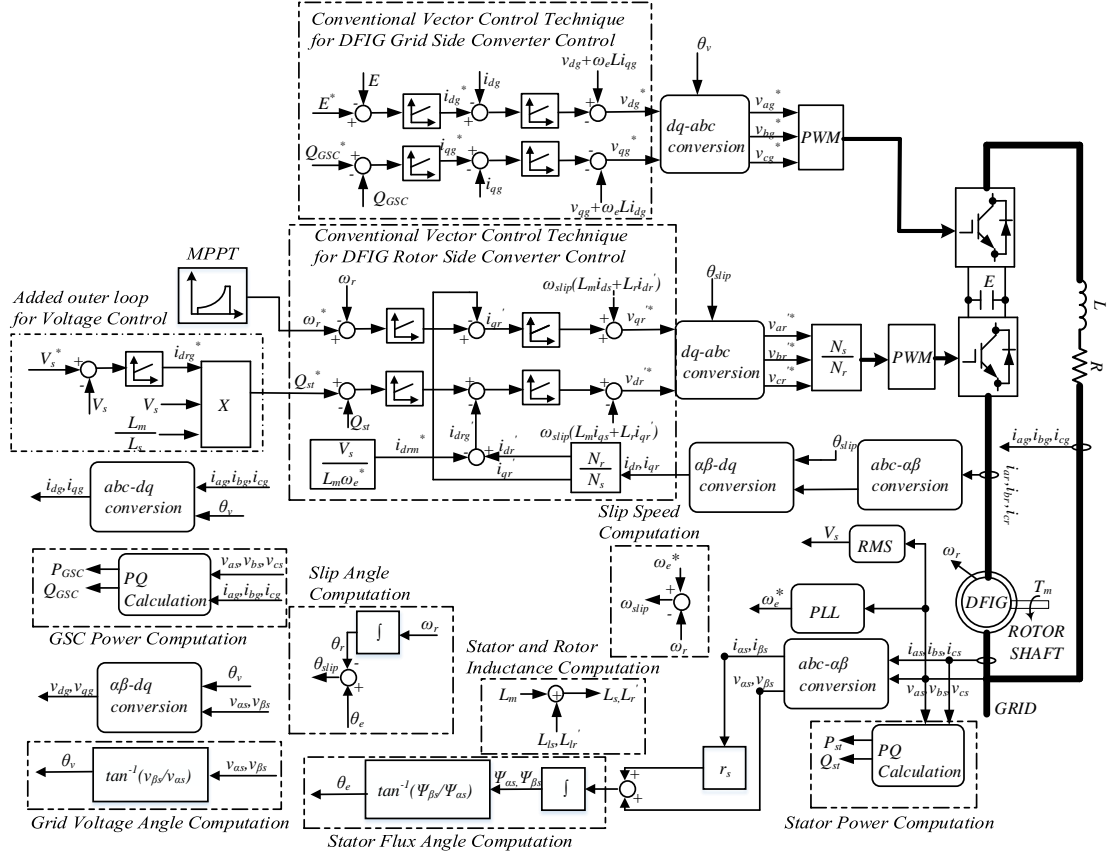


Figure 2.1: Schematic Diagram Representation of Conventional Vector Control of DFIG.

the reactive power generated by DFIG is controlled using d -axis rotor current. The control for the GSC which is used to control the DC link voltage E at a constant value is also shown in Figure 2.1. The GSC can also be used to provide additional reactive power support to the grid as the need arises.

2.1.2 Direct Torque Control (DTC) of DFIG

The direct torque control (DTC) technique, widely applied to SCIM, has also been used to control DFIG because of the good dynamic performance it achieved in [28, 29, 30, 31, 32, 33, 34]. ASEA Brown Boveri (ABB) has been a pioneer in applying DTC techniques in DFIG used for wind energy applications [16]. In DTC, a two-level voltage source converter (VSC) imposes six active vectors and two zero vectors at the

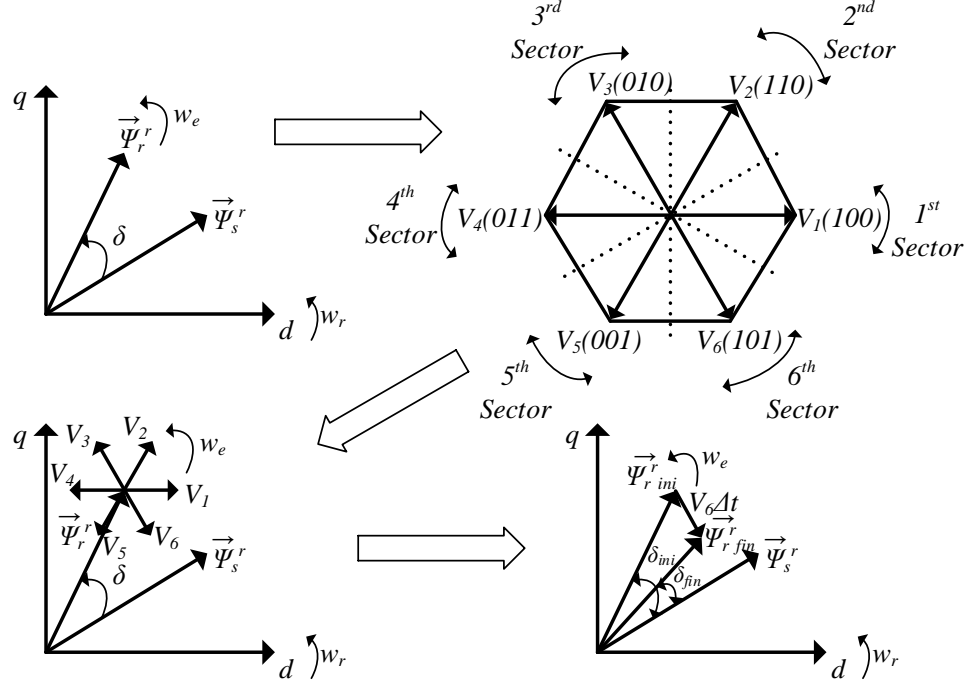


Figure 2.2: Vector Diagram Showing Principle of Direct Torque Control Technique of DFIG.

machine rotor terminals. These voltage vectors when applied for time Δt , produce changes in the rotor flux vector both in magnitude and phase with respect to stator flux vector. This provides required change in the torque produced by the machine and the reactive power generated by the machine [22].

From (A.1), it can be seen that in the rotor reference frame:

$$\vec{v}_r^r = R_r \vec{i}_r^r + \frac{d\vec{\Psi}_r^r}{dt} \quad (2.4)$$

where \vec{v}_r^r is the voltage applied to rotor windings as seen in rotor reference frame, \vec{i}_r^r is the current flowing into the rotor windings as seen in rotor reference frame, $\vec{\Psi}_r^r$ is the rotor flux as seen in rotor reference frame and R_r is the rotor winding resistance.

If the voltage drop in the rotor winding resistance R_r is neglected, (2.4) can be

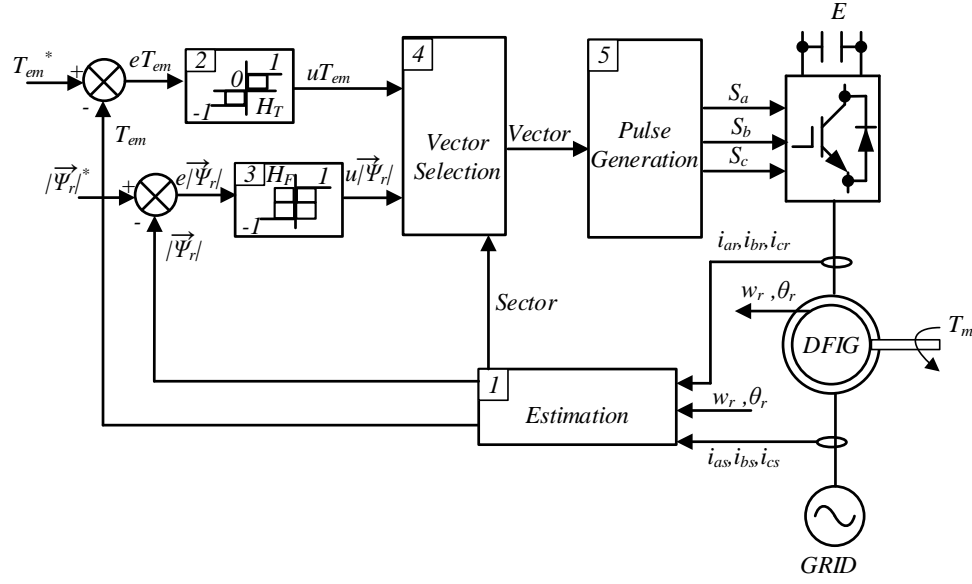


Figure 2.3: Schematic Diagram Showing Direct Torque Control Technique of DFIG.

approximated as,

$$\vec{v}_r^r \cong \frac{d\vec{\Psi}_r^r}{dt} \quad (2.5)$$

From (2.5) above, it can be seen that the rotor flux can be manipulated by applying proper rotor voltage. Assuming a constant time injection Δt , the approximated relation between the magnitude of initial and final flux can be written as,

$$|\vec{\Psi}_r^r|_{fin} \cong |\vec{\Psi}_r^r|_{ini} + \int_0^{\Delta t} \vec{v}_r^r dt \quad (2.6)$$

If the injected rotor voltage is assumed to be constant for small time instant Δt , rotor flux magnitude can be approximated as,

$$|\vec{\Psi}_r^r|_{fin} \cong |\vec{\Psi}_r^r|_{ini} + \vec{v}_r^r \Delta t \quad (2.7)$$

The electrical torque is proportional to the cross product of stator and rotor flux

vectors, i.e.,

$$T_e = k_t \Psi_s \otimes \Psi_r = k_t |\Psi_s| |\Psi_r| \sin(\delta) \quad (2.8)$$

where k_t is a constant dependent on the machine parameters and δ is the angle between stator and rotor flux.

Assuming grid connected operation of DFIG, the stator voltage and hence stator flux can be assumed constant [14]. From (2.8), it can be seen that the torque magnitude can be controlled to a desired value by controlling the rotor flux amplitude, $|\Psi_r|$, and angle δ between rotor flux and stator flux. Thus, if a rotating rotor flux is created which maintains an angular distance of δ with the synchronously rotating stator flux, the torque produced by the machine can be controlled. And, the desired rotor flux magnitude can be created by applying appropriate rotor voltage as seen in (2.7). Depending on the position of the rotor flux and a desired change in the electrical torque and rotor flux magnitude, there is an optimum voltage vector to be applied to the rotor windings of the machine [23, 31].

In order to implement DTC, it is necessary to know the rotor flux vector in magnitude and angle, and the electrical torque. The rotor flux can be obtained using (A.2) in $d - q$ reference frame which can be transferred to $\alpha - \beta$ reference frame to the $\alpha - \beta$ components of the rotor flux. Once that is achieved the magnitude and angle can be obtained as,

$$\begin{aligned} |\Psi_r| &= \sqrt{\Psi_{dr}'^2 + \Psi_{qr}'^2} \\ \angle \Psi_r &= \tan^{-1} \left(\frac{\Psi_{\beta r}}{\Psi_{\alpha r}} \right) \end{aligned} \quad (2.9)$$

where, Ψ_{dr}' and Ψ_{qr}' are the d -axis rotor flux component and q -axis rotor flux component respectively, $\angle \Psi_r$ is the rotor flux position in the vector space and, $\Psi_{\alpha r}$ and $\Psi_{\beta r}$ are the rotor flux components in $\alpha - \beta$ reference frame.

Figure 2.2 illustrates the operating principle of DTC. It can be observed that by

applying rotor voltage vector V_6 , the $|\vec{\Psi}_r^r \sin(\delta)|$ component is reduced which in turn reduces the torque generated by the machine as seen from (2.8).

The control diagram of a standard DTC strategy is shown in Figure 2.3. As seen in Figure 2.3, the control strategy is divided into five different blocks:

1. Estimation block: The estimation block estimates the current magnitude of the rotor flux and the electromagnetic torque generated by the machine. It also estimates the position of the rotor flux with respect to the stator flux along with the current position of the rotor flux in the vector space i.e the sector in which the rotor flux is located.
2. Torque ON-OFF Controller: Based on the torque error, a three level hysteresis controller with H_T hysteresis band is implemented. Depending on the value of the torque error, the output uT_{em} can take a value of -1, 0 or 1. $uT_{em} = 0$ means a zero rotor voltage vector requirement.
3. Flux ON-OFF Controller: Based on the rotor flux magnitude error, a two level hysteresis controller with H_F hysteresis band is implemented. Depending on the flux magnitude error, $e|\vec{\Psi}_r^r|$, the output $u|\vec{\Psi}_r^r|$ can take a value of 1 or -1.
4. Vector Selection: This block selects the proper rotor voltage vector that is required to be applied to the rotor windings to get the desired control on the rotor flux magnitude and the torque.
5. Pulse Generation: This block basically generates the proper switching signals such that the required voltage vector is applied to the rotor windings.

Finally, it should also be mentioned that the proper rotor flux magnitude reference is generated based on the reactive power required to be generated by the machine. The following equation represents the relation between the rotor flux magnitude ad

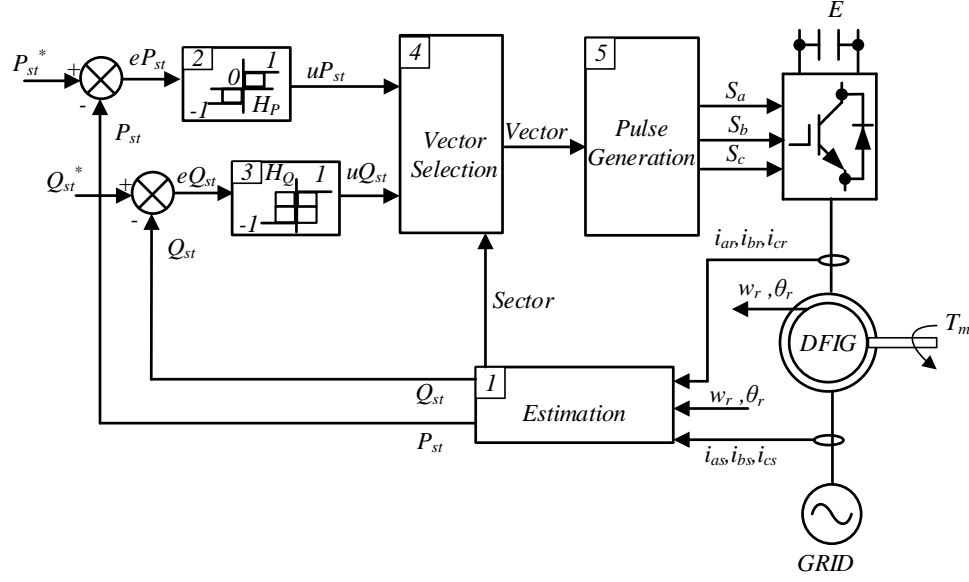


Figure 2.4: Schematic Diagram Showing DPC Technique of DFIG.

the reactive power required and the torque generated by the machine [22, 35].

$$|\vec{\Psi}_r^{r*}| = \sqrt{\left(k_1 |\vec{\Psi}_s| + k_2 \frac{Q_{st}^*}{|\vec{\Psi}_s|}\right)^2 + \left(k_3 \frac{T_{em}^*}{|\vec{\Psi}_s|}\right)^2} \quad (2.10)$$

where k_1, k_2, k_3 are the constants dependent on the machine parameters.

2.1.3 Direct Power Control (DPC) of DFIG

The DPC of DFIG follows the same principle as DTC, the major difference being the controlled variable which are the stator active power (P_{st}) and reactive power (Q_{st}). The active power generated by DFIG, assuming stator flux orientation of the rotating reference frame and manipulating (A.1) and (A.2) is given by,

$$P_{st} = v_{qs} i_{qs} = |V_s| \left(\frac{L_m}{\sigma L_s L_r} \Psi_{qr} \right) = \frac{L_m}{\sigma L_s L_r} |\Psi_s| |\Psi_r| \sin \delta \quad (2.11)$$

Likewise, the reactive power generated by DFIG is given by

$$Q_{st} = v_{qs}i_{ds} = \frac{|\Psi_s|}{\sigma L_s} \left[\frac{L_m}{L_r} |\Psi_s| - |\Psi_r| \cos \delta \right] \quad (2.12)$$

where δ is the angle between stator flux vector and rotor flux vector. Assuming constant stator voltage and hence stator flux, the above equations can be written as,

$$\begin{aligned} P_{st} &= K_1 |\Psi_r| \sin \delta \\ Q_{st} &= K_2 [K_3 - |\Psi_r| \cos \delta] \end{aligned} \quad (2.13)$$

From (2.13), it can be seen that the stator active and reactive power can be properly controlled by controlling the rotor flux magnitude and the angular position of rotor flux vector with respect to stator flux vector [22, 31, 36, 37, 38, 39]. Like in DTC, hysteresis based controller are used to control the active and reactive power of the stator. The hysteresis used can be either two level or three level [31, 38]. As in DTC, DPC also requires the measurement of both stator and rotor currents and also estimation of rotor flux position. The dependency of the DPC technique in machine parameters is studied in [40] and a modified technique to make DPC control technique robust to parameter variation is presented. A schematic of DPC control technique is shown in Figure 2.4. A variation of DPC in which rotor current measurements are not required, as stator flux position is referred to rotor reference frame is presented in [38].

2.1.4 Rotor Flux Magnitude and Angle Control of DFIG

In [41, 42], a new control strategy is investigated, known as rotor Flux Magnitude and Angle Control (FMAC), for DFIG. It exercises control over the generator terminal voltage and output power by adjusting the magnitude and angle of the rotor flux vector. The operating vector diagram of the DFIG as presented in [41] is shown in Figure 2.5. Even though it has been claimed that this control strategy leads to low

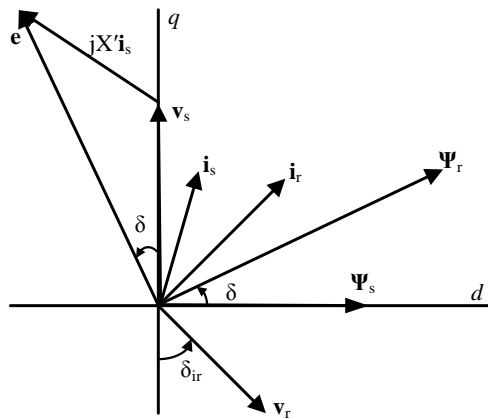


Figure 2.5: Vector Diagram Representation of DFIG Operating Conditions.

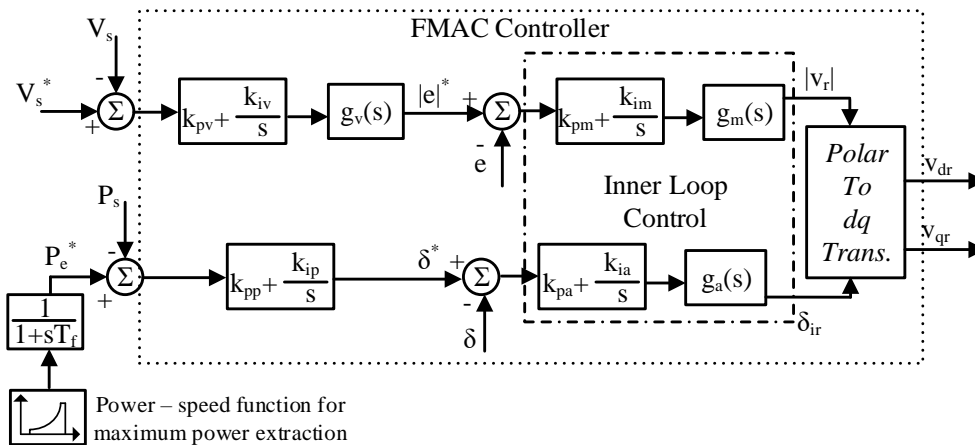


Figure 2.6: Schematic Diagram of the Rotor Flux and Magnitude Control of DFIG.

interaction between the power and voltage control loop, in actual case this form of controller has more active power and reactive power interaction. In the control loop in Figure 2.6, reactive power is shown to be dependent on rotor flux magnitude only and active power dependent on rotor flux angle with respect to stator flux, which is not a valid assumption as seen from (2.13).

In [43], it has been shown that the rotor FMAC technique is less robust as compared to the vector control and the controller design is more complicated as compared to VC because of the Right Hand Side Plane (RHP) zeros in the voltage control loop. The

other disadvantage of the rotor flux magnitude and angle control is its inability to control the machine at a speed close to synchronous speed. The rotor FMAC control technique requires the operational speed of DFIG to be distinct from synchronous speed. Figure 2.6 shows the control schematic of the rotor FMAC controller.

2.1.5 Rotor Resistance Control of DFIG

As seen from (A.4), the electromagnetic torque produced by DFIG can be controlled by the rotor current injected. And, the rotor current injected can in turn be controlled by varying the equivalent rotor resistance of the DFIG. In [44], it has demonstrated that by adding a variable external resistance to the rotor of an induction generator used in a wind turbine, it is possible to manipulate the torque-speed curve and control the output power. In [44], it has been proposed to place a three-phase diode bridge and a DC chopper with a variable duty cycle to vary the equivalent rotor resistance such that the slip rings to access the rotor windings can be avoided. The range of operation of this form of control is narrow and mostly above the synchronous speed. Also this scheme is not practically sensible as large amount of power that can be transferred from rotor windings to grid when operated in super-synchronous mode is basically dissipated in the external resistors decreasing the overall efficiency of the WECS.

Even though the use of external resistors for speed control of induction generator is now considered obsolete, some of the commercially available WTG still use this form of control. Vestas, a leading wind turbine manufacturer uses this kind of control in some of its wind turbine (e.g Vestas V39-600, V66-1.65 MW) [16]. In [45], the authors have compared the performance of ‘Optislip’ scheme and vector control for DFIG, in which it has been concluded that ‘Optislip’ provides a narrow range of speed variation as compared to VC of DFIG. Figure 2.7 shows the control schematic of ‘Optislip’ wind system [46]. As the range of operation for ‘Optislip’ is low, it has been shown that the ‘Optislip’ scheme has more power fluctuations as wind speed

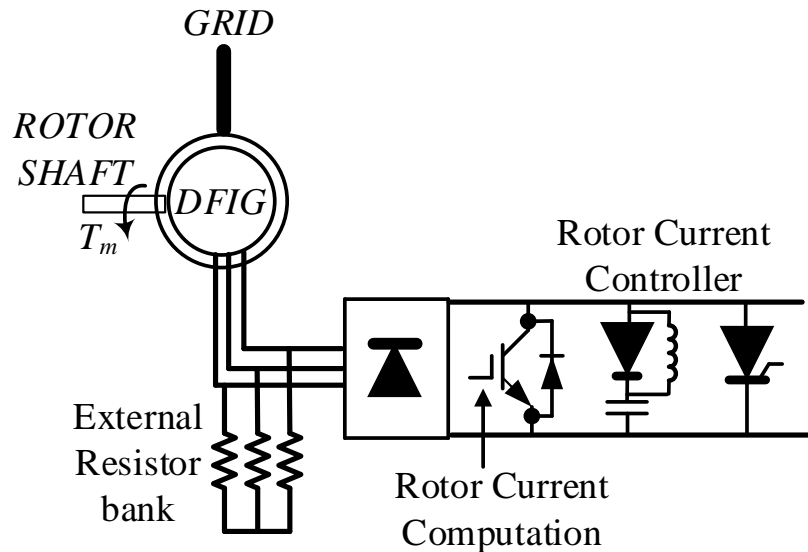


Figure 2.7: Schematic Diagram of the OptiSlip Control of DFIG.

changes as compared to VC for DFIG.

In [46], a comparison of the performances between the ‘Optislip’ pitch regulated wind system (Vestas V39-600) and a fixed speed stall regulated wind system of the same power is performed. It has been concluded that, under grid disturbances, ‘Optislip’ controlled wind turbines have larger stability domain as compared to fixed speed wind turbines and has less power fluctuations as compared to fixed speed systems there by releasing the unwanted pressure and stress to the mechanical parts of the wind turbines. The other major disadvantage of the ‘Optislip’ control technique is its inability to control the reactive power consumed/generated by machine. So a wind turbine implementing ‘Optislip’ control scheme requires an external reactive power compensation device increasing the cost of the system [47].

2.1.6 State Feedback Control (SFC) of DFIG

SFC of DFIG based on the state space representation of the machine is studied in [48, 49]. In this control scheme, a reduced order state space representation of the

machine is derived based on the rotor currents as states, rotor voltages as input and the stator side active and reactive power as outputs. This form of control has been shown to have good dynamic performance as compared to the existing VC technique in [48, 49]. State observers based SFC and VC technique for DFIG is studied in this dissertation.

All the control technique of DFIG discussed so far have been well documented in the literature. The classification of the various control technique discussed in this chapter in measurement based and model based category is shown in Figure 2.8. All these strategies provide good overall performance with little nuance of superiority over one another. A fair comparison would have to include dynamic and steady state performances, current ripple content, and losses in the converters. The VC approach is based on the machine model and is more parameter dependent: the implementation complexity might be higher; currents, voltages, and position need to be measured (although implementation without encoder is feasible) [16]; and the current control dynamics are reasonable with no high sampling frequency. On the other hand, DTC implementation is simpler, even if it is a model-based approach, and is less dependent on machine parameters: high torque dynamics can be achieved, but higher non-constant switching frequencies are typical; a higher current ripple is expected, higher bandwidth of current and voltage sensors are needed and rotor position needs to be measured. Finally, DPC could be even simpler to implement: good power dynamics can be achieved with high variable switching frequency; a higher current ripple is usual and higher bandwidth of current and voltage sensors are also needed, but rotor position does not need to be measured [16].

2.1.7 Control of GSC

The GSC of DFIG is a voltage source converter with a primary aim to maintain the DC link voltage and is operated at unity power factor mode [25]. However, GSC can also be used to provide additional reactive power support to the grid as

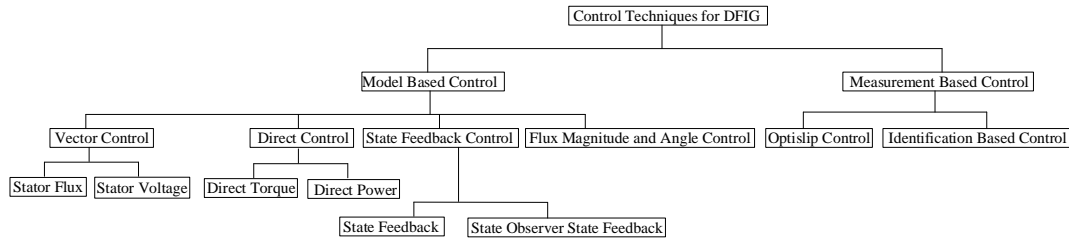


Figure 2.8: Classification of Different Control Techniques for DFIG.

need arises. A stator voltage oriented VC is generally used to control the GSC which enables independent active and reactive power control [25, 50]. The GSC is current regulated with d -axis current regulating the dc-link voltage and q -axis current regulating the reactive power. Alternatively, DPC can also be applied to control of GSC, which also is the decoupled control of active and reactive power [36, 51, 52, 53]. The schematic diagram of GSC is shown in Figure B.1 and the VC technique for GSC is shown in Figure 2.1. Other control strategies that have been proposed for GSC ranges from Proportional Integral (PI) control, hysteresis control, constant switching frequency control, space vector modulation based control, direct power control, grid impedance identification based control, and proportional resonant (PR) control [54, 55, 56, 57, 58].

While PI controller designs are limited to operating at a fixed bandwidth, hysteresis controllers fail to perform well in wider operating ranges as the inverter design is more complex to account for uneven losses due to uneven switching frequency. VC of GSC can achieve optimal mode switching with constant switching frequency and lower losses. However, design of VC is complex and cascaded PI controllers in these designs have limited operating margin as they are designed around a steady operating point. Also as the renewable energy sources are variable and/or intermittent, the vector control cannot be optimized for all operating regions of the inverter. These designs are thus unable to cope with sinusoidal reference signals and periodic disturbances [59]. Further more, the PI controllers have poor disturbance rejection features due to

oversimplifications, loss of performance in the control law, and complications brought due to constant gain derivative and integral actions [60].

Other forms of controllers except for PR designs (such as direct power control, space vector modulation based control and grid impedance identification control) also uses fixed bandwidth based PI designs. PR controllers can enhance the inverter tracking performance, thus bandwidth limitations in conventional PI designs can be alleviated if such controller are designed. However for grid forming mode with strict requirements for the controllers' stability, dynamic capability, and static tracking accuracy, conventional PR designs may perform unsatisfactorily [61]. Ref. [62] proposed an adaptive notch filter-based multipurpose control scheme for grid interfacing inverter under corrupted grid conditions.

2.1.8 Pitch Control of DFIG

Variable pitch control can be used to shed the aerodynamic power captured by the wind turbine. Thus, the aerodynamic power produced by the wind turbine can be controlled by adjusting the pitch angle of the wind turbine. The pitch angle control also helps to maintain the rotor speed at its maximum value. As the pitch control basically acts by moving the turbine rotor blades, it is a slow control because of large inertia of the blades. Because of the slow control, the DFIG rotor accelerates or decelerates due to the mismatch between the electric power and aerodynamic power. As the rotor accelerates or decelerates, it stores or supplies power from its inertial energy. The inertia of the rotor behaves like an inductor in an electrical circuit. It helps smooth the rotor speed variation, and it stores energy during acceleration and restores energy during deceleration [63]. Figure 2.9 shows a typical pitch control technique implemented in wind turbines.

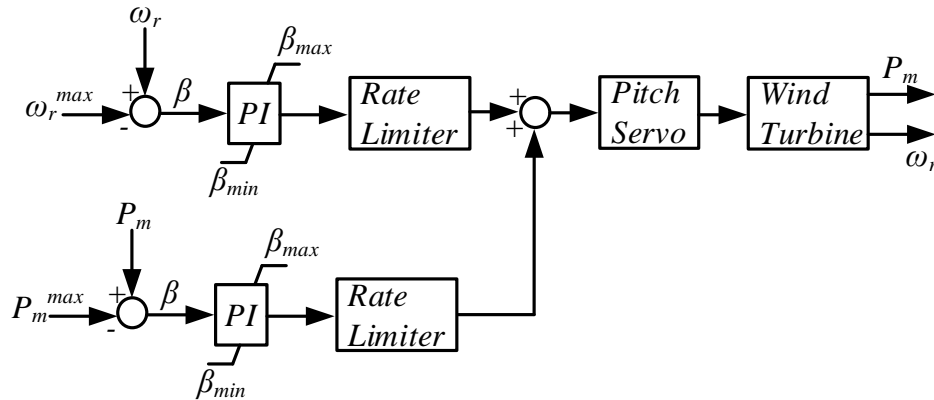


Figure 2.9: Pitch Control Technique for a Wind Turbine System.

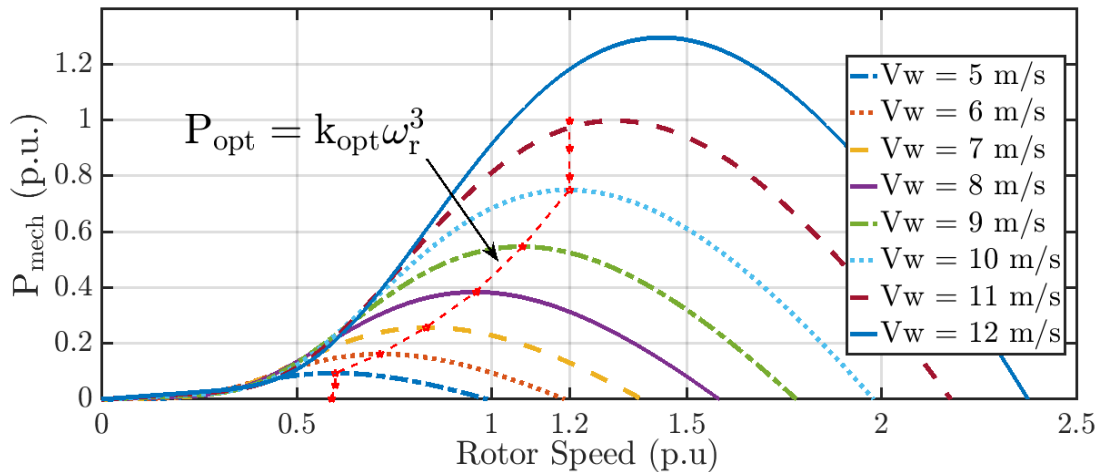


Figure 2.10: Typical Power Speed Curve for a Wind Turbine.

2.1.9 Maximum Power Point Tracking (MPPT) Control

Due to the stochastic nature of the wind, it is desirable to determine the one optimal generator speed that ensures maximum energy yield. A typical power speed profile for a wind turbine generator is shown in Figure 2.10. Figure 2.10 also shows the variation of power output of wind turbine as the wind speed varies. It can be seen that for every wind speed there is a maximum power that can be extracted from the wind turbine by properly adjusting the rotor speed of the generator. The optimal power P_{opt} related to the rotational speed of the generator can be approximated by

the following non-linear relation:

$$P_{opt} = k_{opt}w_r^3 \quad (2.14)$$

where k_{opt} is a function of the parameters of the turbine. e.g. gearbox size, blade radius, blade profile etc. In [64], various MPPT techniques for wind turbines are studied. The available MPPT algorithms can be classified as either with or without sensors, as well as according to the techniques used to locate the maximum peak. Based on simulation results available in the literature, the optimal torque control (OTC) has been found to be the best MPPT method for wind energy systems due to its simplicity. On the other hand, the perturbation and observation (P&O) method is flexible and simple in implementation, but is less efficient and has difficulties determining the optimum step-size. The optimum torque could be controlled as,

$$T_{opt} = k_{opt}w_r^2 \quad (2.15)$$

In [65], a new MPPT algorithm based on the linear relationship between V_{dc}^2 and I_{dc} is developed which is shown to have faster tracking speed and better performance, and is proposed to be suitable for system with high wind turbine inertia. Please refer [66, 67, 68], for a detailed analysis of the existing MPPT algorithms.

2.2 Speed Sensorless Control of DFIG

One of the main issues related to variations in operation of DFIG is attributed towards malfunctions of position and speed sensors of the machine. The main causes are defective sensors and noise generated due to wear and tear. Also, the position encoders used in DFIG has several drawbacks in terms of robustness, reliability, cost, cabling and maintenance [69]. A ‘true’ sensorless operation requires the DFIG to be operated without the use of speed sensors, position encoders and anemometers. This sensor-less method should then be controlled using the same topology that is used for

control with sensors [70]. As most of the existing windfarms uses DFIG, the need to overcome these issues is critical.

Earlier works in sensorless control of DFIG were mostly based on open loop sensorless methods. In those techniques, the rotor position was derived by comparing the estimated and measured rotor currents and the rotational speed was obtained through differentiation [71, 72, 73, 74]. The problem with these techniques are that they are used in open loop and thus do not consider feedback error thus failing to determine whether the estimation error is decreasing. This will develop cumulative errors in estimation making the approach not feasible to implement in real-life scenarios. Also, the speed obtained using this method is generally noisy.

Recently, closed loop feedback error based speed estimation methods have been proposed and successfully implemented. In one approach, model reference adaptive system (MRAS) observer based on two models, the reference model and an adaptive model are presented in [69, 75, 27, 76, 77]. In another approach, sensorless control of DFIG based on phase locked loop (PLL) is proposed in [70, 78, 79], and a hysteresis controller is used in place of conventional Proportional Integral (PI) controller as a rotor current observer. The idea of PLL based estimator is similar to that of MRAS based estimator as both drive the error to zero when the phase shift between estimated vector and reference vector is equal to zero. In [80], a speed adaptive reduced order observer was also designed for sensorless control of DFIG.

There are mainly three main issues that has not yet been attended by the current-state-of-the-art in this research direction. First, the closed loop speed estimation approaches are mainly static model based designs thus making the estimation susceptible to model failures. Second the existing feedback speed estimation approaches are sensitive to parametric changes in the machine. Third, the speed error in these approaches are minimized by tuning a static controller (such as PI controllers), thus making the architecture less robust to input/output variations. Thus, the perfor-

mance of most of these techniques deteriorates when the machine parameter changes. A detailed analysis of the effect of the machine parameter variation in the speed estimation is demonstrated in [80]. In [81], a rotor current based angle estimator is proposed assuming that the value of stator inductance ' L_s ' is known. However, knowledge of ' L_s ' depends on knowing L_m which plays a dominant part in affecting the ' L_s ' value. Similarly, in [82], the authors proposed a back Electromotive-Force (EMF) MRAS-based sensorless control scheme for a grid-connected DFIG. However, the proposed scheme is also dependent on knowledge of machine mutual inductance, ' L_s ' as well as rotor resistance ' R_r '. The change in machine mutual inductance ' L_m ' greatly affects the performance of the speed estimators, especially when using with model based techniques. Hence, it is important to design the speed estimators coupled with machine parameter estimation techniques. A technique to enhance the performance of sensorless operation is presented in [83], where the machine mutual inductance is estimated based on the magnitude of measured and actual rotor currents.

Recently, our research group has proposed speed estimation based on system identification using RLS techniques and designing controllers that provide speed estimate using the identified parameters. The advantage of identification based technique is that it avoids the need for system models and accommodates changes in the system's operating conditions. In [84] an adaptive self-tuning PID based speed estimator using recursive least squares identification was proposed. However, experimental validation of the proposed technique was not reported and also the analysis of the proposed technique was not presented. In [85], a comparison between existing MRAS based speed estimation technique and MVC based estimation technique was presented. It was shown that static controller based MRAS technique has slower performance as compared to identification based technique. Also, it was demonstrated that inability of conventional techniques for faster estimation of rotor position affects the controllability of machine active and reactive power. This dissertation proposes a technique

to solve the problem of DFIG rotor speed estimation and its dependency on accurate knowledge of ' L_m ' by estimating ' L_m ' itself.

CHAPTER 3: MODEL BASED APPROACH: ROTOR CURRENT SENSORLESS STATE ESTIMATORS BASED STATE FEEDBACK CONTROL OF DFIG

This chapter introduces a reduced order state observer architecture for DFIG which is then used to provide estimated feedback signals that can be applied to various existing control topologies used for DFIG control. The state feedback control has been designed for control of both RSC and GSC. Also, the state estimators are applied to both the converters. The observers are developed based on the mathematical model of the DFIG. It has been shown that the proposed controller simplifies the controller design process and also performs better in terms of lower interaction between active power and stator terminal voltage control. In this chapter, an architecture to augment the existing control topology of wind farms is developed so that the dependency of the existing controls on sensors can be reduced. Also, such augmented control topology in use will be able to accommodate the grid requirements as necessitated by the new grid codes [16]. The main advantages of the proposed architecture are:

- The methodology does not require rotor current measurements thus independent on sensor malfunctions or failures.
- The method is simpler than conventional DFIG control and perform well during the changing grid dynamics.
- The approach is scalable and can be implemented in real systems interconnected with larger power grid.

In this chapter, the real time simulation results for a DFIG connected to a grid through a transmission line has also been presented along with HIL simulation on a laboratory set-up and the capabilities of the proposed controller are discussed.

3.1 State Feedback Control (SFC) for DFIG

The control scheme presented in this chapter, relies on the reduced 2^{nd} order state space representation of DFIG for control of terminal voltage and active power output. The state feedback control law drives the states ($d-q$ axis rotor current) to the desired values by manipulation of the input ($d-q$ axis rotor voltage). Likewise, for the DC link voltage control, the GSC was also controlled based on the state feedback law with the inverter output current as states implemented on the average model based state space representation of the converter. The controllability and observability of the system has also been investigated before the design of state feedback controllers and state observers.

The mathematical model of a DFIG in synchronously rotating reference frame in $d-q$ axis has been presented in Appendix A. The mathematical representation of a GCI is presented in Appendix B.

The following assumptions are to be considered before proceeding with the state feedback controller design [86, 87].

- The pair $(A - BK, B)$ for any $o \times n$ real matrix K is controllable if and only if the pair (A, B) is controllable, where o is the order of the inputs and n is the order of states.
- All eigenvalues of $(A - BK)$ can be assigned arbitrarily, provided complex eigenvalues are assigned in conjugated pairs, by selecting a real constant K if and only if (A, B) is controllable.

where A is the state matrix of the system, B is the system input matrix and K is the feedback gain matrix.

In this work, following valid assumptions are made for the design of the DFIG control:

- (a) DFIG is connected to a strong grid.

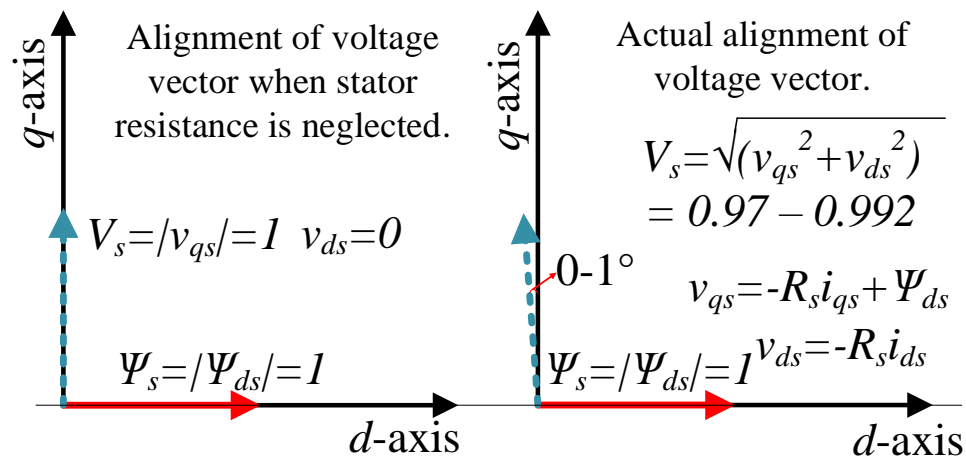


Figure 3.1: Phasor diagram showing the effect of neglecting the stator resistance in the position of voltage vector.

- (b) The synchronously rotating reference frame is aligned with the stator flux. i.e. $\Psi_{ds} = \Psi_s$ and $\Psi_{qs} = 0$.

- (c) Considering the voltage drop in stator resistance is limited to less than 3% of the nominal voltage value, the effect of stator resistance is neglected.

Figure 3.1 represents the d - q axis machine variables drawn on to scale in p.u. quantities based on machine size as a base. It can be seen that the effect of stator resistance in stator voltage alignment is negligible. It can also be observed that for a real machine the voltage vector is not exactly 90° ahead of the flux vector as it is assumed in this chapter. However, the angular difference between the q -axis of reference frame and resultant voltage vector is small enough ($0-1^\circ$) as shown in Figure 3.1 which can be safely neglected for control design purposes.

- (d) Following the consideration made in (c) i.e. neglecting the stator resistance on the voltage vector estimation, it can be assumed that $v_{ds} = 0$ and $v_{qs} = V_s$.

Thus, with this assumption, (A.3) can be modified to

$$\begin{aligned} P_{st} &= v_{qs}i_{qs} \\ Q_{st} &= v_{qs}i_{ds} \end{aligned} \quad (3.1)$$

- (e) The stator current dynamics can be neglected when connected to a strong grid. i.e $p\Psi_{qs} = p\Psi_{ds} \approx 0$ as the effect of the stator transients on the synchronous generator model are also applicable to the DFIG model [88].

With the assumptions made above the following second order state space representation of DFIG can be obtained from (A.1) and (A.2).

$$p \begin{bmatrix} i'_{dr} \\ i'_{qr} \end{bmatrix} = \begin{bmatrix} -\frac{r_r\omega_b}{L_\sigma} & s\omega_b \\ -s\omega_b & -\frac{r_r\omega_b}{L_\sigma} \end{bmatrix} \begin{bmatrix} i'_{dr} \\ i'_{qr} \end{bmatrix} + \begin{bmatrix} \frac{\omega_b}{L_\sigma} & 0 \\ 0 & \frac{\omega_b}{L_\sigma} \end{bmatrix} \begin{bmatrix} v'_{dr} \\ v'_{qr} \end{bmatrix} + \begin{bmatrix} 0 \\ -\frac{s\omega_b L_m \psi_{ds}}{L_s L_\sigma} \end{bmatrix} \quad (3.2)$$

where $L_\sigma = L_r - \frac{L_m^2}{L_s}$, $s = \frac{\omega_s - \omega_r}{\omega_s}$ and $\omega_s = \omega_b$.

The reduced order state space representation of DFIG in (3.2) can be considered of the following form:

$$p.x = A.x + B.u + E \quad (3.3)$$

In (3.3) A is the state or system matrix, B is the input matrix, E can be considered as the constant disturbance in the system and p is the derivative operator, x is the system states and u is the system input.

Likewise, using (A.3) and (A.2), the output active and reactive power output of DFIG at stator terminals can be written as,

$$\begin{bmatrix} Q'_{st} \\ P'_{st} \end{bmatrix} = \begin{bmatrix} \frac{v_{qs}L_m}{L_s} & 0 \\ 0 & \frac{v_{qs}L_m}{L_s} \end{bmatrix} \begin{bmatrix} i'_{dr} \\ i'_{qr} \end{bmatrix} \quad (3.4)$$

where, $Q'_{st} = Q_{st} + \frac{v_{qs}\psi_{ds}}{L_s}$ and $\frac{v_{qs}\psi_{ds}}{L_s}$ is the magnetizing reactive power required by the machine.

Equation (3.4) can be considered to be in the following form:

$$y = C.x \quad (3.5)$$

where, C is the output matrix of the system and y is system output.

Likewise, for GSC with the grid voltage vector oriented control as discussed in appendix B, $v_d = V_g$ and $v_q = 0$. Using (B.2), the state space representation required for GSC control is given by,

$$p \begin{bmatrix} i_d \\ i_q \end{bmatrix} = \begin{bmatrix} -\frac{R}{L} & w_e \\ w_e & -\frac{R}{L} \end{bmatrix} \begin{bmatrix} i_d \\ i_q \end{bmatrix} + \begin{bmatrix} -\frac{1}{L} & 0 \\ 0 & -\frac{1}{L} \end{bmatrix} \begin{bmatrix} v_{di} \\ v_{qi} \end{bmatrix} + \begin{bmatrix} V_g \\ 0 \end{bmatrix} \quad (3.6)$$

For the GSC, the output is considered to be the states itself. Thus, the output equation for the GSC is given by,

$$\begin{bmatrix} i_d \\ i_q \end{bmatrix} = \begin{bmatrix} 1 & 0 \\ 0 & 1 \end{bmatrix} \begin{bmatrix} i_d \\ i_q \end{bmatrix} \quad (3.7)$$

The state space representation of the GSC can be seen to be similar to the representation of the RSC and can be represented by the generic form as in (3.3) and (3.5).

Before, the controller was designed an analysis of the system eigenvalues and controllability was performed based on the A and B matrix obtained above for a specific system with parameters in appendix D. Table 3.1 and 3.2 tabulate the location of system eigenvalues and also the controllability for the RSC and GSC. To implement the proposed controller in real time, the system matrices are created in every instant of time. Then based on the matrices obtained, the controller gains are computed

Table 3.1: Location of Eigenvalues and controllability and observability for RSC control

slip	Rank of Controllability Matrix	Rank of Observability Matrix	Eigenvalues	Controllable	Observable
$\pm s$	2	2	$-5.9250 \pm j 377s$	Yes	Yes

Table 3.2: Location of Eigenvalues and controllability and observability for GSC control

	Rank of Controllability Matrix	Rank of Observability Matrix	Eigenvalues	Controllable	Observable
	2	2	$-0.0010 \pm j 1$	Yes	Yes

online so as to stabilize the system and also get the desired system response. It can be observed from Table 3.1 and 3.2 that DFIG system is controllable and observable and the location of the eigenvalues for RSC depends on the slip condition. Note: the analysis is made for open loop DFIG system representation.

The control law used for state feedback control is of the following form [89]:

$$U = -K.x + G.r - B^{-1}E \quad (3.8)$$

where U is the control input, K is the feedback gain matrix which ensures the closed loop system eigenvalues are all in left half plane, G is the forward gain matrix which ensures that the steady state tracking error is minimized. The third term $B^{-1}E$ is to compensate the effect of disturbance term in the system. The disturbance term mentioned here in case of DFIG is the magnetizing reactive power required by DFIG.

The first step is to compute the feedback gain matrix which places the system closed loop poles at the desired location. This can be done using the robust pole placement algorithm for linear systems [87]. MATLAB implements the algorithm as ‘*place*’ function, and in this work ‘*place*’ function is used to get the feedback gain matrix K based on the system matrix A , input matrix B and desired location of closed

loop system eigenvalues P . The desired location of closed loop system eigenvalues is based on desired closed loop response of the system. In order to improve upon the transient response and robustness during parameter variation, a linear quadratic regulator(LQR) based optimal state feedback controller with integral action, also termed as linear-quadratic-integral (LQI), for steady state reference tracking has been proposed. The gain matrix K is computed by minimizing a quadratic performance index which accounts the expenditure of energy of the control signals and the energy of the plant states.

$$J = \int_{t=0}^{t=\infty} (x_e^T(t)Qx_e(t) + u_e^T(t)Ru_e(t))dt \quad (3.9)$$

where Q and R are positive definite matrices.

However, for the initial test of the proposed technique the desired location of closed loop system eigenvalues is based on user preference and is achieved by computing the feedback gain as

$$K = \text{place}(A, B, P) \quad (3.10)$$

With K determined, using the equations (3.3) and (3.10), the closed loop system dynamics can be written as

$$p.x = A.x + B(-K.x + G.r - B^{-1}.E) + E \quad (3.11)$$

After few algebraic manipulations, (3.11) simplifies to

$$p.x = (A - B.K).x + B.G.r \quad (3.12)$$

With the gain G chosen so that for a reference input, $r(t) = R, t \geq 0$, the steady state output is R . i.e.

$$y_{ss} = \lim_{t \rightarrow \infty} y(t) = R \quad (3.13)$$

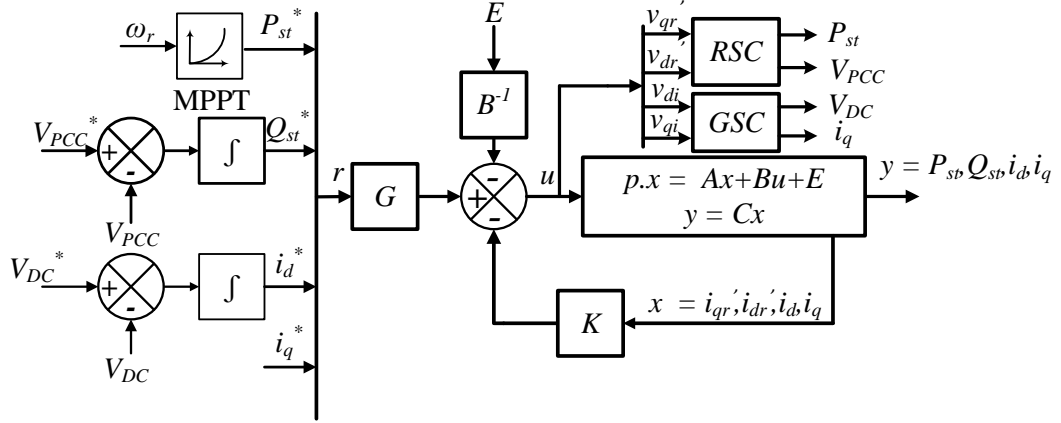


Figure 3.2: Schematic of Proposed State Feedback Control for DFIG.

where y_{ss} is the steady state value of output. During the steady state condition for a fixed input, the state dynamics settles down, thus (3.12) becomes,

$$p.x = 0 = (A - B.K).x_{ss} + B.G.R \quad (3.14)$$

And,

$$x_{ss} = (A - B.K)^{-1}B.G.R \quad (3.15)$$

Thus, the steady state output is given by,

$$y_{ss} = C.x_{ss} = -C(A - B.K)^{-1}.B.G.R \quad (3.16)$$

Finally, using (3.13) in (3.16), the forward gain matrix G is computed as,

$$G = -[C(A - B.K)^{-1}B]^{-1} \quad (3.17)$$

Once these gains are computed, the control signal is computed using the control law (3.8) and the proper PWM signals for the converter is generated. Figure 3.2 represents the schematic diagram of the proposed state feedback control of DFIG. Figure

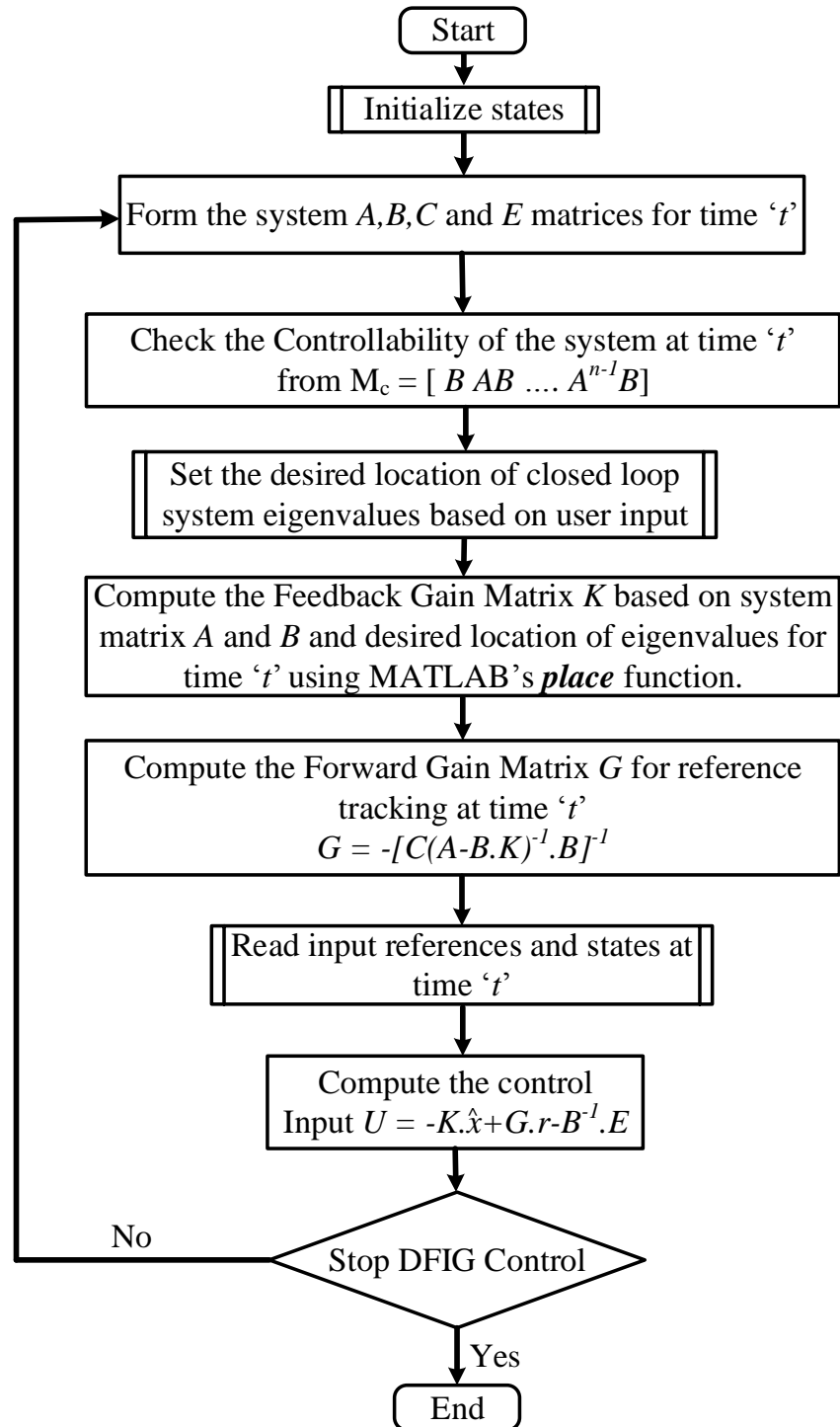


Figure 3.3: Flowchart showing the Control Sequence for proposed State Feedback Controller.

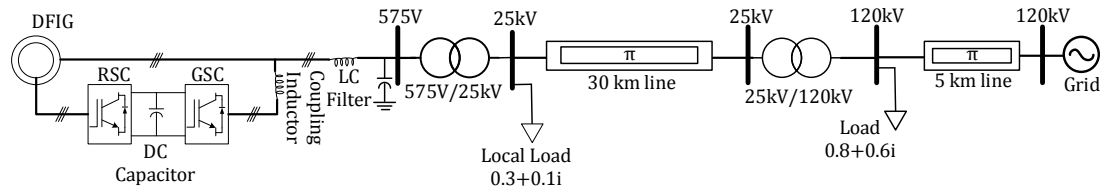


Figure 3.4: One line Diagram of the Studied Test System.

3.3 shows the flowchart that explains the sequence in the proposed state feedback controller works.

3.2 Simulation Results for State Feedback Control (SFC)

In this section, the performance of the SFC without any estimators is discussed. i.e. the states are assumed to be measurable. The performance of the proposed SFC is analyzed on a 1.5 MW DFIG model [90]. Figure 3.4 shows the test system in which the proposed controller is tested.

3.2.1 Response Comparison for Step Changes in Input

Figure 3.5 shows the performance of the SFC and VC implemented for the RSC to track a step change in stator active power. It can be observed that the SFC has a faster response to the step changes for tracking active power reference as compared to the PI gain based VC technique.

3.2.2 Response to Grid Voltage Sag

Figure 3.6 shows the performance of the two controllers for grid voltage sag lasting duration of 0.625 seconds. It can be seen that the SFC has a faster response and tries to uplift the point of common coupling voltage faster than the PI based VC technique.

One of the major reason for better performance of the SFC when compared to VC is that for VC the controller gains are tuned based on a singular operating point and they work fine for the linear region around that set point. However, for the proposed SFC the controller gains are updated continuously based on the system conditions. As

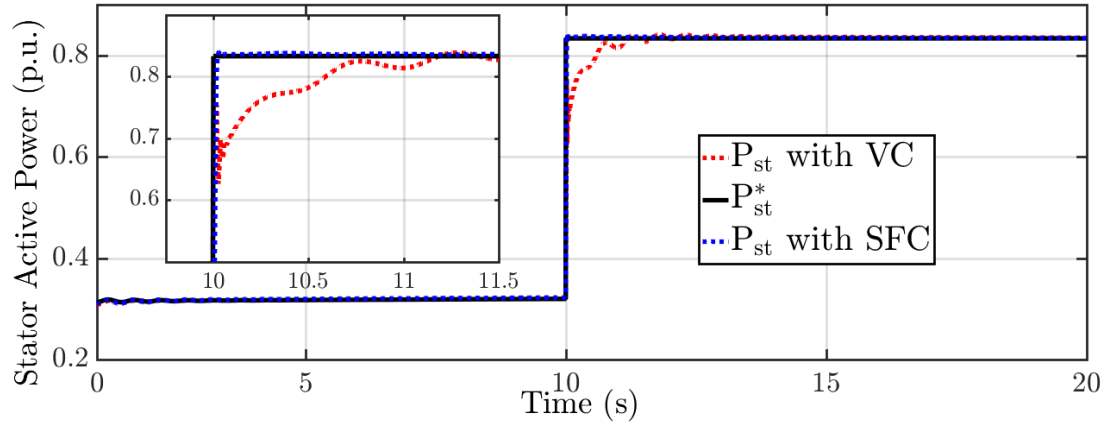


Figure 3.5: Controller Performance Comparison for Step Change in Stator Power.

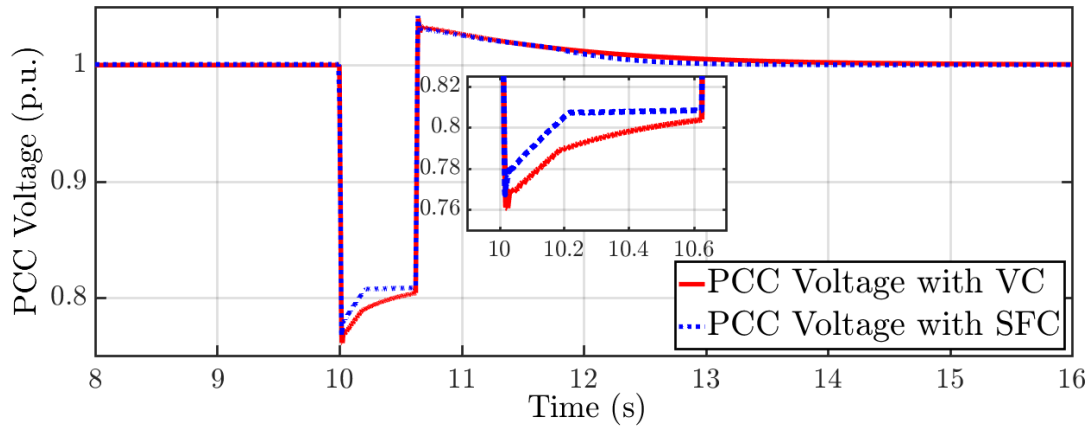


Figure 3.6: Comparison of the Controller Performance for Grid Voltage Sag.

the proposed topology computes system matrices online and computes the controller gain online so as to make the system behave in a similar manner in every operating condition, the system performance remains the same during the whole operating range.

3.2.3 Dynamic Analysis with Real Wind Speed Profile

The performance of controllers was also tested on a 1.5 MW DFIG model [91] with the wind speed profile as shown in Figure 3.7. Figure 3.8 compares the performance of the two controllers in tracking the stator power set point. The stator power set point is determined by the MPPT controller. It can be seen that for sudden changes in reference power the state feedback controller does better tracking, apart from that

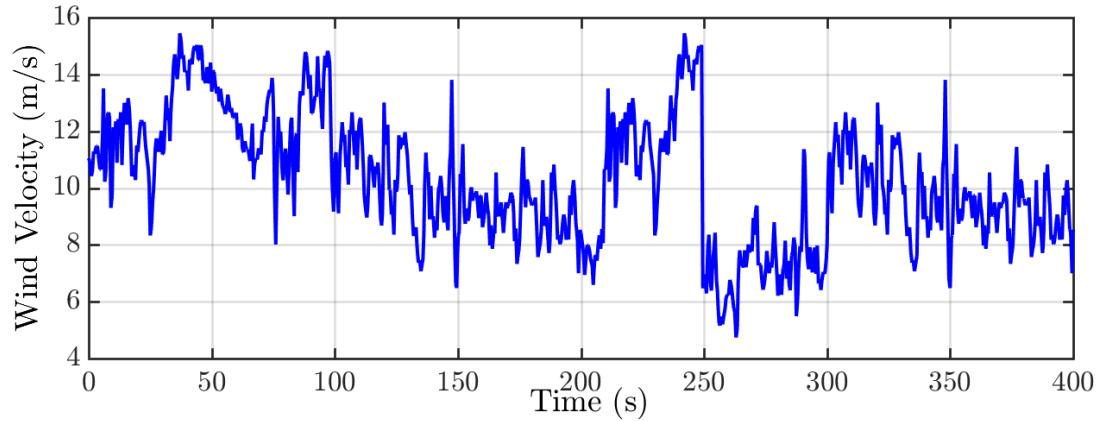


Figure 3.7: Wind Velocity Profile used for Performance Assessment.

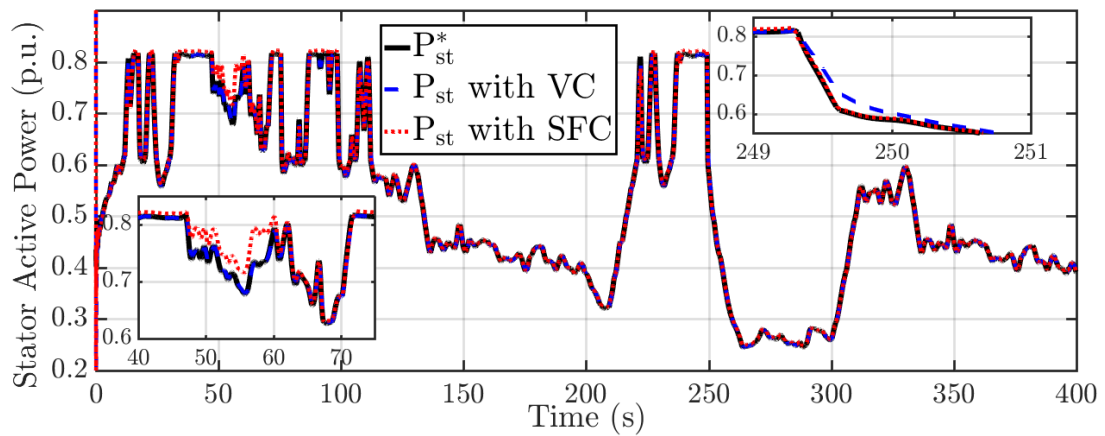


Figure 3.8: Stator Active Power Tracking Performance Comparison between SFC and VC for Dynamic Wind Conditions in 3.7.

the controller performance are almost similar to one another. The PCC voltage regulation is also almost similar when using both the controllers as shown in Figure 3.9. Figure 3.10 shows the DC link voltage control performance using both the state feedback control and the VC technique. It can be seen that both the control technique has almost comparable performance in maintaining DC link voltage even in changing wind conditions. The GSC is operated in unity power factor mode, so the desired q -axis current output of GSC was 0. It can be seen from Figure 3.11 that PI based VC tightly maintains the requirement, where as there is a slight deviation from the desired set point in case of state feedback control. The deviation in this case is still less than 0.2%.

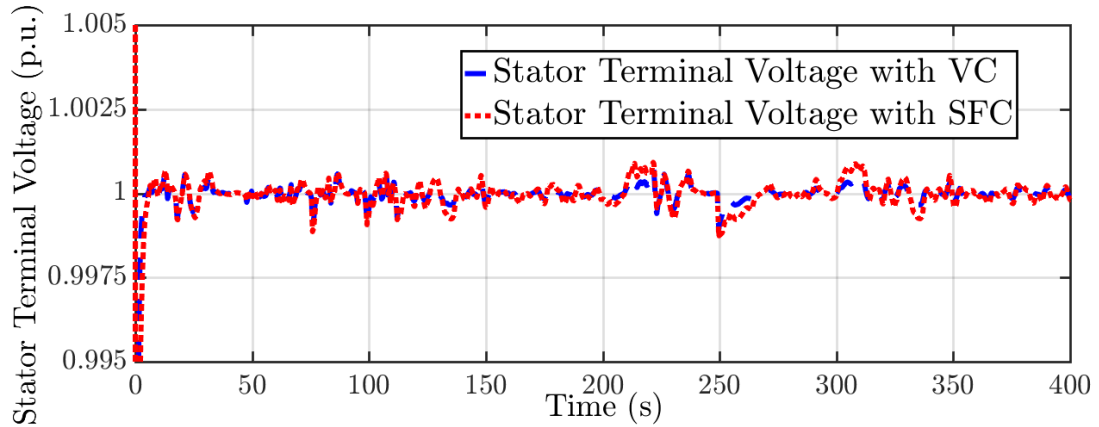


Figure 3.9: DFIG Stator Terminal Voltage Regulation Comparison between SFC and VC for Dynamic Wind Conditions in 3.7.

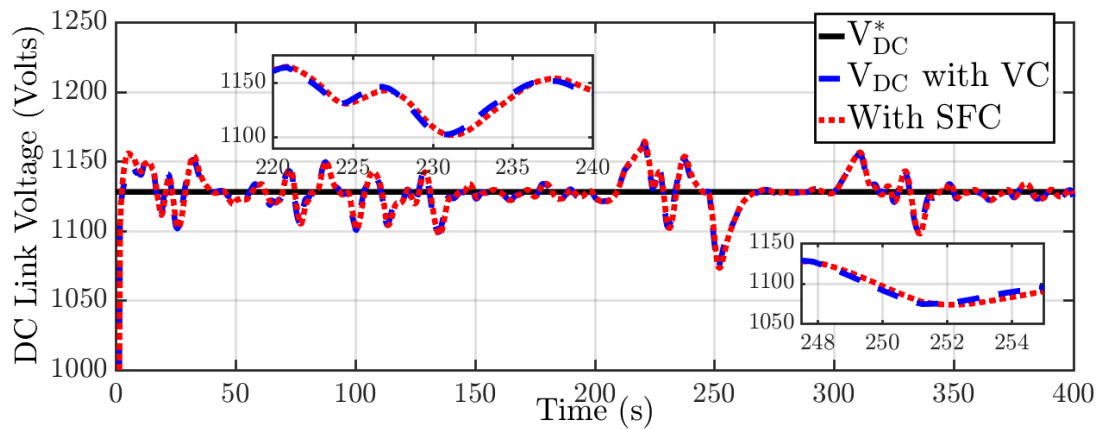


Figure 3.10: DFIG DC link Voltage Regulation Comparison between SFC and VC for Dynamic Wind Conditions in 3.7.

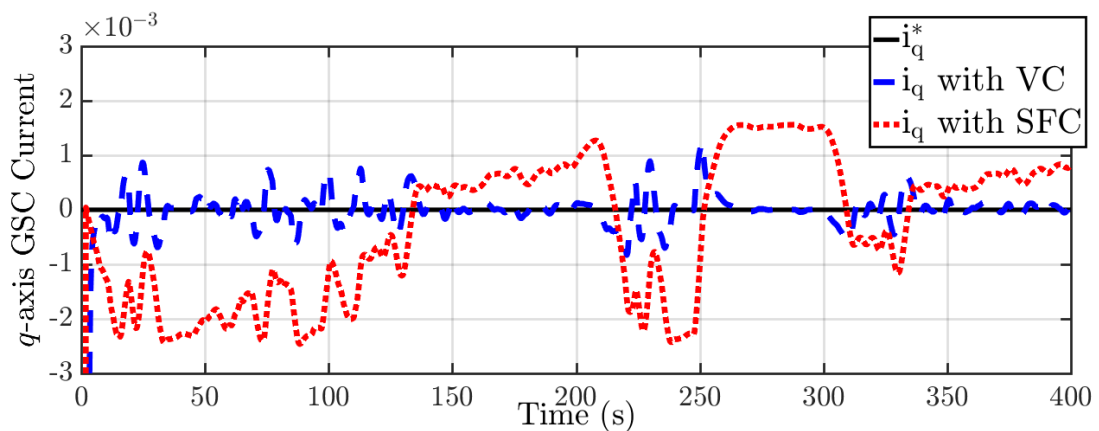


Figure 3.11: q -axis Current Regulation Comparison between SFC and VC for Dynamic Wind Conditions in 3.7.

3.3 Design of State Estimators

A state estimator (also known as state observer) is a system that provides an estimate of the internal state of a given system based on the system model and measurements of system input and output. In control systems, in cases where it is difficult to measure the system states directly, state observers are used to estimate the states of the system such that SFC can be employed. Also, utilizing such control technique enhances the reliable operation of the system. A system should be observable to fully reconstruct the system state from its output measurements using the state observers. In this work, a ‘*Luenberger observer*’, observer is utilized which compares the estimated output of the observer with the real system output such that the error in the state estimation is minimized.

Based on the above derivation for machine dynamics in (3.2) and (3.4), the state observer for DFIG is designed. The following assumptions are considered before proceeding with the state observer design [92, 93].

- The pair $(A - L.C, C)$ for any $o \times n$ real matrix L is observable if and only if the pair (A, C) is observable, where o is the order of outputs and n is the order of states.
- All eigenvalues of $(A - L.C)$ can be assigned arbitrarily (provided complex eigenvalues are assigned in conjugated pairs) by selecting a real constant L if and only if (A, C) is observable.

The observer used in this work is of the following form [93, 94]:

$$p.\hat{x} = A.\hat{x} + B.u + E + L.(y - \hat{y}) \quad (3.18)$$

$$\hat{y} = C.\hat{x} \quad (3.19)$$

where \hat{x} is the estimated state, y and \hat{y} are the actual output and estimated output of the system respectively, L is the gain matrix for the observer and A, B and C are the system state, input and output matrices respectively.

The observer in (3.18), in a deterministic setting is referred to as '*Luenberger observer*'. The observer inputs are the system inputs and outputs, and its state vector is linearly related to the desired state approximation [94]. Substituting (3.19) which is the expression for \hat{y} in (3.18), the closed loop observer equation is obtained as:

$$p.\hat{x} = (A - L.C).\hat{x} + B.u + E + L.y \quad (3.20)$$

As the purpose of the state estimator is to estimate the true state ' x ', the estimation error is desired to reduce over time. The estimation error is given by,

$$e = x - \hat{x} \quad (3.21)$$

As the error signal obeys the differential equation, one gets,

$$p.e = p.x - p.\hat{x} = (A - L.C).e \quad (3.22)$$

Thus, it can be seen that with the observer design above, the state equation for the estimation error is a homogeneous differential equation governed by the $n \times n$ matrix $A - L.C$, where n is the number of the states of the system. If the gain matrix L is chosen such that the eigenvalues of $A - L.C$ are strictly in left half of complex plane, the error equation is asymptotically stable, and the estimation error will decay to zero over time. In this work, the observer gain is chosen such that the closed loop poles of observer is located ten times farther than the poles of the closed loop controlled system. Thus, this selection of stable eigenvalues for the closed-loop system, results in the disturbance suppression at the output both asymptotically and

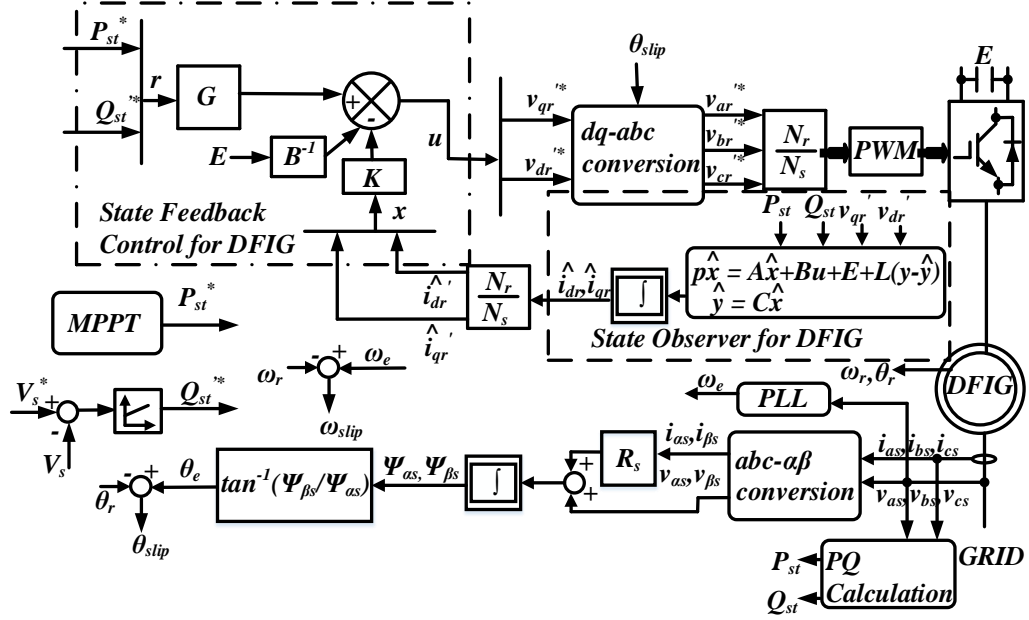


Figure 3.12: Schematic Diagram of the State Estimator based State Feedback Controller.

robustly. This robust tracking still holds for large parameter variations due to changes of load or aging [95]. In this work, the state observer designed is utilized in along with two controllers: a) conventional vector control technique of DFIG which is in use for majority of the DFIG based wind farms (see Figure 3.12), and b) state observer based SFC technique (see Figure 3.13). The observer, as observed in Figure 3.12 and 3.13, can then be used to work with either the conventional VC of DFIG or SFC technique. In terms of machine variables, the observer equation in (3.18) can be represented as (3.23) and (3.24).

$$\begin{aligned}
 p \begin{bmatrix} \hat{i}'_{dr} \\ \hat{i}'_{qr} \end{bmatrix} &= \begin{bmatrix} -\frac{R_r \cdot w_b}{L_\sigma} & s \cdot w_s \\ -s \cdot w_s & -\frac{R_r \cdot w_b}{L_\sigma} \end{bmatrix} \cdot \begin{bmatrix} \hat{i}'_{dr} \\ \hat{i}'_{qr} \end{bmatrix} + \\
 &\begin{bmatrix} \frac{w_b}{L_\sigma} & 0 \\ 0 & \frac{w_b}{L_\sigma} \end{bmatrix} \cdot \begin{bmatrix} v'_{dr} \\ v'_{qr} \end{bmatrix} + \begin{bmatrix} 0 \\ \frac{s \cdot w_s \cdot L_m \cdot \Psi_{ds}}{L_s \cdot L_\sigma} \end{bmatrix} + L \cdot \left(\begin{bmatrix} Q'_{st} \\ P'_{st} \end{bmatrix} - \begin{bmatrix} \hat{Q}'_{st} \\ \hat{P}'_{st} \end{bmatrix} \right) \quad (3.23)
 \end{aligned}$$

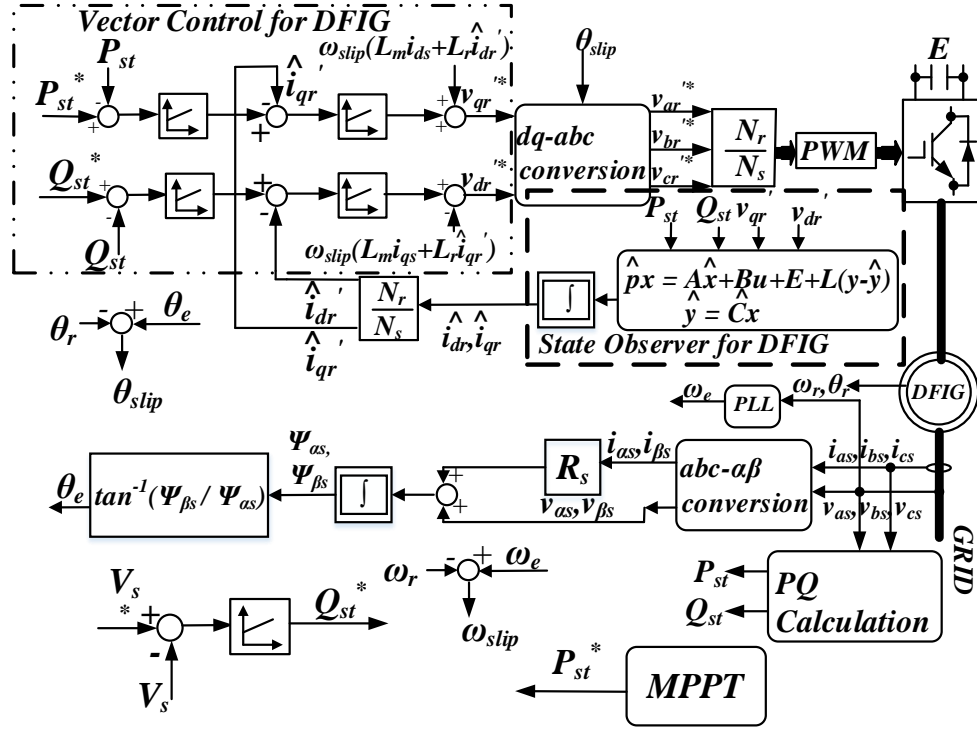


Figure 3.13: Augmented Vector Control Strategy for DFIG with State Observer.

$$\begin{bmatrix} \hat{Q}_{st} \\ \hat{P}_{st} \end{bmatrix} = \begin{bmatrix} \frac{v_{qs} \cdot L_m}{L_s} & 0 \\ 0 & \frac{v_{qs} \cdot L_m}{L_s} \end{bmatrix} \cdot \begin{bmatrix} \hat{i}_{dr} \\ \hat{i}_{qr} \end{bmatrix} \quad (3.24)$$

In this work, the gain matrix L is computed using the same technique that was used earlier in the computation of SFC gain matrix K , where the closed loop system matrix of interest was $A - B.K$. Comparing that with the observer problem, the closed-loop system matrix is $A - L.C$. The structure of those two matrices is similar; only the order of the unknown matrix differs between $B.K$ and $L.C$. Since the eigenvalues of a matrix and its transpose are the same, the observer problem can be formulated the same way as the control problem by considering the matrix $(A - L.C)^T = A^T - C^T L^T$. Now, using the MATLAB function 'place', the matrix L^T is computed which is later transposed again to obtain the required observer gain matrix L .

Apart from the closed loop state observer as explained above, an open loop observer can also be designed for the rotor currents based on the machine equations using stator voltage and currents. From (A.1), and (A.2), and also neglecting the stator dynamics, the rotor currents can be estimated as:

$$i'_{dr} = \frac{v_{qs} + r_s i_{qs} + L_s \dot{i}_{ds}}{L_m} \quad (3.25)$$

$$i'_{qr} = \frac{v_{ds} + r_s \dot{i}_{ds} + L_s \dot{i}_{qs}}{L_m} \quad (3.26)$$

3.4 State Feedback with State Observers

In this section, a discussion on integrating state observers with the SFC, such that there is no need to measure the system states, is presented. In this work, as the system states were the rotor currents, the proposed SFC law with state observers eliminates the need of rotor current sensor. In addition, it has been shown that there is no need of measuring the rotor voltages as well. The reliable and efficient operation of DFIG based wind farms depends on quality of sensors used in the feedback control and is especially so for the aging wind farms. State observers based feedback control methodologies can also help augment the existing control topologies used in DFIG and eliminates the dependency on sensors.

It can be observed from (3.2), that the system state matrix ,‘ A ’, is dependent on the machine slip speed so it should be updated regularly based on the changing slip conditions. Thus to implement the proposed SFC, the system state matrices are computed every sampling instant and based on the system A matrix obtained, the controller gains can be calculated online to stabilize the system and also to achieve the desired system response.

The closed loop system dynamics after the SFC is given by (3.12). Now, the state

observer for the closed loop system is designed to have the following form.

$$p.\hat{x} = (A - B.K).\hat{x} + B.G.r + L.(y - \hat{y}) \quad (3.27)$$

Using (3.19), the closed loop system representation with observer is,

$$p.\hat{x} = (A - B.K - L.C).\hat{x} + B.G.r + L.y \quad (3.28)$$

Integrating (3.28), the estimate of the closed loop state information can be obtained, which can be used in the SFC law in (3.8) for the control of the system.

It is important to note that the closed loop system state eigenvalues can be placed independently of the observer estimate error eigenvalues using the proposed design [92, 96]. Including the system and observed states, the total system dimension with closed loop observer is $2 \times n$. The first n states are actual system states and the remaining n states are the estimation error.

With $y = C.x$ and $u = -K.\hat{x} + G.r - B^{-1}.E$, the system (3.3) modifies to:

$$p.x = A.x - B.K.\hat{x} + B.G.r \quad (3.29)$$

Also, using (3.21), (3.29) modifies to

$$p.x = (A - B.K).x - B.K.e + BGr \quad (3.30)$$

Using (3.22) and (3.30), the combined state equation with both the state of the system and error in state estimation can be represented as,

$$p. \begin{bmatrix} x \\ e \end{bmatrix} = \begin{bmatrix} A - B.K & B.K \\ 0 & A - L.C \end{bmatrix} \begin{bmatrix} x \\ e \end{bmatrix} + \begin{bmatrix} BG \\ 0 \end{bmatrix} r \quad (3.31)$$

As the above system matrix is in upper triangular form, the overall system eigenvalues are a combination of eigenvalues of $A - B.K$ and eigenvalues of $A - L.C$ and each of these eigenvalues can be computed independently. So, in the closed loop system with state observer in SFC mode the stability of the feedback system is independent of the stability of the observer. Also, even if the closed loop system (A, B) pair in (3.31) is uncontrollable with state e being the uncontrollable state, the dynamics of state e as seen in (3.22) is homogeneous in nature, which means for a proper choice of L , the error asymptotically decays with time. In order to place the closed loop eigenvalues at the desired location, a pole placement routine (MATLAB's '*place*' function) is used. In this work, the eigenvalues of the state observers are designed for five times farther than the location of eigenvalues of the SFC. This can be achieved by setting the smallest real part of the observer eigenvalues to be ten times bigger than the largest real part of the closed-loop system eigenvalues [96].

Figure 3.12 shows the proposed state observer based SFC. Figure 3.13 shows the augmentation method of conventional VC with the proposed reduced order state observer. Notice that no rotor current sensors are required using this technique. Also, it can be observed from Figure 3.13, that the proposed state observer technique can be seamlessly integrated with the existing VC topology for DFIG.

Figure 3.14 shows the overall flowchart for the design of state estimator based SFC.

3.5 Simulation Results using 3-Bus System

In this section, the performance of the proposed state observer based SFC is analyzed on a 1.5 MW DFIG model [90]. Figure 3.4 shows the test system in which the proposed controller is tested.

3.5.1 Analysis of the Observer Based Controller with Dynamic Wind Conditions

Figure 3.15 shows the wind speed profile used for testing the proposed controller [97]. Figure 3.16 shows the estimation performance of the proposed state observer

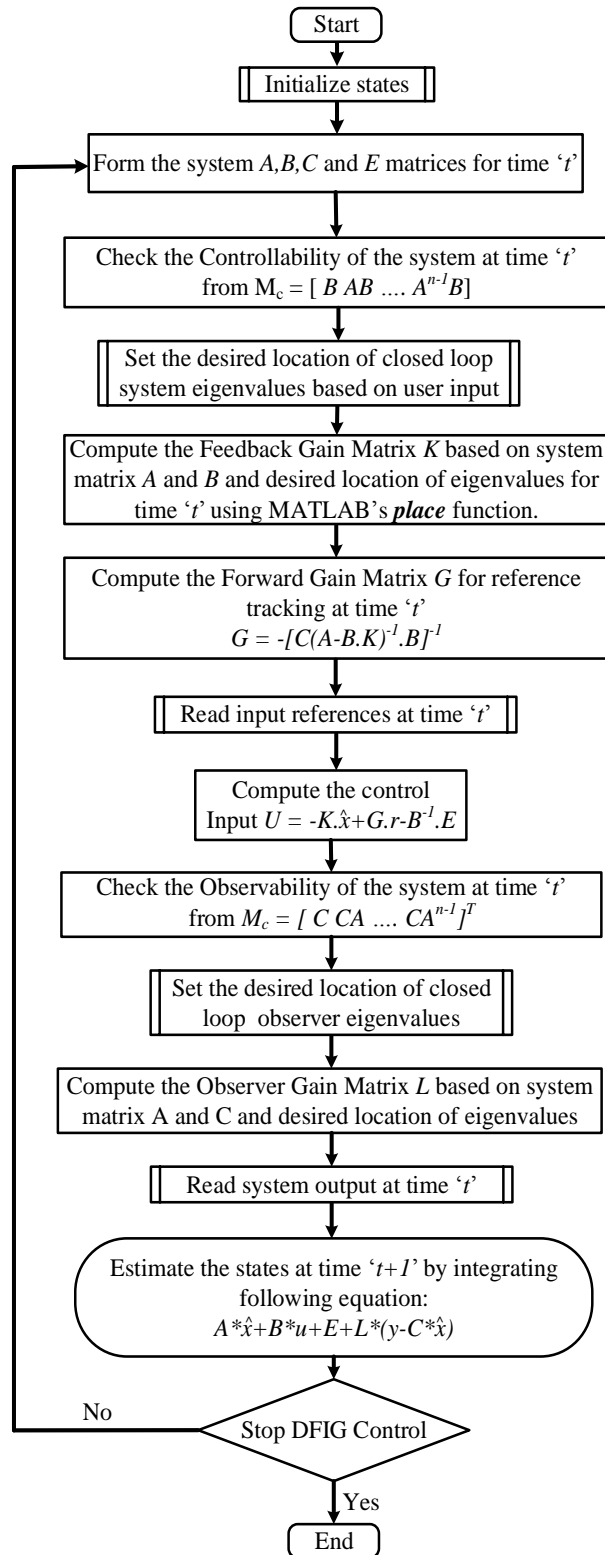


Figure 3.14: Flowchart of the State Estimator based SFC.

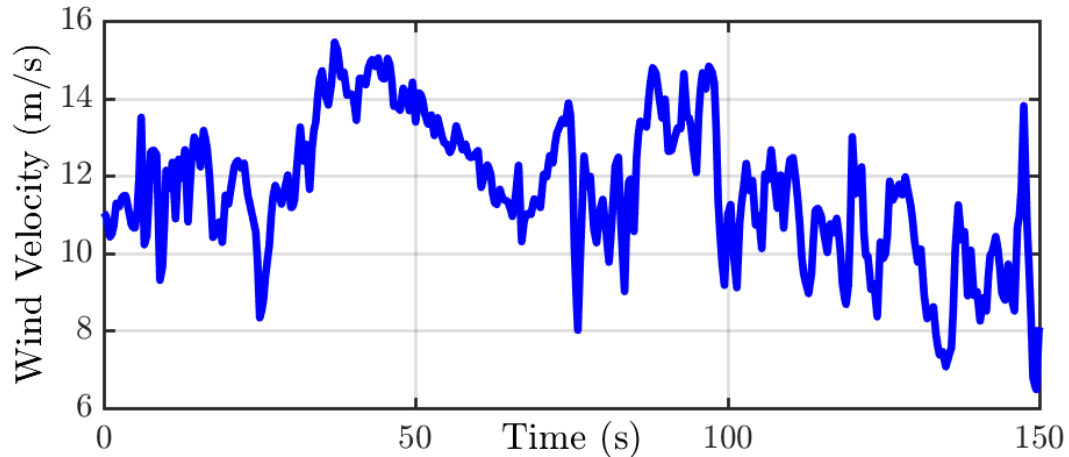


Figure 3.15: Wind speed Profile used for Controller Performance Assessment.

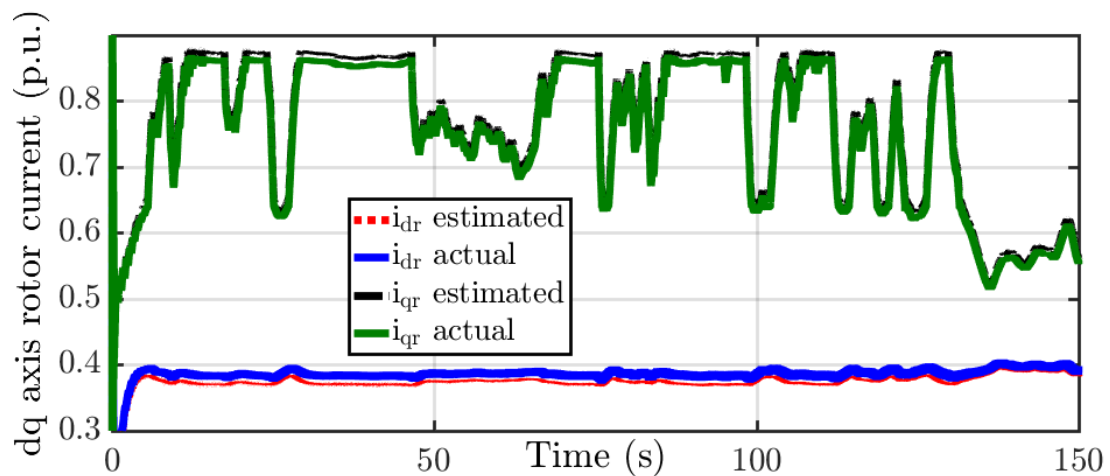


Figure 3.16: Rotor Current Comparisons based on the State Observer.

when used in closed loop with the SFC. It can be seen that the state observer can estimate the current status of the rotor currents to a higher degree of accuracy. There is a minimum offset in the estimated and the actual value of the rotor currents. This does not impact the SFC performance as it can be seen in Figure 3.17 and Figure 3.18. The minimum offset occurs in the estimated and the actual state values due to the assumptions made in Section 3.4. When the synchronously rotating reference frame is aligned with the stator flux, it is assumed that the $\Psi_{ds} = \Psi_s$ and $\Psi_{qs} = 0$, and it is also assumed that $v_{qs} = V_s$ and $v_{ds} = 0$ which helps decouple the active and reactive power. However, due to the presence of the stator resistance, R_s , q -axis

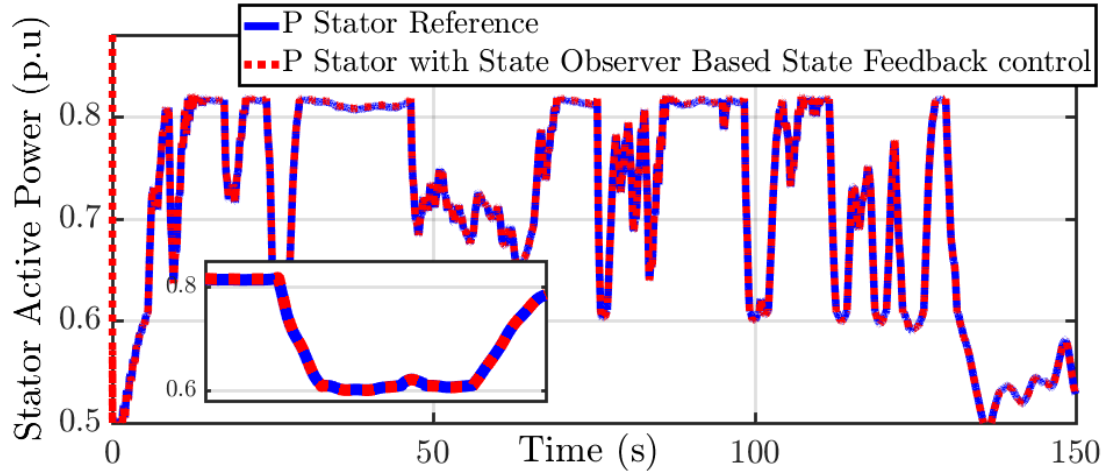


Figure 3.17: Stator Active Power Tracking Performance Analysis with State Observer based State Feedback Control.

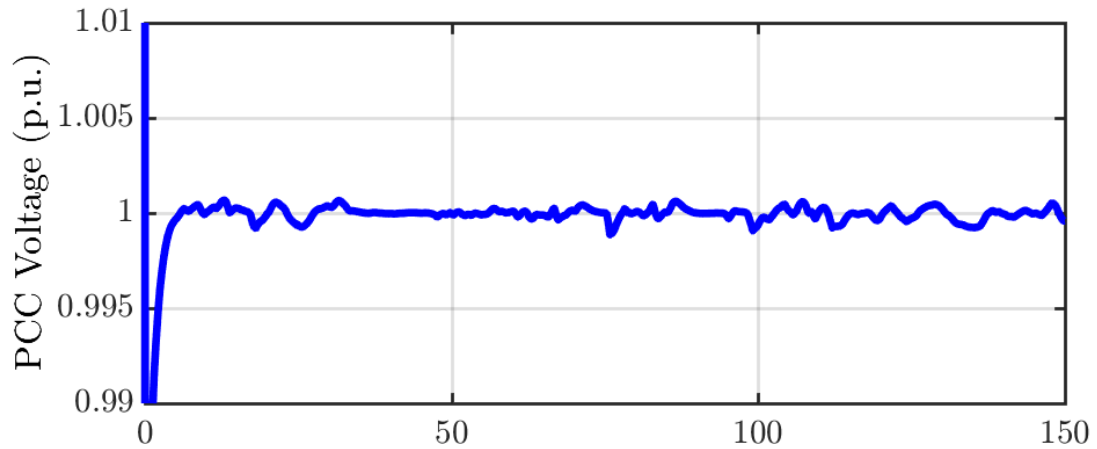


Figure 3.18: PCC Voltage Control with State Observer based State Feedback Control.

stator voltage v_{qs} is not equal to V_s , and d -axis stator voltage v_{ds} is not equal to zero as assumed in this work (i.e. due to the stator resistance, R_s , the voltage vector is not exactly 90 degree phase behind the flux vector). This leads to slight deviation in the system output assumed in (3.4) which in turn, leads to a small deviation that is evident in the actual and estimated system states.

In this chapter, to compare the two reduced order feedback control methodologies (a. state observer based SFC and b. state observer based VC) with one another, the augmented VC was also tuned using the reduced order dynamical model of the system

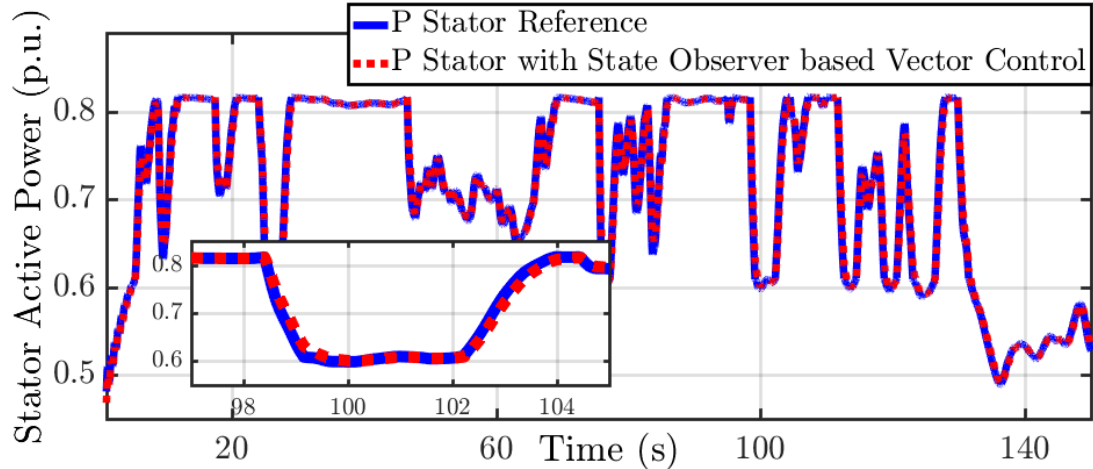


Figure 3.19: Stator Active Power Tracking Performance with State Observer based Vector Control.

but for a wind speed corresponding to 1.1 p.u. rotor speed.

From Figure 3.17, it can be seen that the proposed state observer based SFC can accurately track dynamically changing stator active power reference with respect to the changing wind conditions. Also at about 100s, when there is a step change in stator active power reference, it can be seen that the controller acts immediately and performs well to track the required stator power. Figure 3.18 shows the performance of the proposed SFC for voltage regulation at PCC. It can be seen that the proposed controller can tightly regulate the voltage at PCC during changing active power with respect to the wind.

Figure 3.19 shows the performance of the modified VC for stator active power tracking. It can be seen that the controller can track the desired set point with minimum steady state error. As it can be seen from Figure 3.17 and Figure 3.19, the SFC with state observer is faster than than the VC with the state observer. However, in terms of voltage regulation it can be seen from Figure 3.20 that the vector control with state observer has less deviation around set point of 1 as compared to SFC with state observer in Figure 3.18. Figure 3.21 shows the comparison between two forms of controllers on the DFIG rotor speed. Fast control action of the SFC

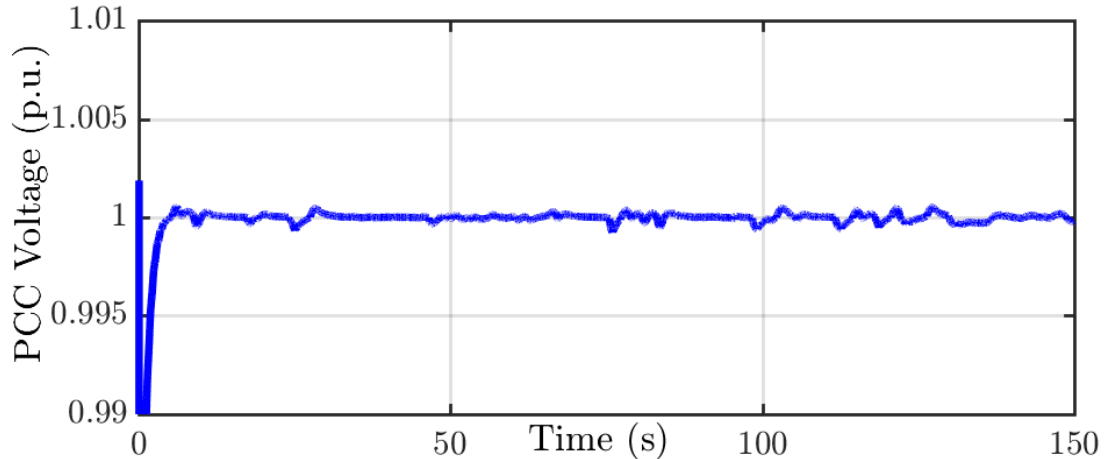


Figure 3.20: PCC Voltage Control with State Observer based Vector Control.

Table 3.3: Rotor Current Estimation Error

Current	Mean Error (%)	Absolute Maximum Error(%)	Absolute Minimum Error(%)
Nominal Rotor Resistance			
<i>d</i> -axis	0.1	0.78	≈ 0
<i>q</i> -axis	-1.31	2.13	≈ 0
$1.2 \times$ Nominal Rotor Resistance			
<i>d</i> -axis	0.068	0.74	≈ 0
<i>q</i> -axis	-1.37	2.17	≈ 0

causes rotor oscillations when the rotor speed is close to maximum rated speed after which the pitch controller starts to act (1.2 p.u in this case). As pitch controller and VC are relatively slower, there is less difference between mechanical power and electrical power even though there is change in wind speed, which keeps the rotor stable. However, in the case of SFC, as the controller action is fast, the electrical power changes fast when compared to the wind speed changes causing a change in difference between mechanical power and electrical power leading to rotor oscillations. Note that this oscillation happens when there are wind speed changes around the rated speed (e.g 100-110 secs) and subsides as the pitch controller maintains the mechanical power at 1 p.u at higher wind speed as it can be seen from 40 to 50 secs.

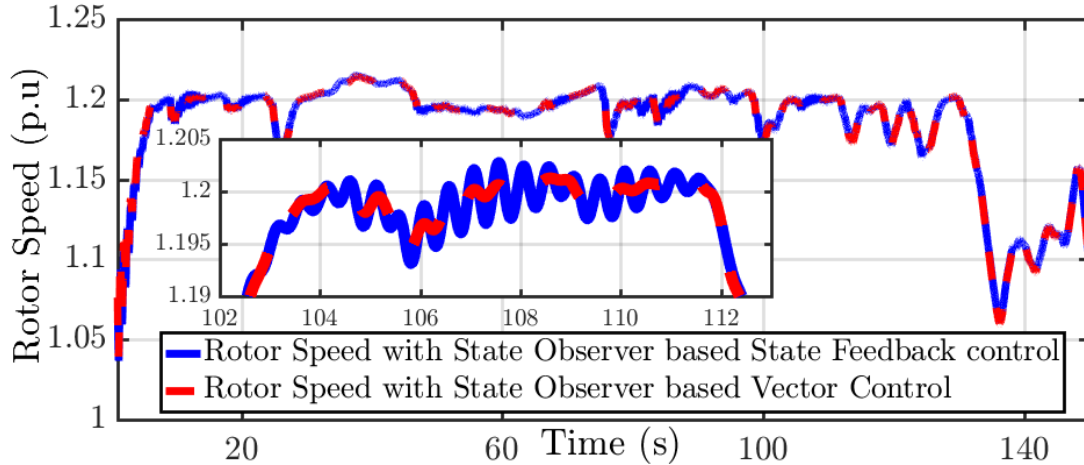


Figure 3.21: Rotor Speed Oscillations with the two Proposed Controllers.

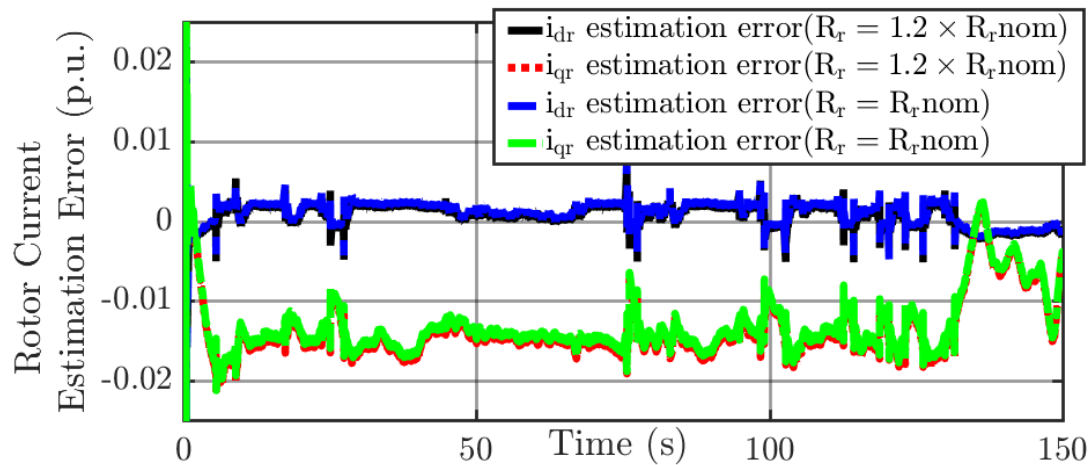


Figure 3.22: Rotor current Estimation Error during Rotor Resistance Variation.

3.5.2 Analysis of Observer Based Controller for Changes in DFIG Rotor Resistance

As the rotor resistance varies, the reduced order model considered in the controller design varies as well [98]. Several work discusses the effect of rotor resistance variations. In [99] a rotor temperature estimation technique is presented which can be integrated with the proposed technique for augmenting the performance of the controller.

In this work, the variations in the rotor resistance and the effect of that on parametric (change in system state matrix A) and the functional changes (such as voltage

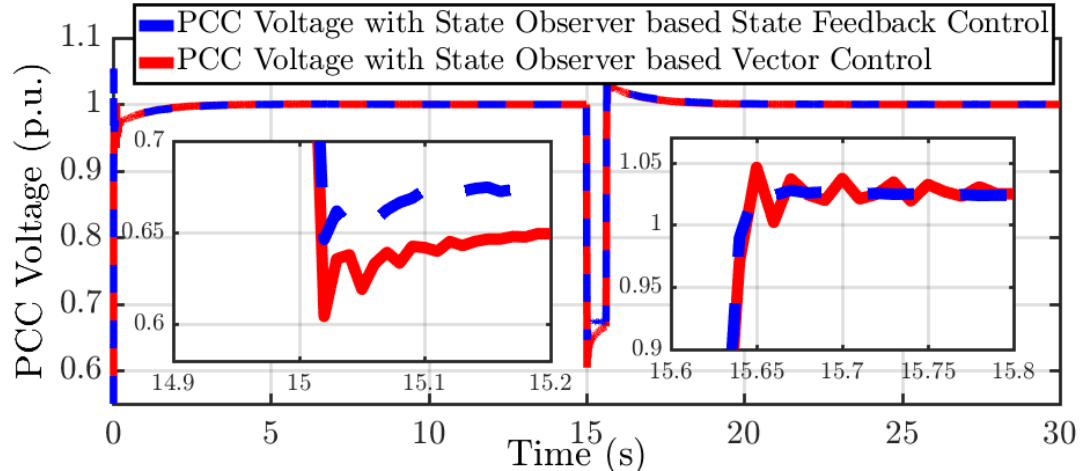


Figure 3.23: Comparison of the Two Controllers during Grid Voltage Sag.

drop on slip ring brushes) are taken into consideration. It can be seen from (3.23) that when there are changes in A matrix the closed loop system eigenvalues changes. The controller gain K is thus adjusted for this change accordingly. Similarly, the changes in the voltage drop affect the state estimation error ϵ . The property of the estimation technique is that the output estimation error is asymptotically made to zero and thus the estimated rotor currents are driven close to the actual value.

Figure 3.22 shows the rotor current estimation error during the condition when the rotor resistance is known and during a condition when rotor resistance is supposed to increase by 20% due to temperature variation. In both cases, it can be seen that the proposed state observer can estimate the rotor current to a fair degree of accuracy. Also, note that when the rotor resistance increases by 20%, the rotor current estimation error increases. However, the error is still in a narrow range such that the estimated current can still be used for the feedback control. Also, it is interesting to note that the i_{qr} estimation error is proportional to the slip speed. It was observed that i_{qr} estimation error is close to zero when the machine operates close to synchronous speed. Table 3.3 compares the performance of the proposed reduced order state observer in terms of estimation error for the nominal rotor resistance condition as well as when the rotor resistance is increased by 20%.

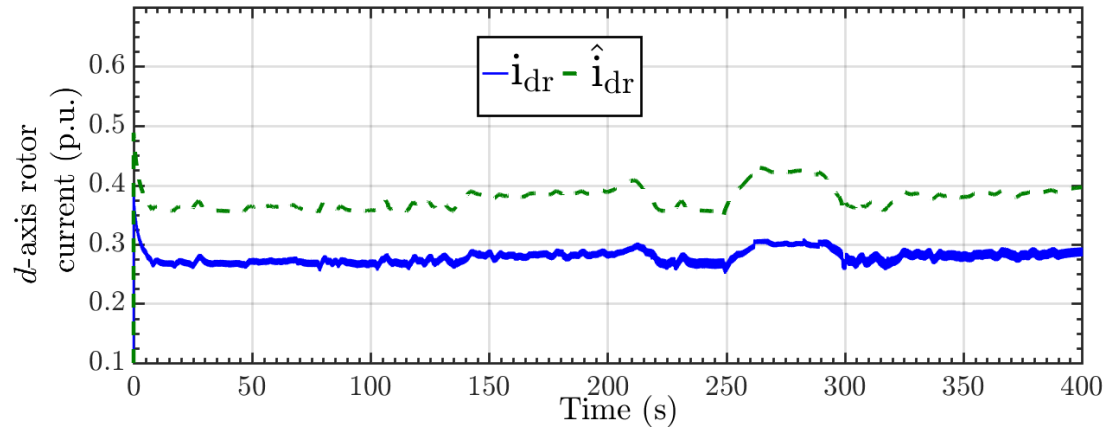


Figure 3.24: d -axis Rotor Current Estimation Comparison with 50% L_m Variation.

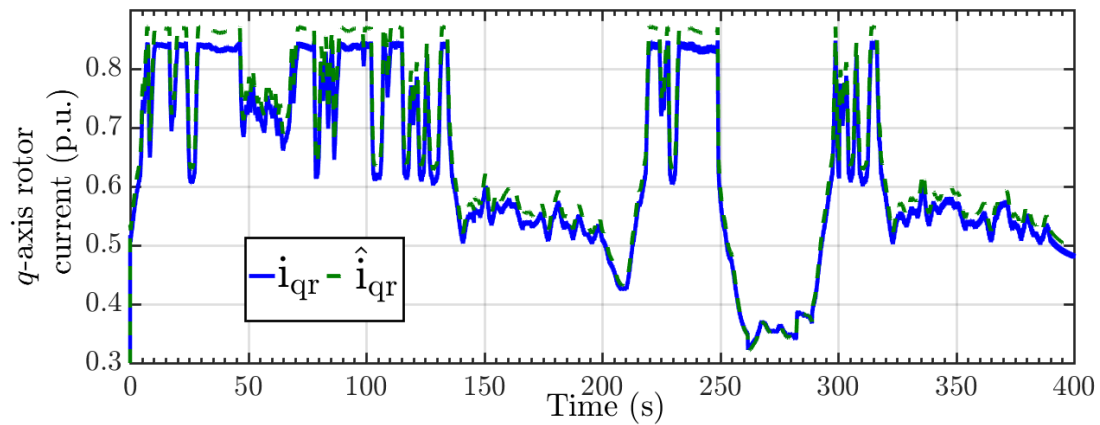


Figure 3.25: q -axis Rotor Current Estimation Comparison with 50% L_m Variation.

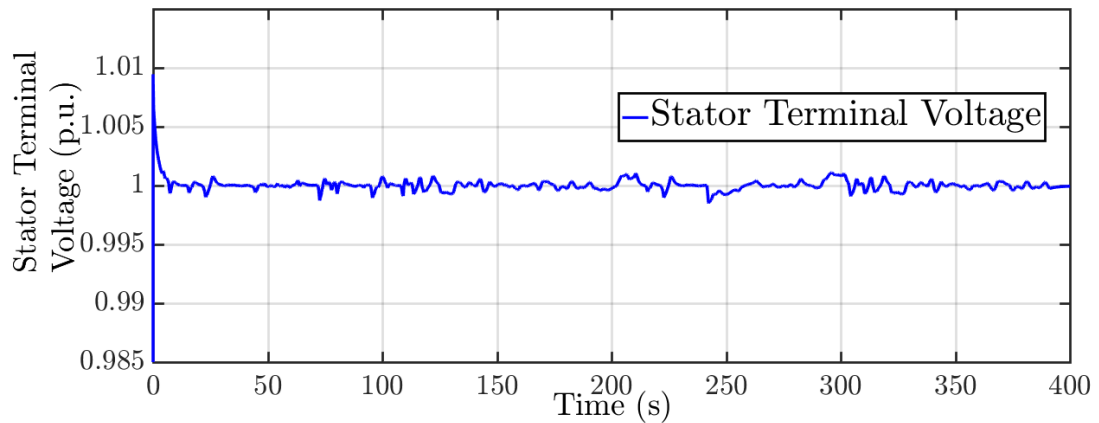


Figure 3.26: DFIG Terminal Voltage Control with State Observer based SFC with 50% L_m Variation.

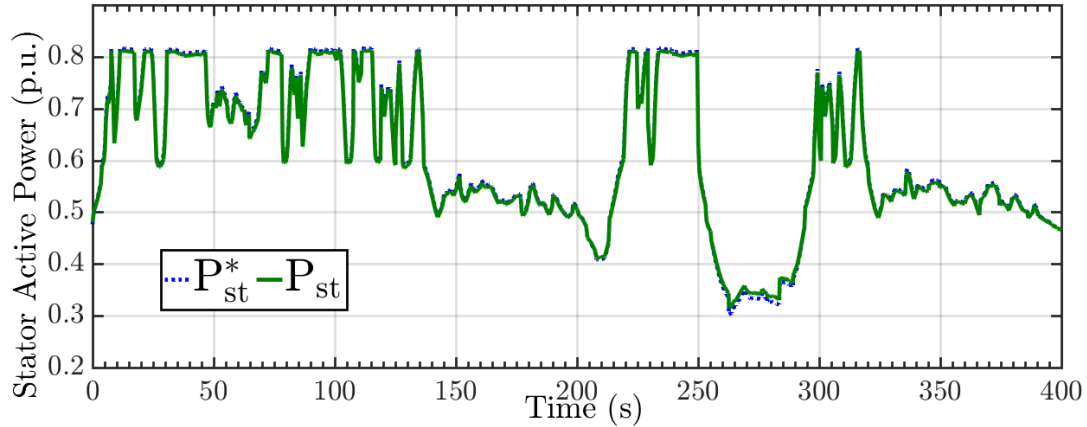


Figure 3.27: Stator Active Power Tracking with Estimators with $1.5 L_m$.

3.5.3 Analysis of the Observer Based Controller During Grid Voltage Sag

In this case, the performance of the two controllers were tested for a grid voltage sag condition in which the grid voltage drops to 0.6 of its nominal value for 0.625 seconds starting at 15 seconds. This particular test was selected to ensure that when the proposed architecture is used no additional external voltage ride through mechanism is required in the DFIG and none of the operating limits of the DFIG are violated. Figure 3.23 shows the comparison between the two state observer based feedback control performance during grid voltage sag conditions. It can be seen from Figure 3.23 that the state observer based state feedback control performs better during both the voltage sag condition and also has less voltage oscillations during the recovery period.

3.5.4 Simulation Results for Mutual Inductance Variation

It is desirable to test the performance of the machine control for its performance for parameter variations. In this work, the effect of machine mutual inductance parameters on state observer based SFC is studied. The test was performed on dynamic wind profile shown in Figure 3.7. Figure 3.24 shows the comparison between estimated d -axis rotor current and actual rotor current with 50 % variation in the mutual inductance. It can be seen that the estimated current has now more offset

as compared to the case without parameter variation. Similar results can be seen in figure 3.25, which shows the comparison between estimated q-axis rotor current and actual rotor current with 50 % variation in mutual inductance .Figure 3.26 shows the voltage control performance of the state feedback controller with state estimation with 50 % variation in mutual inductance. It can be seen that even though the estimated current has offset as compared to the actual current, the controller is still able to maintain the terminal voltage strictly at 1 p.u. Figure 3.27 shows the stator active power control performance of the state feedback controller with state estimation with 50 % variation in mutual inductance .

3.6 Simulation Results on a Modified IEEE 39 Bus System

The proposed controller is implemented on wind integrated IEEE 39 bus system on a real-time digital simulation platform. For this purpose, 200MW wind farm is connected at Bus-39 and Bus 25 as shown in Figure 3.28. The wind integrated 39 bus system is modeled in RSCAD/RTDS and the controller is implemented in MATLAB. RSCAD/RTDS and MATLAB are interfaced using GTNET-SKT for data transfer. Figure 3.29 shows the real-time implementation architecture of the controller.

For performance evaluation of the proposed observer based feedback control strategies on larger scale system, case studies as shown in Table 3.4 were designed. The controller performance is validated during variable wind speeds and grid fault conditions. Three cases are considered. In the first case, the performance of the controller is tested for varying wind speed for controller comparisons. In the second case, the performance of the state observer is evaluated for a dynamic wind profile. In the third case, the performance is evaluated during grid fault conditions and with dynamic wind profile. The test results for third case, show that the estimator based design can help sustain the fault ride through of the DFIG.

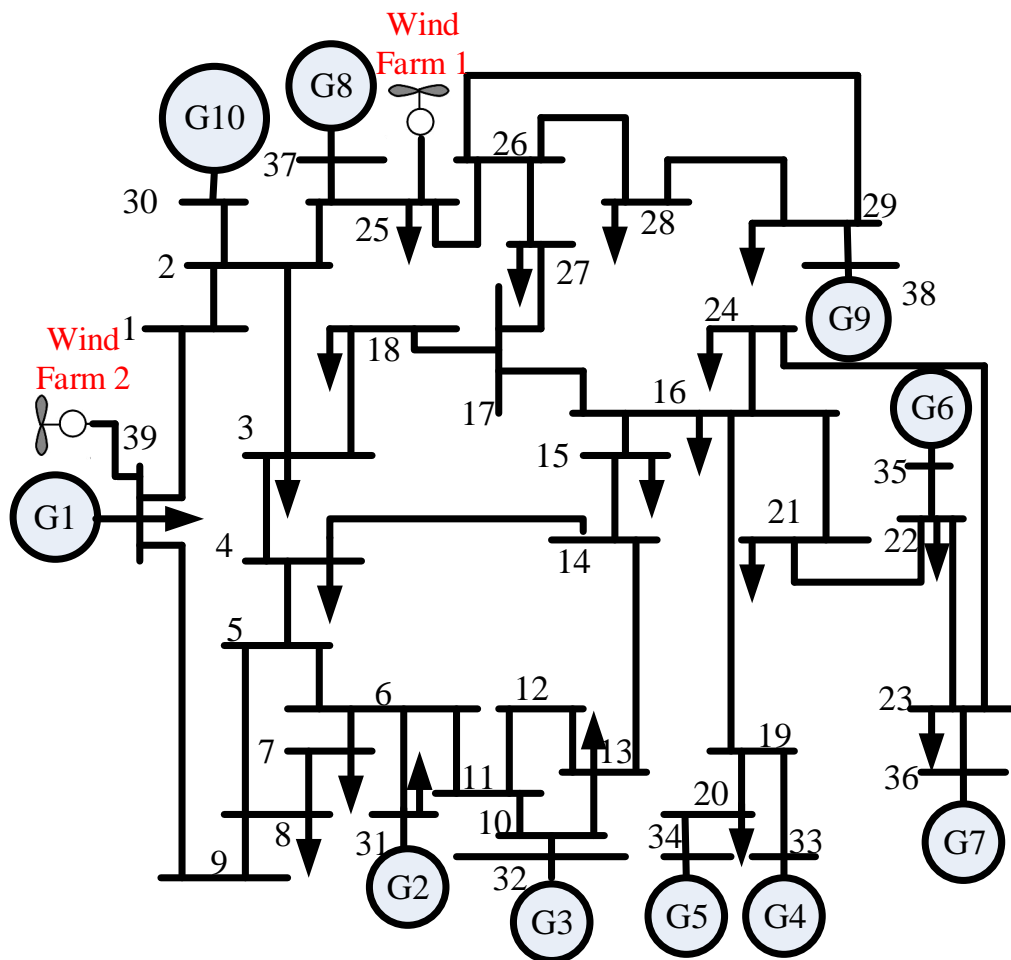


Figure 3.28: Wind integrated IEEE 39-bus System.

3.6.1 Comparison Between State Observer Based Feedback Controllers

For accurate comparison of the two reduced order state feedback control methodologies, the augmented vector control was also tuned using the feedback from reduced order state observer of the system. For this study, windfarm was connected at bus 17 in Figure 3.28. The wind speed profile used for this study is shown in Figure 3.30. In Figure (3.31 to 3.34), the first 16 seconds of simulation shows the performance of the controller with only varying wind speed. After 16 seconds, a 3-phase bolted fault is initiated for a time duration of 0.1 sec at bus 39. Figure 3.31 shows the estimated rotor current from the state observer along with the actual rotor current

Table 3.4: Case Studies on Large Scale System

Cases	Wind Farm	Wind Bus	Wind Profile	Test Scenario	Comparison	Comment
Case A	Bus 17	Figure 3.30	Steady State & Fault at Bus 39	State Observer Based VC & SFC	Controller comparison & performance evaluation	
Case B	Bus 25 & 39	Figure 3.35	State Estimation performance for dynamic wind profile	State Observer estimation comparison	State Observer performance evaluation	
Case C	Bus 25 & 39	Figure 3.35	Fault at bus 39	Response of windfarm at bus 39 & bus 25 for fault	Performance Analysis of observer based VC	

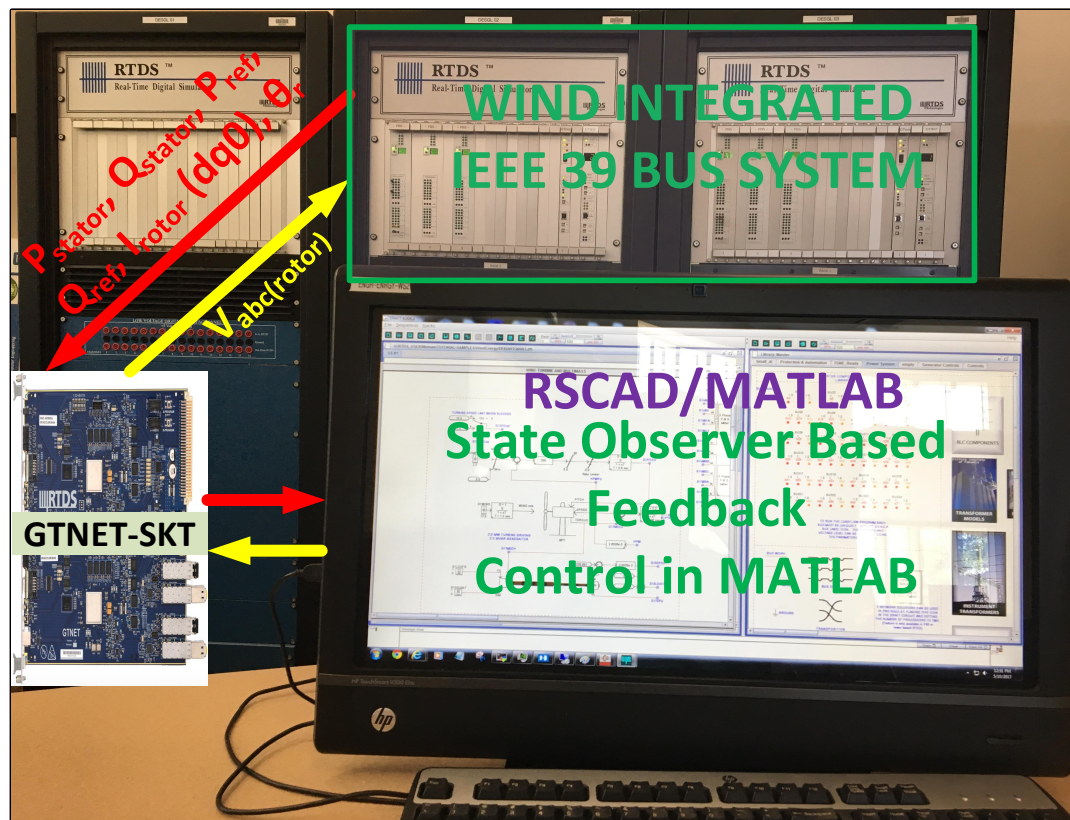


Figure 3.29: Real-Time Implementation Architecture.

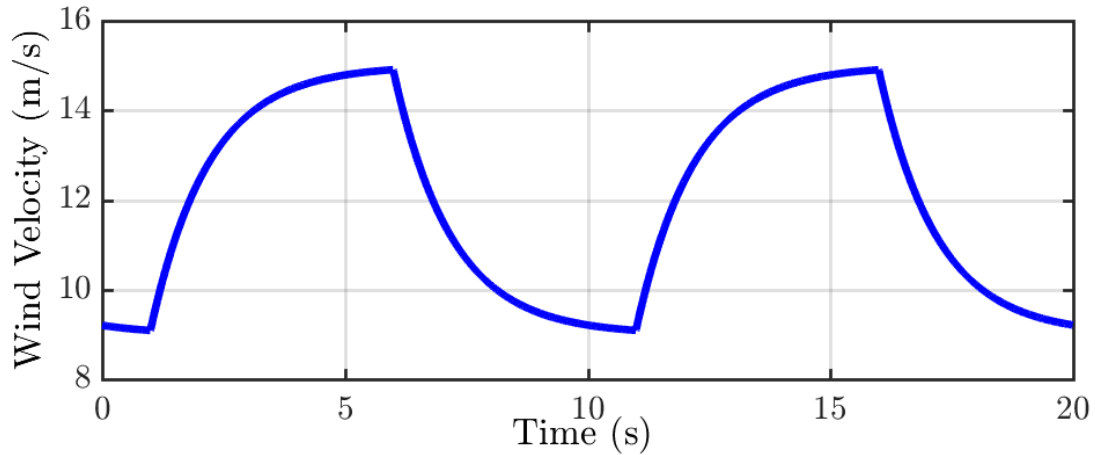


Figure 3.30: Wind speed Profile used for Case A.

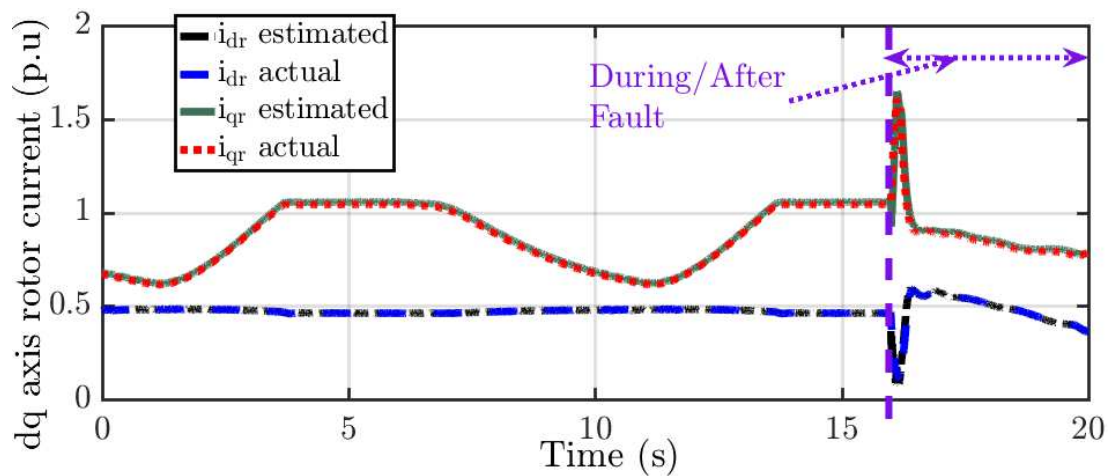


Figure 3.31: d - q axis Rotor Current Estimation during Steady State and Grid Fault Condition.

for this operating scenario. From Figure 3.32 it can be seen that the proposed state observer based control can accurately track dynamically changing stator active power reference with respect to the changing wind conditions. Also it can be seen that the controller can track the desired set point with minimum steady state error. Figure 3.33 shows the performance of the proposed state observer based feedback controllers for voltage regulation at the PCC. It can be seen that the proposed controller can tightly regulate the voltage at PCC during changing active power with respect to the wind. Figure 3.34 shows the comparison between the DFIG rotor speed.

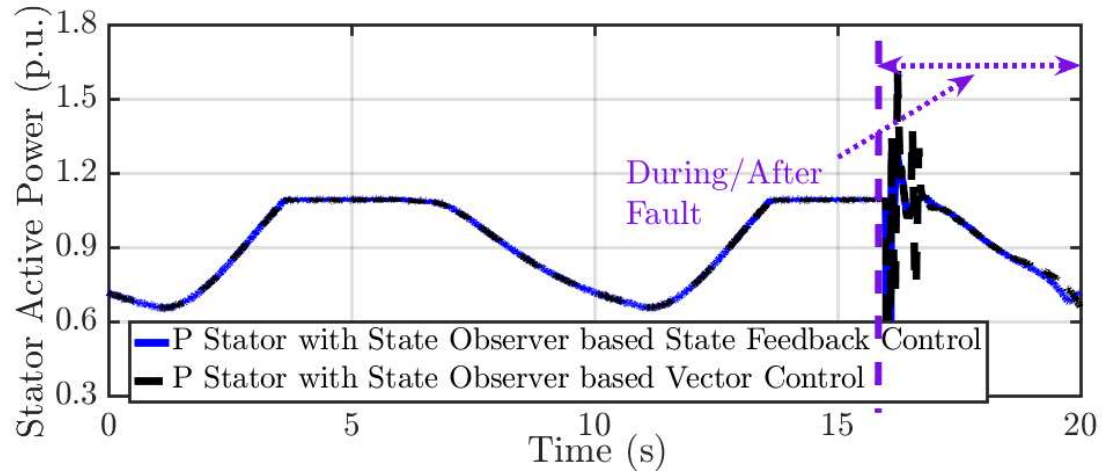


Figure 3.32: Stator Active Power Tracking Performance Comparisons in Steady State and Grid Fault Condition with the Two Controllers.

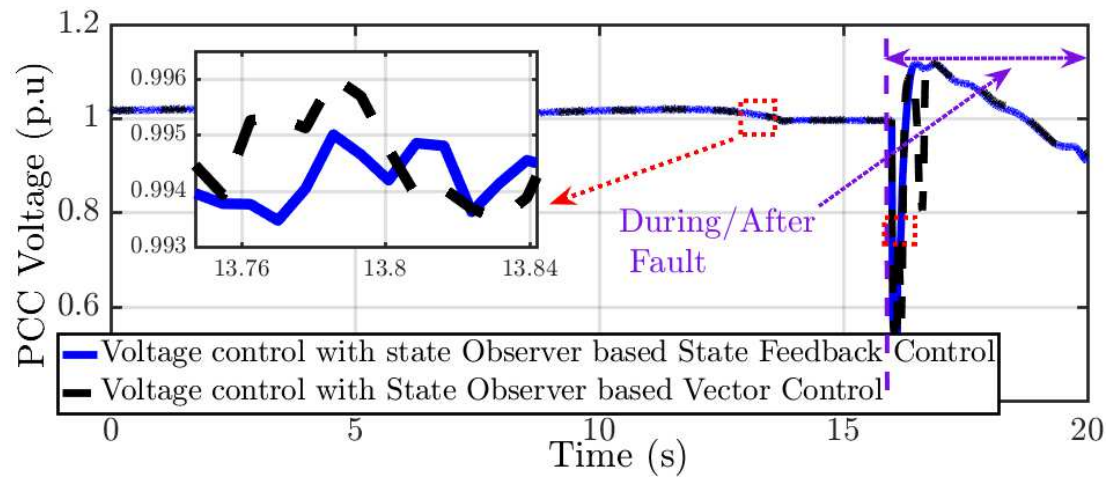


Figure 3.33: Voltage Profile Comparisons in Steady State and Grid Fault Condition with the Two Controllers.

3.6.2 Analysis of the State Observer Based State Feedback Control (SFC) for Dynamic Wind Conditions

Figure 3.35 shows the wind speed profile used for testing the proposed controller on the real-time experimental test-bed. Figure 3.36 shows the estimation performance of the proposed state observer when used in closed loop with the state feedback controller for windfarm 1 connected to bus 25. It can be observed that the state observer can estimate the current value of the rotor current to a higher degree of accuracy.

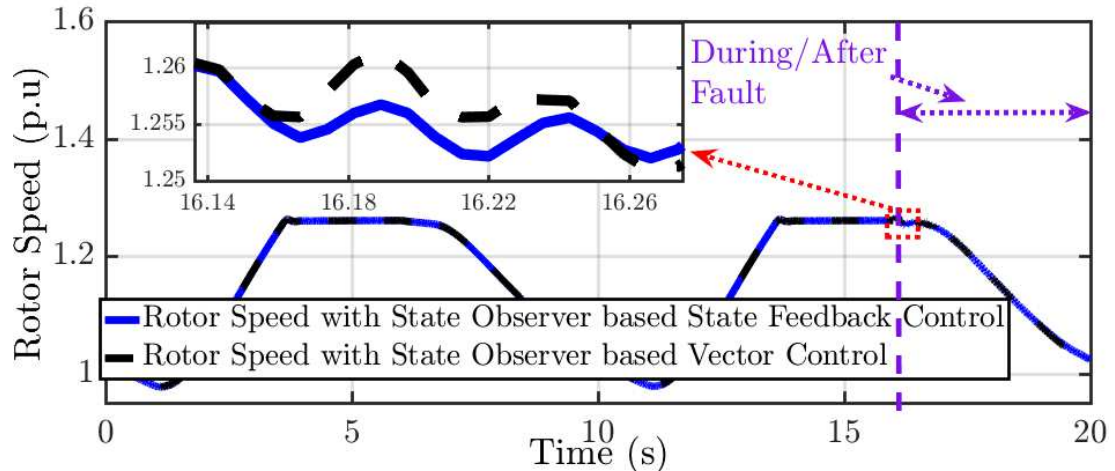


Figure 3.34: Rotor Speed Comparisons in Steady State and Grid Fault Condition with the Two Controllers.

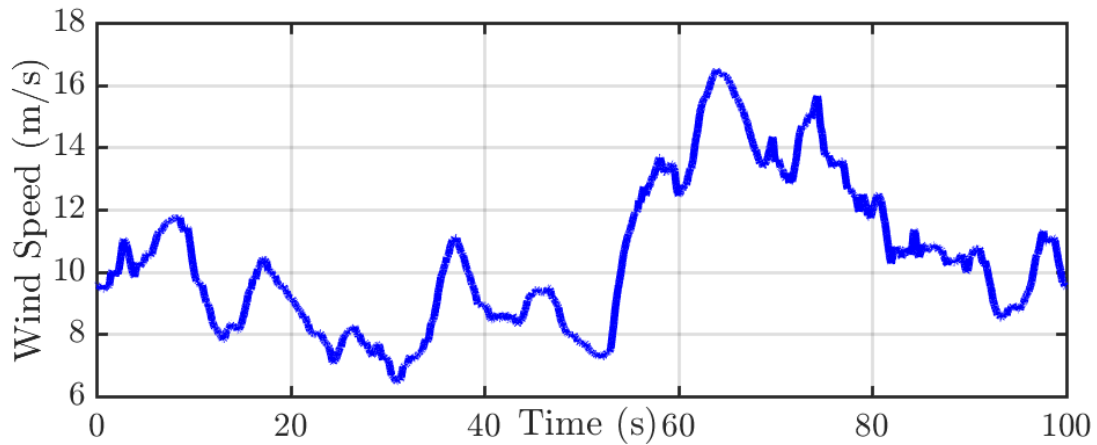


Figure 3.35: Wind speed Profile used for the Study.

3.6.3 Analysis of the Observer Based Vector Control(VC) For System Fault

To analyze the behavior of DFIG based windfarm with the proposed control methodology, a 3-ph bolted fault is initiated for a time duration of one and half cycle at bus 39, where the DFIG based wind farm 2 is connected. The stator active and reactive power before, during and after the fault is shown in Figure 3.37. The current estimation performance of the proposed observer during grid fault conditions is shown in Figure 3.38. It can be observed from Figure 3.38 that the estimator can estimate the rotor current during grid fault conditions. This performance of the rotor current

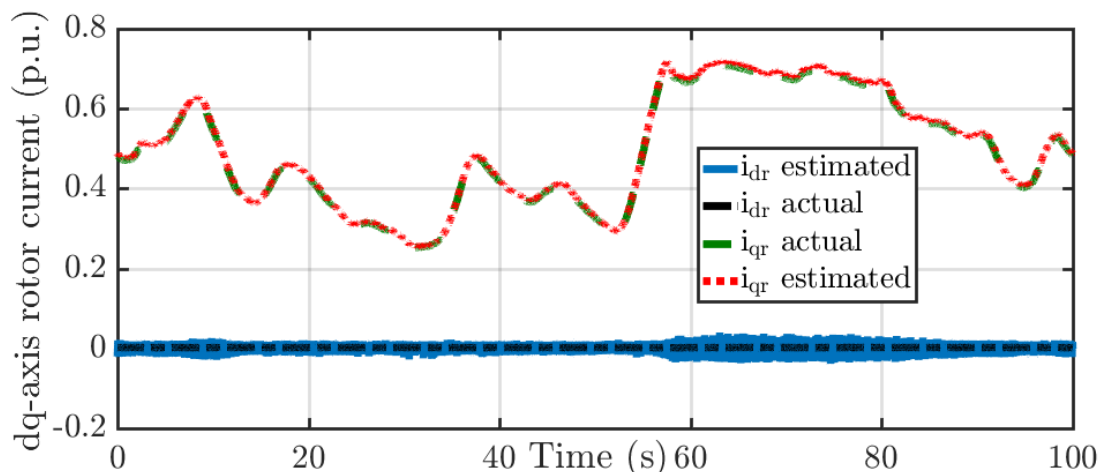


Figure 3.36: Rotor Current Estimation for Dynamic Wind Conditions.

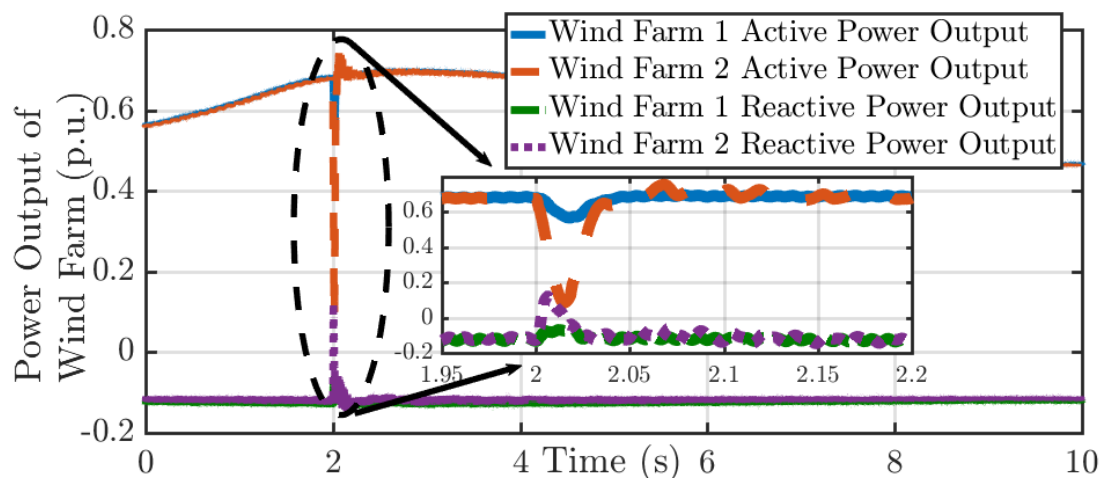


Figure 3.37: Stator Active Power Tracking Performance Comparisons.

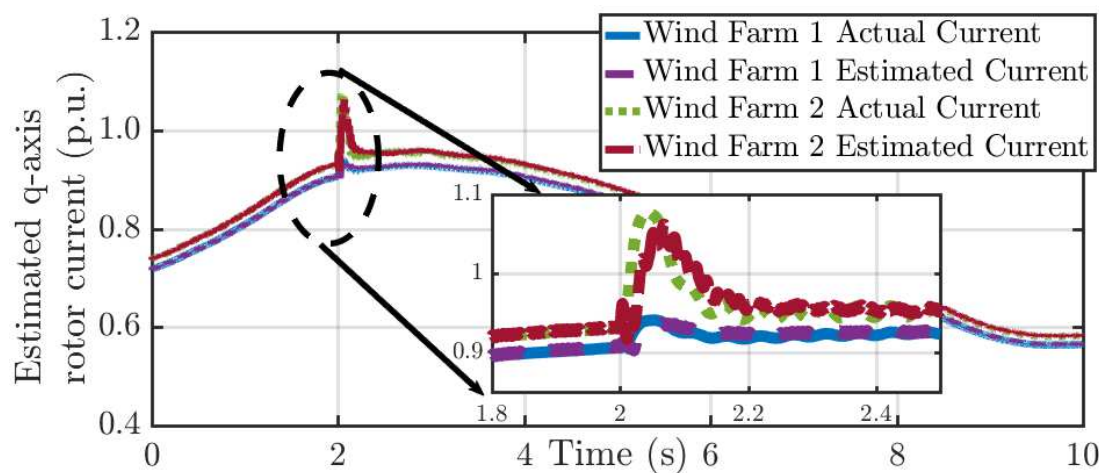


Figure 3.38: Rotor Current Estimation Comparison during Grid Fault Conditions.

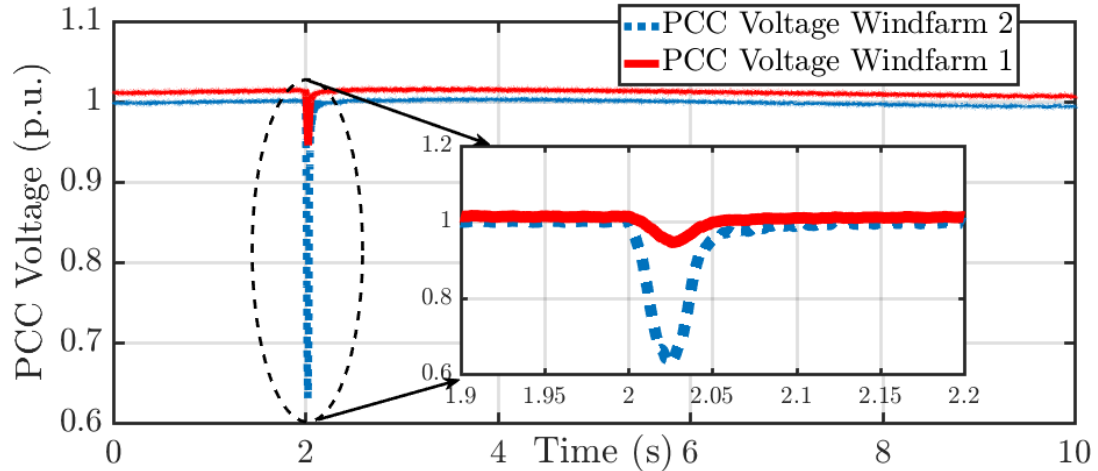


Figure 3.39: Voltage Profile Comparisons for Different Wind Farms.

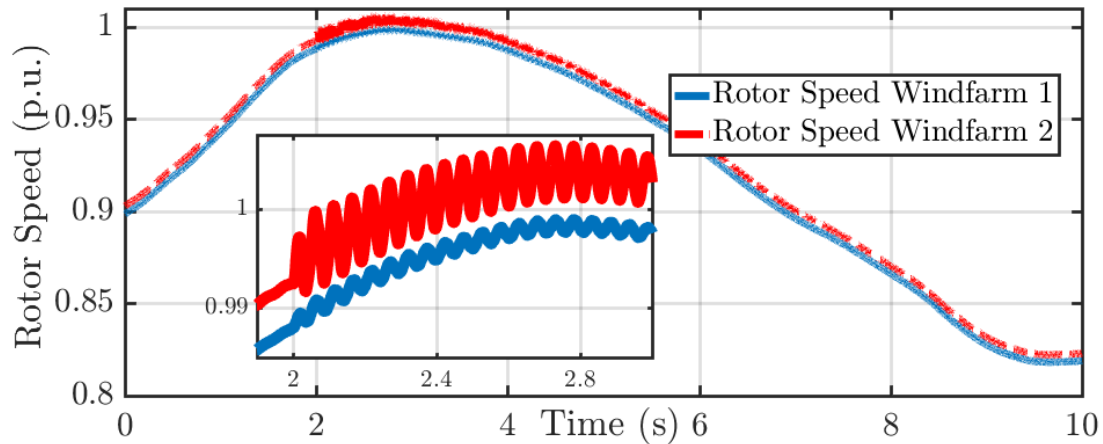


Figure 3.40: Rotor Speed for Different Wind Farm.

estimator is especially helpful when the DFIG based windfarm is expected to remain connected in the power grid during grid fault conditions. The PCC voltage at wind farm 1 and 2 is shown in Figure 3.39. The voltage sag in windfarm 1 is less as compared to windfarm 2 as it is farther away from the fault location. The DFIG rotor speed for windfarm 1 and windfarm 2 is shown in Figure 3.40. The oscillations in rotor speed for wind farm 2 is caused by the mismatch between mechanical power input and electrical power output of machine during and after the fault. The oscillations are also due to the slight mismatch between estimated current and actual current. The mismatch in current estimation has direct impact on active power output and

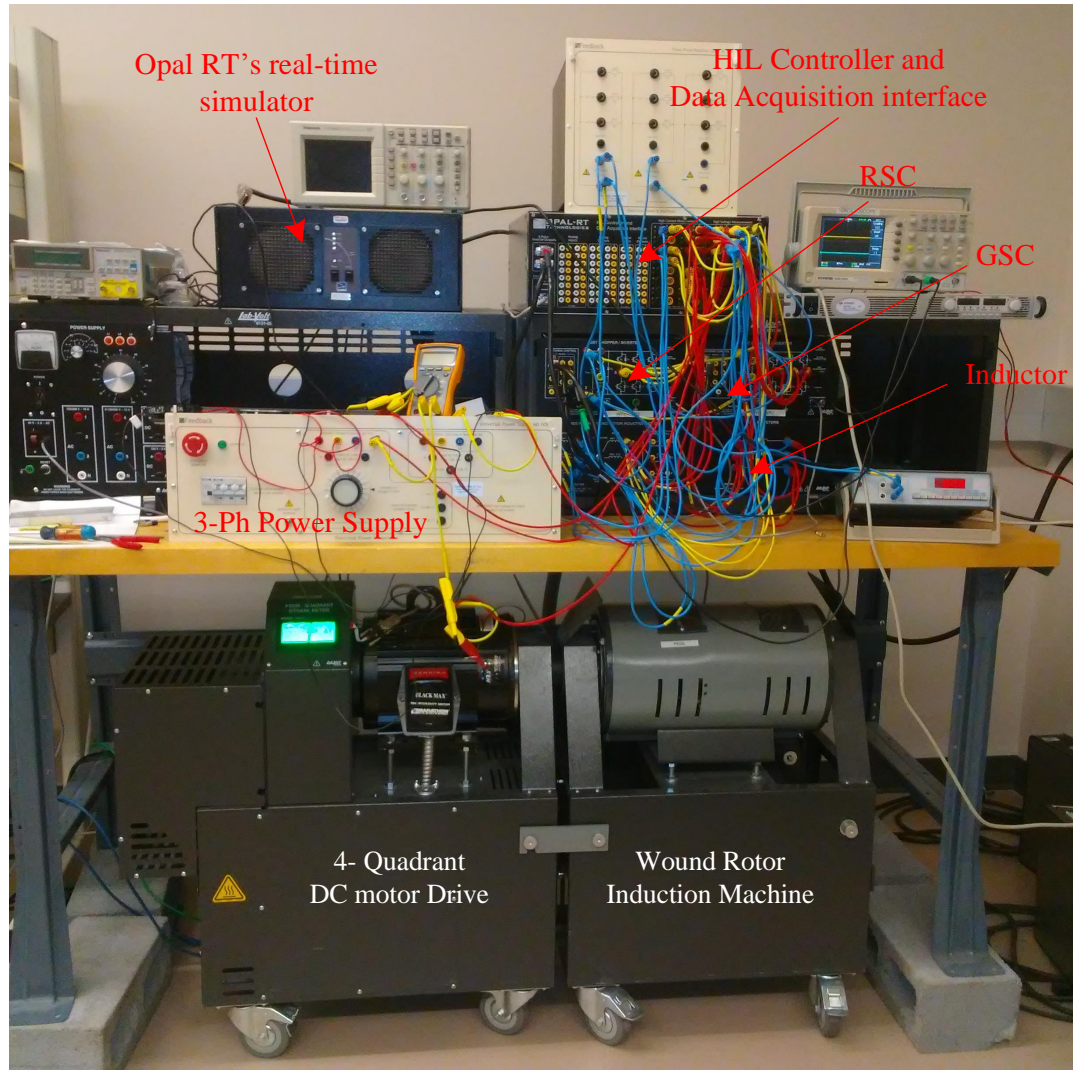


Figure 3.41: Experimental Setup.

hence electromagnetic torque of the machine. However, it can also be observed that the rotor oscillations damped out over time after the fault is cleared and current estimation error is minimized.

3.7 Hardware-in-the-Loop (HIL) Simulation Results

In this section, the performance of the proposed state observer based SFC is analyzed on a 2 kW DFIG set up using HIL simulation platform in a laboratory testbed. Figure 3.41 shows the laboratory setup used for testing the performance of the proposed controller. The RSC was controlled using the state observer based SFC, how-

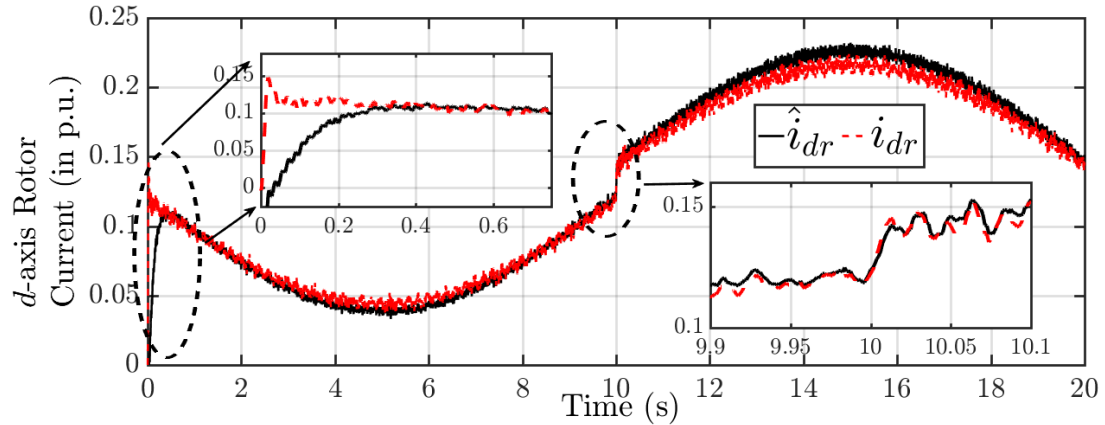


Figure 3.42: Comparison of Actual d -axis Rotor Current with the Estimated d -axis Rotor Current.

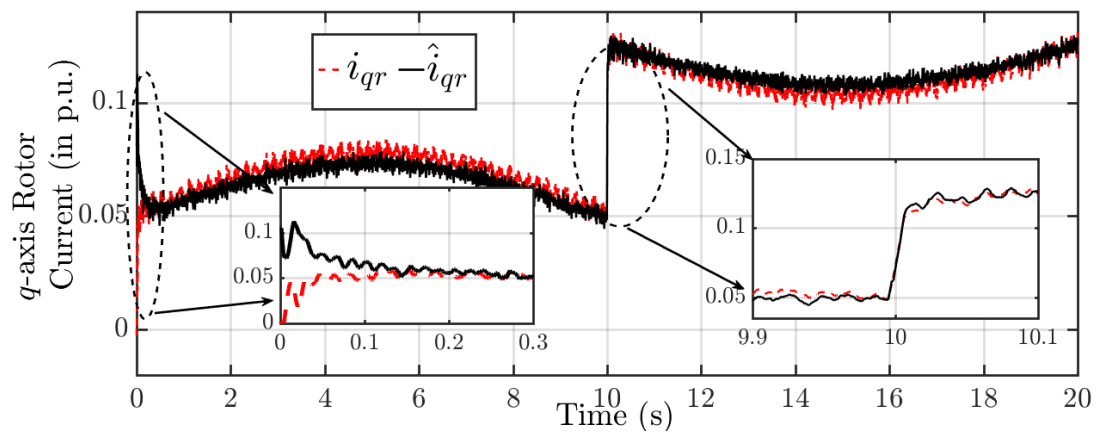


Figure 3.43: Comparison of Actual q -axis Rotor Current with the Estimated q -axis Rotor Current.

ever, the GSC was controlled using vector controlled technique with GSC maintaining the DC link voltage at 400V at unity factor. The ratings of the hardware setup used in provided in Appendix D.

3.7.1 Analysis of the State Observer based Controller for Dynamic Changes in Stator Power References

The closed loop performance of the proposed state observer based SFC was first tested for its suitability to implement in the closed loop control. Figure 3.42 and 3.43 shows the performance of the proposed state observer for estimating the rotor currents in the machine. It can be observed from Figure 3.42 and 3.43 that the proposed state

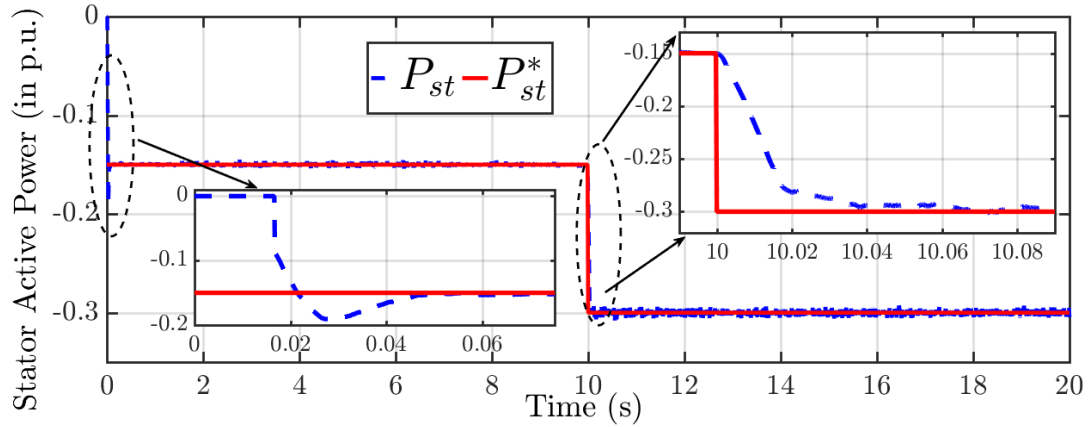


Figure 3.44: Stator Active Power Tracking Performance of the Proposed State Observer based SFC.

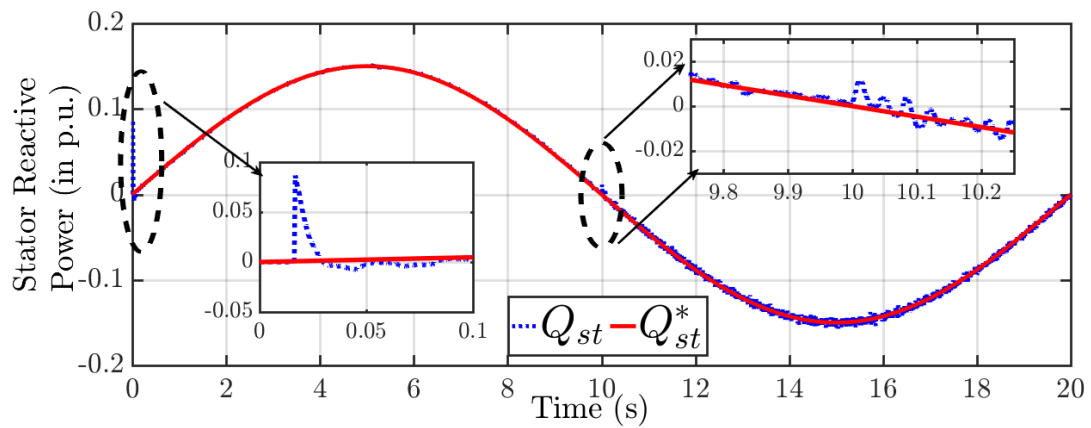


Figure 3.45: Stator Reactive Power Tracking Performance of the Proposed State Observer based SFC.

observer technique can estimate the rotor current in the machine within 0.2 secs of the simulation start time. Also, it can be observed from Figure 3.42 and 3.43 that once the observer converges to the actual value of the rotor currents, the error between the actual value and the estimated value of the rotor current is minimal and doesn't have much impact of the active and reactive power control of the DFIG as shown in Figure 3.44 and 3.45. To test the active and reactive power tracking performance of the proposed controller, a variable rotor speed profile starting at 1500 rpm and reaching 2100 rpm at 20secs was used, so that the machine operates both in sub-synchronous and super-synchronous mode. The laboratory DFIG was run in speed input mode

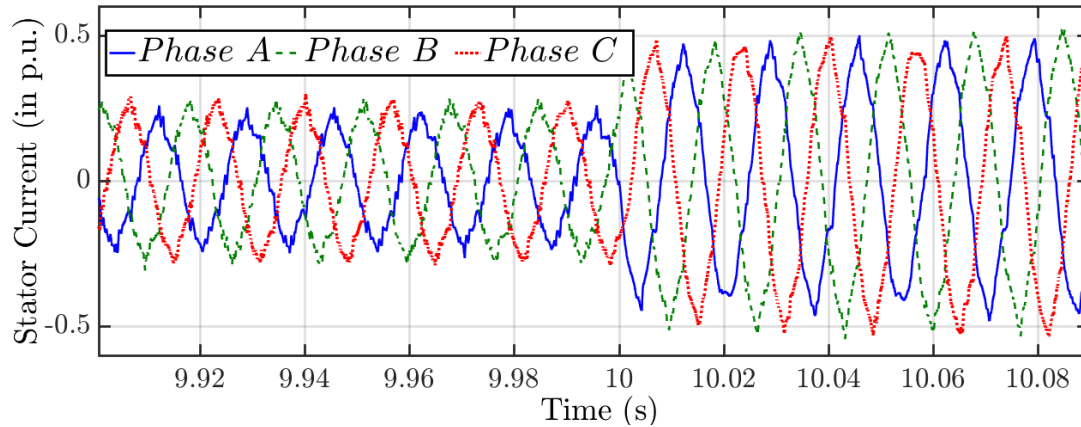


Figure 3.46: Instantaneous Stator Current.

with the DC motor drive generating the required torque to run the machine at the set speed. A step change in active power from 0.15 pu to 0.3 pu was used to access the performance of the proposed control technique. It can be observed from fig 3.44 that the state observer SFC has a faster response with no overshoot once the state observer converges as can be seen by the active power tracking performance at around 10s in Figure 3.44. For the reactive power tracking performance of the DFIG using the state observer based SFC a sinusoidal reference of amplitude 0.15 pu with a time period of 20 secs was used. It can be seen that the proposed state observer based SFC has a good tracking performance throughout the simulation time. During the start of the simulation before the observer converges, we can see a small overshoot in the reactive power which can be associated with the reactive power drawn by the machine. Also, by observing Figure 3.45, it is evident that the proposed control technique has lesser interaction between active power control and reactive power control loop as the step change in active power at 10 secs has minimal impact on the reactive power control loop. Figure 3.46 shows the instantaneous stator current at around 10 secs.

3.8 Chapter Summary

This chapter presented state estimator based SFC architecture for DFIG. First, the design of SFC considering the states are measurable is presented. Then the state ob-

server from the state-space model of the machine is designed. The design of controller and observer was discussed in detail and controllability and observability of the system is studied. The application of these state observer with VC and SFC is discussed. From the simulation results, it can be observed that the SFC showed equal performance when compared to VC and for sudden fast changes performed better. The proposed method is simple, effective and as it uses model reduction, and the architecture can be used to simplify controller design for large scale systems. The remarkable advantage of the reduced order based SFC proposed was an easier design and applicability in real-time implementation without significant computational delay because of the smaller sizes of state feedback matrix. It has been shown that the proposed state estimator based SFC showed very good performance when compared to state observer based VC technique. Also, the proposed method is simple and reduces the dependency of rotor current measurements in control of DFIG even when using with conventional vector control technique. The proposed controller has been implemented in a real-time simulation platform and HIL platform to show the feasibility. It has been observed that the architecture reduces computational complexity as the system state matrices for the reduced state model is much smaller when compared to actual system states. The proposed method is simple, effective and the architecture has been demonstrated for a large scale systems. The effect of machine parameter variations in the SFC was also studied and the results showed that the proposed SFC is robust to machine parameter variations even though the observer performance degrades as the parameter variation occurs. With the rotor current estimators the DFIG control can be implemented without the use of the rotor side quantities measurements. This can reduce the cost involved in the sensors and also increase the reliability of the system.

CHAPTER 4: MEASUREMENT BASED APPROACH: PARAMETRICALLY ROBUST DYNAMIC SPEED ESTIMATION BASED CONTROL FOR DFIG

This chapter presents a speed estimation based VC architecture for DFIG. The main advantage of the proposed architecture is that with this methodology the generator can be operated without a speed sensor and position encoder. The method calculates the machine parameters online using a RLS technique based on identifying the transfer function relating to rotor speed and position error. A minimum variance regulator ensures that the position error is minimum by proper estimation of the speed. For illustration, first, the small signal model of the machine and the regulator design is discussed. Then, a methodology is proposed, in which machine's mutual inductance is estimated on-line, so that the estimation approach is robust to changes in the machine parameters. Second, the control architecture with the speed estimation technique is discussed. The proposed approach is validated using a real-time simulation platform for a GE 1.5 MW wind turbine (both for steady state operations and grid disturbance conditions) and with hardware-in-the-loop experimental set up for a 2kW DFIM. Simulation and experimental results demonstrate desired steady-state and dynamic performance of this sensorless control approach for DFIG-based WECS.

The main contributions of the architecture can be summarized as follows:

- The proposed approach is based on machine dynamic model as it develops an online transfer function of the rotor speed and position error using a recursive identification routine based on measured quantities.
- The proposed approach is insensitive to parametric changes in the machine.
- The proposed approach establishes an online tuning method for speed error thus

ensuring that the architecture is robust.

- The method ensures faster speed estimation thus improving the controllability. Also the approach is tested using an experimental test-bed.
- As the speed estimation is performed using a second order model of the system, the computational burden of the proposed technique is not high.
- The proposed approach can help maintain the machine's operational stability during grid disturbance conditions which is critical for improving grid fault ride through capabilities.

4.1 Speed Observer for DFIG

In this chapter, the speed and position observer for DFIG rotor is based on designing an adaptive model and a reference model inspired from [27, 85]. This technique reduces the error in the reference and estimated current signal by dynamically adjusting the estimated rotor speed. The reference model used is the measured rotor current and the adaptive model is based on estimated rotor current through use of machine dynamics in (A.1) and (A.2). An estimation of the rotor current, \hat{i}_r , is computed based on measure-able stator voltage, v_s , and stator current, i_s . In stationary reference frame, the p.u. stator flux can be computed using (A.2) as

$$\psi_s = -L_s i_s + L_m i_r e^{j\theta_r} \quad (4.1)$$

where i_r represents the measured rotor current (at slip frequency) and θ_r is the position of the rotor with respect to stationary reference frame. From (4.1), the rotor current is obtained as,

$$i_r = \frac{\psi_s + L_s i_s}{L_m} e^{-j\theta_r} \quad (4.2)$$

Replacing θ_r in (4.2), with an estimation of the rotor angle, $\hat{\theta}_r$ and measured rotor current i_r with estimated rotor current, \hat{i}_r , the expression in (4.3) can be obtained for the estimated rotor current \hat{i}_r in stationary reference frame.

$$\hat{i}_r = \frac{\psi_s + L_s i_s}{L_m} e^{-j\hat{\theta}_r} \quad (4.3)$$

From this, an estimation of error between i_r and \hat{i}_r can be calculated by properly defining an error function. The error in $\alpha - \beta$ components between the measured rotor current i_r and estimated rotor current \hat{i}_r is defined as the angle between cross product and dot product between \hat{i}_r and i_r computed using *atan2* function. Let 'c' represents the magnitude of the cross product between i_r and \hat{i}_r and 'd' represents the dot product between i_r and \hat{i}_r . That is

$$\begin{aligned} c &= |i_r| |\hat{i}_r| \sin(\theta_{err}) \\ d &= |i_r| |\hat{i}_r| \cos(\theta_{err}) \end{aligned} \quad (4.4)$$

where θ_{err} is the angle between vectors i_r and \hat{i}_r . It is worth noting that correct estimation of rotor speed and position is achieved when $\theta_{err} \cong 0$. The error function 'ε' is defined using the 'arctangent' of the ratio of cross product and dot product as,

$$\epsilon = \text{atan2}\left(\frac{c}{d}\right) \quad (4.5)$$

It can be seen that the error is driven to zero when the cross product approaches zero and the dot product is a positive number. This happens when the measured current vector aligns with the estimated current vector. The *atan2* function eliminates the chances of incorrect rotor position estimation. Under normal estimation, the error function can be determined as the cross product. However, the cross product can be zero when two vectors are 180° apart as well, but at that instant the dot product of

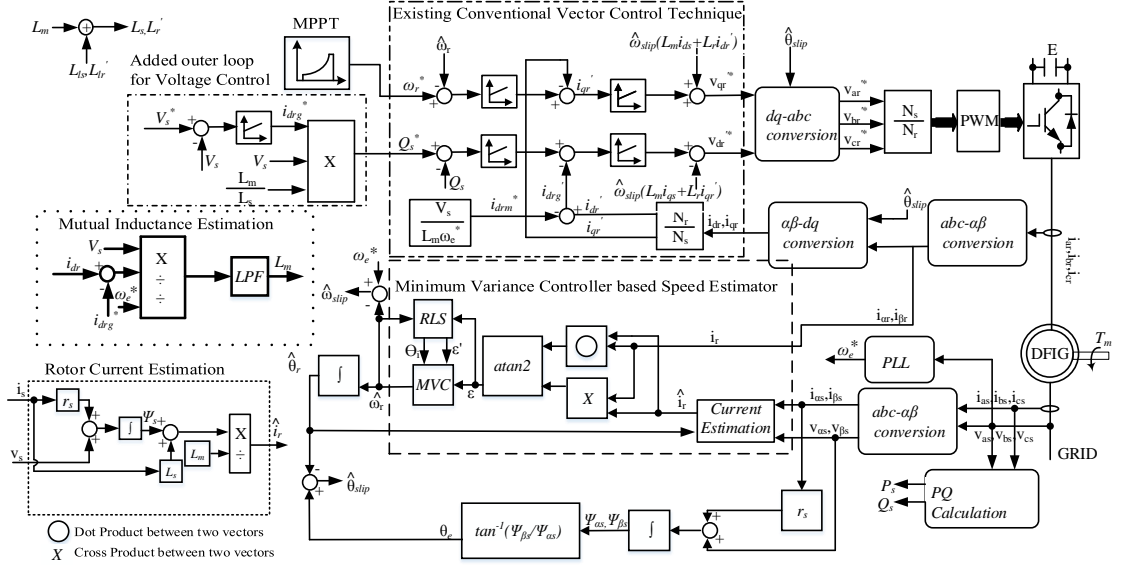


Figure 4.1: Proposed Sensorless VC Scheme for a Grid Connected DFIG.

the vectors would result in negative quantity. As ‘atan2’ function takes care of sign of the cross product and dot product of the estimated currents and actual currents, the error is driven to zero only when the estimated rotor current almost aligns with the measured rotor current. Figure 4.1 also shows the proposed speed and position estimation technique applied along with the conventional VC for active and reactive power control of the DFIG.

4.2 Main Contributions: Dynamic Speed Estimation for DFIG

This section presents the design for the parametric variation robust speed estimation. Figure 4.2 shows the small signal model of the proposed architecture.

4.2.1 Small Signal Model of Proposed Estimator

To derive the small signal model of the proposed system, *atan2* as the error function is approximated as follows [85]

$$\epsilon = \text{atan2}\left(\frac{c}{d}\right) = 2 * \text{atan}\left(\frac{c}{\sqrt{c^2 + d^2} + d}\right) \quad (4.6)$$

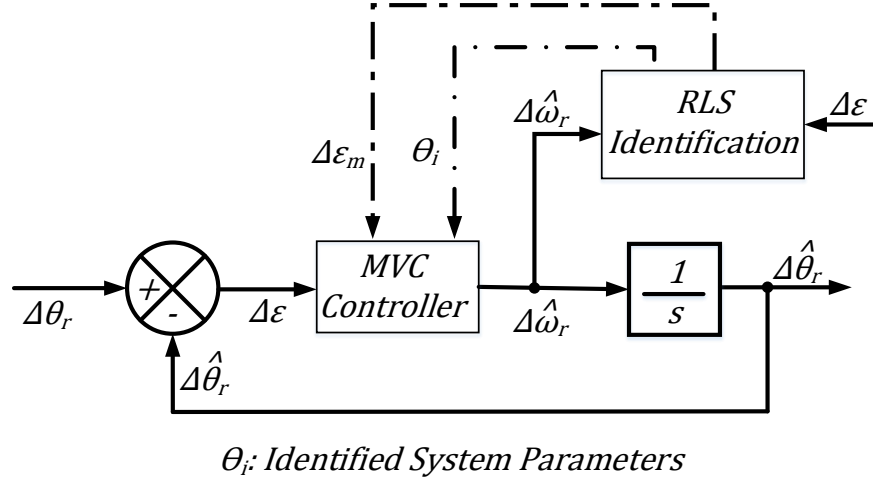


Figure 4.2: Small Signal Model of Proposed Speed Estimator.

Using the Taylor series approximation of $atan(z)$ as,

$$atan(z) = z - \frac{z^3}{3} + \frac{z^5}{5} - \dots \quad (4.7)$$

After neglecting the higher terms of $atan(z)$ (as z , the position estimation error, approaches zero for steady state condition), from (4.6) and (4.7) following approximation of $atan2$ function is obtained.

$$atan2\left(\frac{c}{d}\right) = 2 \times \frac{c}{\sqrt{c^2 + d^2} + d} \quad (4.8)$$

Table 4.1 compares the output of the $atan2$ function with the output of the $atan2$ approximation in (4.8). In doing so, the denominator d is fixed at 1. It can be seen that the above approximation has a minimal error, when approximating small ratio of magnitude of cross product c and dot product d .

Table 4.1: atan2 Approximations for Small Deviations

Deviation around 0 ($ c $)	atan2 from MATLAB (<i>radians</i>)	Approximated atan2 (<i>radians</i>)	Absolute Estimation Error (<i>degrees</i>)
-0.25	-0.2450	-0.2462	0.0012
-0.15	-0.1489	-0.1492	0.0003
-0.05	-0.05	-0.05	0
0.05	0.05	0.05	0
0.15	0.1489	0.1492	0.0003
0.25	0.2450	0.2462	0.0012

Using (4.4) and (4.8), the error expression (4.6) reduces to

$$\epsilon = \text{atan2}\left(\frac{c}{d}\right) = \frac{2|i_r||\hat{i}_r|\sin(\theta_{err})}{|i_r||\hat{i}_r| + |i_r||\hat{i}_r|\cos(\theta_{err})} \quad (4.9)$$

Also, it is important to note that the estimated current, \hat{i}_r is rotating at a relative speed of $w_r - \hat{w}_r$ with respect to the actual current, i_r . If the initial conditions are to be neglected, the θ_{err} can be written as

$$\theta_{err} = \frac{\omega_r - \hat{\omega}_r}{s} \quad (4.10)$$

where ω_r and $\hat{\omega}_r$ are the actual rotor speed and estimated rotor speed, s is the derivative operator.

A small signal model of the error function is then derived assuming that all the machine parameters are correctly known, and at the stable operating point, $i_{r0} = \hat{i}_{r0}$ and $\theta_{err} = 0$. Linearizing the error function (4.9) and estimation error (4.10), the small signal model after some algebraic rearrangement can be obtained as

$$\Delta\epsilon = \Delta\theta_{err} = \frac{\Delta w_r - \Delta\hat{w}_r}{s} \quad (4.11)$$

where $\Delta\epsilon$ is the error in alignment of \hat{i}_r with respect to i_r and Δw_r and $\Delta\hat{w}_r$ are the

deviations in the actual and estimated speed.

The derived small signal model in (4.11) assumes ideal conditions ignoring the non-linear effects such as sampling delays, machine parameter variations and distortion in the DFIG voltages and currents. To deal with this non-linearities the relation between error ϵ and estimated rotor speed $\hat{\omega}_r$ is identified using the RLS based identification technique, and once the relation between ϵ and $\hat{\omega}_r$ is obtained, those parameters are used by a MVC acting as a regulator to drive the error in (4.9) to zero by adjusting $\hat{\omega}_r$. This improves the controller robustness.

4.2.2 Machine Parameter Sensitivity

The proposed speed estimation technique with RLS and MVC acting as a regulator produces incorrect estimation of rotor angle if the machine parameters are not correctly identified. As the estimated rotor angle is used to demodulate the rotor currents and rotor voltage reference generation, an incorrect estimation of the rotor position effects the control performance of the DFIG. The dependency of the rotor angle estimation in the machine parameter can be obtained using a small signal model. From (4.3) it can be seen that the rotor current estimation is dependent on the stator inductance L_s and machine mutual inductance L_m . As stator inductance L_s is the sum of stator leakage inductance L_{ls} and L_m and L_{ls} is a small quantity as compared to L_m , it can be verified that accurate rotor current and the rotor position estimation is dependent on accurately identifying machine mutual inductance L_m . It has been shown in [80] that a variation in mutual inductance estimation by 50% can lead to angle estimation error of upto 15° .

The small signal model of (4.3) in synchronously rotating reference frame is obtained as

$$\hat{i}_r = \frac{\psi_s}{L_m} + \left(1 + \frac{L_{ls}}{L_m}\right) i_s \quad (4.12)$$

Note that in synchronously rotating reference frame the currents are seen as DC quantity. The rotor position can be safely neglected for engineering purposes as the rotor position in synchronously rotating reference frame is in close proximity to the reference frame. Now, if L_{ls}/L_m is ignored, (4.12) can be written as

$$\hat{i}_r = \frac{\psi_s}{L_m} + i_s \quad (4.13)$$

Assuming that the stator flux is well regulated, the machine operating point does not change and $i_{r0} = \hat{i}_{r0}$. A small change in the machine parameter leads to the following changes in the rotor current estimation.

$$\Delta \hat{i}_r = \frac{i_{s0} \Delta L_m - i_{r0} \Delta L_m}{L_m} \quad (4.14)$$

where i_{s0} steady state stator current. From (4.14), it can be seen that if $L_{ls} \ll L_m$, the error in rotor current estimation varies linearly with the variation of the machine mutual inductance. Also, the rotor current estimation depends on the machine operating condition.

At the steady state condition, variation in mutual inductance varies the phase and magnitude of the estimated rotor current. This phase error is corrected by the RLS based observer and MVC controller. However, this may introduce an offset of $\Delta\theta$ in the rotor position estimation. Therefore, an incorrect estimation of the L_m is equivalent to an offset in the measured position [27] of the encoder.

The speed estimator is mainly affected by incorrect estimation of L_m . The estimated rotor current obtained from (4.3) is dependent on accurate estimation of stator flux, which in turn is dependent on stator resistance. However, as stator resistance has negligible effects on stator flux estimation, rotor current estimation in (4.3) is robust to variations against stator resistance [27]. As the rotor resistance does not affect the estimation of rotor currents, the proposed speed estimator is not affected

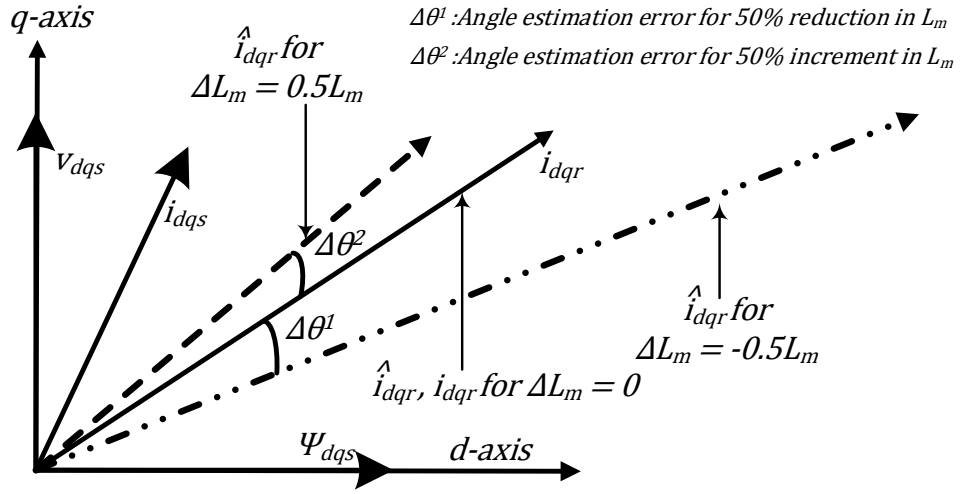


Figure 4.3: Phasor Diagram showing the Effect of L_m Variation on Rotor Position Estimation.

by its variations. Figure 4.3 shows the effect of variation of the machine mutual inductance.

4.2.3 Minimum Variance Controller

Once the system identification is achieved, MVC is designed which gives a proper estimate of $\hat{\omega}_r$ that minimizes the error in rotor position estimation, ϵ . For MVC design, the system is assumed to be described by the CARMA model [85, 100] which in terms of the speed estimation error and estimated speed is given as:

$$\epsilon(k) = \frac{B(q^{-1})}{A(q^{-1})} \times \hat{w}_r(k) + \frac{C(q^{-1})}{A(q^{-1})} \times \varrho(k) \quad (4.15)$$

where ϱ represents the error in model representation and noises in the system.

Using the system time delay information, MVC minimizes the variance of the output at $k+d$ with respect to the expected value of output at $k+d$ using the information gathered at up to time instant k . This means controller goal is to minimize the following objective function: $J(k) = E\{\epsilon(k+d)^2\}$, where d is the assumed system delay and E represents the expected value of the output d steps into the future. In this

paper, the system equations are represented as:

$$\begin{aligned}
A(q^{-1})\epsilon(k) &= B(q^{-1})\hat{w}_r(k) + C(q^{-1})\varrho(k) \\
A(q^{-1}) &= 1 + a_1q^{-1} + a_2q^{-2} \\
B(q^{-1}) &= q^{-1}(b_0 + b_1q^{-1}) \\
C(q^{-1}) &= 1
\end{aligned} \tag{4.16}$$

$C(q^{-1}) = 1$ suggests that the noise ϱ considered is a white noise with mean of zero and variance of 1. From (4.15) and (4.16), it can be seen that,

$$(1 + a_1q^{-1} + a_2q^{-2})\epsilon(k) = q^{-1}(b_0 + b_1q^{-1})\hat{w}_r(k) + \varrho(k) \tag{4.17}$$

and,

$$\epsilon(k) = q^{-1}(-a_1 - a_2q^{-1})\epsilon(k) + q^{-1}(b_0 + b_1q^{-1})\hat{w}_r(k) + \varrho(k) \tag{4.18}$$

If the time index in prediction is shifted by one (i.e $q^{-d}Y(k+d) = Y(k)$), (4.18) can be written as

$$\epsilon(k+1) = (-a_1 - a_2q^{-1})\epsilon(k) + (b_0 + b_1q^{-1})\hat{w}_r(k) + \varrho(k+1) \tag{4.19}$$

In (4.19), LHS represents output signal one step into the future and the RHS contains information about present and past output signals, present and past control signals and future estimation error signals.

The control action $\hat{w}_r(k)$ is computed in order to optimize the variance of the output single step in the future

$$\begin{aligned}
\underset{\hat{w}_r(k)}{Min}\{J(k)\} &= \underset{\hat{w}_r(k)}{Min}E\{\epsilon(k+1)^2\} = \\
\underset{\hat{w}_r(k)}{Min}E\{[(-a_1 - a_2q^{-1})\epsilon(k) + (b_0 + b_1q^{-1})\hat{w}_r(k) + \varrho(k+1)]^2\} & \tag{4.20}
\end{aligned}$$

In (4.15), as the model estimation error is assumed to be a white noise, and its future values cannot be correlated with past signals. Therefore, the minimum variance will be achieved when the sum of the first two components is set to zero.

$$(-a_1 - a_2q^{-1})\epsilon(k) + (b_0 + b_1q^{-1})\hat{w}_r(k) = 0 \quad (4.21)$$

Overall MVC has the following form

$$\hat{w}_r(k) = \frac{a_1 \times \epsilon(k) + a_2 \times \epsilon(k-1) - b_1 \times \hat{w}_r(k-1)}{b_0} \quad (4.22)$$

As mentioned in [100], the properties of control signal when the MVC is used depend critically on the sampling interval. A low sampling time gives a large variance in the control signal, and a high sampling time gives a low variance. In this paper, a controller sampling time which is 20 times slower than the simulation sampling time is chosen such that variation in the estimated speed $\hat{\omega}_r$ is minimum. If a sampling time equal to the simulation time step is used, a moving average of the estimated speed $\hat{\omega}_r$ based on at least 15-20 estimates sampled at the simulation time step is suggested to get a smoother estimate of rotor speed.

4.2.4 Closed Loop Response of Proposed Speed Estimator

With the estimated speed derived in (4.22) and assuming the convergence of RLS algorithm to a proper parameters of the system, from (4.16) one gets,

$$\epsilon(k) = \varrho(k) \quad (4.23)$$

From (4.23), it can be observed that the MVC law let the closed loop speed estimation error converges to the noise in the system which has a mean of zero.

4.2.5 Asymptotic Properties of MVC with RLS Identification

Consider the time shifted output of the model of the system as obtained from RLS algorithm as,

$$y(k+d) = \phi^T(k)\hat{\theta} + \epsilon(k+d) \quad (4.24)$$

where $\phi^T(k)$ is the matrix containing past input and output data and $\hat{\theta}$ represents the estimated system parameters. From the discussion in 4.2.4, with the control law implemented in the system, it can be observed that,

$$\phi^T(k)\hat{\theta}(k+d) = 0 \quad (4.25)$$

Considering at an equilibrium the estimated parameters $\hat{\theta}$ are constant and satisfy the normal equation as [100],

$$\frac{1}{t} \sum_{k=1}^t \phi(k)y(k+d) = \frac{1}{t} \sum_{k=1}^t \phi(k)\phi^T(k)\hat{\theta}(t+d) \quad (4.26)$$

Using (4.25) it follows that

$$\frac{1}{t} \sum_{k=1}^t \phi(k)y(k+d) = \frac{1}{t} \sum_{k=1}^t \phi(k)\phi^T(k) \left(\hat{\theta}(t+d) - \hat{\theta}(k+d) \right) \quad (4.27)$$

Thus it can be observed that if the estimate $\hat{\theta}(t)$ converges as $t \rightarrow \infty$, and the regression vectors are bounded, the right-hand side in (4.27) goes to zero. This leads to the conclusion that the system output which in this case is the error ϵ converges to zero asymptotically.

4.2.6 Estimation of Mutual Inductance of DFIG

In this paper, an augmentation of existing VC technique is proposed such that machine mutual inductance can be estimated. In stator flux oriented reference frame (synchronously rotating), after using (A.2), the reactive power on the stator side given

by (A.3) modifies to

$$Q_{st} = -\frac{v_{qs}\psi_{ds}}{L_s} + \frac{v_{qs}L_m}{L_s}i_{dr} \quad (4.28)$$

The rotor current i_{dr} can be divided into two components, one that branches towards the magnetizing reactance and the other one that is responsible for generating reactive power at the stator terminals or maintaining the terminal voltage at the stator side.

Thus, (4.28) will be

$$Q_{st} = \underbrace{\left(\frac{-v_{qs}\psi_{ds}}{L_s} + \frac{v_{qs}L_m}{L_s}i_{drm} \right)}_{Q_{mag}} + \underbrace{\frac{v_{qs}L_m}{L_s}i_{drg}}_{Q_{gen}} \quad (4.29)$$

From (4.29), it can be seen that the stator reactive power can be divided into two components:

- Magnetizing component.
- Reactive power generating component.

If the no load magnetizing reactive power from stator is desired to be zero i.e., all the machine magnetizing reactive power is supplied from the rotor side and machine does not consume magnetizing reactive current from stator, Q_{mag} in (4.29) can be equated to zero. Further, after neglecting the stator transients in (A.1), L_m can be approximated as

$$L_m = \frac{v_{qs} + R_s i_{qs}}{i_{drm}} \quad (4.30)$$

Using (4.30), one can get an appropriate estimate of the machine's mutual inductance, if the magnetizing component of the d -axis rotor current is known. To get the value of i_{drm} , it has been assumed that the reactive power generating component of rotor current i_{drg} is equal to i_{drg}^* generated by the outer loop voltage control. So, in steady

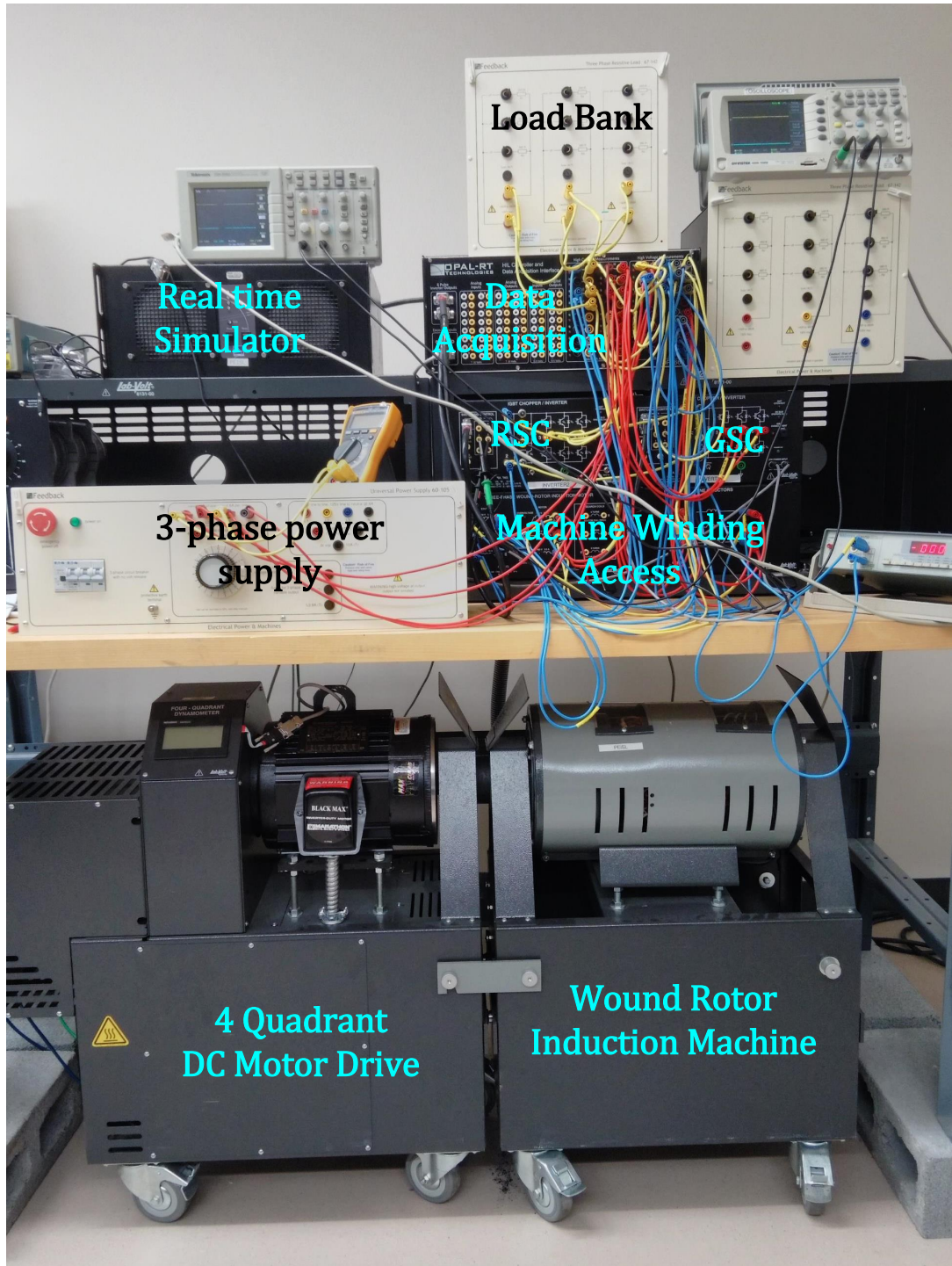


Figure 4.4: Hardware Set-up Used.

state, i_{drm} is equal to difference between measured rotor current i_{dr} and reference for reactive power generating component of rotor current i_{drg}^* as shown in mutual

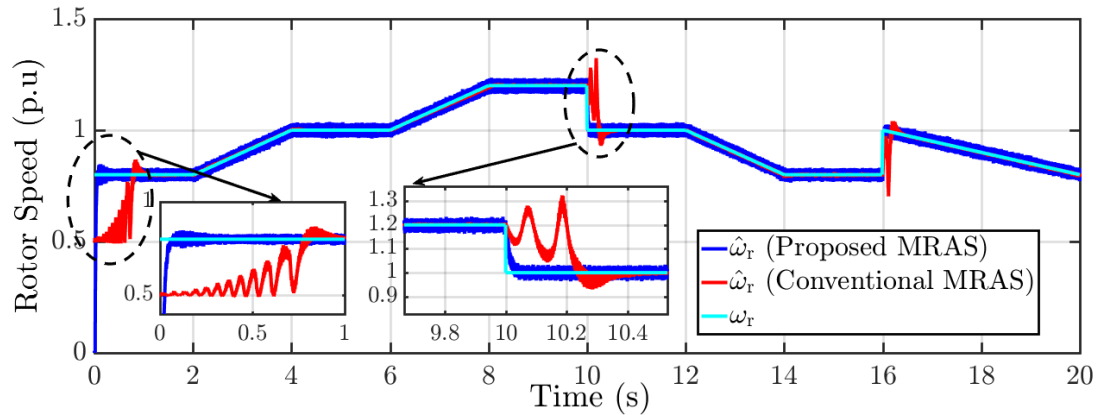


Figure 4.5: Rotor Speed Estimation Comparison between the Proposed MRAS Technique and Conventional MRAS Technique.

inductance estimation block in Figure 4.1. The low pass filter before the mutual inductance output is required to make the time constant of the mutual inductance estimation slower than the voltage control loop, which in this chapter is used at 1.5 seconds. The implementation of the proposed speed estimation technique is discussed next based on the control schematic represented in Figure 4.1.

4.3 Experimental Results

The control system shown in Figure 4.1 and system identification architecture shown in Figure 4.2 has been implemented on a 1.5 MW GE wind turbine [90] as a single machine connected to infinite bus through transmission line in a real time simulation set up. Further the experimental system is studied using a 2kW DFIM driven by a DC motor in a laboratory setup. The schematic diagram for experimental rig is shown in Figure 4.4.

4.3.1 Comparison with the Conventional MRAS based Speed Estimation Technique

The performance of the proposed speed observer was compared with the existing speed observer on a test case with DFIG parameters as listed in D. This test is carried out in a speed input mode for the machine assuming the external MPPT controller

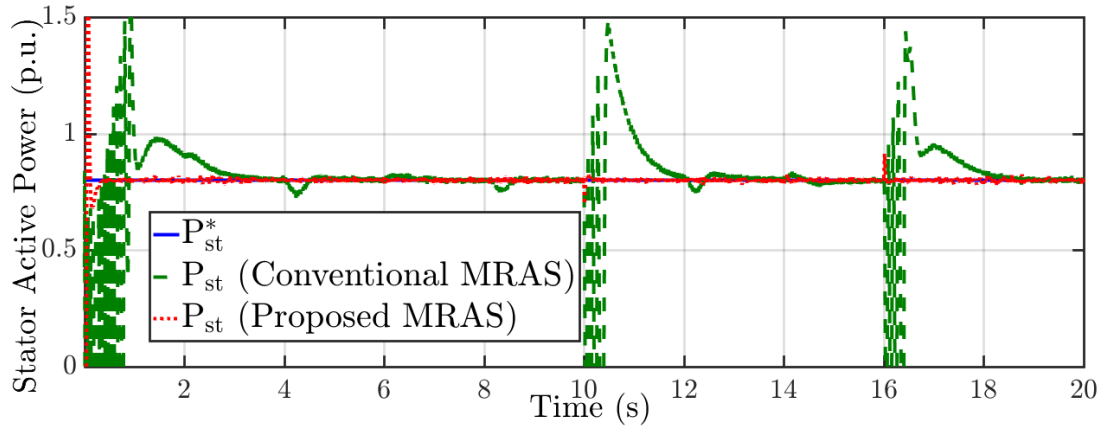


Figure 4.6: Active Power Tracking Performance Comparison of DFIG with Speed Estimated using the Proposed MRAS technique and conventional MRAS Technique.

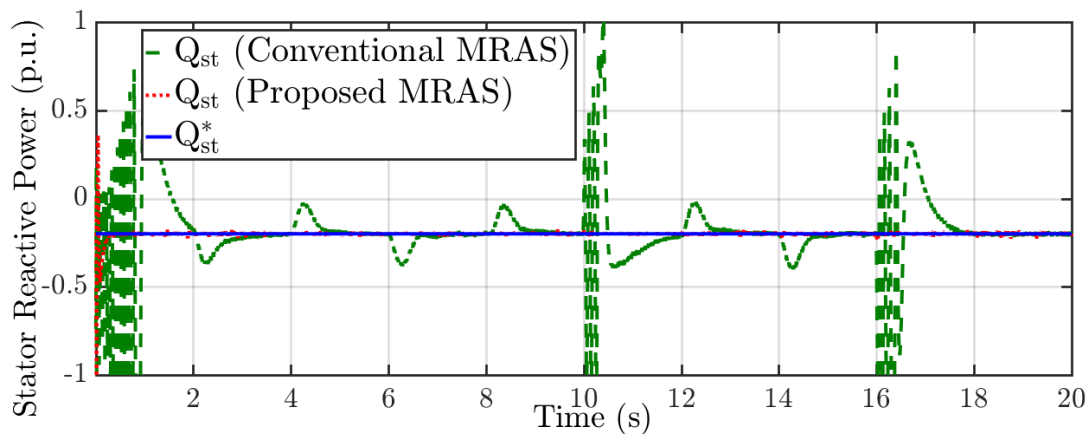


Figure 4.7: Reactive Power Tracking Performance Comparison of DFIG with Speed Estimated using the Proposed MRAS technique and conventional MRAS Technique.

is present in the system for the pitch control and the power reference of the stator is kept at 0.8 p.u. with the DFIG consuming a reactive power of 0.25 p.u. from the grid. The grid is simulated as an infinite bus with a constant voltage source. Both speed observers were tested out for the same stator active and reactive power reference and with the similar rotor speed profile. The test speed profile along with the performance of the two speed sensorless scheme is shown in Figure 4.5. From Figure , it can be observed that the RLS based rotor speed estimation performs better than the MRAS observer based speed estimation especially when there is sudden change in the rotor speed. The major reason behind this is the use of static controllers

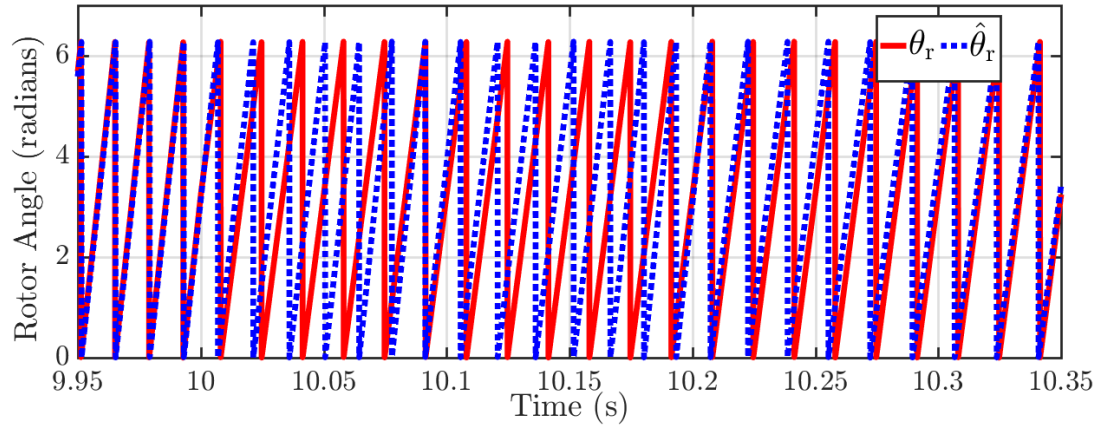


Figure 4.8: Angle Performance Comparison of DFIG with Speed Estimated using the Conventional MRAS Technique.

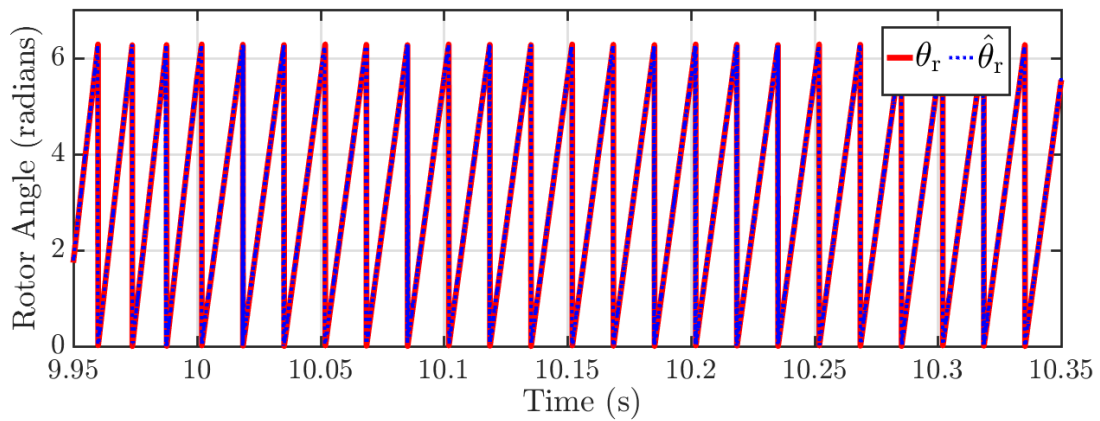


Figure 4.9: Angle Performance Comparison of DFIG with Speed Estimated using the Proposed MRAS Technique.

in the MRAS based speed estimation technique. In the proposed speed estimation technique whenever there are changes in rotor speed, the identified system parameters θ , adjusts themselves and corrects the controlled variable error to zero within few sampling time through the use of MVC. As there are no integrators involved in the controller, it acts faster, which makes it suitable to use for speed estimation on the fly. The corresponding active and reactive tracking performance of the machine subjected to speed changes in Figure 4.5 is shown in Figure 4.6 and Figure 4.7 respectively.

Figure 4.8 and 4.9 shows the angle estimation performance between the proposed RLS identification based MRAS based rotor angle estimation and conventional MRAS

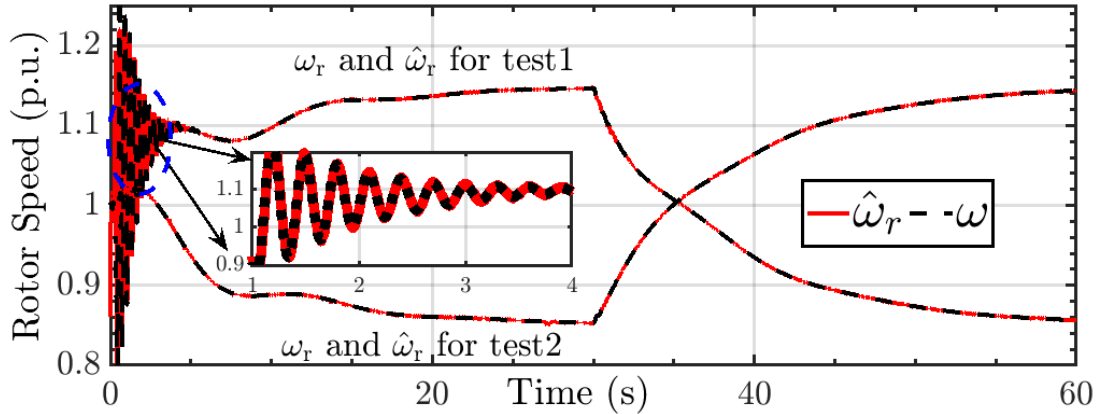


Figure 4.10: Estimated Rotor Speed and Actual Rotor Speed for Step Changes in Wind Speed.

based rotor angle estimation. The disadvantages of having a static controller is evident in Figure 4.8. During the time period around 10 secs, when there was a sudden drop in rotor speed from 1.2 pu to 1 pu as shown in Figure 4.5, it can be observed that the angle estimation from the conventional MRAS based speed observer suffers, the effect of which can be seen in the active and reactive power control of the DFIG stator in Figure 4.6 and Figure 4.7. As the angle estimated by the proposed speed observer settles down quickly as can be seen in Figure 4.9, it does not have high impact on the active and reactive power control of DFIG.

4.3.2 Real Time Simulation results for Speed Estimation

In real-time simulation, the GE 1.5 MW DFIG is modeled along with the two mass model for the turbine, such that the rotor speed used for the pitch controller is also the estimated rotor speed. The simulation time step used in real time simulation is 50 *us* and the controller and identification time step is 1000 *us*.

4.3.2.1 Step Changes in Wind Speed

Figure 4.10 shows the actual rotor speed and estimated rotor speed for a step change in wind speed which causes rotor speed to vary from 1.15 p.u to 0.85 p.u (test 1) and 0.85 p.u. to 1.15 p.u (test 2) respectively at around 30 secs. The initial transients

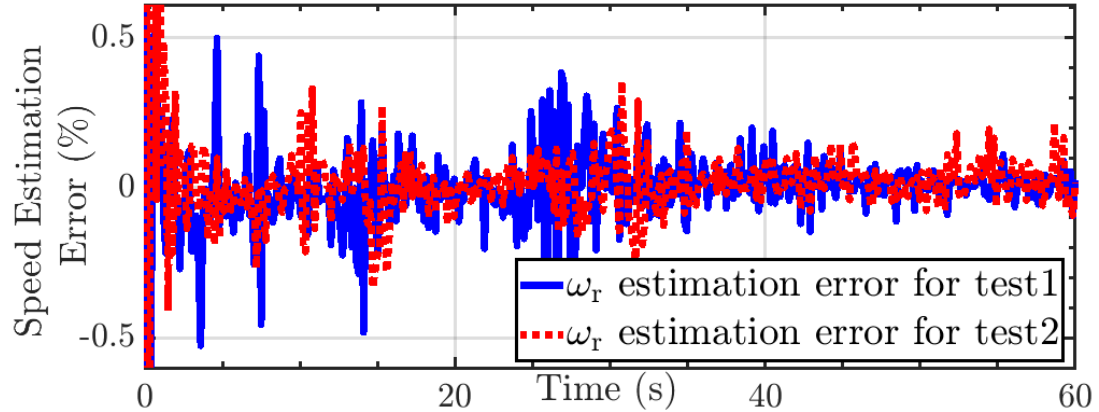


Figure 4.11: Speed Estimation Error for Rotor Speed Changes Case in Figure 4.10.

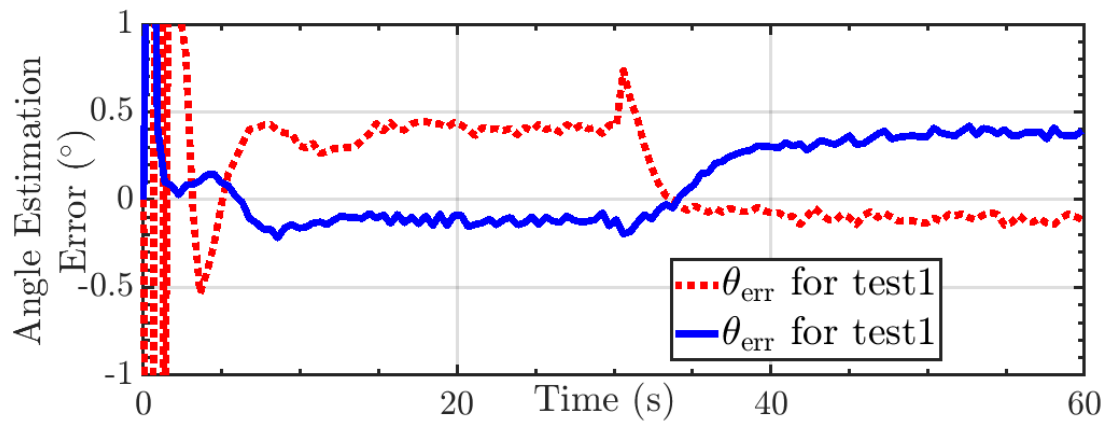


Figure 4.12: Angle Estimation Error for Rotor Speed Changes Case in Figure 4.10.

in the rotor speed is because the real time simulation was not started in steady state and the wind turbine system takes certain time to reach steady state condition. It can be seen that the proposed speed estimator can catch up and estimate the machine speed within few seconds, even before the rotor speed transients diminish. The speed catching capability of the proposed estimator is evident from Figure 4.10. Figure 4.11 shows the rotor speed estimation error in % when the step changes in wind speed causes rotor speed to change as shown in Figure 4.10. It has been observed that the proposed speed estimator converges to the actual rotor speed within 4 seconds of the machine start-up and the error is limited within $\pm 0.5\%$ after that settling time.

Figure 4.12 shows the rotor angle estimation error in degrees. It can be observed that the rotor angle estimation error is below 1° for the whole range of operation.

However, it can also be seen that for super-synchronous mode of operation, the angle estimation error is higher as compared to sub-synchronous mode of operation. This is because of the changes in the mutual inductance estimation as shown in Figure 4.13. From Figure 4.13, it can be seen that the proposed mutual inductance estimator has a lesser accuracy (96%) when operated in super-synchronous mode as compared to sub-synchronous mode of operation (99% accuracy). The changes in accuracy can be attributed to voltage drop in the stator winding resistance, R_s , which has been neglected in the mutual inductance estimator design. This becomes prominent as current in the stator is larger in magnitude in super-synchronous mode.

4.3.2.2 Dynamic Simulation based on Real Wind Speed Profile

Figure 4.14 shows the wind speed profile used in the real-time simulation study of the proposed speed estimation technique. The wind speed profile is obtained from [97]. Figure 4.15 shows the performance of the proposed speed estimator for the mentioned wind conditions in Figure 4.14. The initial speed catching operation of the proposed estimator can also be seen in Figure 4.15. It can be seen that the proposed estimator closely estimates the rotor speed of DFIG over the entire operating range. The active power generated by DFIG for the wind conditions is shown in Figure 4.16. It can be clearly seen that with the proposed speed estimation technique one can get a good control of the machine's output active power. The stator terminal voltage control performance of the vector control with proposed speed estimator is shown in Figure 4.17. Figure 4.18 shows the performance of the mutual inductance calculator for the varying wind conditions. It can be observed that the calculated value of the mutual inductance falls within (93 – 99%) of the actual mutual inductance of the machine. The rotor position estimation error for the wind conditions is shown in Figure 4.19. It can be clearly seen that, for the whole range of operation, the angle estimation error is limited within $\pm 1^\circ$ which does not have significant impact on the overall control of the machine.

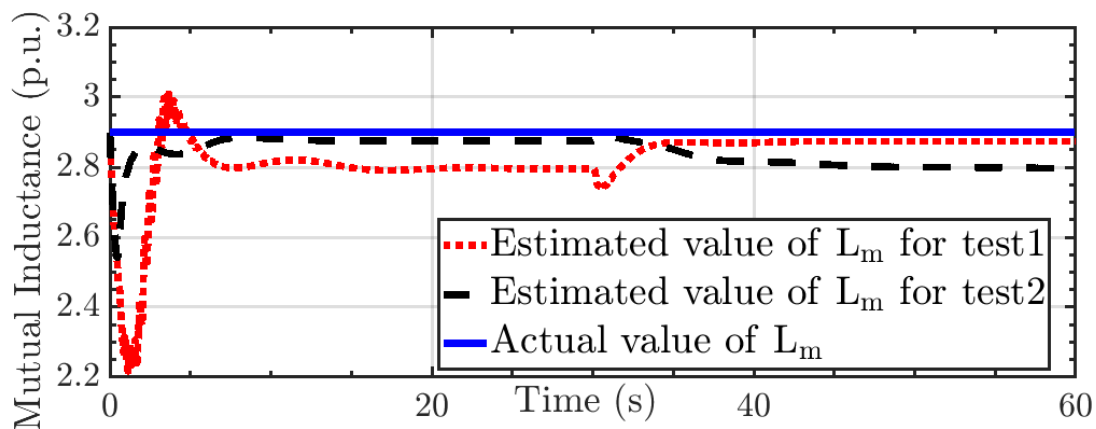


Figure 4.13: Mutual Inductance Estimation for Rotor Speed Changes Case in Figure 4.10.

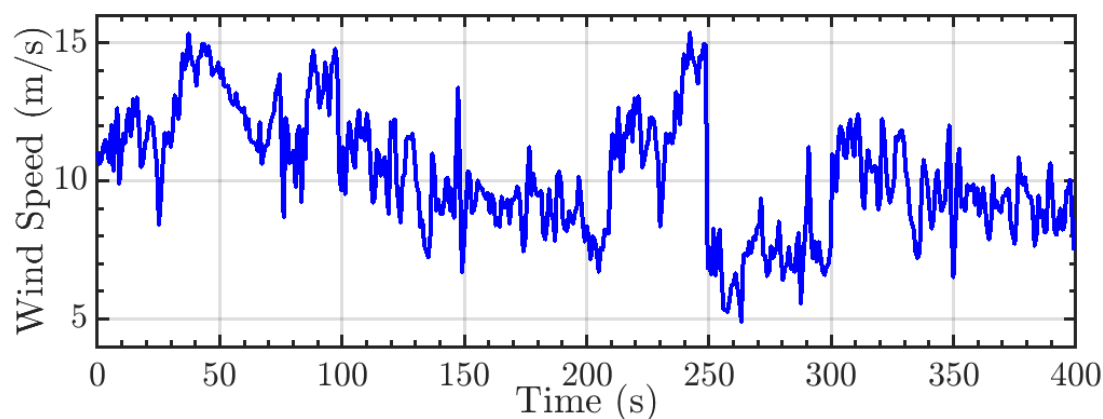


Figure 4.14: Wind Speed Profile Used.

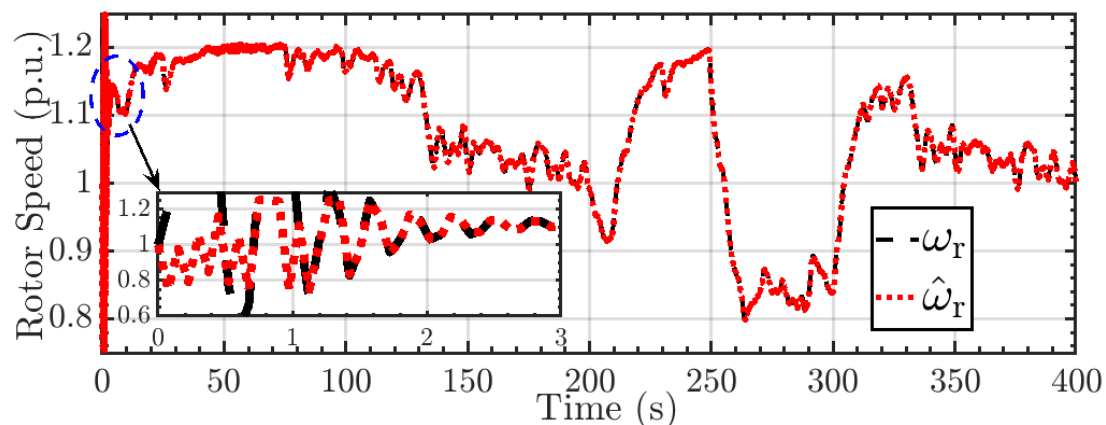


Figure 4.15: Rotor Speed Estimation Performance of Proposed Speed Estimator for Wind Conditions in Figure 4.14.

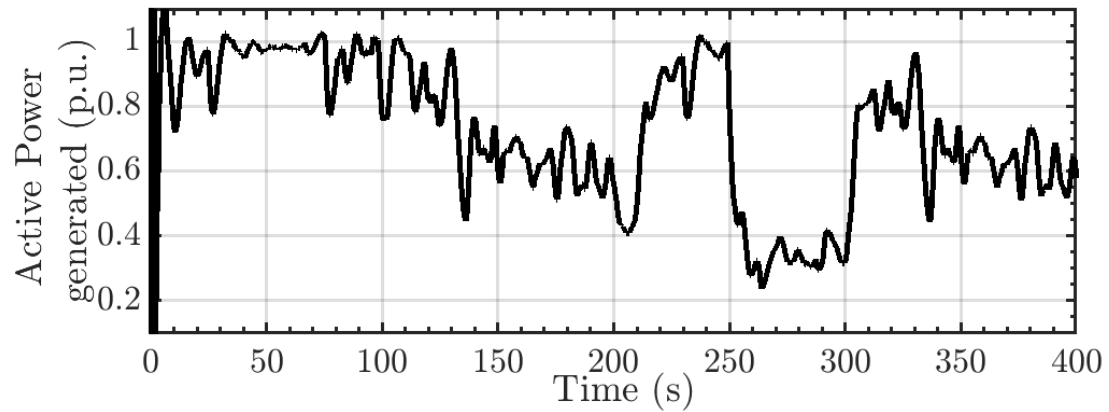


Figure 4.16: Active Power Generated by Sensorless Vector Controlled DFIG for Wind Conditions in Figure 4.14.

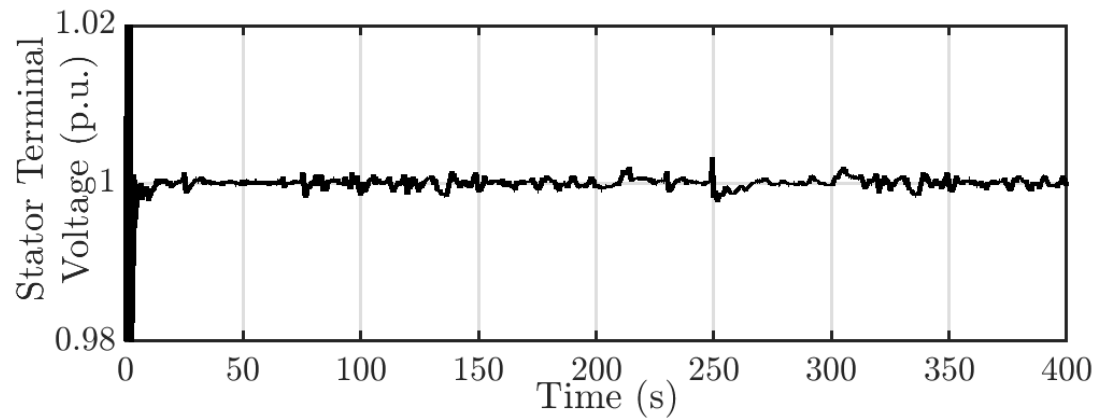


Figure 4.17: Stator Terminal Voltage Control by Sensorless Vector Controlled DFIG for Wind Conditions in Figure 4.14.

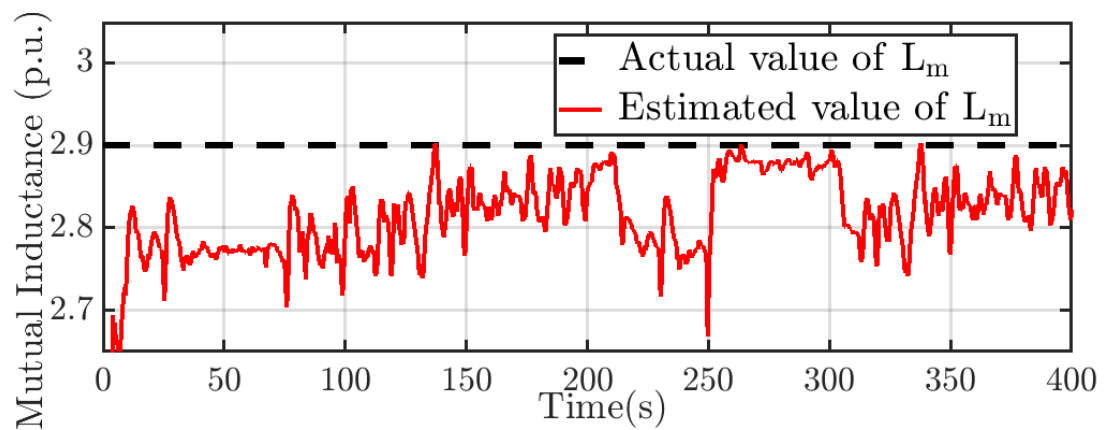


Figure 4.18: Mutual Inductance Estimation in a Sensorless Vector Controlled DFIG for Wind Conditions in Figure 4.14.

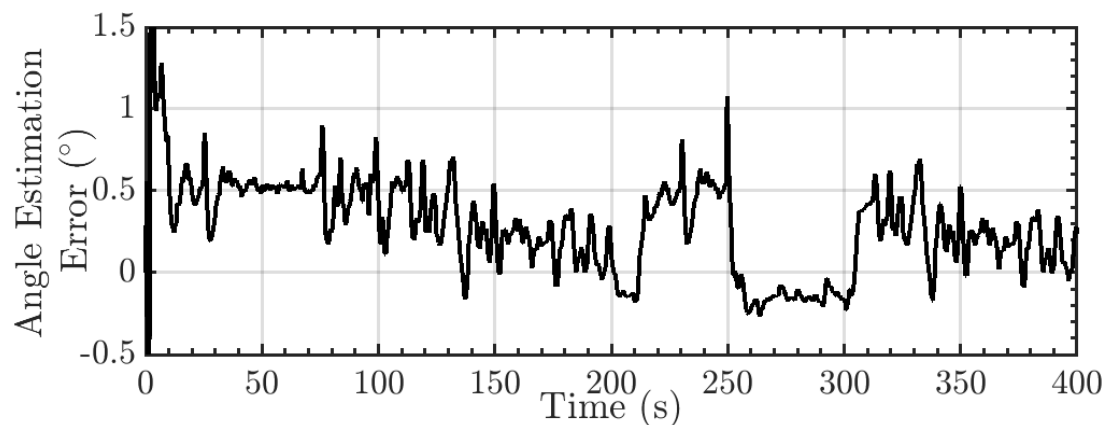


Figure 4.19: Rotor Position Estimation Error in a Sensorless Vector Controlled DFIG for Wind Conditions in Figure 4.14.

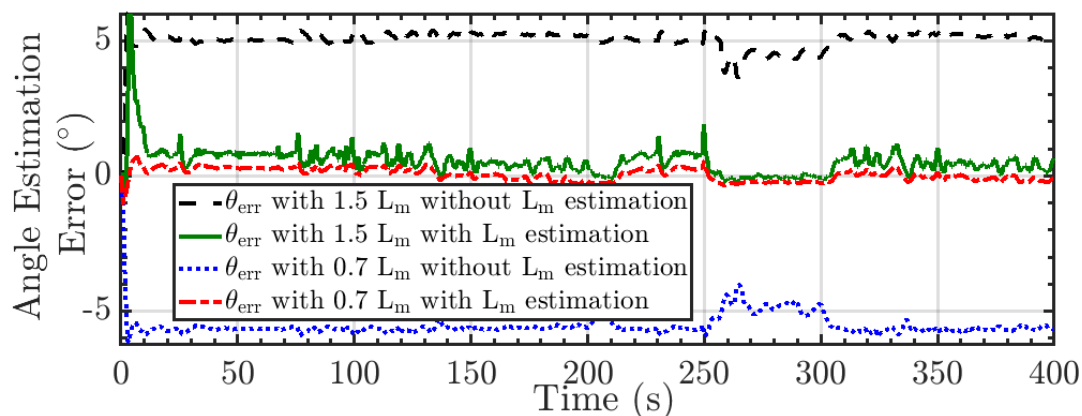


Figure 4.20: Angle Estimation Error for Changes in Machine Mutual Inductance with and without L_m Estimation.

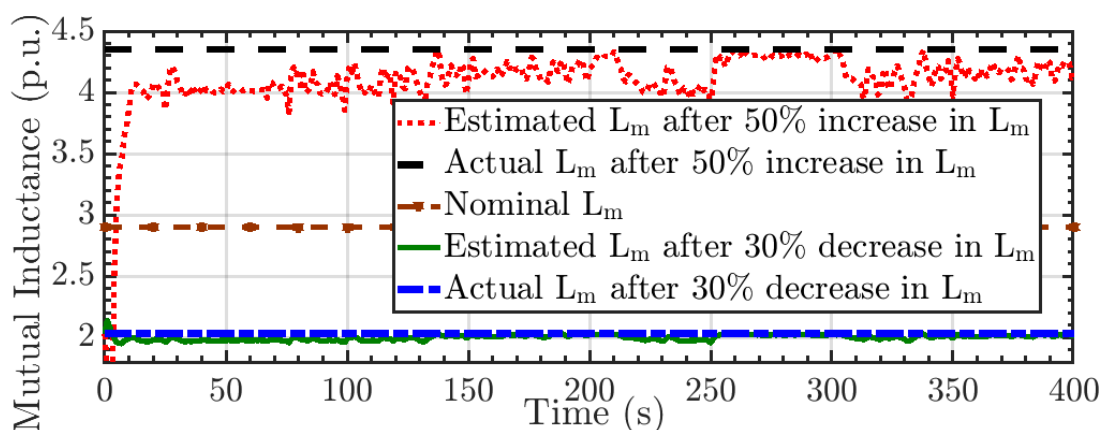


Figure 4.21: Mutual Inductance Estimation Error for changes in Machine Mutual Inductance.

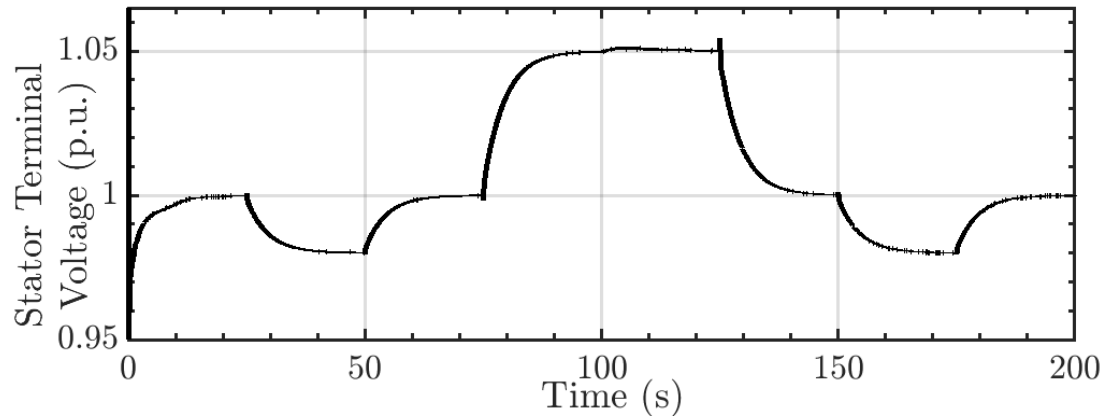


Figure 4.22: Voltage Control Performance when the Proposed Speed Estimation was used along with Conventional Vector Control.

Table 4.2: Changes in Stator Terminal Voltage Reference

Time (s)	0 -25	25 -50	50 -75	75 -100	100 -150	150 -175	175 -200
Voltage (p.u.)	1	0.98	1	1.05	1	0.98	1
Speed (p.u.)	0.85	0.85	0.85	0.85	1.15	1.15	1.15

4.3.2.3 Performance with Mutual Inductance Variation

Figure 4.20 shows the angle estimation error when the machine parameters are varied. It can be seen that when the machine mutual inductance is increased by 1.5 times and the mutual inductance is not estimated, a positive angle estimation error is obtained as expected from phasor diagram in Figure 4.3. Likewise, when the mutual inductance is decreased by 30 %, the angle estimation error is negative as expected. The angle estimation error is minimized when the mutual inductance was estimated online. Figure 4.21 shows the estimated mutual inductance when the machine parameters were varied. It can be seen that the proposed L_m estimator closely estimates the machine mutual inductance with a minimum accuracy of 95%.

4.3.2.4 Performance with Stator Terminal Voltage Variation

The performance of the proposed speed estimator and mutual inductance estimator was also tested in varying rotor speed and stator terminal voltage conditions. The

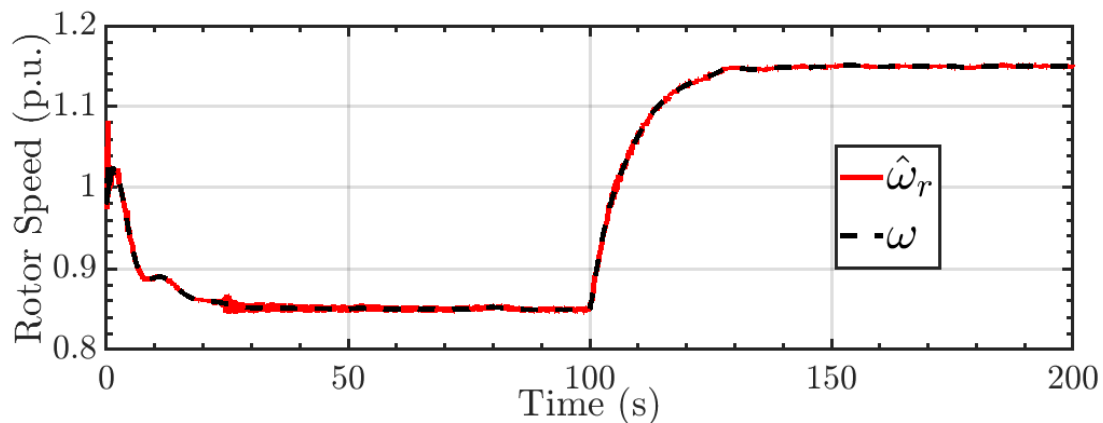


Figure 4.23: Speed Estimation during PCC Voltage Variations.

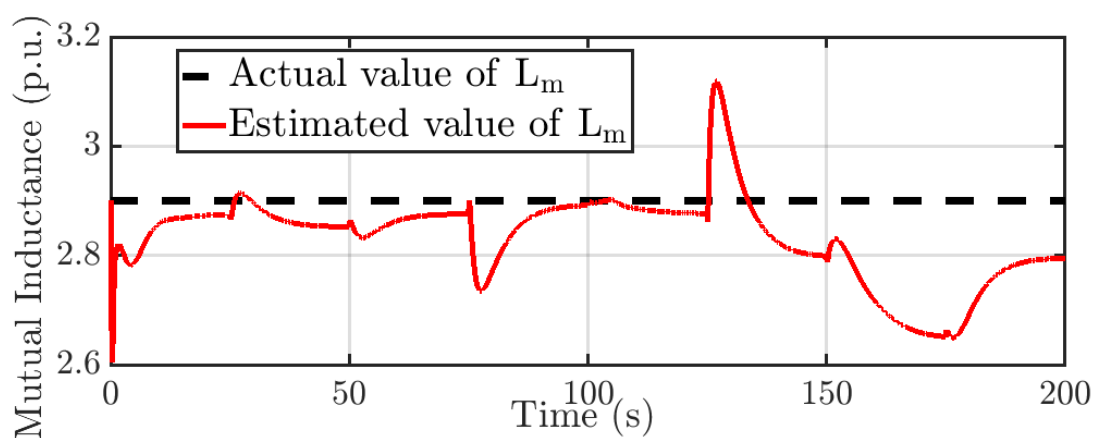


Figure 4.24: Mutual Inductance Estimation for changes in PCC Voltage.

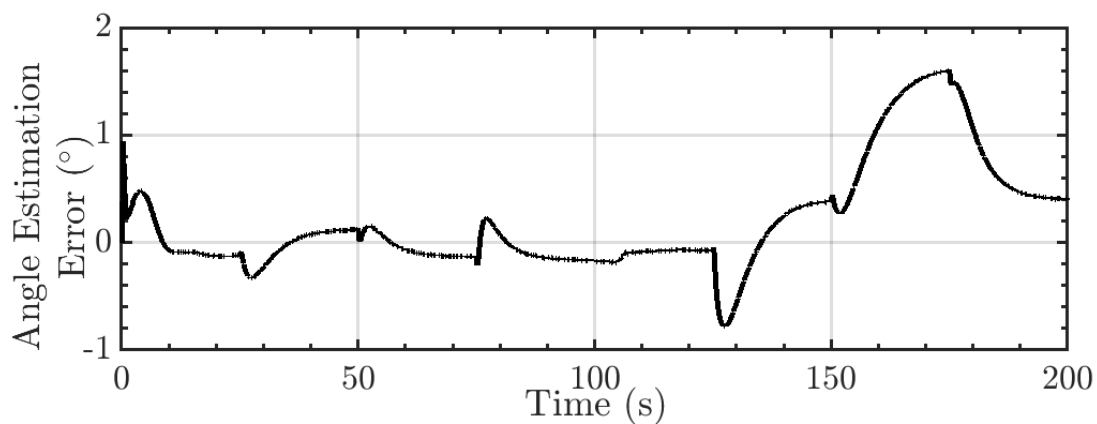


Figure 4.25: Rotor Position Estimation Error for Voltage Changes.

stator terminal voltage regulation performance of the vector control is shown in Figure 4.22. The reference stator voltage and wind speed was changed (so as to obtain change

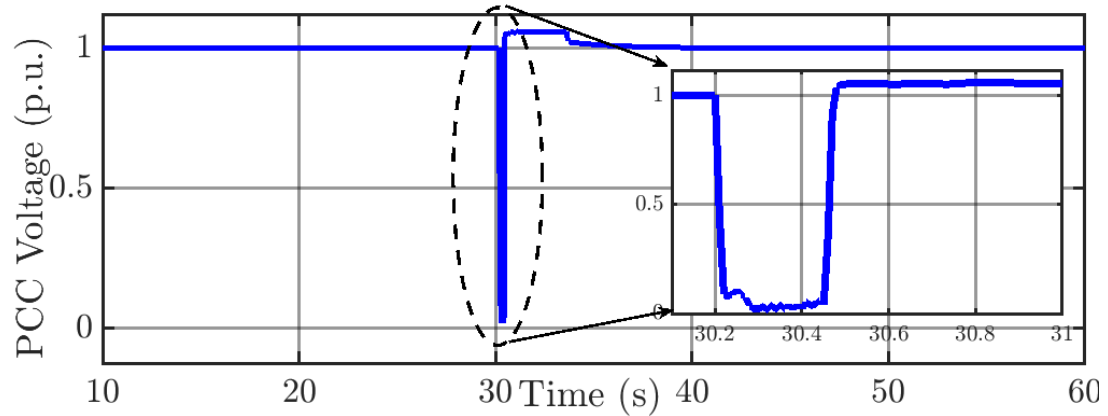


Figure 4.26: PCC Voltage Response for a Three Phase Short Circuit Fault.

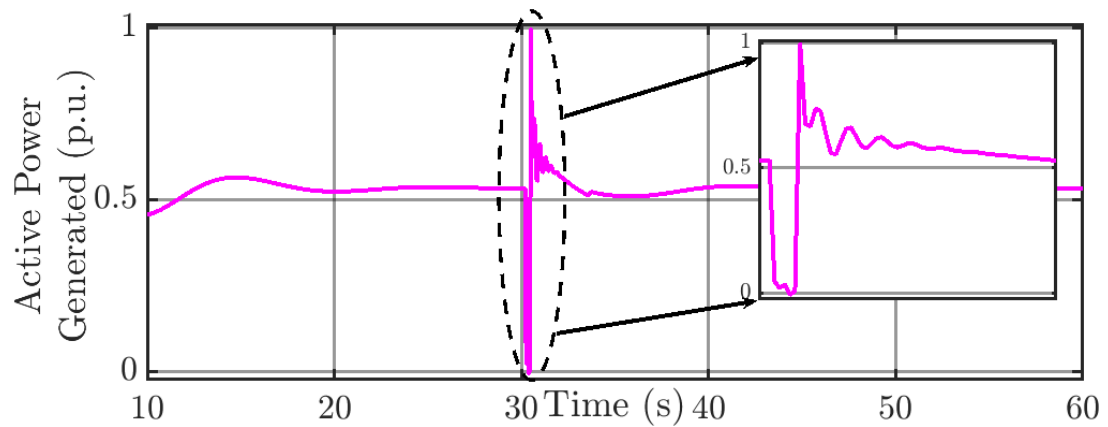


Figure 4.27: Active Power Generation Response for a Three Phase Short Circuit Fault with Proposed Speed Estimation Technique used in Vector Control.

in rotor speed) as shown in Table 4.2.

The speed estimation performance during the voltage variation case is shown in Figure 4.23. The performance of the mutual inductance calculation is shown in Figure 4.24 and the angle estimation error is shown in Figure 4.25. It can be seen that as the stator voltage varies, the calculated value of the mutual inductance varies as well, but the error in mutual inductance estimation is still within $\pm 8\%$ of the nominal value. Also it was observed that the angular position estimation error was maintained within $\pm 1.5\%$ for the variation of the stator voltage.

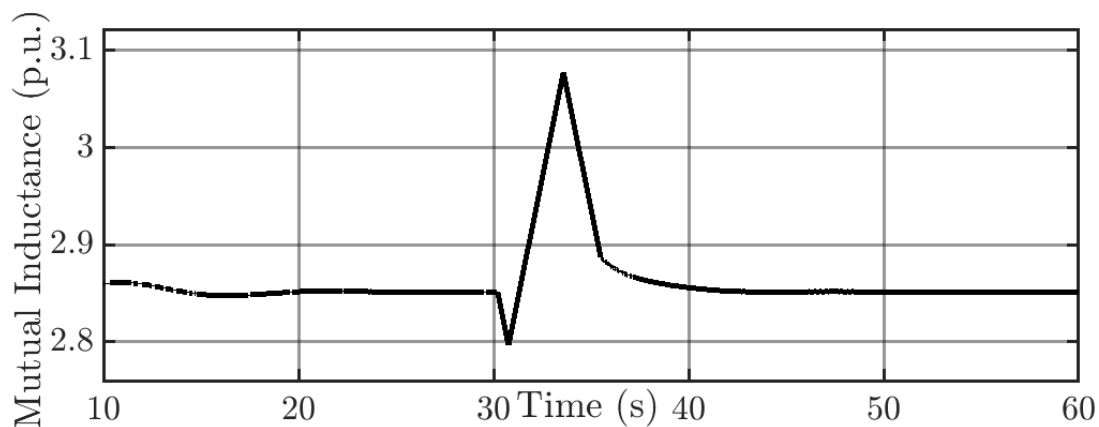


Figure 4.28: Mutual Inductance Estimation Performance for a Three phase Short Circuit Fault with Proposed L_m Estimation Technique.

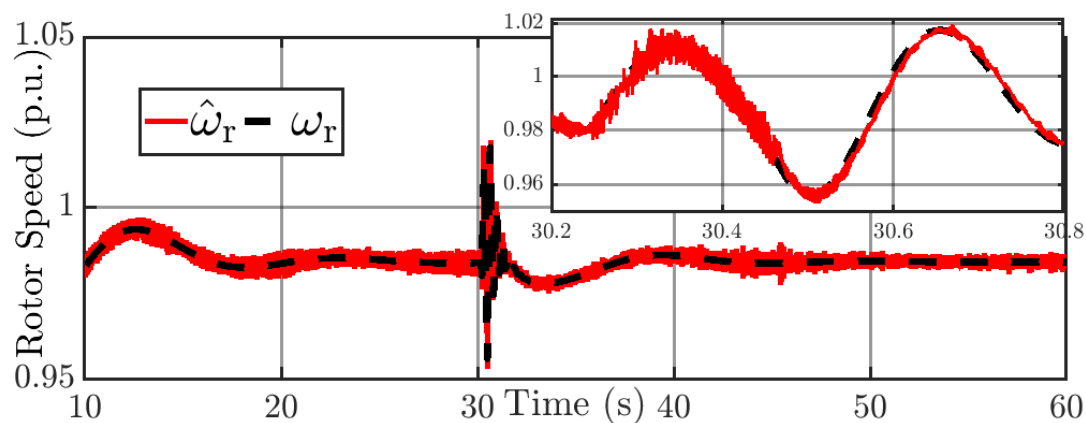


Figure 4.29: Rotor Speed Estimation Performance for a Three phase Short Circuit Fault with Proposed Speed Estimation Technique.

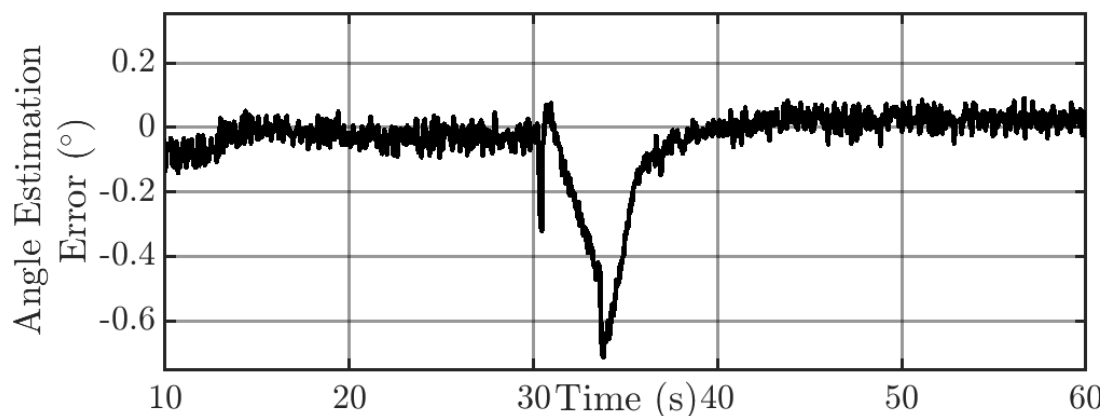


Figure 4.30: Angle Estimation Error for a Three phase Short Circuit Fault with Proposed Speed Estimation Technique.

4.3.2.5 Performance of the proposed speed estimator technique during grid fault conditions

It is important that the DFIG ride through the system faults such that the overall system stability can be maintained. As the knowledge of rotor position is important for overall control of DFIG, the speed estimation technique should be tested for its performance during grid fault conditions. In this paper, the proposed speed estimation technique is tested for a 15 cycle three phase fault close to the machine terminals to test the suitability of the proposed speed estimator for grid fault ride through applications. Figure 4.26 shows the voltage ride through performance of DFIG with control approach shown in Figure 4.1. It can be observed that the proposed speed estimation technique can help maintain the stable operation of the machine during grid disturbances. Figure 4.27 shows the active power generated by DFIG before, during and after three phase fault when the proposed speed estimation technique was used along with the conventional vector control. Figure 4.28 shows the mutual inductance estimation performance of the proposed approach during grid fault. It can be observed that the proposed technique deviates from the correct value of machine mutual inductance during grid fault, but the estimation quickly reverts back to close to the actual value once the fault is cleared, which is helpful in maintaining the overall operational stability of the machine. Figure 4.29 shows the rotor speed estimation during grid fault conditions with the proposed speed estimation technique. Figure 4.30 shows the angle estimation error in degrees during grid fault condition with the proposed speed estimation technique. It can be observed that the proposed technique can quickly correct the angle estimation error after the fault and even during the fault the rotor position estimation error is less than 1° which helps in grid fault ride through.

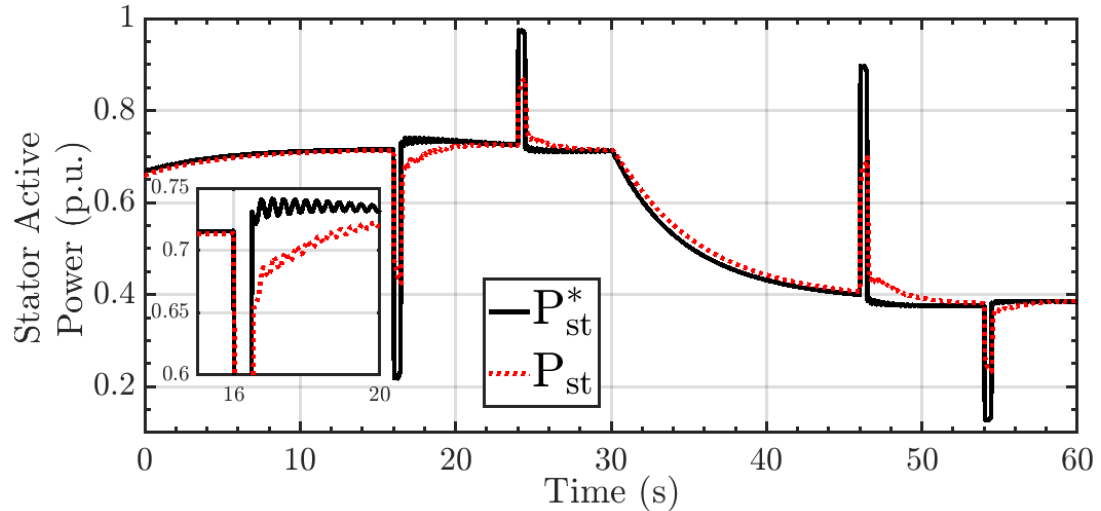


Figure 4.31: Stator Active Power Tracking Performance of Proposed Sensorless Control.

4.3.2.6 Rapid changes in power output for frequency support

The performance of the proposed speed estimator was also tested during the rotor oscillations when there is a mismatch between electrical power output and mechanical power. The scenario can occur when the DFIG is used in frequency regulation mode, in which in order to support grid frequency, the output power of DFIG could be increased or decreased suddenly for a short time. This causes the rotor speed oscillations which the proposed speed estimator should be able to track. Figure 4.31 shows the performance of the stator active power tracking for sudden step changes in the active power reference. The rotor speed estimation during the rotor speed oscillations is shown in Figure 4.32. The effect of the variation of stator active power in mutual inductance calculation and angle estimation is shown in Figure 4.33 and 4.34 respectively.

4.3.2.7 Compatibility of the proposed speed estimation technique with other existing DFIG control technique

The compatibility of the speed estimation technique should be tested with the various control topologies that are currently in use for DFIG control to validate

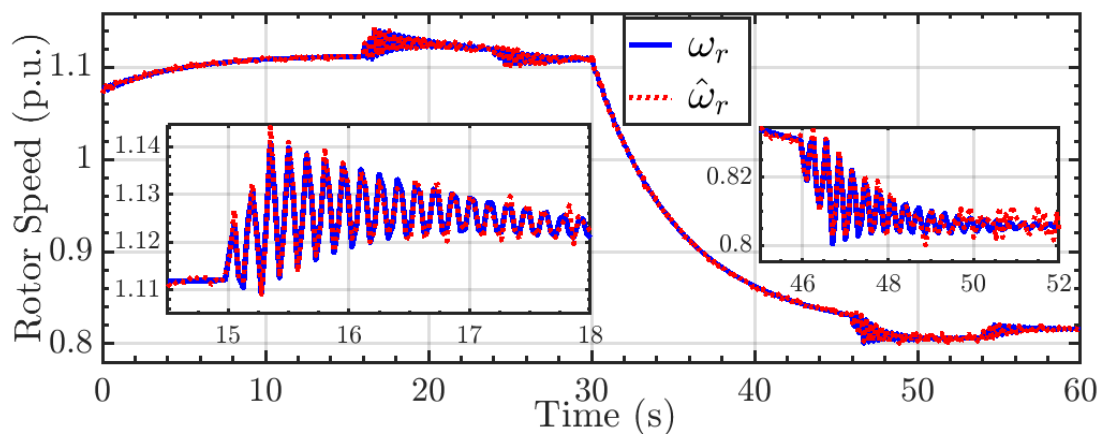


Figure 4.32: Estimated Speed and Actual Speed when the DFIG is used for Frequency Regulation Causing Rotor Oscillations.

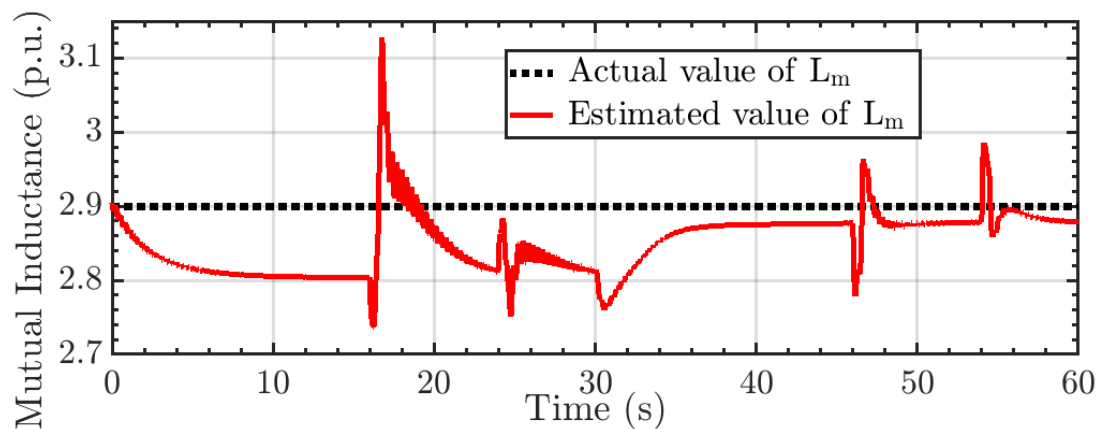


Figure 4.33: Mutual Inductance Estimation Performance when DFIG is used for Frequency Regulation with Proposed L_m Estimation Technique.

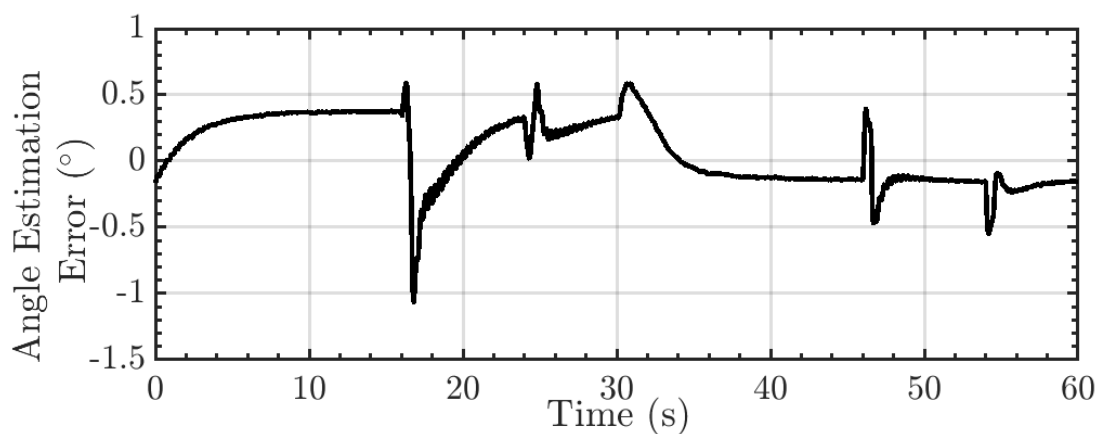


Figure 4.34: Angle Estimation Error when DFIG is used for Frequency Regulation with the Proposed Rotor Position Estimation Technique.

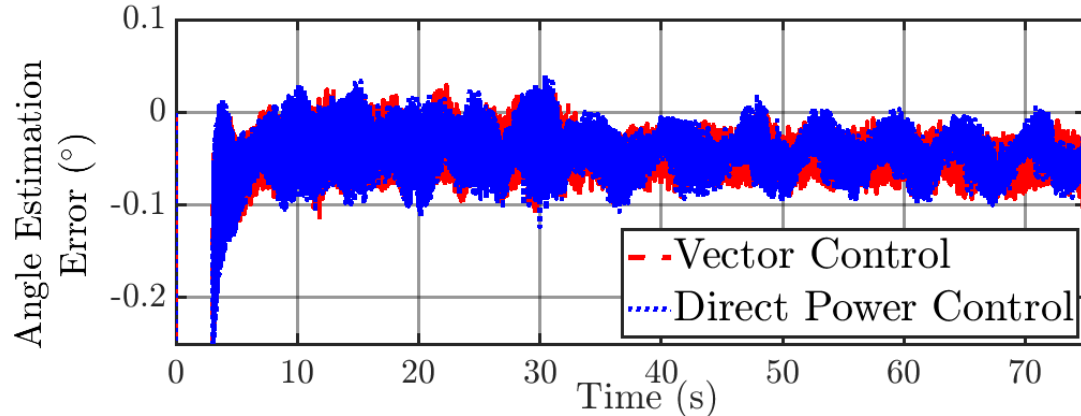


Figure 4.35: Angle Estimation Error Comparison for Vector Control and Direct Power Control of DFIG with the Proposed Rotor Position Estimation Technique.

the usefulness of proposed technique. In this paper, the proposed speed estimation technique was also applied to the direct power control(DPC) topology discussed in [?] to test its compatibility. The results in Figure 4.35 show that the rotor position estimation error with the proposed technique when applied to DPC is comparable to the case when applied to conventional vector control. Figure 4.36 shows the speed estimation performance comparison of the proposed speed estimation technique when applied to conventional vector control and DPC. It can be observed that the speed estimation performance is comparable for both the existing DFIG control technique. The stator active power reference output for vector control and DPC is shown in Figure 4.37. It can be observed that with DPC technique due to the uneven switching of the RSC the active power output has more fluctuations than the vector control technique [101, 102]. However, still with the noise in the active power output the proposed speed estimation technique works well with DPC of DFIG.

4.3.3 Hardware in the Loop (HIL) Simulation Results

The laboratory setup used in the work is shown in Figure 4.4. The hardware-in-the-loop simulation was run in the speed input mode and only the performance of the proposed speed estimator was tested. Figure 4.38 shows the comparison of the estimated rotor angle along with actual rotor angle obtained from the position

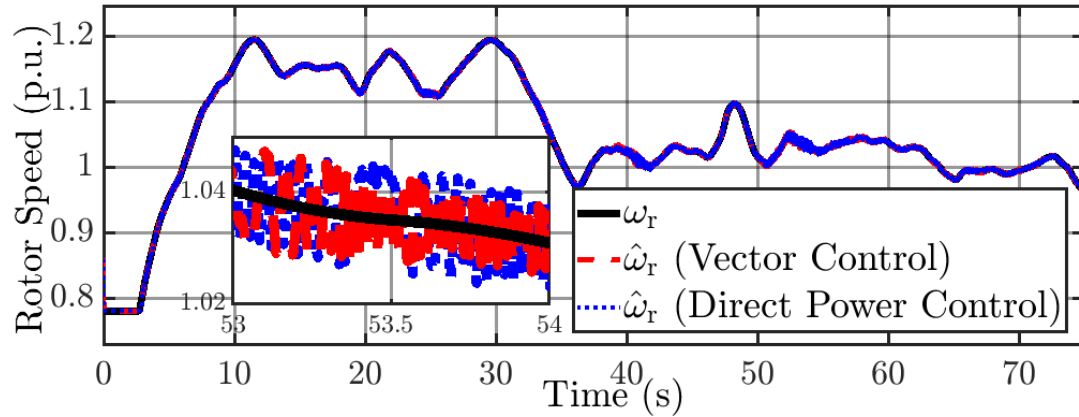


Figure 4.36: Speed Estimation Performance Comparison for Vector Control and Direct Power Control of DFIG with the Proposed Speed Estimation Technique.

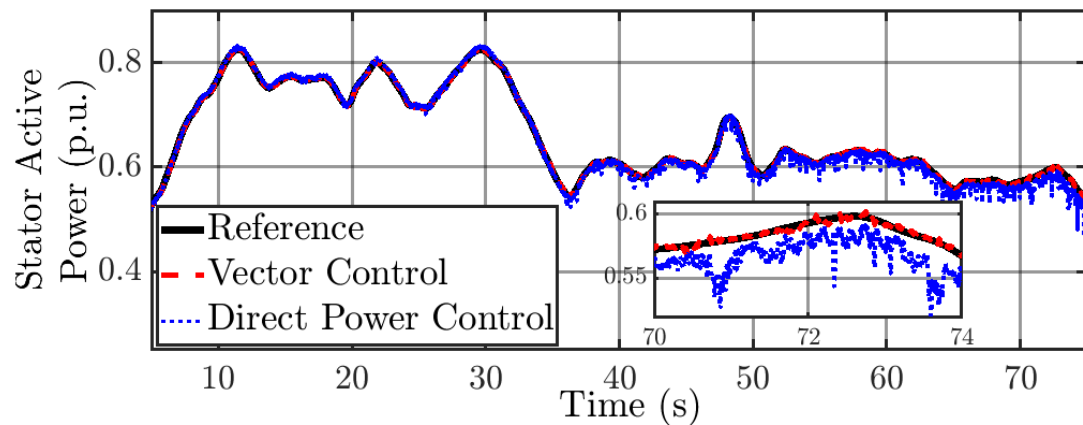


Figure 4.37: Active Power Control Performance Comparison for Vector Control and Direct Power Control of DFIG with the Proposed Speed Estimation Technique.

encoder in the setup. It can be observed that the estimated rotor angle is close to the actual rotor angle. The slight phase shift in the estimated rotor angle can be associated with the computational delay. Figure 4.39 shows the comparison between the estimated rotor speed and the actual rotor speed. It can be seen that there is negligible difference between estimated rotor speed and actual rotor speed. During the step changes in rotor speed, the estimated rotor speed takes certain time to catch up to the actual speed because of the sampling and computational delay, as the speed estimator sampling time is 20 times slower than the HIL control sampling time. The noise in the estimated rotor speed is introduced through the rotor current

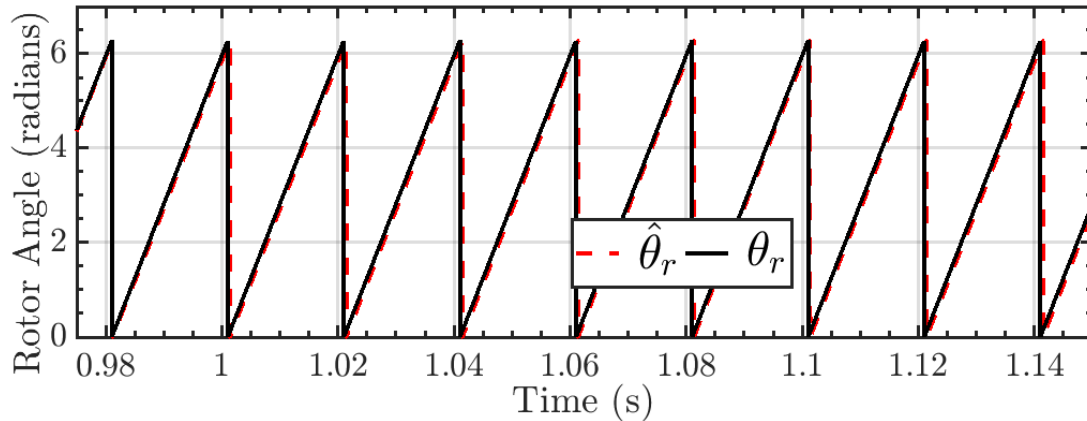


Figure 4.38: Rotor Angle Estimation Comparison from Hardware Setup.

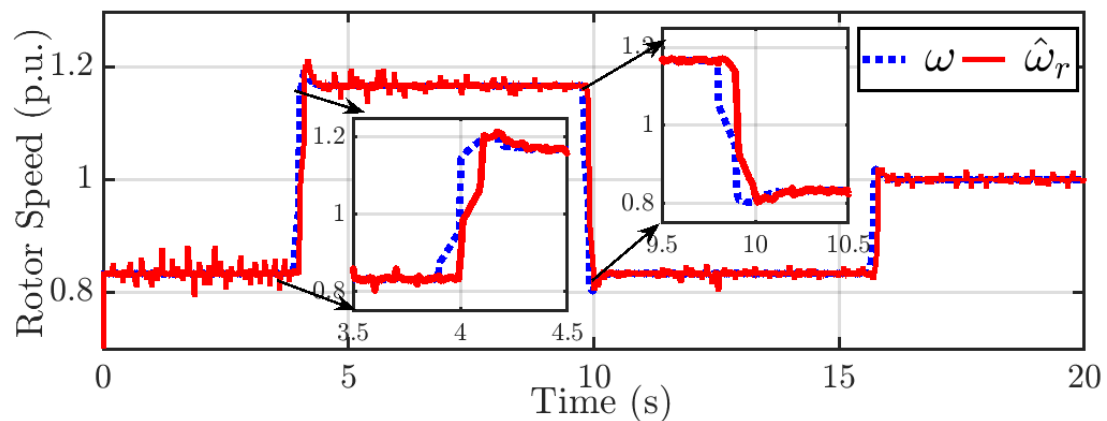


Figure 4.39: Rotor Speed Estimation Performance Comparison for Hardware Setup.

measurements. Figure 4.40 shows the rotor speed estimation error obtained from HIL simulation. It can be observed that the speed estimation error rises during the sudden step changes in the rotor speed but falls back close to zero within few milliseconds. Figure 4.41 shows the instantaneous rotor current for a step change in rotor speed from 1.19 pu to 0.81 pu at around 10 seconds. The stator active and reactive power control performance for the hardware implementation of the proposed speed sensorless vector control is shown in Figure 4.42.

4.4 Chapter Summary

In this chapter, a system identification based technique coupled with MVC law which enables, the operation of DFIG without rotor position and speed sensors is

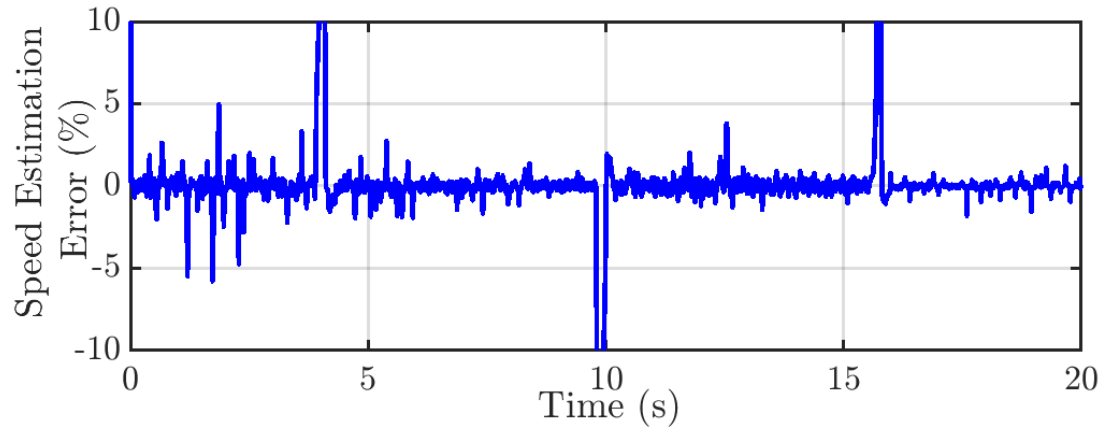


Figure 4.40: Speed Estimation Error for Hardware Setup.

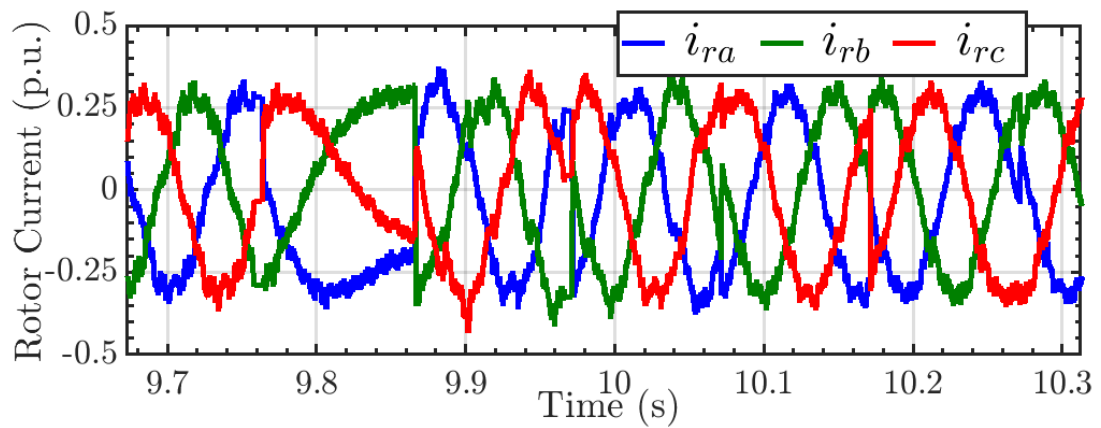


Figure 4.41: Instantaneous Rotor Current as seen in Hardware Setup.

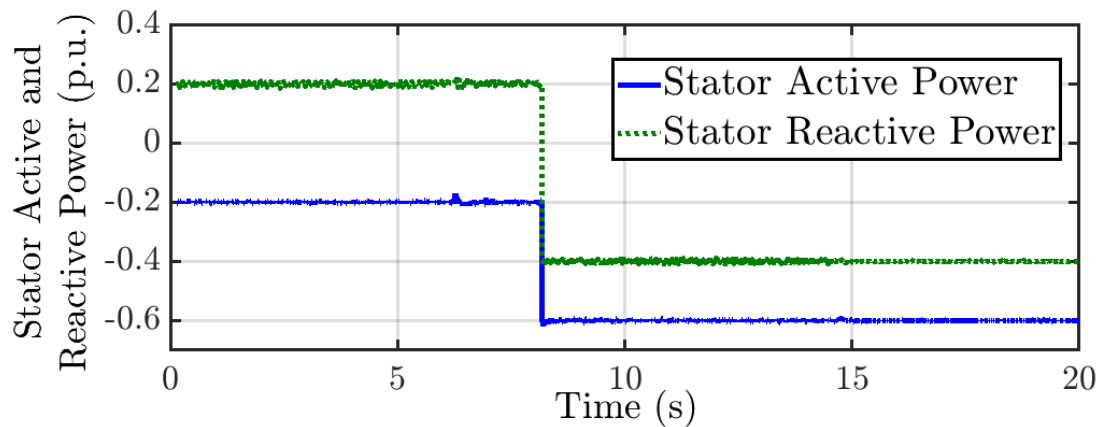


Figure 4.42: Stator Active and Reactive Power Profile in Hardware Setup.

presented. The proposed speed sensorless operation of DFIG has been made robust to parameter variation of the machine by online estimation of the mutual inductance

L_m of the machine. It has been observed that the proposed technique for speed sensorless control can be an effective alternative for increasing the reliable operation of DFIG based WECS. The closed loop convergence of the proposed speed estimator is discussed. The proposed speed estimation technique is compared with the existing MRAS based technique and is tested at wide range of operating points with real wind speed profile. Real time simulation result as well as HIL results show that the proposed rotor speed and position estimation technique has shown good performance both during steady state and grid disturbance conditions.

CHAPTER 5: MEASUREMENT BASED APPROACH: SYSTEM IDENTIFICATION BASED CONTROL APPROACH FOR DFIG

In this chapter, a current sensorless adaptive control framework for active and reactive power output of DFIG, a three phase grid connected inverter (TPGCI) equivalent to GSC of DFIG is presented. The controller designed is MVC using plant model data from RLS based system identification. The design of the controller is discussed and the test cases demonstrating the effectiveness of the proposed control framework is presented. The motivation behind the design of this controller is to increase the reliability of operation of the DFIG and reduce the dependency of knowledge in system parameter for controller tuning. Conventional controllers such as VC depends on the rotor current measurements for effective control, whereas, the proposed MVC based adaptive control of DFIG does not require the rotor side quantities to be measured. The other advantage of the proposed controller is the simplicity in design, its adaptability under varying operating conditions and the ability of the controller to perform without the need to measure rotor side current and voltage quantities for DFIG and output current for TPGCI.

5.1 Adaptive Minimum Variance Controller for Grid Connected DFIG in Synchronously Rotating DQ Reference Frame

5.1.1 Model of DFIG for Adaptive Control Design

The dynamic equations modeling the DFIG in per unit based on synchronously rotating reference frame is given in Appendix A.

Following assumptions are made for the design of the proposed adaptive controller for DFIG:

a) The DFIG is connected to a strong grid.

b) The synchronously rotating reference frame is aligned with the stator flux. i.e $\Psi_{ds} = \Psi_s$, $\Psi_{qs} = 0$ and $v_{ds} = 0$, $v_{qs} = V_s$.

c) The stator flux dynamics can be neglected when connected to a strong grid. i.e $p\Psi_{qs} = p\Psi_{ds} \approx 0$.

Considering the assumptions above and separating the real and imaginary parts, the following equations can be deduced from (A.1)

$$\begin{aligned}\Psi_{qs} &= -r_s i_{ds} \\ \Psi_{ds} &= v_{qs} + r_s i_{qs}\end{aligned}\tag{5.1}$$

Using (A.2) and (5.1), the rotor voltage equations can be written as,

$$v'_{dr} = r'_r i'_{dr} + p \frac{\sigma L'_r i'_{dr}}{\omega_b} - \omega_{slip} \left(\frac{\sigma L_s L'_r}{L_m} i_{qs} - \frac{r_s L'_r}{L_m} i_{ds} \right)\tag{5.2}$$

$$v'_{qr} = r'_r i'_{qr} + p \frac{\sigma L'_r i'_{qr}}{\omega_b} - \omega_{slip} \left(\frac{\sigma L_s L'_r}{L_m} i_{ds} - \frac{L'_r}{L_m} (v_{qs} + r_s i_{qs}) \right)\tag{5.3}$$

where $\sigma = \frac{L'_r L_s - L_m^2}{L_s L'_r}$.

From (5.2), it can be observed that the rotor $d - q$ axis voltage referred to stator side can be divided into two components. i.e.

- component depending on dynamics of i'_{dr} and i'_{qr} respectively.
- compensation terms that couple the $d - q$ axis component with one another.

Thus,

$$v'_{dr} = v''_{dr} + v'''_{dr}\tag{5.4}$$

$$v'_{qr} = v''_{qr} + v'''_{qr}\tag{5.5}$$

where

$$\begin{aligned}
v''_{dr} &= \left(r'_r + p \frac{\sigma L'_r}{\omega_b} \right) i'_{dr} \\
v'''_{dr} &= -\omega_{slip} \left(\frac{\sigma L_s L'_r}{L_m} i_{qs} - \frac{r_s L'_r}{L_m} i_{ds} \right) \\
v''_{qr} &= \left(r'_r + p \frac{\sigma L'_r}{\omega_b} \right) i'_{qr} \\
v'''_{qr} &= -\omega_{slip} \left(\frac{\sigma L_s L'_r}{L_m} i_{ds} + \frac{L'_r}{L_m} (v_{qs} + r_s i_{qs}) \right)
\end{aligned} \tag{5.6}$$

Using the assumption made above, (A.3) can be written as

$$\begin{aligned}
P_{st} &= \frac{L_m v_{qs}}{L_s} \left(\frac{v''_{qr}}{r_r + p \frac{\sigma L_r}{\omega_b}} \right) \\
Q_{st} &= -\frac{v_{qs} \Psi_{ds}}{L_s} + \frac{L_m v_{qs}}{L_s} \left(\frac{v''_{dr}}{r_r + p \frac{\sigma L_r}{\omega_b}} \right)
\end{aligned} \tag{5.7}$$

It can now be observed that the stator active and reactive power output of DFIG can be controlled by controlling the v''_{qr} and v''_{dr} component of rotor voltage respectively. Thus the goal of the proposed adaptive control of DFIG is to generate the proper sequence of v''_{qr} and v''_{dr} to regulate the stator active and reactive power.

5.1.2 Adaptive Control of DFIG

Figure 5.1 shows a general schematic diagram of a adaptive control system. The adaptive control system is comprised of three main components. a) The plant to be controlled b) System identifier c) Controller based on identified system parameters. For active and reactive power control of DFIG, the plant to be controlled is represented by (5.7).

MVC is a digital control technique utilizing the parameters of the transfer function representing the system along with the past inputs and outputs. The goal of MVC is

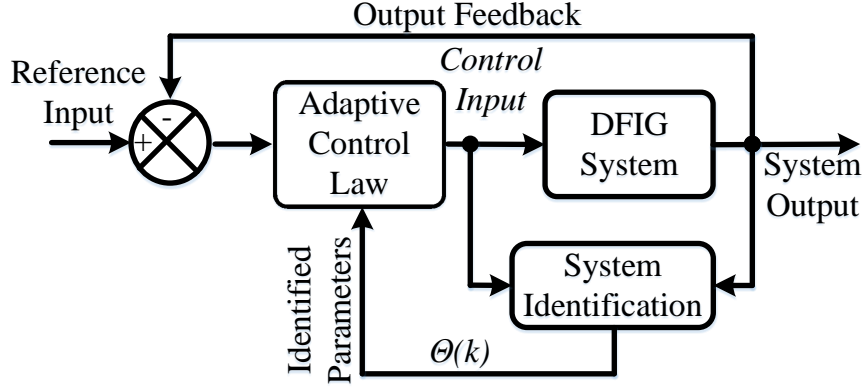


Figure 5.1: Schematic Representation of an Adaptive Control System.

to closely regulate the active and reactive power of the DFIG by generating proper rotor voltage sequence to be applied to the rotor windings.

The derivation of the MVC law for stator active power is shown below and the similar process is followed for the control law derivation of the stator reactive power. For MVC design, the system is assumed to be described by the CARMA model. i.e.

$$\epsilon_p(k) = \frac{B(z^{-1})}{A(z^{-1})} \times v_{gr}''(k) + \frac{C(z^{-1})}{A(q^{-1})} \times \varrho(k) \quad (5.8)$$

where, $\epsilon_p(k) = P_{st}^*(k) - P_{st}(k)$, v_{gr}'' is the q-axis rotor voltage applied at k^{th} instant in time, ϱ is the error in the model representation.

Using the system time delay information, MVC minimizes the variance of the output at $k+d$ with respect to the expected value of output at $k+d$ using the information gathered at up to time instant k . i.e the controller goal is to minimize the following objective function: $J(k) = E\{\epsilon_{P_s}(k+d)^2\}$, where d is the assumed system delay. And, E represents the expected value of the output d steps into the future. Based on the derivation of the relation between stator power variables and rotor voltages in section 5.1.1, a first order representation of the system is selected in controller design.

From (5.8), the following can be deduced:

$$A(z^{-1})\epsilon_{P_s}(k) = B(z^{-1})v''_{qr}(k) + C(z^{-1})\varrho(k) \quad (5.9a)$$

$$A(z^{-1}) = 1 + a_1z^{-1} \quad (5.9b)$$

$$B(z^{-1}) = b_0z^{-1} \quad (5.9c)$$

$$C(z^{-1}) = 1 \quad (5.9d)$$

From the system equation in (5.9a), it can be observed that,

$$(1 + a_1z^{-1})\epsilon_{P_s}(k) = b_0z^{-1}v''_{qr}(k) + \varrho(k) \quad (5.10)$$

and

$$\epsilon_{P_s}(k) = -a_1z^{-1}\epsilon_{P_s}(k) + b_0z^{-1}v''_{qr}(k) + \varrho(k) \quad (5.11)$$

Now, if the time index in prediction is shifted by one step, (5.11) can be written as,

$$\epsilon_{P_s}(k+1) = -a_1\epsilon_{P_s}(k) + b_0v''_{qr}(k) + \varrho(k+1) \quad (5.12)$$

In (5.12), left hand side of the equation is the output signal one step ahead into the future. The right hand side contains the information about present output signal, input signal and future model estimation error.

Now, the control action $v''_{qr}(k)$ is computed in order to optimize the variance of the output one step ahead in the future.

$$\begin{aligned} \underset{v''_{qr}(k)}{Min}\{J(k)\} &= \underset{v''_{qr}(k)}{Min}E\{\epsilon_{P_s}(k+1)^2\} = \underset{v''_{qr}(k)}{Min}E\{[(-a_1)\epsilon_{P_s}(k) + \\ &(b_0)v''_{qr}(k) + \varrho(k+1)]^2\} \end{aligned} \quad (5.13)$$

Equation (5.13) contains present inputs, present outputs and future model estimation error. As model estimation error is assumed to be white noise, its future values cannot be correlated with past and/or present signals. Therefore, the minimum variance will be achieved when the sum of the first two components is set to zero. i.e.

$$-a_1\epsilon_{Ps}(k) + b_0v''_{qr}(k) = 0 \quad (5.14)$$

Thus, the MVC law for active power control is given by,

$$v''_{qr}(k) = \frac{a_1\epsilon_{Ps}(k)}{b_0} \quad (5.15)$$

Similarly, the MVC law for reactive power control is obtained as,

$$v''_{dr}(k) = \frac{a_1\epsilon_{Qs}(k)}{b_0} \quad (5.16)$$

The schematic representation of the proposed adaptive control for active and reactive power regulation of stator side of DFIG is shown in Figure 5.2.

5.1.3 Simulation Results for MVC for DFIG

The proposed controller was tested in MATLAB SimPowerSystems simulation with fixed step discrete time domain simulation of 25 μs and the system identification and control was performed at 150 μs . The control system of Figure 5.2 have been implemented using a 1.5 MW DFIG model [90] into two different modes. First, the performance of the proposed controller is tested for step changes in stator active and reactive power references with rotor speed as mechanical input to the machine. Second, the performance of the controller is analyzed for a complete WT model along with two mass model for turbine and pitch control for dynamic wind conditions with torque as the mechanical input to the machine. Figure 5.3 shows the test system in

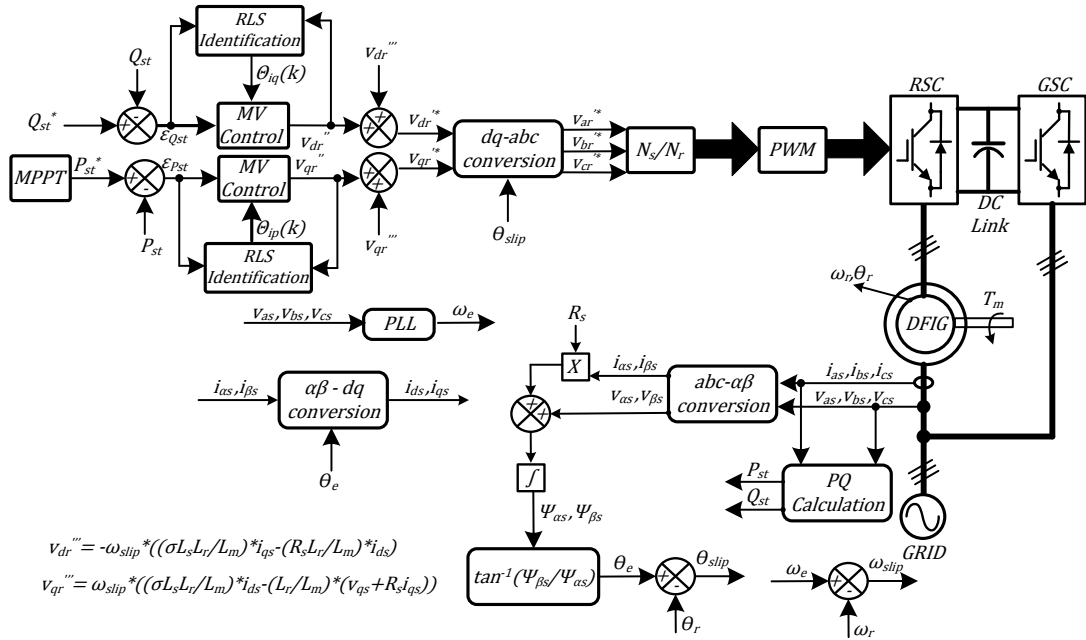


Figure 5.2: Proposed Adaptive Control Scheme for DFIG.

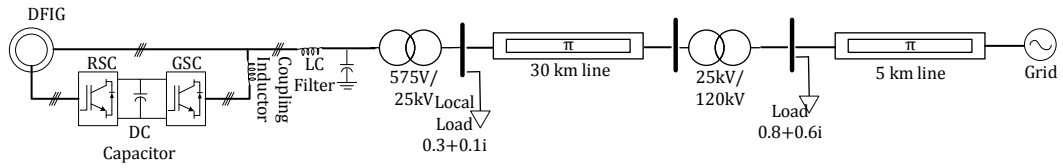


Figure 5.3: One Line Diagram of the Test System used to access Controller Performance.

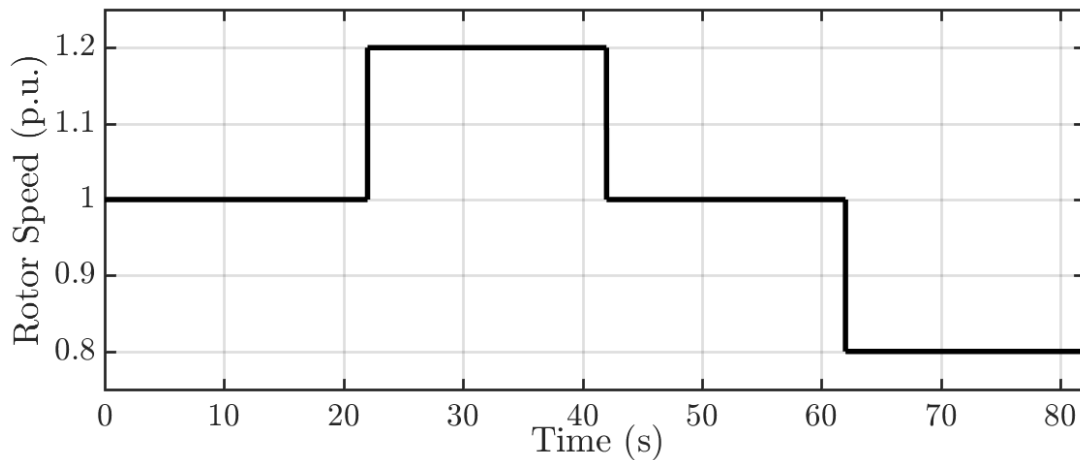


Figure 5.4: Rotor Speed Profile used to access the Performance of Proposed Control.

which the proposed controller is tested.

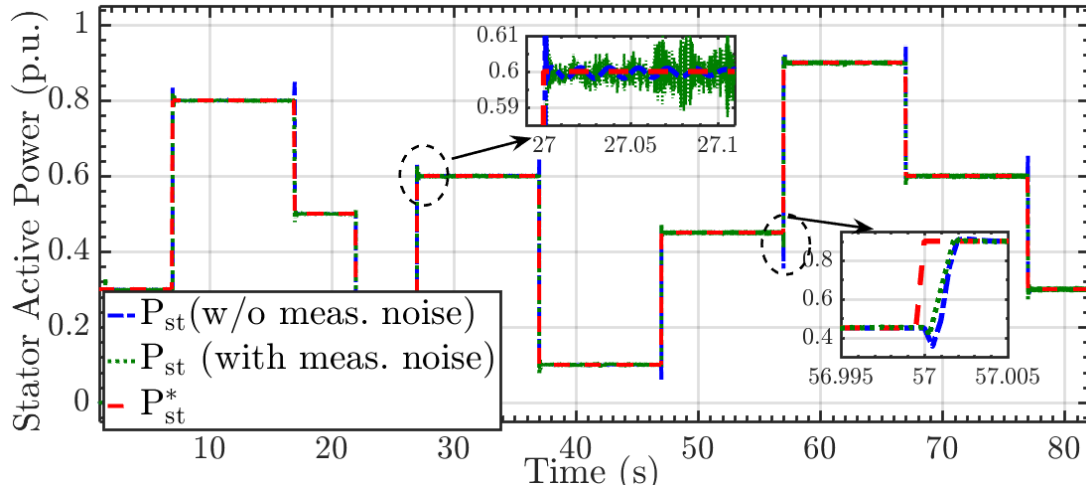


Figure 5.5: Stator Active Power Tracking Performance with Proposed Control.

5.1.3.1 Test with step changes in power

The controller performance was tested on the system shown in Figure 5.3 for a rotor speed profile shown in Figure 5.4. This test mainly analyze the controller performance at various operating speeds of the machine including super-synchronous, synchronous and sub-synchronous speed. The stator active power tracking performance of the proposed controller is shown in Figure 5.5. It can be seen that the proposed controller can instantly track the step changes in the stator active power with minimum overshoot and rise time. Similarly, the stator reactive power tracking performance of the proposed controller is shown in Figure 5.6. It can be observed that the proposed form of controller introduces oscillations in the controlled variable which damps slowly but the magnitude of the oscillations are fairly small. Also, it can be observed from Figure 5.5 and Figure 5.6, that measurement noises (of upto 5%) have minimal effect on the control using proposed adaptive control. For higher level of measurement noises, proper filter design in the control loop is advised. The d-q axis stator and rotor currents corresponding to the step changes in active and reactive power of Figure 5.5 and Figure 5.6 is shown in Figure 5.7.

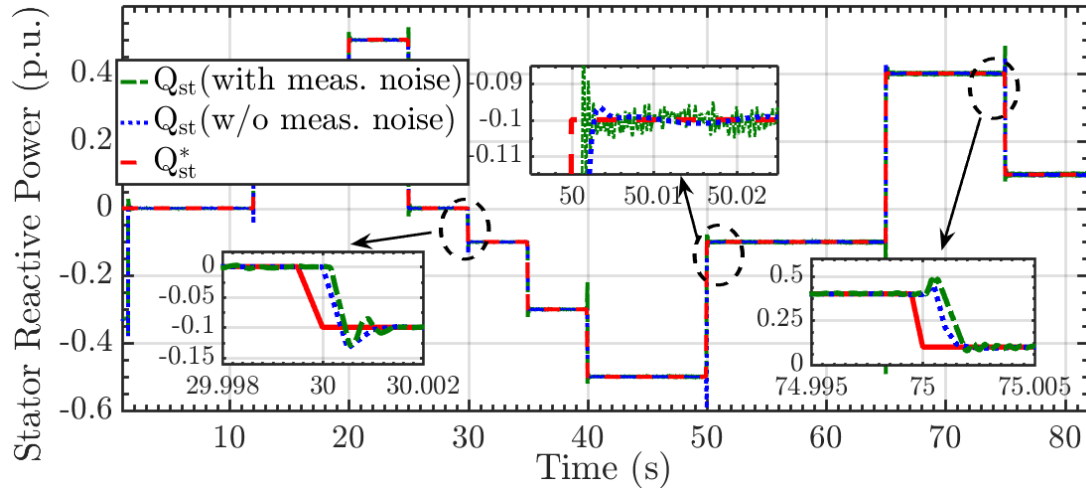


Figure 5.6: Stator Reactive Power Tracking Performance with Proposed Control.

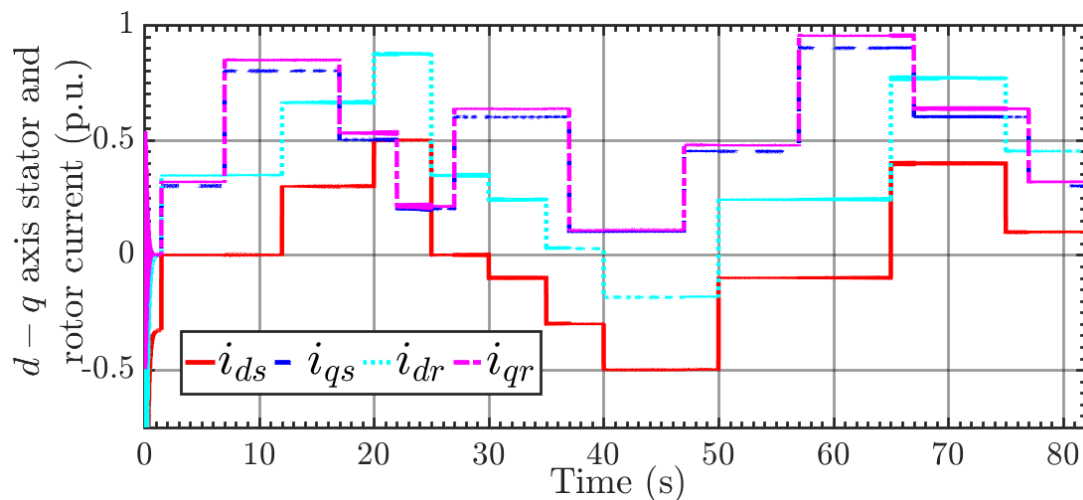


Figure 5.7: $d - q$ axis Stator and Rotor Currents for Step Changes in Active and Reactive Power.

5.1.3.2 Performance analysis during dynamic wind conditions

The proposed adaptive control was also tested on dynamic wind conditions obtained from [97] for comparison with the existing vector control. The wind speed profile is shown in Figure 5.8. The performance of the proposed controller and the Proportional Integral (PI) based vector control is shown in Figure 5.9. It can be observed that for the dynamic changes in the wind speed, the proposed controller can strictly track the reference active power obtained from MPPT whereas the vector

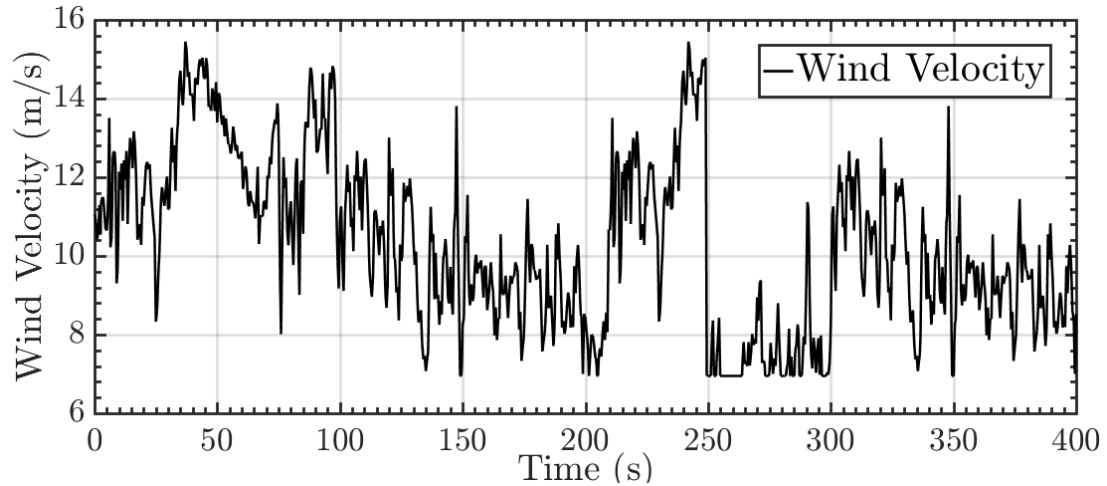


Figure 5.8: Wind Speed Profile used to access Performance of the Controller.

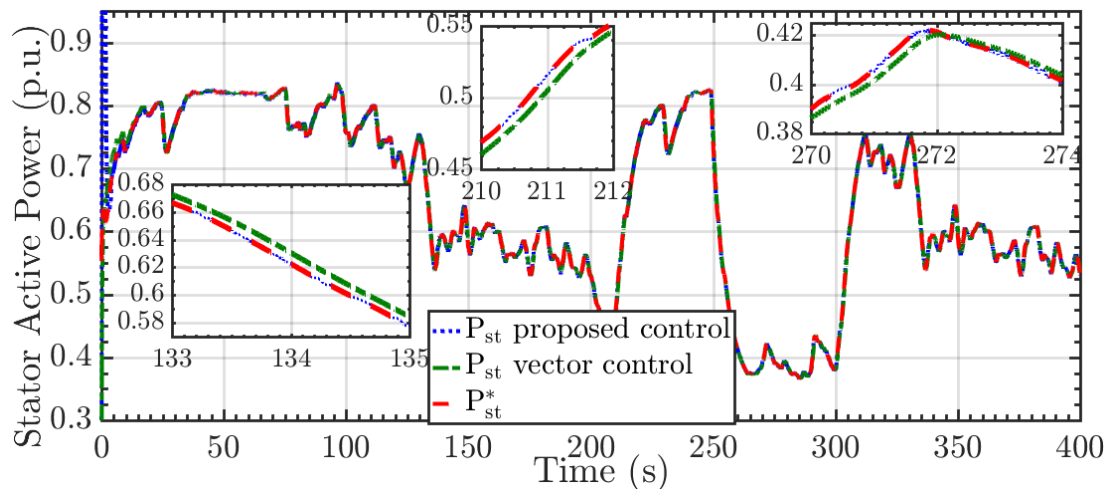


Figure 5.9: Stator Active Power Tracking Performance Comparison of Vector Control and Proposed Adaptive Control.

control lags behind as the controller is static and was optimized for a particular wind speed. The superior performance of the proposed controller during dynamic wind conditions can be attributed to the online system identification based control which updates the system model as the operating conditions change.

5.1.3.3 Performance analysis for a grid voltage sag

The performance of the proposed adaptive control was also compared to the conventional vector control during voltage sag conditions. For this test, the reference

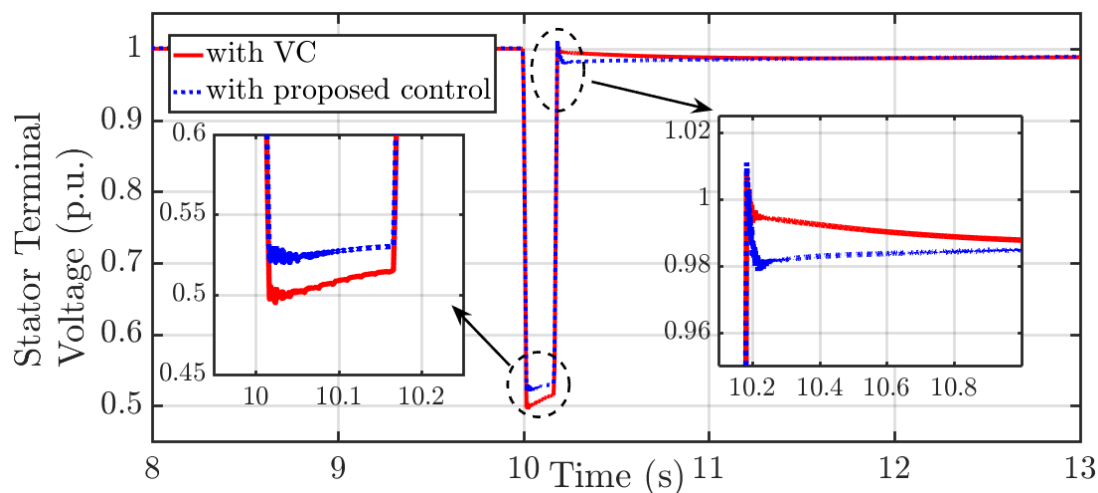


Figure 5.10: Performance Comparison of Vector Control and Proposed Adaptive Control during Grid Voltage Sag.

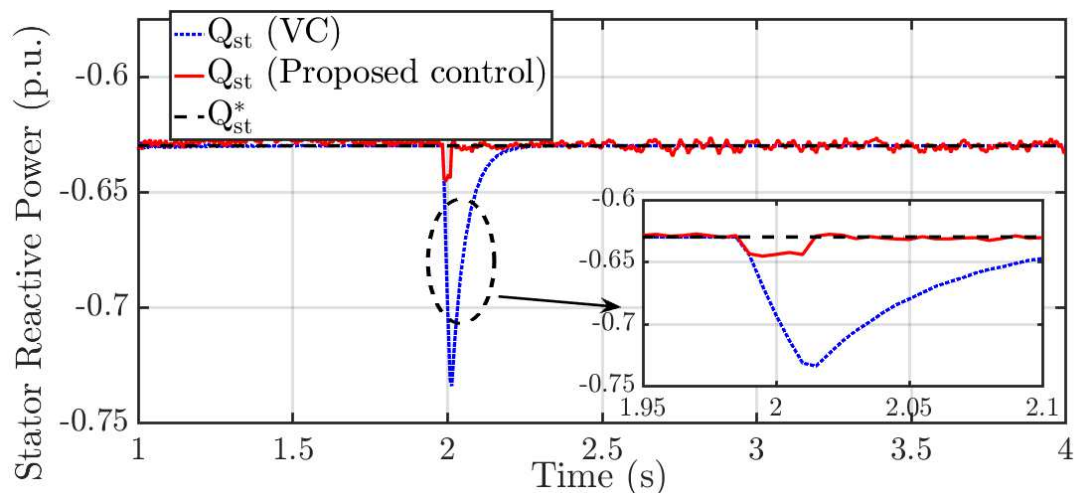


Figure 5.11: Performance Comparison of Vector Control and Proposed Adaptive Control during Machine's L_m Variation.

reactive power for both the proposed control and vector control was generated using an outer PI based voltage control loop. A grid voltage sag of 50% lasting for 10 cycles was created at 10 s, the results in Figure 5.10 show that the terminal voltage sag is lesser when proposed controller was used. This can be attributed to faster Q tracking capability of the proposed controller when compared to the static PI based vector control.

5.1.3.4 Performance analysis for machine parameter variation

The performance of the proposed control architecture was tested on a mathematical model of DFIG for a 50% variation in machine mutual inductance at 3 secs. The result comparing the performance of the conventional vector control and proposed control is shown in Figure 5.11. It can be observed that after sudden change in the machine parameter, the proposed controller recovers faster as compared to the conventional vector control.

This section presented an adaptive MVC based on identified system parameters from RLS algorithm based system identification. First, the design of the proposed controller was discussed. Then the proposed controller was tested on a 1.5 MW DFIG based wind turbine system. It has been shown that the proposed controller demonstrated comparable performance (if not better) when compared to conventional VC technique. Most importantly, the proposed method is simple and reduces the complexity of control design as compared to conventional VC technique.

5.2 Adaptive Minimum Variance Control of Grid Connected Three Phase Inverters in Synchronously Rotating DQ Reference Frame

This section presents a system identification based minimum variance architecture for active and reactive power control of a GCI. The controller is adaptive as the parameters in the control law are updated online based on identification that relate the output (active and reactive power) and the input (direct and quadrature axis voltage references). The main advantage of the proposed controller is the simplicity in design and its adaptability under varying operating conditions. The paper discusses the design of the controller and presents the simulation results from tests performed using MATLAB SimPowerSystems along with the HIL implementation. The results show that the proposed controller can be a better alternative to the existing cascaded PI based VC for grid connected inverters.

5.2.1 Model of Grid Connected Inverter

A typical configuration of a GCI is shown schematically in Figure B.1. As shown in Figure B.1, the major components of a renewable energy based system are a) renewable energy source, the output of which is generally available as DC power b) A three phase inverter, which converts the DC power from the renewables to AC power on the grid side. c) A control strategy for maintaining the active power output of GCI or DC link voltage on the renewable energy side and reactive power output of the GCI. d) A coupling inductor to connect the inverter to the grid and which also acts as the current filter on the output of the inverter. The modern GCIs are bidirectional converters meaning the power can flow from DC side to AC side and vice versa.

Typically, a VC approach is used for GCI control, with a reference frame oriented along the grid voltage vector position, which enables decoupled control of active and reactive power flowing between grid and the GCI. GCI is current regulated with the d -axis current component controlling the active power flow or DC link voltage and the q -axis current component used to control reactive power flow. In this work, a Sinusoidal Pulse Width Modulation (SPWM) technique is used for generating the firing signals for the Insulated Gate Bipolar Transistors (IGBTs) used in the inverter.

The mathematical representation of a grid connected inverter is presented in Appendix B. From (B.2), it can be observed that v_{di} and v_{qi} can be separated into two components:

1. Components v'_{di} and v'_{qi} which control current i_d and i_q respectively.
2. Components v''_{di} and v''_{qi} which compensate the coupling between d and q -axis components.

Thus,

$$\begin{aligned} v_{di} &= v'_{di} + v''_{di} \\ v_{qi} &= v'_{qi} + v''_{qi} \end{aligned} \quad (5.17)$$

where,

$$\begin{aligned} v'_{di} &= (R + pL) i_d \\ v''_{di} &= v_d - \omega_e L i_q \\ v'_{qi} &= (R + pL) i_q \\ v''_{qi} &= v_q + \omega_e L i_d \end{aligned} \quad (5.18)$$

where, p is the derivative operator $\left(\frac{d}{dt}\right)$.

Thus, the controller objective is to generate proper sequence of v'_{di} and v'_{qi} which controls i_d and i_q respectively.

The angular position of the supply voltage used in the abc to dq transformation is given by,

$$\theta_e = \int \omega_e dt = \tan^{-1} \left(\frac{v_\beta}{v_\alpha} \right) \quad (5.19)$$

where, v_α and v_β are the alpha and beta components of the grid voltage vectors.

Aligning the d -axis of the reference frame along the stator voltage position obtained from (5.19), v_q is zero, and, if the grid is assumed to be of constant voltage magnitude, v_d is also constant. The active and reactive power output of the GSC is then given by [25],

$$P_{GCI} = v_d i_d \quad Q_{GCI} = v_d i_q \quad (5.20)$$

Thus, from (5.20) it can be observed that the active power output (P_{GCI}) of the GSC

is controlled by i_d and the reactive power output (Q_{GCI}) is controlled by i_q , which in turn is controlled by v'_{di} and v'_{qi} respectively.

5.2.2 MVC control of GCI

In this work, the plant to be controlled is represented by (5.18). For MVC design, the system is assumed to be described by the CARMA model. i.e.

$$\epsilon_{P_o}(k) = \frac{B(z^{-1})}{A(z^{-1})} \times v'_{di}(k) + \frac{C(z^{-1})}{A(q^{-1})} \times \varrho(k) \quad (5.21)$$

where, $\epsilon_{P_o}(k) = P_{GCI}^*(k) - P_{GCI}(k)$, $P_{GCI}^*(k)$ is the reference active power to be delivered to the grid, $P_{GCI}(k)$ is the actual active power being delivered, v'_{qi} is the q-axis voltage sequence applied at k^{th} instant in time in the inverter, ϱ is the error in the model representation, i_q^* is generated from the outer loop.

Using the system time delay information, the MVC minimizes the variance of the output at $k + d$ with respect to the expected value of output at $k + d$ using the information gathered at up to time instant k . i.e the controller goal is to minimize the following objective function: $J(k) = E_x\{\epsilon_{P_o}(k + d)^2\}$, where d is the assumed system delay and E_x represents the expected value of the output d steps into the future, which in this case is zero.

Based on the derivation of the relation between GCI power variables and inverter voltages in section 5.2.1, a first order representation of the system is selected in this work. Even though the LCL filter configuration is used in the simulation platform, the order of identification used for grid forming mode can be still a first order representation as the impact of LCL filter on the dominant converter dynamics is negligible owing to the frequency-scale separation between the LCL filter dynamics and the outer control loops (e.g., dc-link voltage and ac-bus voltage control loops). The bandwidths of the outer control loops are usually much less than the bandwidth

of the inner current control loop. In this range, the ac-side filter behaves mainly as an L filter [103, 104]. Thus, as the filter can be reduced to a first order equivalent, a first order identification of system for terminal voltage control should be sufficient for proper control.

$$\begin{aligned}
 A(z^{-1})\epsilon_{P_o}(k) &= B(z^{-1})v'_{di}(k) + C(z^{-1})\varrho(k) \\
 A(z^{-1}) &= 1 + a_1z^{-1} \\
 B(z^{-1}) &= b_0z^{-1} \\
 C(z^{-1}) &= 1
 \end{aligned} \tag{5.22}$$

From the system equation in (5.22), it can be observed that,

$$\epsilon_{P_o}(k) = -a_1z^{-1}\epsilon_{P_o}(k) + b_0z^{-1}v'_{qi}(k) + \varrho(k) \tag{5.23}$$

Now, if the time index in prediction is shifted by one, (5.23) can be written as,

$$\epsilon_{P_o}(k+1) = -a_1\epsilon_{P_o}(k) + b_0v'_{qi}(k) + \varrho(k+1) \tag{5.24}$$

In (5.24), left hand side is the output signal one step ahead into the future. The right hand side contains the the information about present output signal, present input signal and future model estimation error.

The control action $v'_{qi}(k)$ is computed in order to optimize the variance of the

output one step ahead in the future.

$$\begin{aligned} \underset{v'_{di}(k)}{Min}\{J(k)\} &= \underset{v'_{di}(k)}{Min}E_x\{\epsilon_{P_o}(k+1)^2\} = \\ \underset{v'_{di}(k)}{Min}E_x\{[(-a_1)\epsilon_{P_o}(k) + (b_0)v'_{di}(k) + \varrho(k+1)]^2\} \end{aligned} \quad (5.25)$$

Equation (5.25) contains present inputs, present outputs and future model estimation error. As model estimation error is assumed to be white noise, and its future values cannot be correlated with past and/or present signals. Therefore, the minimum variance will be achieved when the sum of the first two components is set to zero. i.e.

$$-a_1\epsilon_{P_o}(k) + b_0v'_{di}(k) = 0 \quad (5.26)$$

Thus, the MVC law for active power control is given by,

$$v'_{di}(k) = \frac{a_1\epsilon_{P_o}(k)}{b_0} \quad (5.27)$$

Similarly, the MVC law for reactive power control is given by,

$$v'_{qi}(k) = \frac{a_1\epsilon_{Q_o}(k)}{b_0} \quad (5.28)$$

where, $\epsilon_{Q_o}(k) = Q_{GCI}^*(k) - Q_{GCI}(k)$. Q_{GCI}^* is the reference reactive power to be delivered to the grid and Q_{GCI} is the actual reactive power delivered.

Figure 5.12 represents the overall control structure proposed in this work for GCI.

5.2.3 Closed loop system bandwidth

The closed loop system bandwidth for active power control loop assuming active power control of the GCI as Single Input Single Output System (SISO) is shown in Figure 5.13 for PI based control, PR control and proposed minimum variance

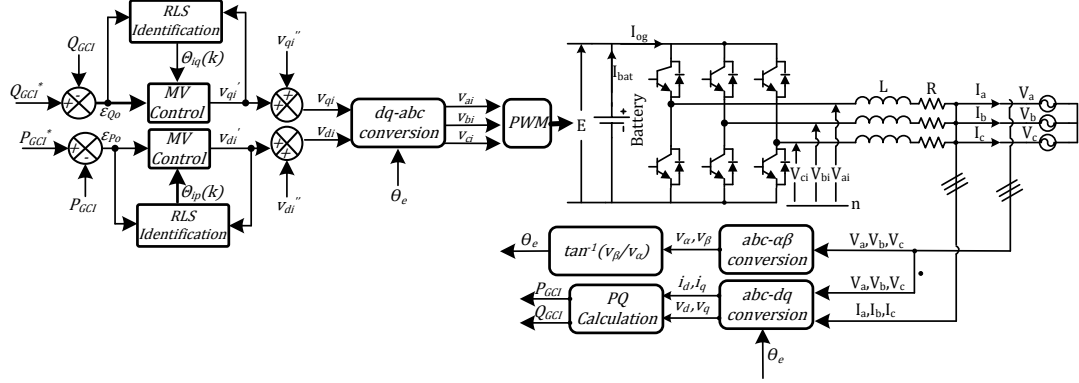


Figure 5.12: Proposed Adaptive Control Scheme for GCI.

controller respectively. The closed loop system bandwidth was obtained for PI and PR based control by assuming the knowledge of the system parameters are known. For the case of PI controller, inner loop is a current controller and outer loop is a power controller. For PR controller a resonant filter is designed. Likewise the bandwidth for the case with minimum variance controller was obtained based on the constant controller gain as obtained in (5.27) and using the identified transfer function model at time 't'= 5 secs for operating scenario as shown in Figure 5.14. It can be observed that the PI control has a lower bandwidth as compared to PR controller and proposed controller. The PI controller bandwidth can be increased if a faster response is required by multiple-state feedback and increasing the controller gain however, that pushes the system towards stability limit, which is not desirable [104].

5.2.4 Simulation Results

The proposed adaptive control architecture was tested in MATLAB/Simulink SimPowerSystems for a GCI test system. The GCI system used in MATLAB simulation was a 0.5 MVA used as Grid Side Converter (GSC) on a 1.5 MVA DFIG system. It was assumed that DC link voltage was maintained using a battery energy storage system in parallel so that the GSC can be operated in power control mode. The con-

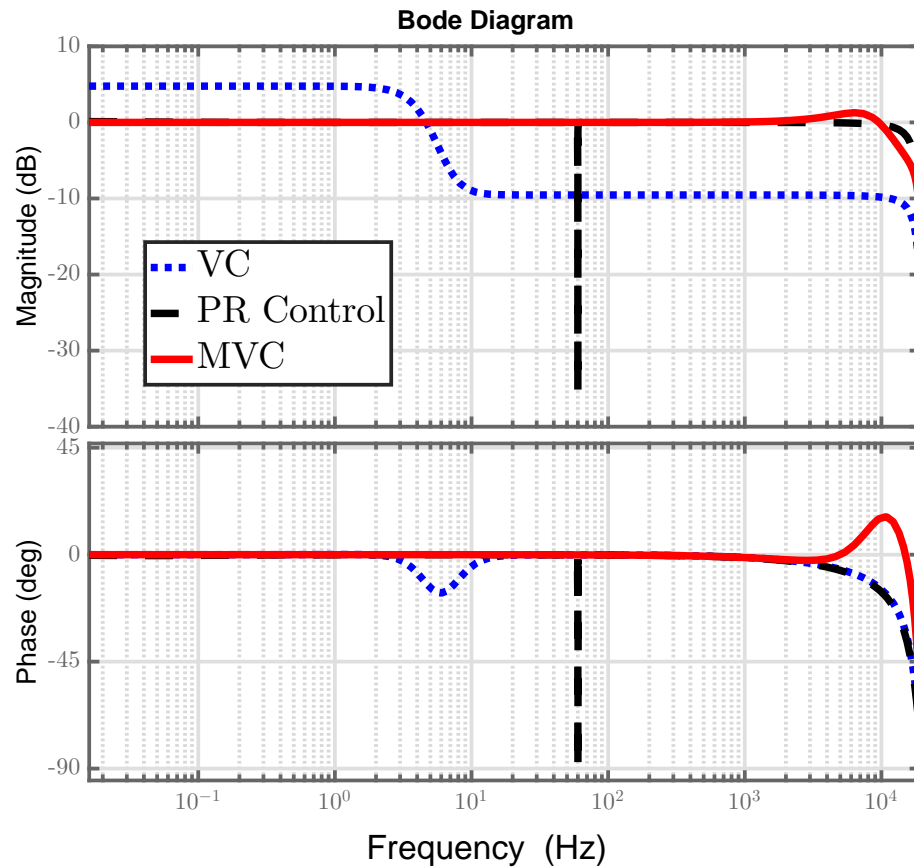


Figure 5.13: Closed loop System Bandwidth with Different Controllers Active Power Control Loop for Results shown in Figure 5.14.

troller was tested for various step changes for the active and reactive power output from the GSC. In Figure 5.14, comparison of power tracking of the proposed architecture, proportional resonant controller and the conventional cascaded PI based vector control technique for a step change in active power reference is shown. It can be seen that the proposed architecture has lesser oscillations when compared to vector control. Also, the proposed controller has faster dynamic response; this indicates that the controller can adjust the control output even for sudden large changes in the reference set point. This ability of the proposed control makes it suitable to be used along with the variable and intermittent energy resources like PV and wind farm.

Figure 5.15 illustrates the reactive power tracking capability of the proposed ar-

Table 5.1
Comparison of Response Time between Proposed Adaptive Controller and other
Controllers

Simulation Case	Response Time (s)		
	PI Control	PR Control	Proposed Control
Figure5.14	0.041	0.039	0.022
Figure 5.15	0.079	0.078	0.019
Figure5.18	0.680	0.640	0.022
Figure 5.19	0.739	0.700	0.019
Figure 5.21	0.075	-	0.028
Figure 5.22	0.068	-	0.023

chitecture. The performance is similar to the active power tracking. The proposed controller for Q control, however, has a steady state error which is less than 0.5%. This can be associated with the lack of integral component in the proposed control architecture. Figure 5.16 and Figure 5.17 illustrates the comparison of instantaneous phase A current and the Total Harmonic Distortion (THD) for the same phase respectively. From the instantaneous current waveform in Figure 5.16, it can be observed that the proposed technique has a smoother waveform around the peak. From Figure 5.17, it can be observed that the proposed control technique results in lower THD in the current output of the GCI. The reason for the lower THD with the proposed control technique can be linked to the modification of the modulating signal such that the power output measured at the inverter terminals has minimum contribution from harmonic components. More importantly, the lower order harmonics are lower in amplitude which makes the harmonic filter design easier both in terms of size and cost. It can be seen that the proposed adaptive control architecture performs better than or equal to VC method and can be used as an alternative to existing control topologies. It is worth noting that the PI controller is tuned based on the model of the inverter presented in section 5.2.1. Same model in section 5.2.1 is used for designing the adaptive controller so that the comparison is relevant.

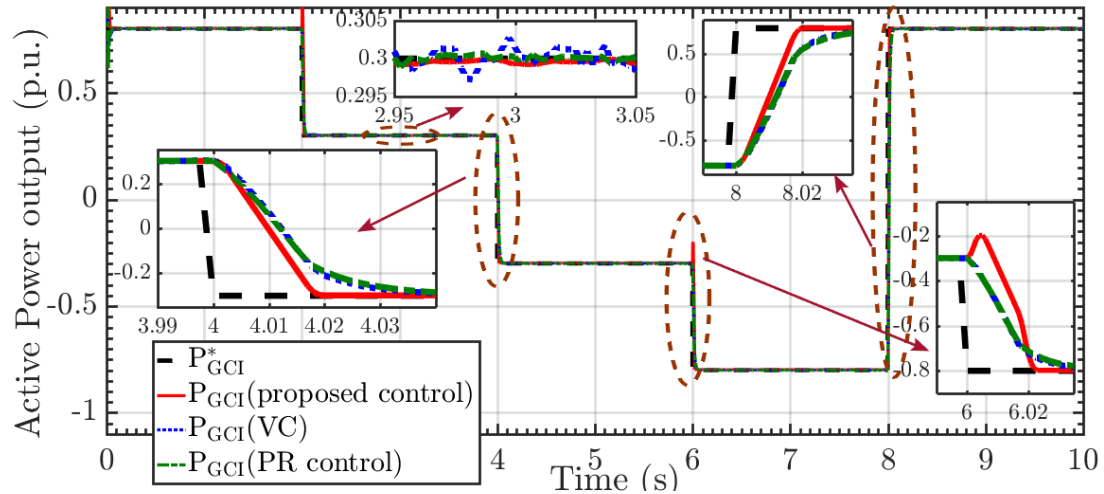


Figure 5.14: Comparison of Active Power Tracking for Step Changes in the Reference Set-points.

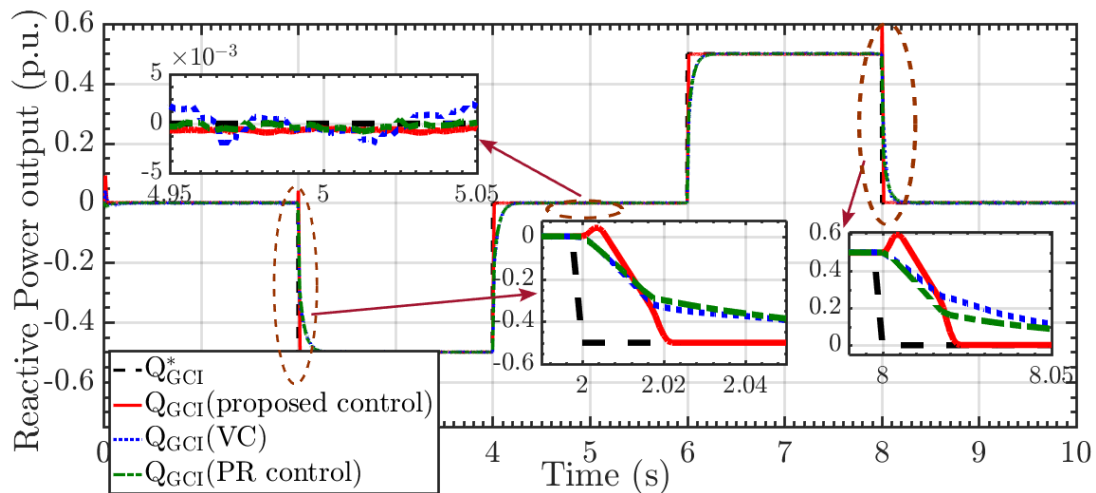


Figure 5.15: Comparison of Reactive Power Tracking for Step Changes in the Reference.

5.2.4.1 Performance Comparison Between Conventional Control and Proposed Control

In order to demonstrate the robustness of the proposed control when compared to conventional vector control technique, both controllers were tested for a variation of line inductance. Inductance and resistance of the coupling filter that interfaces the inverter with the grid is increased by 50% and 1000% respectively. Figure 5.18 and Figure 5.19 shows the active and reactive power tracking performance of the

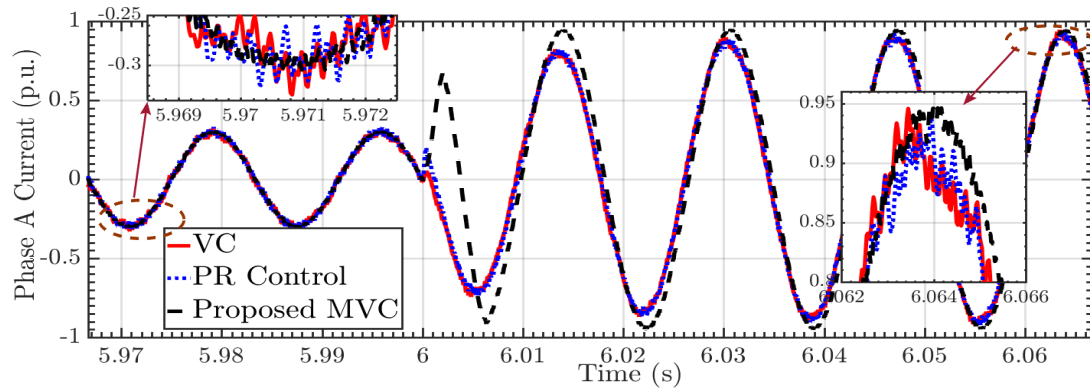


Figure 5.16: Phase A Current Comparison.

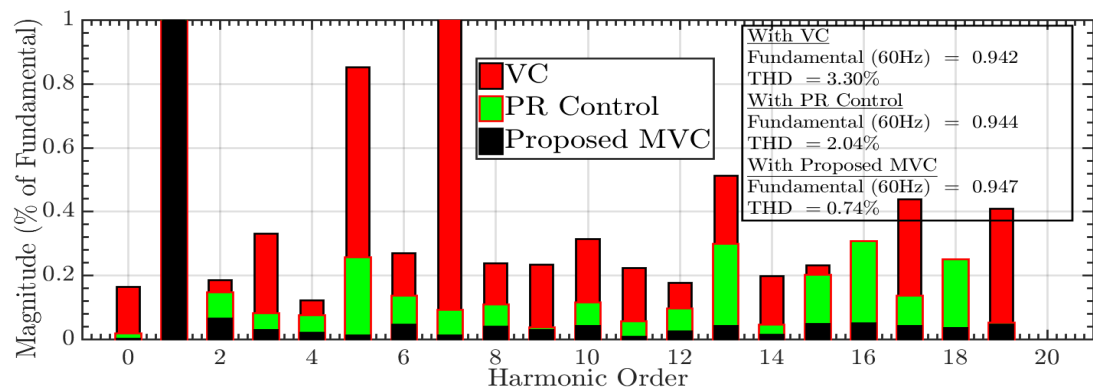


Figure 5.17: Comparison of Output Current Harmonics Spectrum when operated in Grid Connected Mode.

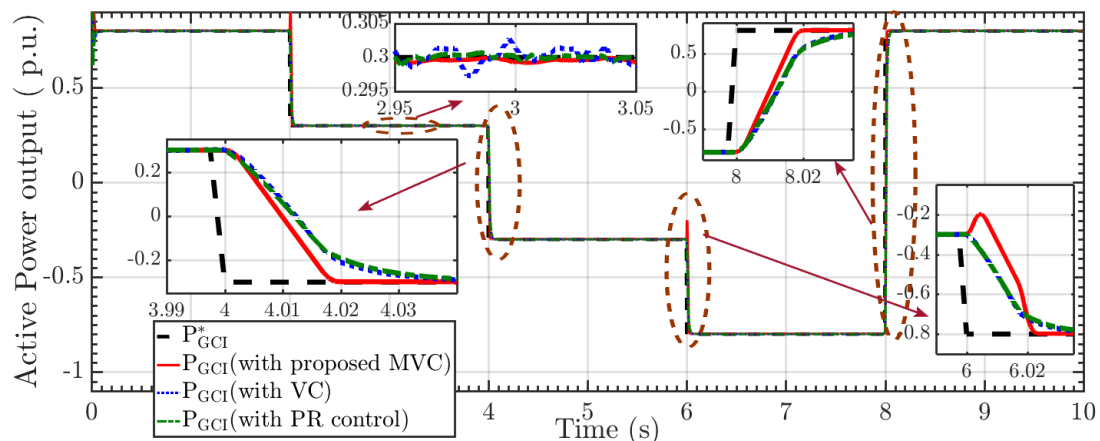


Figure 5.18: Comparison of Active Power Tracking for Step Changes in the Reference and Changes in Coupling Inductance.

proposed controller, PR controller and the conventional PI based vector controller.

It can be observed from Figure 5.18 and Figure 5.19 that the performance of the PI

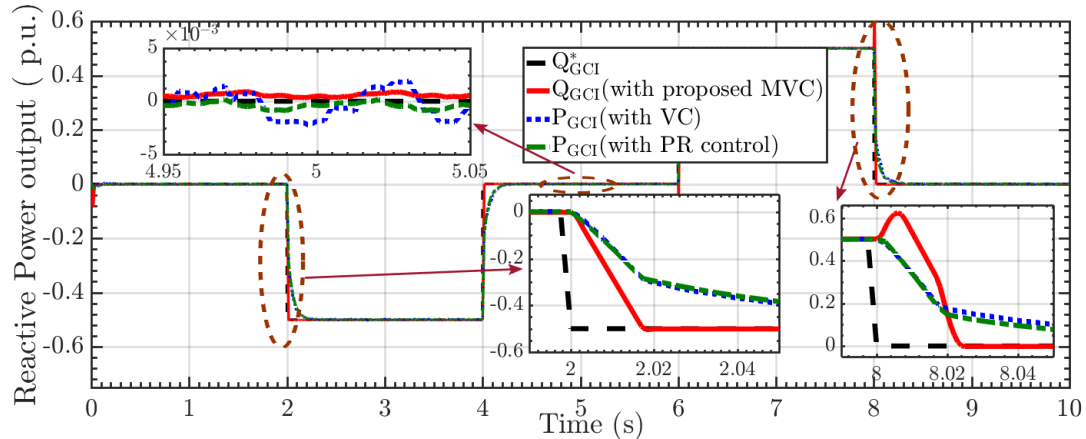


Figure 5.19: Comparison of Reactive Power Tracking for Step Changes in the Reference and Changes in Coupling Inductance.

controller has degraded as compared to the results in Figure 5.14 and Figure 5.15. However, the performance of the proposed adaptive controller has not degraded as much. This is primarily due to the fact that system identification can update the identified system parameters and the controller output is updated accordingly. The performance comparison of the proposed control with the conventional PI control and PR controller for the different cases studied in terms of response time (the time it takes the system response to reach within 1% of the reference input) is shown in Table 5.1. It can be seen that, the proposed controller has smaller response time when compared to other controllers. Also, compared to the conventional vector control, where two sets of inner loop and two sets of outer loop control should be designed, the proposed controller needs only one set of control for each of active and reactive power. Also, the proposed controller does not require current feedback which can be a major advantage in terms of controller robustness.

5.2.5 HIL Experimental Results

The proposed control architecture for GCI is also tested using HIL test-bed (see Figure 5.20). The experimental test-bed consists of a 50V L-N lab supply with the DC voltage maintained at 150V and limited to a power rating of 320 watts. The inverter

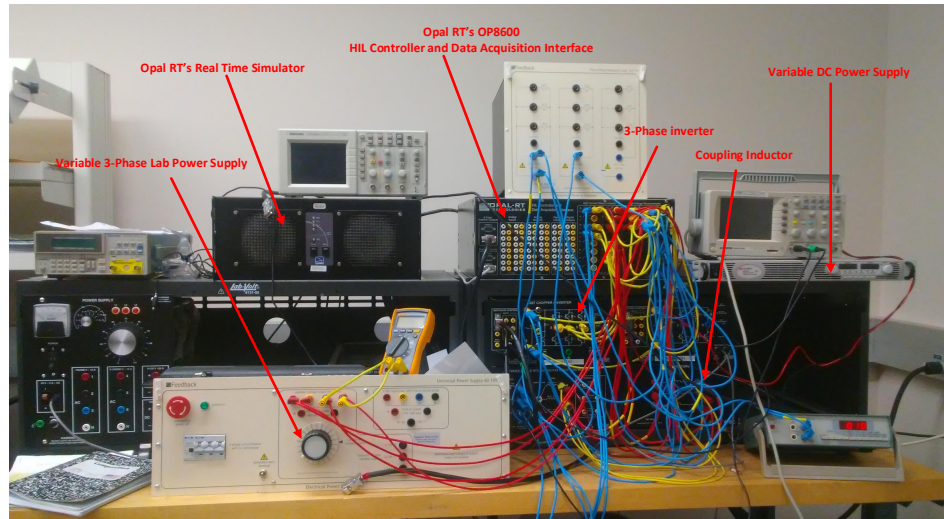


Figure 5.20: Experimental Test-bed Used for testing the Proposed Control Architecture.

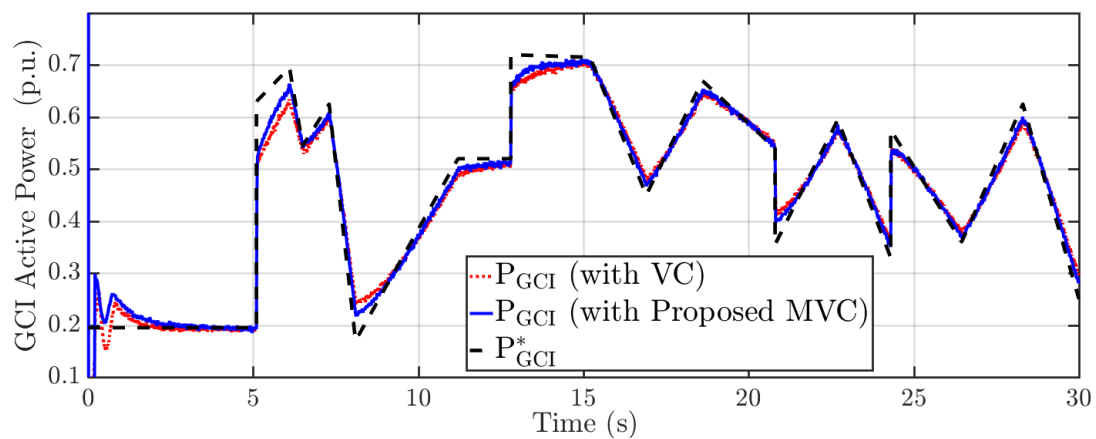


Figure 5.21: Comparison of Active Power Tracking on Experimental Test-bed.

control is optimized for a base of 350 VA with base voltage of 50V L-N. Other hardware specifications and parameters are given in Appendix A. Figure 5.21 shows the active power tracking performance with HIL implementation for the proposed controller and conventional vector control. It can be observed that the proposed controller has a faster response as compared to the conventional vector control. Figure 5.22 shows the reactive power tracking performance with HIL implementation. It can be observed that the proposed controller has a faster response as compared to the conventional vector control and has lesser overshoot. Figure 5.23 shows the corresponding d-axis

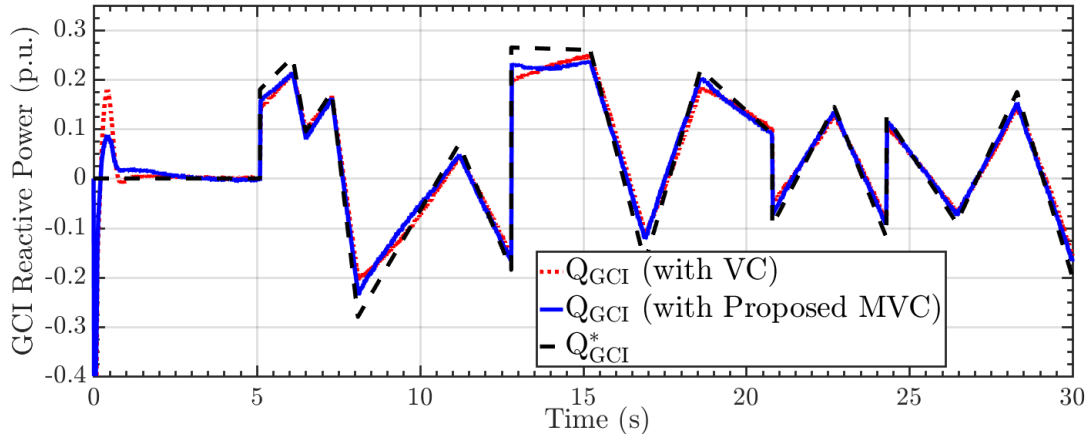


Figure 5.22: Comparison of Reactive Power Tracking on Experimental Test-bed.

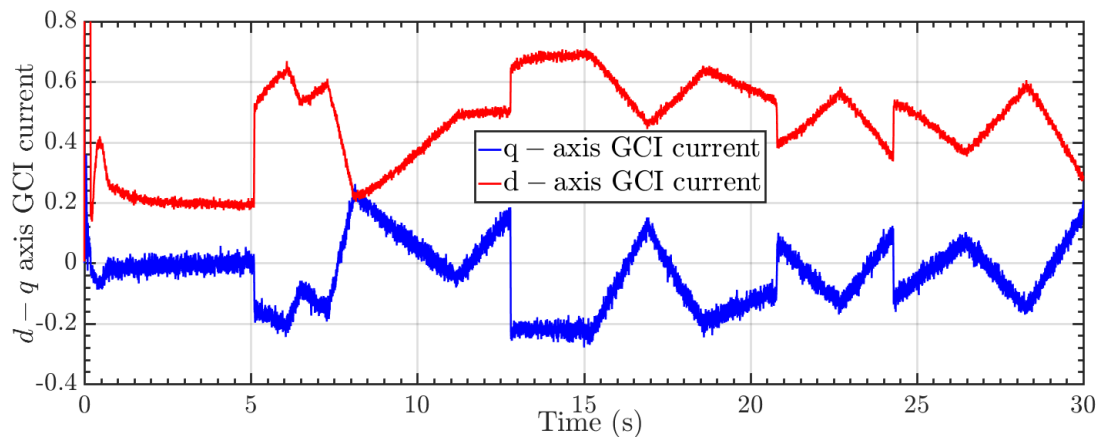


Figure 5.23: GCI $d-q$ -axis Current using the Proposed Controller during Active and Reactive Power Tracking.

and q -axis current of the GCI during the active and reactive power tracking with the proposed controller. The hardware in the loop implementation of the proposed control technique demonstrates the suitability of the proposed control scheme to be used for three phase inverter control.

5.3 System Identification based Sensorless Control Approach for DFIG

Although a good performance is achieved by the reference frame orientation based VC, it needs appropriate decoupling, introduces rotary transformation, and requires much tuning work assuming knowledge of system parameters to ensure machine's operational stability over the whole operating range due to the multiple loops in

the controller [105, 106]. Also, the whole feedback loop is dependent on correct measurements of active power/rotor speed and reactive power (for outer loop) and rotor currents for inner loop which makes the controller heavily dependent on the sensors. Controllers that are less dependent on sensors or minimum number of sensors are always favorable as any unplanned downtime is not desired by the system operator. Also, as WT technologies are rapidly evolving in terms of complexity and size, there is an urgent need for cost effective operation and maintenance (O&M) strategies. Wind turbines are hard-to-access structures, and they are often located in remote areas. These factors alone increase the (O&M) cost for wind power systems. Also, poor reliability directly reduces availability of wind power due to the turbine downtime [107]. Especially unplanned downtime represents one of the main cost drivers of a modern wind farm [18]. In [18], it was noted that for geared WTs with sizes larger than 1 MW, the sensors, controller and communication system failure rates combined can amount up to 24% of the total failure rates and up to 7% downtime, which results in significant amount of power lost from wind sources as the wind energy penetration is still on the rise. In [108, 109], state observers are used for rotor current estimation which are then used as feedback signals in VC so as to make WECS more reliable. However, the issue with the approach presented in [108, 109] is that speed observers are dependent on the knowledge of the system parameters like stator and rotor resistances and inductances.

To overcome this large tuning work, reduce the controller design complexity, and dependency on sensors and knowledge of system parameters in VC, an output feedback controller for the DFIG based on identified system model is proposed. The motivation behind the design of this controller is to increase the reliability of operation of the DFIG through less dependency on sensors and simplify the controller design process. The major advantages of the proposed technique can be summarized as:

- The controller is tuned online and does not require proper knowledge about the DFIG system parameters beforehand.
- The design of proposed control technique is simple, robust, and can be easily implemented in the existing inverters without having significant changes to the control architecture in use.
- The method performs well during changing grid dynamics as well as during dynamic wind fluctuations.
- The approach is scalable and can be implemented in real systems interconnected with larger power grid.
- The controller is adaptive in nature meaning any parametric change that bring about changes in dynamics of DFIG is identified and the controller is updated accordingly.
- The controller minimizes the use of sensor required for DFIG control.

In this section, a comprehensive system identification based adaptive controller is proposed for grid connected DFIG system including both GSC and RSC. The system identification is based on RLS estimation which provides the auto-regressive moving average exogenous (ARMAX) model of the system. The controller uses the identified system parameter for DFIG control and MVC architecture has been used that minimizes the variance of the system output from its reference set-point. The stability properties of the proposed controller is discussed. The system identification based control approach is utilized for control of RSC, GSC and speed estimation of DFIG. Theoretical results are validated based on real-time simulation for 1.5 MW wind turbine system. The schematic of proposed control is shown in Figure 5.24.

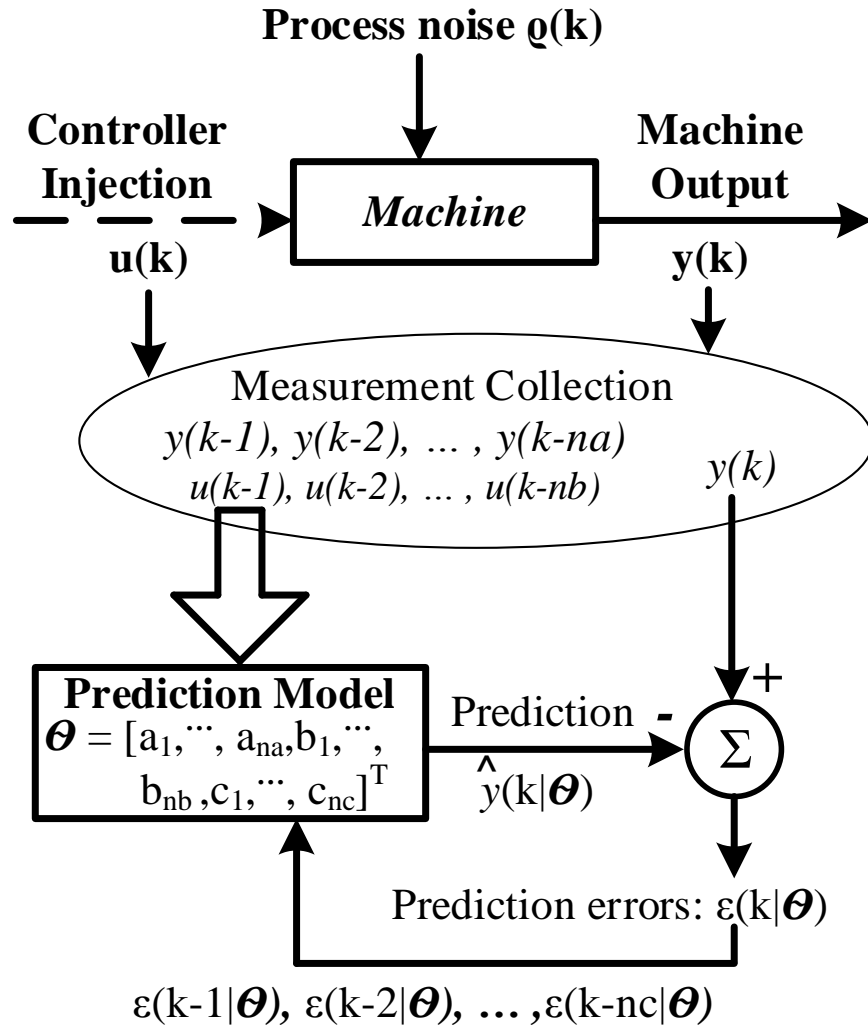


Figure 5.25: System identification process data flow diagram.

equivalent or better control for wide operating range of the DFIG in dynamic wind conditions. Case B demonstrates the claim that the DFIG operational reliability is increased with the proposed control as compared to VC. This has been demonstrated using the responses of DFIG with VC and proposed control after a rotor current sensor fault. Case C demonstrates the low voltage ride through capability of DFIG operated with proposed control demonstrating that the proposed control can maintain operational stability even during grid disturbances. Case D validates the claim that the proposed control can maintain similar closed loop response even after parameter

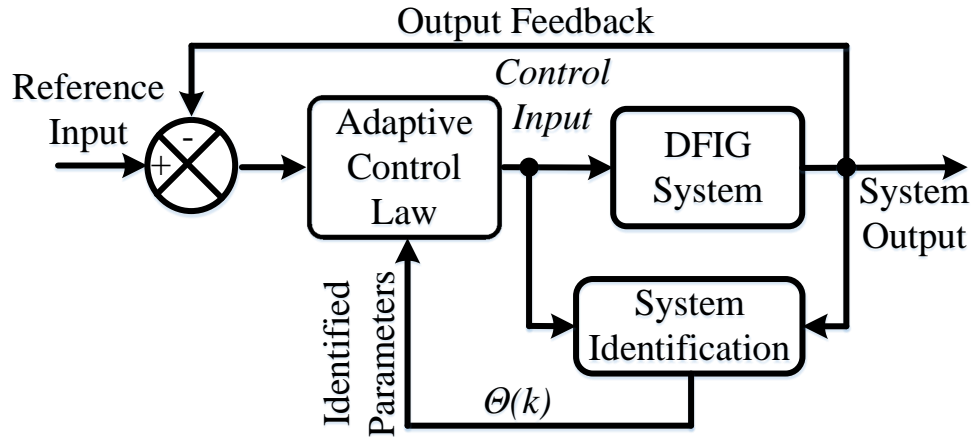


Figure 5.26: System identification based adaptive control approach.

Table 5.2: Performance Comparison in Dynamic Wind Conditions

Control	Maximum Absolute Error (%)		Absolute Mean Error (%)	
	VC	Proposed	VC	Proposed
V_{PCC}	1.52	0.71	0.0003	0.11
ω_r	4.95	2.2	0.07	0.0012
E	3.67	2.67	0.081	0.0067
Q_{GSC}	0.22	0.42	0.0006	0.0014

variation. This test compares the response of the proposed controller and VC for conditions with nominal L_m and when L_m is doubled.

5.3.1.1 Case A: Validation of Suitability of Proposed Controller during Dynamic Wind Changes

The proposed controller has been tested for wide range of operating regions using the actual wind power data obtained from [97] which is shown in Figure 5.27. This was performed to test the applicability of the proposed controller in real-life operating scenario. This set of test case uses the proposed GSC and RSC control along with the proposed speed estimation technique and compares the result with the VC applied to GSC and RSC but with proposed speed estimation. Figure 5.28 shows the rotor speed

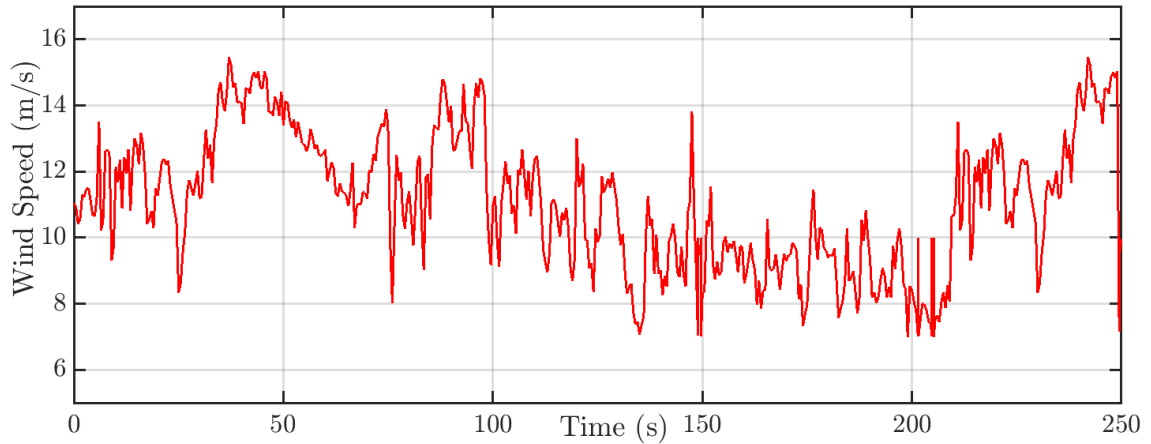


Figure 5.27: Case A: Wind Speed used to test the Performance of Proposed Controller.

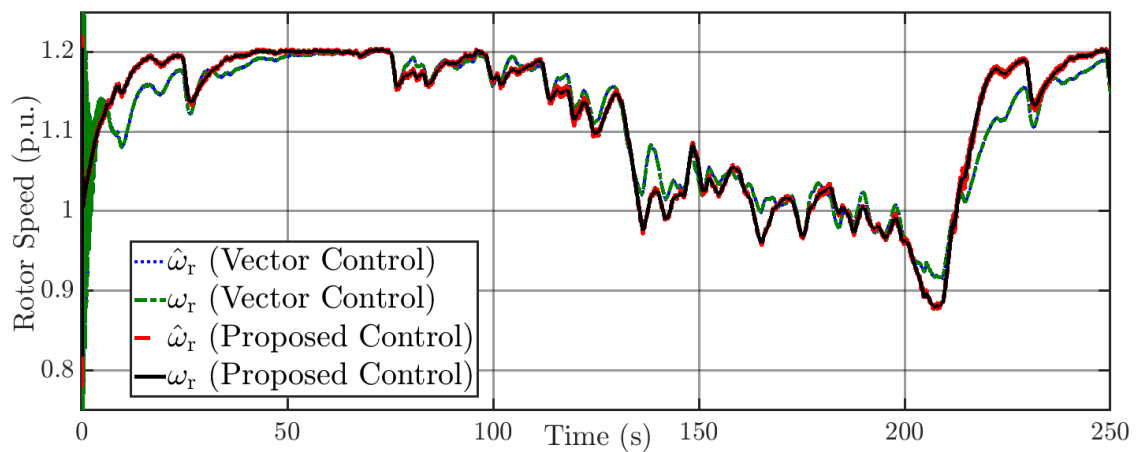


Figure 5.28: Case A: DFIG Rotor Speed Estimation Comparison with Proposed Adaptive Speed Estimation Technique when using Vector Control and Proposed Identification Based Control.

estimation performance comparison with the proposed speed estimation technique but with different control technique employed in the system. It can be observed that the proposed speed estimation technique can work well with either of the DFIG control approach.

Figure 5.29 shows the comparison between the total power generated from DFIG when using VC and proposed identification based control for wind speed shown in Figure 5.27. The variation in the response of the two controller can be attributed with the differences in the characteristic of the controller and their response times. The

Table 5.3: Difference between Mechanical Power Input and Electrical Power Output with the Proposed Technique and Vector Control

Control	Maximum Absolute Difference (p.u.)	Mean Absolute Difference (p.u.)
Proposed	0.7466	0.1101
VC	0.7873	0.1268

difference between the mechanical power input to the turbine and electrical power output of turbine is crucial in understanding the torsional stress in the rotor shaft. It can be observed from Figure 5.30 that the DFIG rotor is subjected to lesser torsional stress with the proposed control as compared to the VC. This is particularly due to the fast control action of proposed control as opposed to VC. Figure 5.31 compares the PCC voltage regulation using DFIG with the proposed approach and the VC approach. It can be observed that both the controller has similar performances with the voltage deviation around the set-point when the active power output of wind varies changing within $\pm 1\%$ for both controllers. Figure 5.32 shows the DC link voltage regulation comparison with the proposed control and VC employed in GSC. Figure 5.33 shows the reactive power output from GSC when asked to operate in unity power factor mode. It can be observed from Figure 5.32 and Figure 5.33 that the proposed control implemented in GSC has comparable performance with VC with the error percentage changing within $\pm 1.5\%$ for both the control approaches. Table 5.2 tabulates the percentage error in reference tracking, for RSC and GSC, with proposed control and VC, for the dynamic wind conditions. Table 5.3 tabulates the mean difference and maximum absolute difference between mechanical power input to wind turbine and electrical power output of wind turbine with the proposed control and VC. It can be seen that with the proposed approach the mean difference and maximum difference between mechanical power input and electrical power output of DFIG based WT is minimized.

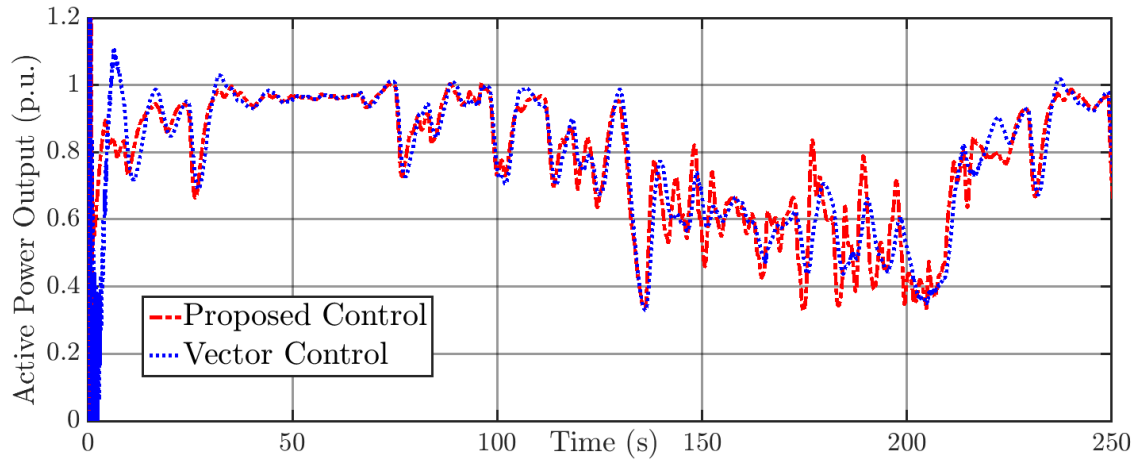


Figure 5.29: Case A: Comparison between Total Power Generated from DFIG when using Vector Control and Proposed Identification Based Control for Wind Speed shown in Figure 5.27.

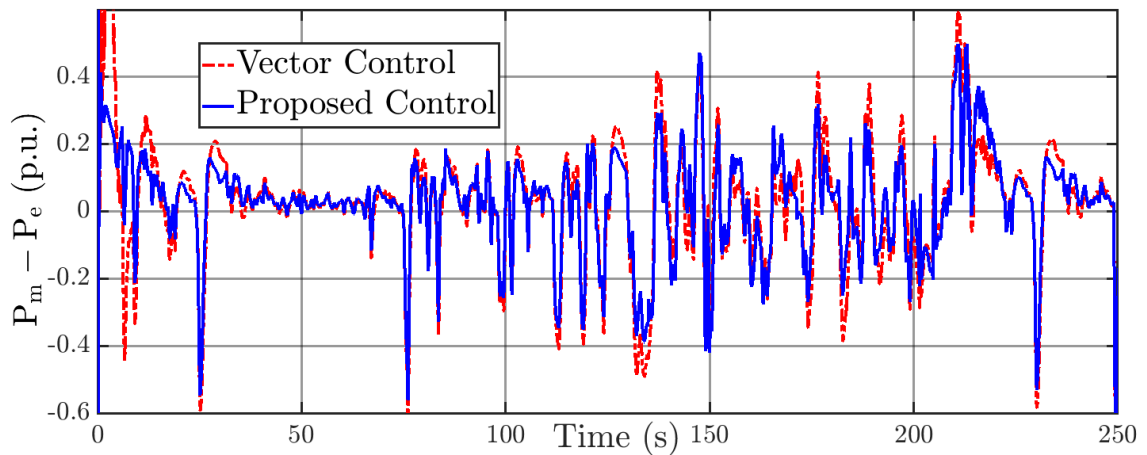


Figure 5.30: Case A: Comparison between Mechanical Power Input and Electrical Power Output when using Vector Control and Proposed Identification based Control for Wind Speed shown in Figure 5.27.

5.3.1.2 Case B: Performance Analysis for Rotor Current Sensor Failure

In order to demonstrate the advantage of the proposed identification based control with respect to the conventional VC a rotor current sensor failure scenario was created¹. The sensor configuration used for this test case is tabulated in Table 5.4. As the proposed control loop does not require any rotor current feedback, as can be observed

¹Please note that this test was carried out without the speed estimation control loop as the speed estimation uses the measured current signals as reference signals.

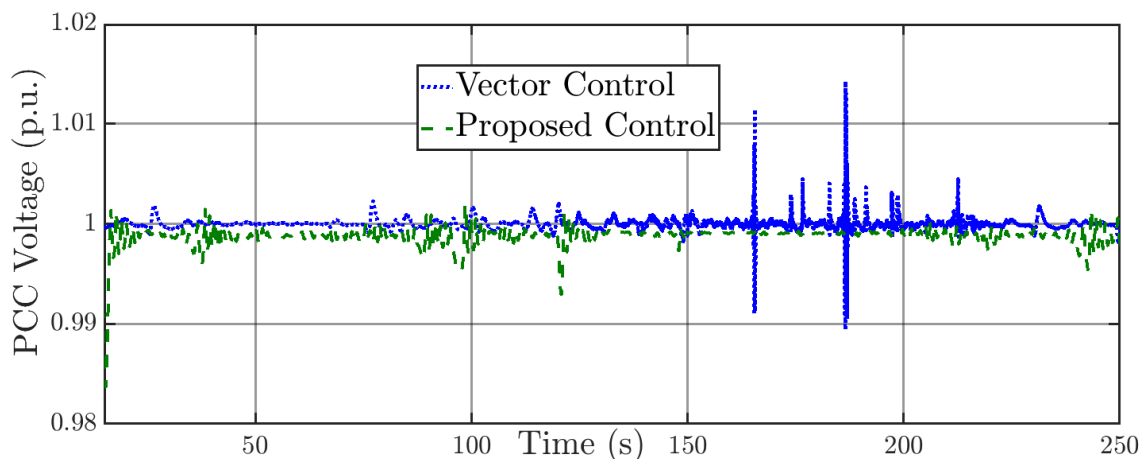


Figure 5.31: Case A: Comparison between PCC Voltage Regulation from DFIG when using Vector Control and Proposed Identification based Control for Wind Speed shown in Figure 5.27.

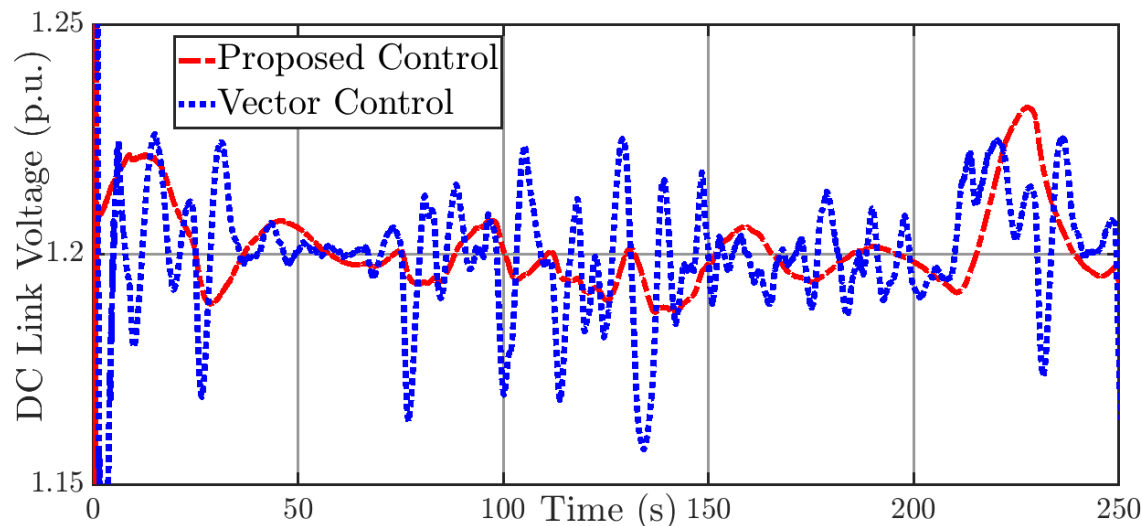


Figure 5.32: Case A: Comparison between DC link Voltage when using Vector Control and Proposed Identification based Control for Wind Speed shown in Figure 5.27.

in Figure 5.34 that the proposed control still maintains stable machine operation following the sensor failure. However, as the VC depends on the inner loop current feedback, the stability of the machine is lost after the current measurements are no longer available after 5 secs. This will lead to downtime of WT and the WT can only be operational once the rotor current issue is fixed. Use of proposed identification based control on WTs can help avoid such sensor failure related downtimes. Figure

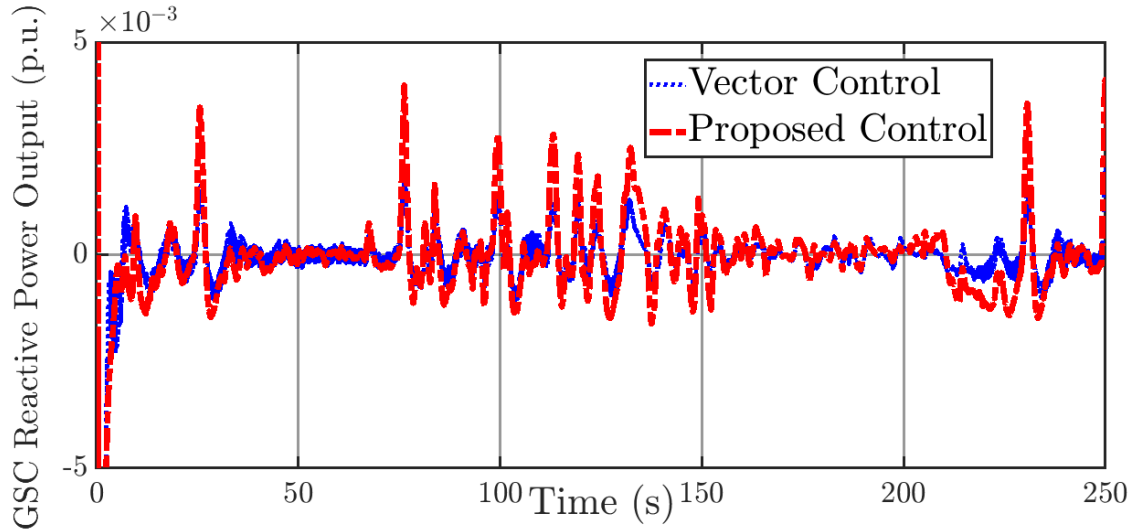


Figure 5.33: Case A: Comparison between GSC Reactive Power Output when using Vector Control and Proposed Identification based Control for Wind Speed shown in Figure 5.27.

Table 5.4: Sensor Configuration for Case B

Time	Sensors Available for DFIG Control
0-5 s	Rotor Current, GSC Current & Speed Sensor
5+ s	GSC Current & Speed Sensor

Table 5.5: Response Characteristics for Case C

Controller	Rise Time (s)	Settling Time (s)	Overshoot
Vector Control	0.4	0.7	5.5%
Proposed Control	0.07	3.7	1.8%

5.35 shows the rotor speed of DFIG following a rotor current sensor fault. It can be observed that with the proposed control the machine stability is intact as opposed to VC.

5.3.1.3 Case C: Performance Analysis for a Grid Fault

DFIG-based WTs are found to be very sensitive to grid disturbances, especially to voltage sags [110]. In such a scenario, it is desirable to test the performance of the proposed system identification based control technique for grid faults. Figure 5.36 shows the performance comparison of the proposed controller and the conventional

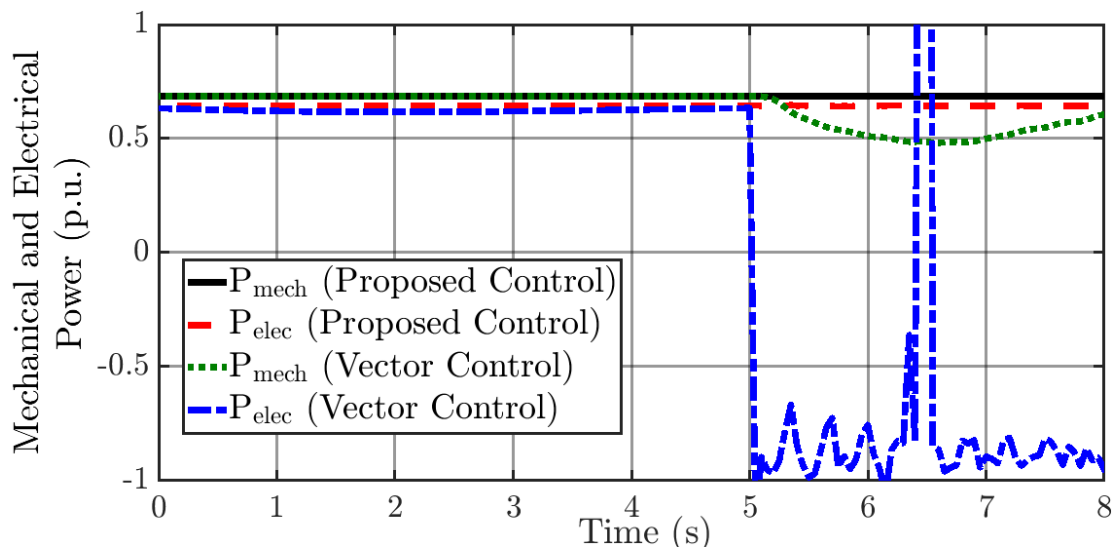


Figure 5.34: Case B: Comparison between DFIG Mechanical and Total Electrical Power Generated following a Rotor Current Sensor Failure with VC and proposed identification based Control

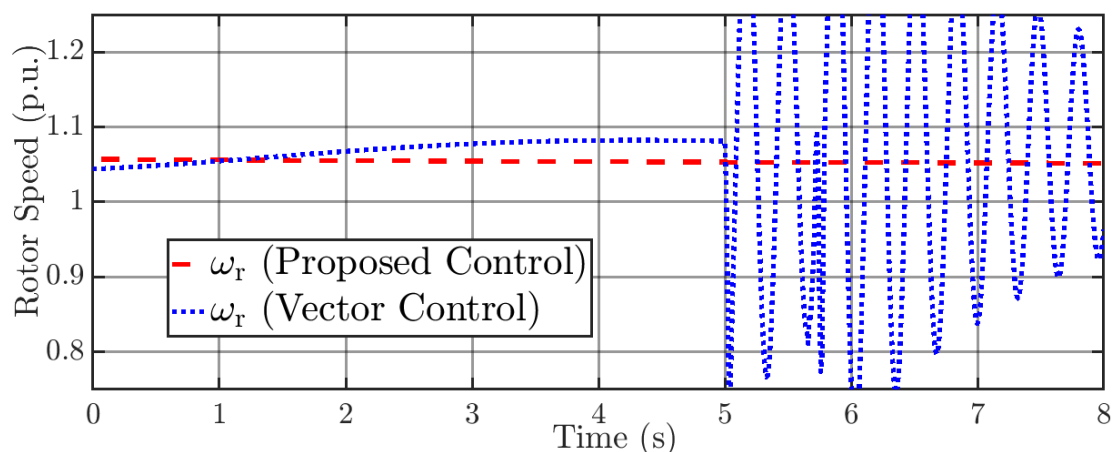


Figure 5.35: Case B: Comparison between DFIG Rotor Speed following a Rotor Current Sensor Failure with VC and Proposed Identification based Control

VC following a grid voltage sag. It can be observed that with the proposed technique the voltage recovery is much faster as compared to the VC. Also, it is important to notice that the voltage rise phenomena does not occur with the proposed control due to the lack of error accumulation component in proposed control as opposed to VC. Table 5.5 tabulates the voltage sag magnitude and recovery characteristics of the

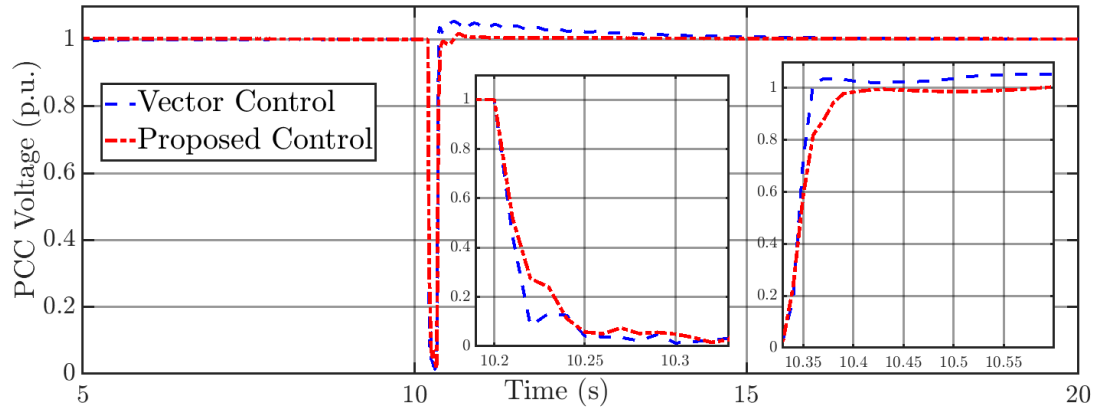


Figure 5.36: Case C: Comparison between PCC Voltage Regulation from DFIG when using Vector Control and Proposed Identification based Control following a Three phase to Ground Fault.

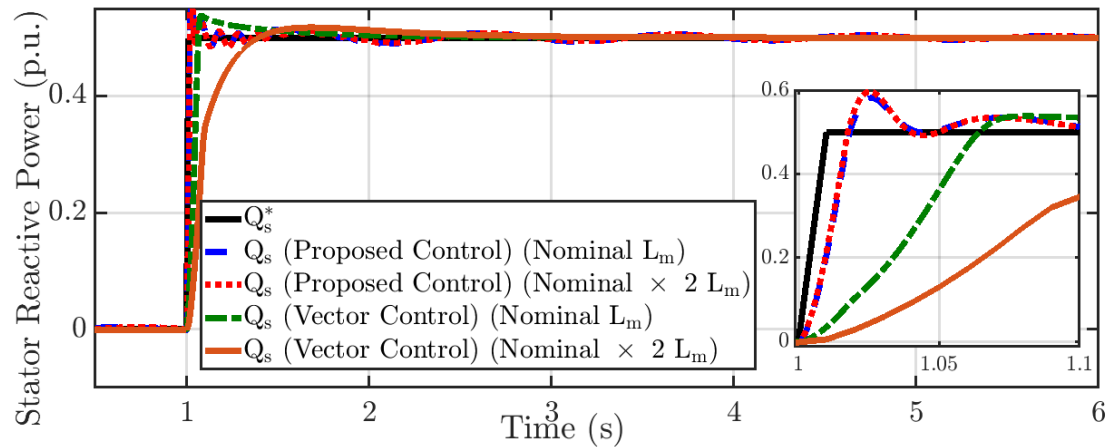


Figure 5.37: Comparison between Proposed Identification based Control and Vector Control for Step Changes in Stator Reactive Power after Changes in Machine Mutual Inductance

Table 5.6: Case D: Step Response Characteristics Comparison between Proposed Control and Vector Control for Parameter Variation

Controller	Parameter	Rise Time (s)	Settling Time (s)	Overshoot (%)
VC	Nominal L_m	0.06	0.6	7.5
VC	Nominal $\times 2 L_m$	0.25	1.05	3.5
Proposed	Nominal L_m	0.02	0.4	12
Proposed	Nominal $\times 2 L_m$	0.02	0.4	13

proposed controller and VC for a grid disturbance.

5.3.1.4 Case D: Performance Analysis for Machine Parameter Variation

As the proposed identification based control estimates the machine dynamics online based on the control input and output signals applied to and obtained from the machine, any variation in the machine parameters are also taken care by the controller. In order to demonstrate advantage of the proposed controller, which does not require retuning of the controller to get similar response as in nominal conditions, machine mutual inductance L_m is varied by twice its nominal value. The response of the controller for a step change in stator reactive power reference (Q_s^*) was studied to validate the parameter variation in-dependency of the proposed controller. The result in Figure 5.37 shows that the proposed controller had almost similar response for reference tracking even after variation in L_m . With the proposed controller a slight increase in overshoot to 13% from 12% was observed as compared to reduction by 4% with VC. However, as can be seen in Figure 5.37 and as tabulated in Table 5.6 the response of VC has changed drastically when the mutual inductance changed with the rise time increasing to 0.25 secs as opposed to 0.06 secs in nominal case. The rise time with the proposed controller was approximately 0.02 secs in both cases. In the case studied, the VC was designed in nominal to have rise time of less than 0.1 seconds and damping of less than 10%, for the proposed controller the controller objective was to minimize the variance two steps ahead in future which resulted in controller characteristics as tabulated in Table 5.6.

5.4 Chapter Summary

In this chapter, system identification based decoupled control of active and reactive power for a DFIG and GCI has been presented. The model of DFIG based WT system and TPGCI is discussed and design approach of conventional VC as well as proposed control is established. The results show that the proposed system identification based approach results in better operational reliability of DFIG based WECS and TPGCI.

CHAPTER 6: CONTROL OF LARGE SCALE DFIG TO PROVIDE REACTIVE POWER SUPPORT TO BULK POWER GRID

In this chapter, use of DFIG based wind farm to provide reactive power support to the bulk power grid is studied. The reactive power support capability of DFIG based wind farm has been prioritized over active power support. A novel dynamic reactive power estimation based transient voltage control for grid integrated DFIG by coordinating RSC, GSC and pitch control is designed and its performance analysis has been performed.

As wind turbine installations have moved beyond the relatively strong portion of the network in US power grid, the grid codes have been evolved under different jurisdictions in the US, helping to define WPP interconnection specifications within the bulk power system and drive improvements in wind turbine system design, particularly for control and electric power systems [111]. In response, the wind industry, including the American Wind Energy Association (AWEA) and the Western Electricity Coordinating Council (WECC), have developed proposals for interconnection standards and guidelines specific to wind generation [111]. The grid code requirements address LVRT capability, supervisory control and data acquisition (SCADA) capability, and power factor design criteria. In 2012, NERC's Integration of Variable Generation Task Force (IVGTF) released a special assessment of its "Interconnection Requirements for Variable Generation" to address voltage and frequency ride-through, reactive and real power control, and frequency/inertial response criteria specific to the technical characteristics of variable generation [112]. Recommendations from IVGTF to update standards and procedures are currently being implemented.

The WPP interconnection standard focuses on the technical aspects such as power

quality, active and reactive power control, voltage control, active power feed-in at overfrequency/underfrequency and LVRT capability. Out of these grid code requirements, the LVRT capability of the DFIG based windfarm with the proposed adaptive control technique has been demonstrated in earlier chapters. In this chapter and the next, the active and reactive power support capability of DFIG based wind farm to mitigate the power system oscillations and enhance the transient stability has been studied.

It has been shown that the wind generators are not much affected by the low frequency oscillations due to fast control capability of power electronic-based controllers [41, 113]. However, as components in the power system they can have an impact on the oscillations and transient energy of synchronous generators. Grid connection of a DFIG for power generation changes the power system load flow and introduces dynamic interactions with the synchronous generators [114]. If the wind farm buses are considered as the PQ buses, the concept of controllable loads can be applied. Let P_j and Q_j denote the total real and reactive power leaving the j th bus via transmission lines, then, the power equations on the wind farm buses could be written as [113],

$$d_{P_j} \Delta \omega_j + \sum_{k \in \mathcal{N}_j} B_{jk} V_j V_k \sin(\delta_{jk}) = P_j^* + \Delta P_j, \quad j \in \mathcal{W} \quad (6.1)$$

$$d_{Q_j} \Delta V_j - \sum_{k \in \mathcal{N}_j} B_{jk} V_j V_k \cos(\delta_{jk}) = Q_j^* + \Delta Q_j, \quad j \in \mathcal{W} \quad (6.2)$$

where, P_j^* and Q_j^* are the final steady state power outputs, ΔP_j and ΔQ_j the changes in power due to control references as $P_j = P_j^* + \Delta P_j$ and $Q_j = Q_j^* + \Delta Q_j$, and d_P and d_Q are damping coefficients based on virtual local power sharing principal.

Due to asynchronous nature of the DFIG, the wind generator voltage angle and grid angle can be considered decoupled. Figure 6.1a shows the operation of DFIG in PQ control mode during a sudden change in the grid voltage angle (due to a

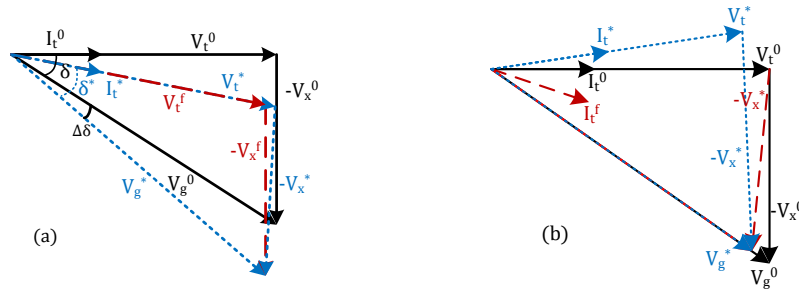


Figure 6.1: Vector diagram of (a) Angle deviation (b) Voltage deviation. V_g : Grid voltage, V_t : DFIG Stator Terminal Voltage, V_x : Line Voltage Drop, I_t : Current flowing through DFIG, δ Angle between Terminal and Grid Voltage, Superscript: 0: Initial Steady State Vectors, f : Transient Vectors (after the fault), $*$ = Final Steady State Vectors.

transient fault). It can be observed from the figure that the DFIG control can adjust its terminal voltage such that the active and reactive power can be maintained at the same level before the grid disturbance. Figure 6.1b shows the operation of DFIG during a grid voltage deviation. It can be seen that even after the voltage sag in the grid, DFIG tries to maintain the reference active and reactive power, by changing its terminal voltage and current based on changes in the grid. In the above case, it can be observed that after the grid voltage changed from V_g^0 to V_g^* , the DFIG terminal voltage changes from V_t^0 to V_t^* , and current changes from I_t^0 to I_t^* such that the initial value of the active and reactive power is maintained. Also, from the above phasor diagram, it should be noted that, the severity of the changes in grid voltages is not large enough to cause DFIG to violate its operating limit and disconnect from the grid. Thus from the phasor diagram, it can be observed that DFIG based wind farm can only contribute to enhancement of system transient stability if they have supervisory control that forces contribution from DFIG. In this chapter and the next, novel system identification based supervisory control approach has been presented to provide active and reactive power support to the bulk power grid.

6.1 Analysis of Dynamic Reactive Power Estimation Based Coordinated Reactive Power Support from Grid Integrated DFIG

This section presents a novel dynamic reactive power estimation based transient voltage control for grid integrated DFIG by coordinating RSC, GSC and pitch control. During transient grid voltage changes, the proposed architecture calculates a reference reactive power and required active power using the designed adaptive controller and P-V droop controller respectively. Then, a dynamic reactive power estimation algorithm evaluates the machine limits and operating conditions to ensure that maximum reactive power support is achieved. Based on this, the existing machine and pitch controllers are coordinated. The test results with professional grade nonlinear simulator considering practical GE 1.5MW system parameters show that, when compared to the existing DFIG control methodologies, the approach provides at an average 20-30% improvement in voltage support and ensures maximum reactive power support without violating machine limits.

The major advantages of the proposed architecture are:

- The method dynamically calculates the reactive power capability during changing wind and grid conditions and effectively de-rates the active power augmenting pitch controller to enable maximum reactive power support.
- The method dynamically integrates the RSC and GSC with the proposed adaptive and PV droop controller.
- The architecture can be seamlessly integrated with the existing WTG controllers in the field and ensures the machine limits are not violated.

6.1.1 Reactive Power Capability Limits of DFIG

In this section, a method to dynamically estimate the reactive power limits of DFIG considering the controller operation is presented. The machine reactive power limits

are calculated online using machine equations which is used to augment the existing controllers in DFIG. This ensures that the reactive power support from DFIG can be provided during grid voltage sag conditions without violating the machine limits.

6.1.1.1 Illustrative Example

Consider a 1.5 MW GE wind generator [90] with a mathematical model discussed in Appendix A and with controller illustrated in Figure 2.1. Reactive power capabilities are evaluated for various operating conditions considering a two-mass mathematical model with nonlinear dynamics designed in DigSilent Power Factory [115]. The reactive power capabilities of the DFIG and power converters are limited due to the following parameters, 1) rotor voltage 2) rotor current 3) stator current and, 4) stator voltage. For DFIG based wind turbine, the active power passing through the converter is roughly around 25% of the total power, while the slip speed is around $\pm 30\%$ around synchronous speed. Considering these operating conditions, limitations can be mathematically represented as follows:

6.1.1.2 Rotor Voltage Limitations

Neglecting the stator transients and stator resistance, the stator voltage ' v_s ' can be represented as,

$$v_s = v_{ds} + jv_{qs} = j\omega_s (\Psi_{ds} + j\Psi_{qs}) \quad (6.3)$$

Using (A.2),

$$v_s = j\omega_s (-L_s I_s + L_m I_r) \quad (6.4)$$

where I_s and I_r represents the stator and rotor current vector respectively.

$$v_s = j\omega_s \left(-L_s \frac{\Psi_r - L_r I_r}{-L_m} + L_m I_r \right) \quad (6.5)$$

As $s = \frac{\omega_{slip}}{\omega_s}$, using (A.1) can be obtained.

$$sv_s = \frac{L_s}{L_m}v_r - \frac{L_s L_r}{L_m} \left(1 - \frac{L_m^2}{L_s L_r}\right) j\omega_{slip} I_r \quad (6.6)$$

$$s \frac{L_m}{L_s} v_s = v_r - L_r \sigma j\omega_{slip} I_r \quad (6.7)$$

where $\sigma = 1 - \frac{L_m^2}{L_s L_r}$ and as $L_m \approx L_s$, neglecting the inductive voltage drop it can be observed that, $v_r \approx s.v_s$, which suggests that the rotor voltage referred to the stator side should be equal to the slip voltage in p.u to maintain the stator voltage at 1 p.u.. For example, if the DFIG is being operated at a maximum slip of 0.3 (including the dynamic conditions when there is sudden wind gust), the rotor voltage that needs to be supplied is just 0.3 pu, which is generally less than the actual voltage rating that the rotor windings can withstand. As in this work, the rotor windings to stator windings turn ratio is 0.379, we have considered the rotor voltage limit to be 0.379 pu which is the actual insulation limit of the rotor voltage winding. One should note that the PQ plot in this work is drawn based on the insulation limit of 0.379 pu, instead of the operating limit of 0.3 pu. Considering the above magnitude limit for rotor voltage, the capability curve of DFIG can then be obtained by neglecting the derivative terms in (A.1) and assuming $v_{dr} = v_r \cos(\theta)$, $v_{qr} = v_r \sin(\theta)$, $v_{qs} = v_s$, $\Psi_{ds} = \Psi_s$ and solving for the current quantities with (A.2) into consideration. θ is the angle between rotor voltage vector and its d -axis component. Figure 6.2 shows the overall capability curve of DFIG considering the rotor voltage limit only. From Figure 6.2, it can be seen that the rotor voltage can be a limiting factor for reactive power generation only at higher slip conditions. Thus operating near large slip conditions is not recommended as this may violate rotor voltage limits.

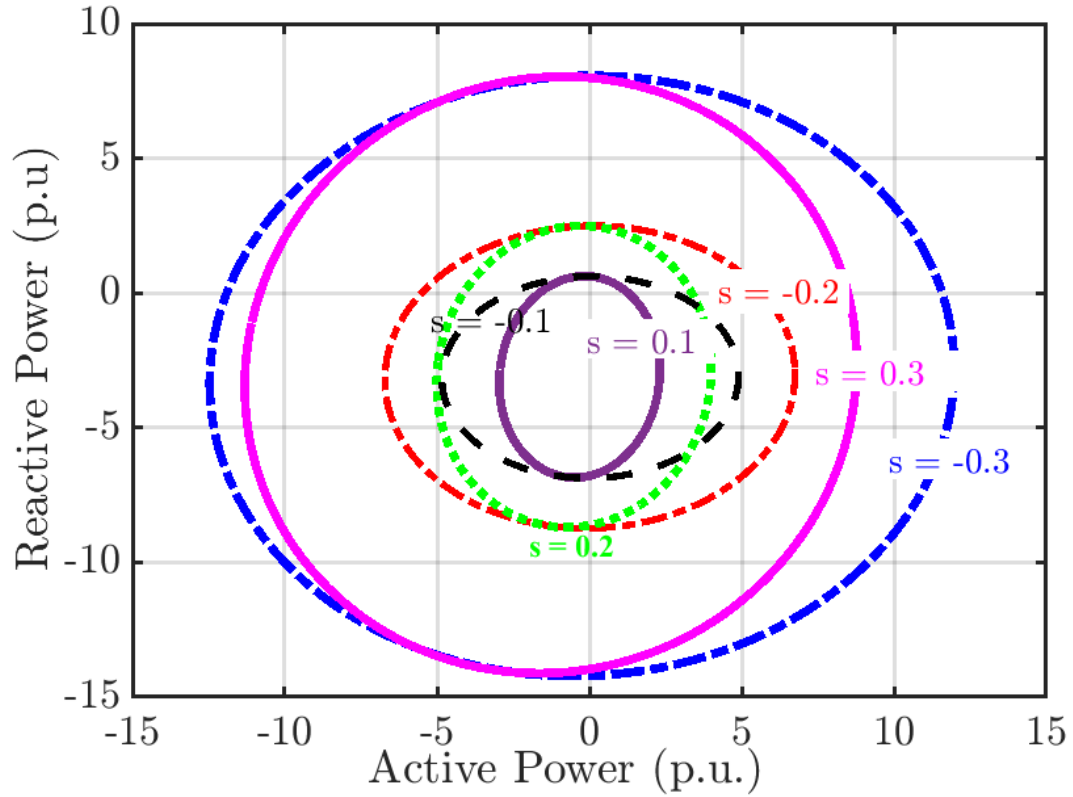


Figure 6.2: Capability curve of DFIG considering Rotor Voltage Limit.

6.1.1.3 Rotor Current and Stator Current Limitation

Considering the DFIG is controlled in stator flux oriented reference frame and assuming ideal grid conditions, i.e.

$$v_{qs} = 1 \text{ p.u.}, v_{ds} = 0, \Psi_{qs} = 0, \Psi_{ds} = 1 \text{ p.u.} \quad (6.8)$$

From (A.3) and (6.8),

$$P_{st} = v_{qs} i_{qs} = v_{qs} \left(\frac{\Psi_{qs} - L_m i_{dr}}{-L_s} \right) = v_{qs} \frac{L_m}{L_s} i_{qr} \quad (6.9)$$

With the q -axis rotor current limited as per the active power generated, considering the rotor current limit, the stator side reactive power that can be generated is given

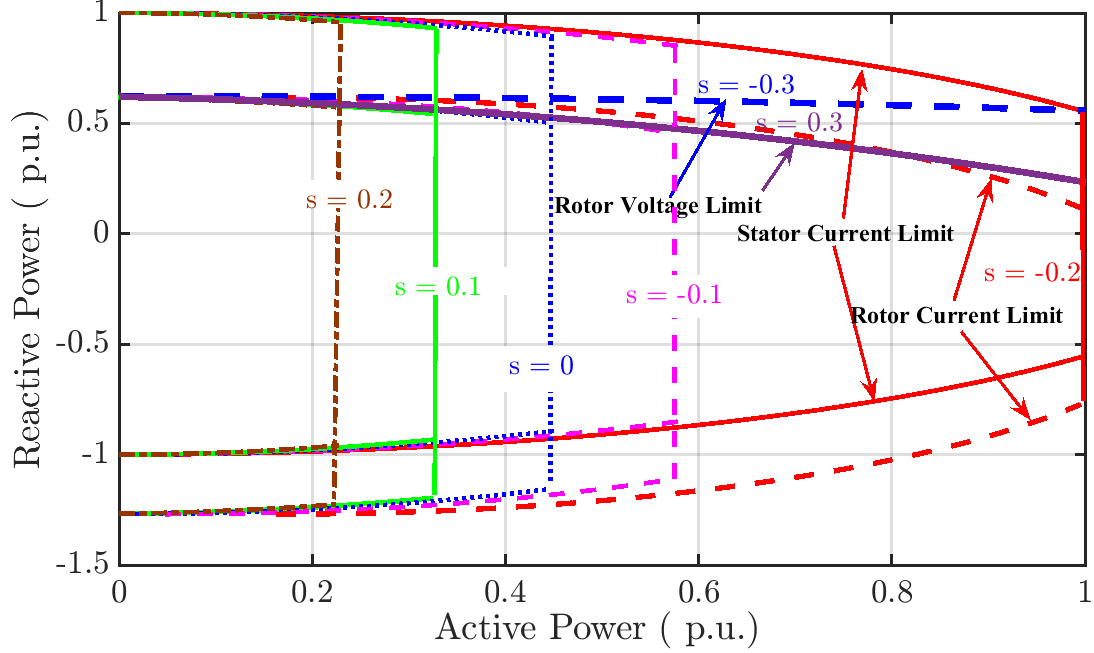


Figure 6.3: Capability curve of DFIG without Considering GSC's Reactive Power Capability Illustrating Individual Limits for Stator Current, Rotor Current and Rotor Voltage.

by,

$$Q_{st} = v_{qs} i_{ds} = v_{qs} \left(\frac{\Psi_{ds} - L_m i_{dr}}{-L_s} \right) = v_{qs} \left(\frac{\Psi_{ds} - L_m \sqrt{1 - i_{qr}^2}}{-L_s} \right) \quad (6.10)$$

Likewise for stator current limit,

$$P_{st} = v_{qs} i_{qs} \quad (6.11)$$

$$Q_{st} = v_{qs} i_{ds} = v_{qs} \sqrt{1 - i_{qs}^2} \quad (6.12)$$

6.1.1.4 Stator Voltage Limitations and Inverter Limits

From equations in 6.1.1.3, it can be observed that the capability curve of DFIG changes linearly with respect to the stator voltage. For GSC, as it has to supply the slip power extracted from the rotor, the active current is determined by the slip condition. The maximum reactive power that can be extracted from the GSC is limited by the rating of the converters used. Thus the reactive power limit is given

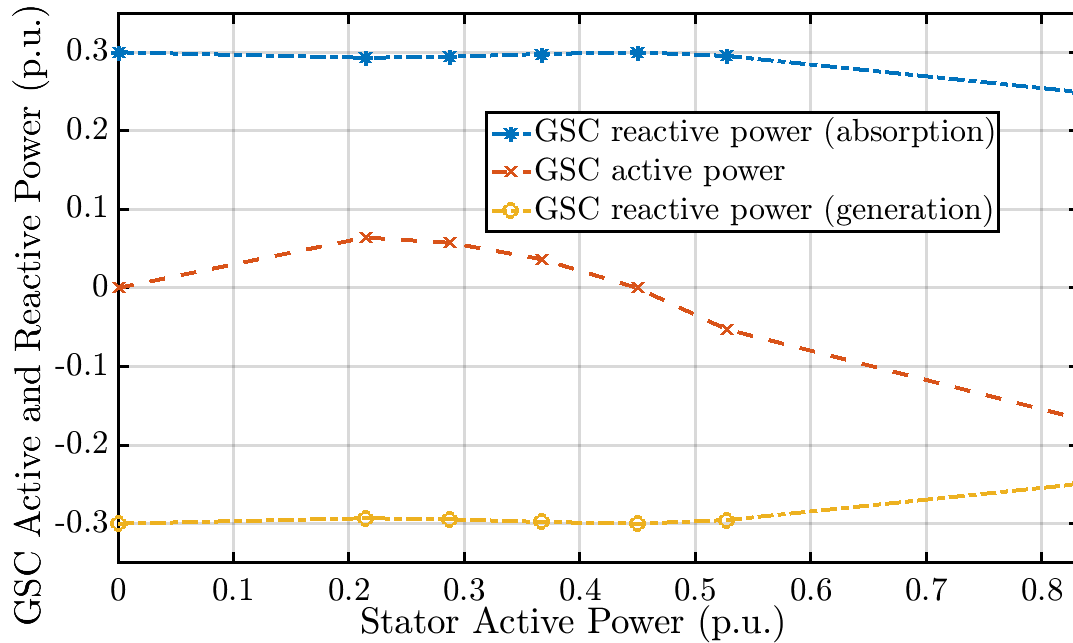


Figure 6.4: Active and reactive power variation of GSC as a function of active power generated from stator.

by,

$$Q_{GSC} = \sqrt{S_{GSC}^2 - P_r^2} = \sqrt{S_{GSC}^2 - s^2 P_s^2} \quad (6.13)$$

where S_{GSC} is the rating of the GSC and P_r is the active power fed from GSC converter is determined by the slip conditions. Figure 6.4 shows the active and reactive power variation of GSC as a function of active power generated from stator which is dependent on wind conditions.

6.1.1.5 Overall Capability Curve of DFIG Including GSC

Figure 6.5 illustrates the capability curve with a voltage limit of 0.35 p.u (includes 0.05p.u is the resistive and reactive drop) for 1.5MW GE WT [90] (operational limit of rotor voltage, not winding limit). From Figure 6.5 it can be seen that the reactive power generation from DFIG is generally limited by the rotor current limit and the reactive power absorption is limited by the stator current limit. The overall capability curve of DFIG considering GSC's reactive power ability is also shown in Figure 6.5. It

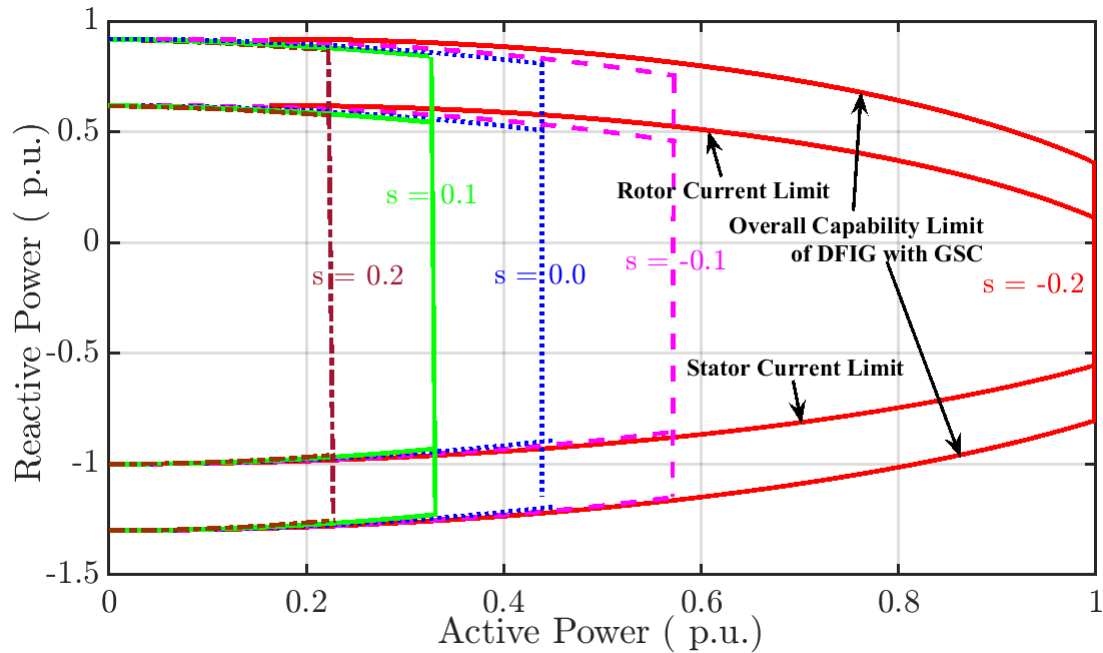


Figure 6.5: Overall Capability Curve of DFIG.

can be observed from Figure 6.5, that inclusion of GSC enhances the reactive power generation and absorption capability of DFIG system, when compared to Figure 6.3. From the above discussions, the following conclusions can be drawn:

- The limiting factor for the production of the reactive power will typically be the rotor current, as the required magnetizing reactive power is provided by the rotor current.
- The limiting factor for the absorption of the reactive power is the stator current, as reactive power absorption is mostly done through the stator windings.
- During dynamic conditions, when the rotor slip is large the reactive power production can be limited by the rotor voltage, but the pitch controller action can help avoid operating in such high slip operating point.
- The grid side converter can contribute to the reactive power production and absorption based on its rated capacity and the operating point of the WTG.

Table 6.1: Variation of Reactive Power Limits of DFIG with Various Slip and Loading Conditions

slip (p.u.)	Nominal	Reactive Power		Adjusted	Adjusted Reactive	
	Active Power (p.u.)	Limits (p.u.)		Active Power (p.u.)	Power Limits (p.u.)	
		Generation	Absorption		Generation	Absorption
0.2	0.225	0.867	-1.255	0.1	0.903	-1.29
0.1	0.325	0.841	-1.23	0.2	0.886	-1.27
0	0.445	0.803	-1.196	0.32	0.861	-1.25
-0.1	0.575	0.752	-1.15	0.45	0.825	-1.21
-0.15	0.795	0.646	-1.02	0.67	0.752	-1.10
-0.2	0.995	0.368	-0.809	0.87	0.563	-0.95

For the above mentioned cases the rotor circuit is operated under normal conditions. However, if the rotor is temporarily overloaded for a few seconds during grid dynamics, maximum up to 20%, it could provide additional network support [116]. If a PQ capability diagram for a wind farm at the connection point is required, the effect of step up transformer, wind farm grid and auxiliary equipment should also be taken into account.

Table 6.1 shows the changes in the reactive power capability limits of a 1.5 MW DFIG system for various loading conditions of DFIG under varying slip conditions. It can be seen that for an active power de-rating of 0.125 p.u, larger increments of reactive power limit can be obtained when the DFIG is operating at higher speed conditions. However, for lower speed conditions, it should be noted that larger reactive power limit is available. Thus it can be concluded that for all the slip conditions adjusting the active power provides better reactive power absorption or generation capability.

6.1.1.6 Online Computation of Reactive Power Limit

For online operation, the reactive power capability of the WTG is calculated every sample time based on the rotor current and voltage at each operating point. For

1. Get calculated v_{qs} , i_{qs} , i_{qr} and P_{st}^{*} , Q_{st}^{*}
2. Check if P_{st}^{*} is within allowed mechanical limits.
3. If yes: $P_{st}^{*} = P_{st}^{*}$ else set P_{st}^{*} to maximum or minimum limits calculated using machine rating (see Appendix D).
4. Compute Q_{st} limit based on (6.10) and (6.12).
5. Check if Q_{st}^{*} is within Q_{st} limit:
 If yes: $Q_{st}^{*} = Q_{st}^{*}$ and $flag = 0$
 else $Q_{st}^{*} = Q_{st}$ limit, $flag = 1$.
6. If $flag = 0, i_q^{*} = 0$, else $flag = 1$, set i_q limit based on (B.3) and (6.13).

Algorithm 1: Online dynamic reactive power estimation

this, first the stator current, rotor current and stator voltage is calculated or sensed. Then the maximum and minimum limits of the reactive power at that operating point are calculated. Then the reactive power of the WTG is estimated. Algorithm 1¹ illustrates the online dynamic reactive power capability estimation method.

6.1.2 Co-ordination Control Strategies for Extended Reactive Power Support

Based on the reactive power capability of the wind turbine (farm), in this work the proposed architecture co-ordinates the RSC control, GSC control and pitch control to effectively respond to the grid reactive power needs without violating the limits of the machine, which ensures the machine stability and longer operating lifetime. The coordination is based on a reactive power reference generation considering reactive power estimation discussed in the Section 6.1.1, and augmentation of Pitch control, RSC reactive power control and GSC reactive power control. Each of these is discussed next.

In the proposed control, the reactive power reference is generated using the adaptive

¹Note: The capability limits of DFIG in the work that follows is computed considering the stator and rotor current limits only as rotor voltage limits generally doesn't limit the capability of DFIG during normal operating conditions of DFIG. It is worth noting that the rotor voltage limits can be included if that is required for any other type of turbines. In this case (A.1) and discussion in Section 6.1.1.2 should be considered.

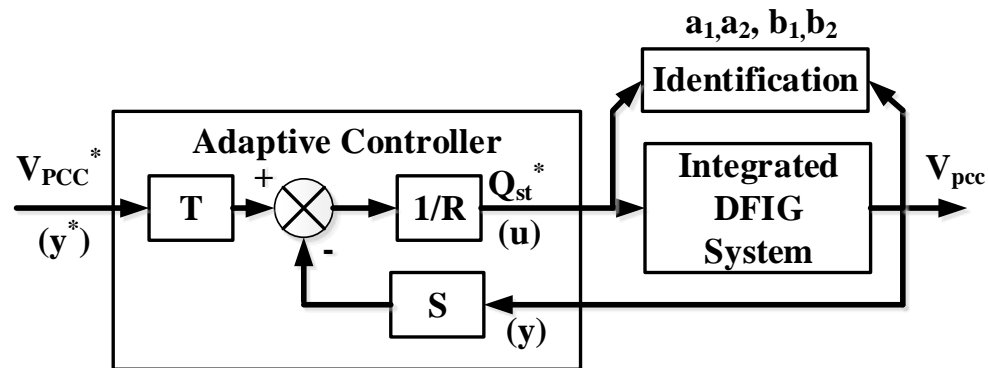


Figure 6.6: Block Diagram Representation of an Adaptive Controller.

control framework, instead of conventional PI control, as the reactive power to be generated should maintain certain PCC voltage depends on changing grid conditions and adaptive controller has been shown to perform better than PI controller under such conditions.

6.1.2.1 Reactive Power Reference Generation

From the previous discussions, it can be noted that generating a reference reactive power Q_{st}^* from the PCC voltage reference, V_{PCC}^* is extremely critical for coordinated control. For accomplishing this, an adaptive control architecture using a small signal model that can dynamically adjust and accurately generate Q_{st}^* based on the system changes is designed. The architecture is evolved from a Self-Tuning Regulator (STR) design [117, 118]. Figure 6.6 shows the basic block diagram of the proposed adaptive control, where the system to be controlled is the DFIG and control input is Q_{st}^* and system output is V_{PCC} . A RLS identification method [117, 118, 119, 100] is utilized for getting an online transfer function between input and output. The adaptive controller is a feedback controller that changes input Q_{st}^* to drive the system output towards the reference signal V_{PCC}^* or set point. Considering the identified transfer function is of second order the identified system can be represented in a time-series form modeled

as difference equation,

$$V_{PCC}(k) + a_1 V_{PCC}(k-1) + a_2 V_{PCC}(k-2) = b_1 Q_{st}^{*'}(k-1) + b_2 Q_{st}^{*'}(k-2) \quad (6.14)$$

where V_{PCC} is the PCC voltage at various time instants, $Q_{st}^{*'}$ is the input samples at the same time and a_1 , a_2 , b_1 and b_2 are identified coefficients using RLS. This can be represented as,

$$\frac{V_{PCC}(q^{-1})}{Q_{st}^{*'}(q^{-1})} = \frac{b_1 q^{-1} + b_2 q^{-2}}{1 + a_1 q^{-1} + a_2 q^{-2}} = \frac{B(q^{-1})}{A(q^{-1})} \quad (6.15)$$

where q^{-1} is the time shift operator. The open loop characteristic equation of the above relationship is

$$1 + a_1 q^{-1} + a_2 q^{-2} = 0 \quad (6.16)$$

From (6.16) the open loops poles can be derived using the online identification. Matching (6.16) with a desired second order transfer function with appropriate damping ratio and natural frequency, a pole shifting factor α ($0 \leq \alpha \leq 1$) can be derived where α is the ratio of open loop poles to the desired closed loop poles [100]. Then the overall closed loop characteristic equation can be written as,

$$(1 + \alpha q^{-1})(1 + a_1 \alpha q^{-1} + a_2 \alpha^2 q^{-2}) = 0 \quad (6.17)$$

The control architecture is evolved from STR where the structure of the closed loop system with control can be represented as (see Figure 6.6)

$$Q_{st}^{*'}(q^{-1}) = \frac{T(q^{-1})}{R(q^{-1})} V_{PCC}^*(q^{-1}) - \frac{S(q^{-1})}{R(q^{-1})} V_{PCC}(q^{-1}) \quad (6.18)$$

To obtain self-tuning regulator, it is assumed that

$$\begin{aligned}
 R(q^{-1}) &= (1 + q^{-1})(1 + r_1q^{-1}) \\
 S(q^{-1}) &= s_0 + s_1q^{-1} + s_2q^{-2} \\
 T(q^{-1}) &= s_0 + s_1 + s_2
 \end{aligned} \tag{6.19}$$

Using (6.15) and (6.18),

$$\frac{V_{PCC}(q^{-1})}{V_{PCC}^*(q^{-1})} = \frac{B(q^{-1})T(q^{-1})}{A(q^{-1})R(q^{-1}) + B(q^{-1})S(q^{-1})} \tag{6.20}$$

Comparing $A(q^{-1})R(q^{-1}) + B(q^{-1})S(q^{-1})$ using (6.19) with (6.17), it can be observed that,

$$\begin{aligned}
 r_1 + b_1s_0 &= 1 - a_1 + \alpha + a_1\alpha \\
 r_1(a_1 - 1) + b_1s_1 + b_2s_0 &= a_1 - a_2 + a_1\alpha^2 + a_2\alpha^2 \\
 r_1(a_2 - a_1) + b_1s_1 + b_1s_2 &= a_2 + a_2\alpha^3 \\
 -a_2r_1 + b_2s_2 &= 0
 \end{aligned} \tag{6.21}$$

Using (6.21) with pre-specified α and estimated a_1 , a_2 , b_1 and b_2 the four unknown parameters r_1 , s_0 , s_1 and s_2 can be easily computed. Further using (6.19) in (6.18), the control signal can be presented as,

$$Q_{st}^*(q^{-1}) = \frac{s_0 + s_1 + s_2}{(1 - q^{-1})(1 + r_1q^{-1})} V_{PCC}^*(q^{-1}) - \frac{s_0 + s_1q^{-1} + s_2q^{-2}}{(1 - q^{-1})(1 + r_1q^{-1})} V_{PCC}(q^{-1}) \tag{6.22}$$

Equation (6.22) can be compared to a conventional PID structure [117, 118, 119, 120]

which can be written as,

$$Q_{st}'(q^{-1}) = \frac{-T_s K_i}{(1 - q^{-1})(1 + r_1 q^{-1})} \{V_{PCC}^*(q^{-1}) - V_{PCC}(q^{-1})\} + K_p \{V_{PCC}^*(q^{-1}) - V_{PCC}(q^{-1})\} + \frac{K_d(1 - q^{-1})}{T_s(1 + r_1 q^{-1})} \{V_{PCC}^*(q^{-1}) - V_{PCC}(q^{-1})\} \quad (6.23)$$

Comparing (6.22) and (6.23),

$$\begin{aligned} K_p &= \frac{(s_1 + 2s_2)}{(1 + r_1)} \\ K_i &= \frac{-(s_0 + s_1 + s_2)}{T_s} \\ K_d &= T_s \left[\frac{r_1 s_1 - (1 - r_1) s_2}{1 + r_1} \right] \end{aligned} \quad (6.24)$$

As the focus is to self-tune the integral controller only, the value of K_d is kept at zero.

6.1.2.2 Controller Implementation Methodology

Initially for a step response, the values of a 's and b 's are estimated from an online identifier. From this, the open loop poles are calculated. The desired characteristic equation is set based on 10% overshoot and 0.6 damping ratio. From which the pole shifting factor is calculated. For the proposed design, the pole shifting factor is designed as 0.98 for a sampling period of 1ms. Using (6.21) with pre-specified α and with estimated the four unknown parameters r_1 , s_0 , s_1 and s_2 can be computed. K_p and K_i is then computed online using (6.24).

6.1.3 Proposed Controller Augmentation for RSC and GSC

In this approach, first the dynamic reactive power calculation is used to augment RSC voltage controller and to regulate the stator reactive power. During this whole operation, the reactive power reference $i_q^* = 0$ for GSC. Then, depending on the RSC limitation, the algorithm determines the limits for GSC. Further, the GSC augmen-

tation loop is activated (See Algorithm 1).

6.1.3.1 Proposed RSC Voltage Controller Augmentation

The augmentation is based on calculating a P-V droop and machine dynamic loading. In order to establish a P-V droop, for a particular ΔV_{PCC} , i_{qr} should be reduced by adding a value of $K_{qr}\Delta V_{PCC}$ to P_{st}^* which can then increase the reactive power limit the machine can supply. As the reactive power limit is extended, the reactive power that can be supplied by staying within the machine limits increases, thus increasing the effectiveness of voltage control. It is also worth noting that for a small duration the limit (short term machine limits) of the reactive power can be set 20% more than the machine capability. Figure 6.7 further illustrates this effect. It can be seen that during a voltage sag, the active power can be reduced, and additional reactive power margin can be obtained if the operating point is moved from A to B thus improving the grid voltage. The drop in active power can be calculated as a P-V droop, and increment in reactive power can be obtained using the adaptive PI controller (please refer to Section 6.1.2.1 for further details). A reactive power augmentation can be initiated based on this. In this illustration, we could achieve 34% increase in reactive power capability for a 19% reduction in active power. For calculating the P-V droop coefficient, the power droop was designed to be 8% considering the maximum machine contribution that ensures system stability.

6.1.3.2 Proposed GSC Voltage Control Augmentation

In this augmentation, when rotor current reaches to its limits and system needs more reactive power, GSC controller is activated turning on the flag (see Algorithm 1). The PI controller design for the outer loop then generates the required i_q^* and coordinated with the GSC inner loop to generate additional reactive power required. The proposed tuned PI controller parameters are shown in Appendix. The proposed controller has the following properties:

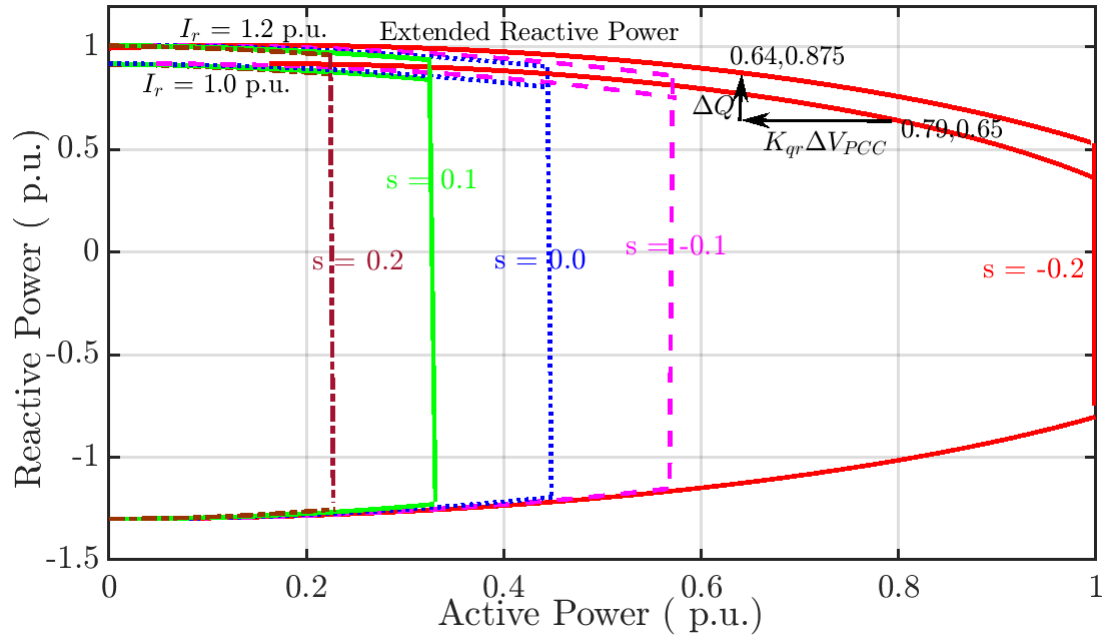


Figure 6.7: Extended Reactive Power Capability using Droop Constant (GSC included).

- Avoids the risk of circulating current flows between stator and GSC by separating the GSC activation if system requires more reactive power and rotor current reaches its maximum value I_r^{max} .
- Providing two time-scale control architecture; using RSC as a default controller for its first response and GSC acting as a supplementary controller.

6.1.4 Proposed Pitch Control Augmentation

It is worth noting that proposed RSC and GSC augmentation without mechanical power control may result in increased rotor oscillation, thus stressing mechanical parts of DFIG. In order to mitigate this adverse effect, a pitch angle augmentation methodology is included such that the mechanical power input to DFIG is limited by adjusting the pitch angle. It is worth noting that rotor speed oscillations can occur if mechanical and electrical torque is not synchronized. Synchronization is accomplished by de-rating the mechanical torque by adding a component of pitch based droop constant $K_v \Delta V_{PCC}$ with existing pitch angle β textcoloredfig. 2.i. The

mechanical power, in watts, developed by the wind turbine at any given wind velocity, v_w [m/s] is

$$P_m = \frac{1}{2} \rho \cdot A \cdot C_p(\lambda, \beta) \cdot v_w^3 \quad (6.25)$$

where ρ is the density of air, and A is the area swept by the turbine. λ is the ratio of the turbine blade tip speed and wind speed and is known as the tip speed ratio. Assuming at particular operating point for small duration, keeping constant v_w and turbine speed, linearizing P_m with respect to β ,

$$\Delta P_m = \left. \frac{\partial P_m}{\partial \beta} \right|_{\substack{\lambda=\lambda_{REF} \\ \beta=\beta_{REF}}} \quad (6.26)$$

At steady state conditions, $P_{st} = \frac{P_m}{1-s}$ which means $\Delta P_s = K_s \Delta P_m$ where K_s is the slip dependent constant term. From (6.26), it can be seen that $\Delta P_{st} = K_s K_\beta \Delta \beta$ as $K_{qr} = \frac{\Delta P_{st}}{\Delta V_{PCC}}$. This implies $\Delta \beta = \frac{\Delta V_{PCC} K_{qr}}{K_s K_\beta} = K_v \Delta V_{PCC}$ from which $K_v = \frac{K_{qr}}{K_s K_\beta}$. Please refer to [120, 121] for more details.

The overall flowchart of the proposed online operational mode adaptive and dynamic reactive power augmented controllers along with pitch control is shown in Figure 6.8. The self-tuning augmented dynamic controller provides a) voltage balancing at the PCC during voltage frequency changes in the grid b) reactive power reference for the proposed RSC controller c) seamless augmentation of RSC and GSC controller.

6.1.5 Implementation Test on Interconnected Power Grid

The proposed architecture is tested on two systems for interconnection studies; a) Kundur's two-area test system [122] which is used to study the capability of the adaptive PI controller to generate appropriate reactive power reference to reduce V_{PCC} dynamics and b) an IEEE 68 bus power grid [3] used to study the capability of the proposed controllers coordination features.

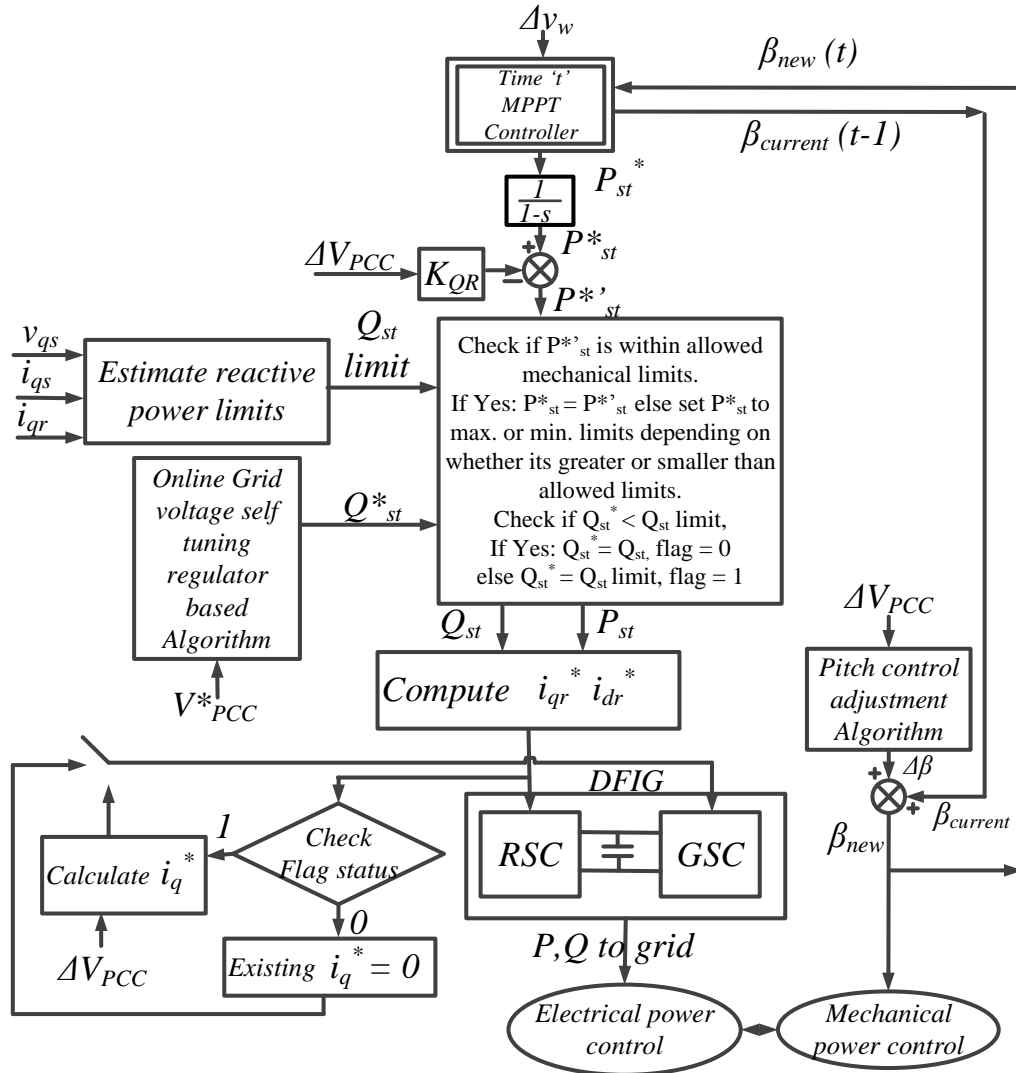


Figure 6.8: Overall Controller Design Flowchart.

6.1.5.1 Study of Kundur Two Area Power System

This system consists of two areas containing two 900 MVA synchronous generators each connected by weak tie lines. The overall system is modified with one aggregated wind farm (see Figure 6.9). The wind farm has 20 1.5 MW GE wind turbines. The total wind farm output is thus 30 MW at bus 14 and is balanced by equivalent load. For assessing the performance of the PI controller two case studies are performed. 1) Three phase to ground fault study, and 2) Low voltage study. The

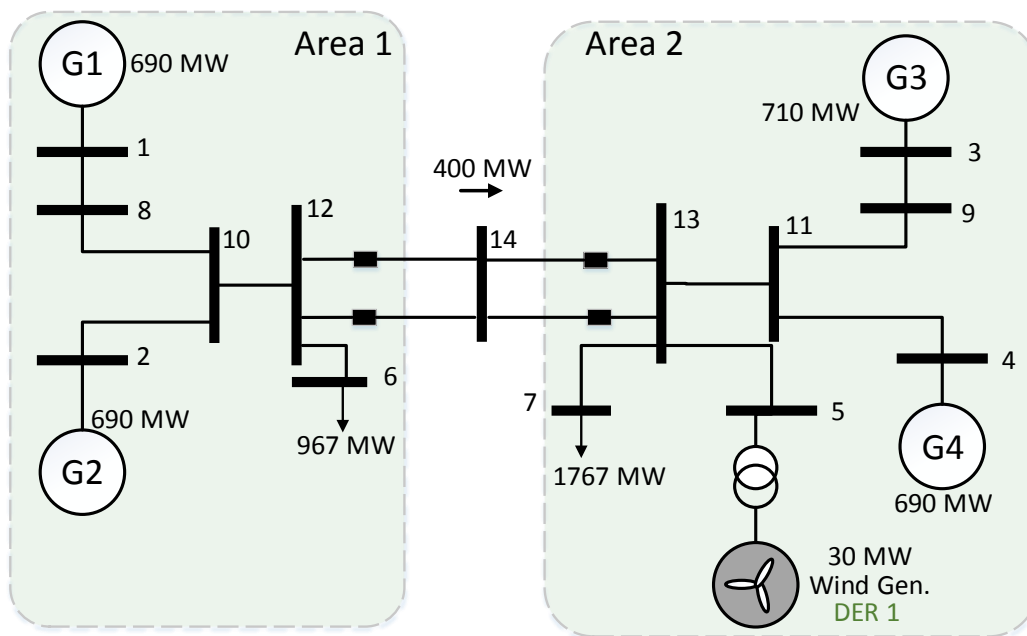


Figure 6.9: Kundur Two Area Four Machine Test System.

tests on Kundur Two area system compares the performance of a) proposed controller with self-tuning regulator when active power de-rating is considered (with droop) b) Proposed controller with self-tuning regulator when active power de-rating is not considered (without droop) and c) Conventional voltage controller. For the proposed controller, the reactive power limits are determined online based on the operating condition as mentioned before.

6.1.5.2 Three Phase to Ground Fault

In this study, a 3 phase ground fault is created at 3 sec for the duration of 0.1 sec at bus 14. Figure 6.10 shows the used wind profile for this study. The improvement of PCC bus voltage (bus 5) is shown in Figure 6.11. Figure 6.11 compares the performance of conventional PI based controller with proposed STR based droop and no droop control. It can be seen from Figure 6.11, that the proposed form of controller has faster recovery action and less voltage overshoot after grid fault conditions.

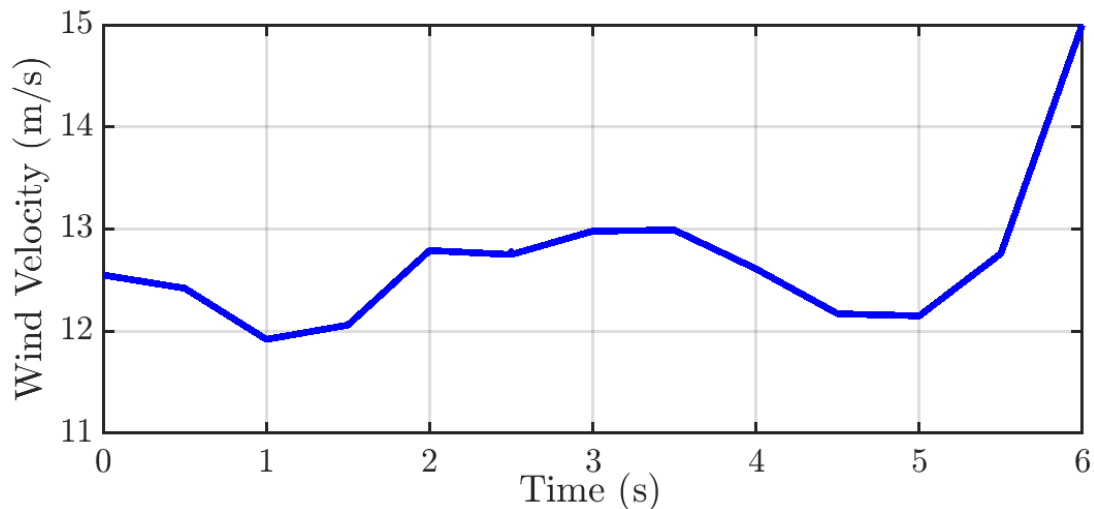


Figure 6.10: Wind Speed Profile Used .

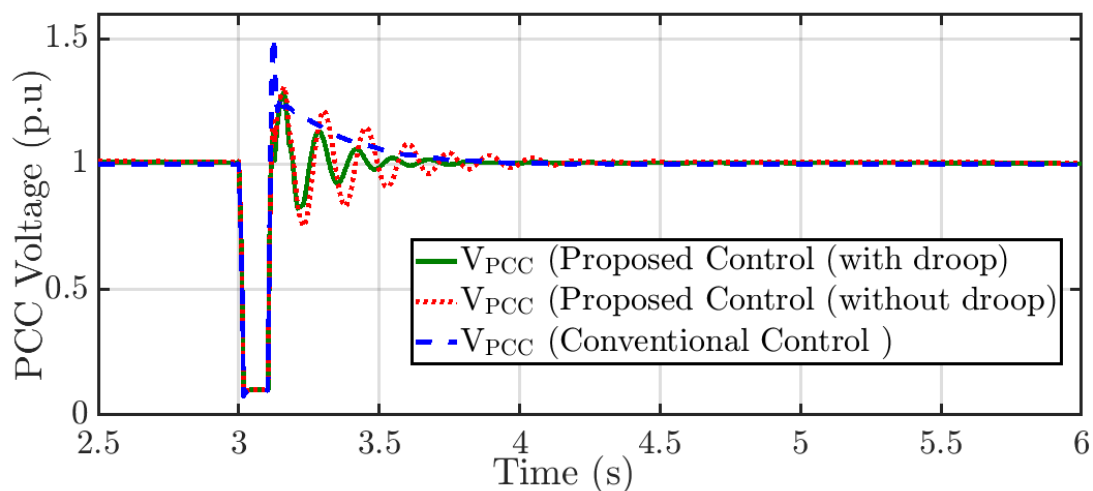


Figure 6.11: PCC Voltage During Three phase Ground Fault.

6.1.5.3 Grid Voltage Sag Study

In this study, a low voltage condition was created at PCC at 3s, continuing up to 0.2 s by using reactive sink at PCC bus. A comparison between a) Existing voltage control b) Proposed controller and c) Proposed controller with GSC reactive power support deactivated is demonstrated. Figure 6.12 shows the overall contribution of the proposed architecture compared to conventional PI controller, whereas fig. 15(b) shows injected reactive power to the grid.

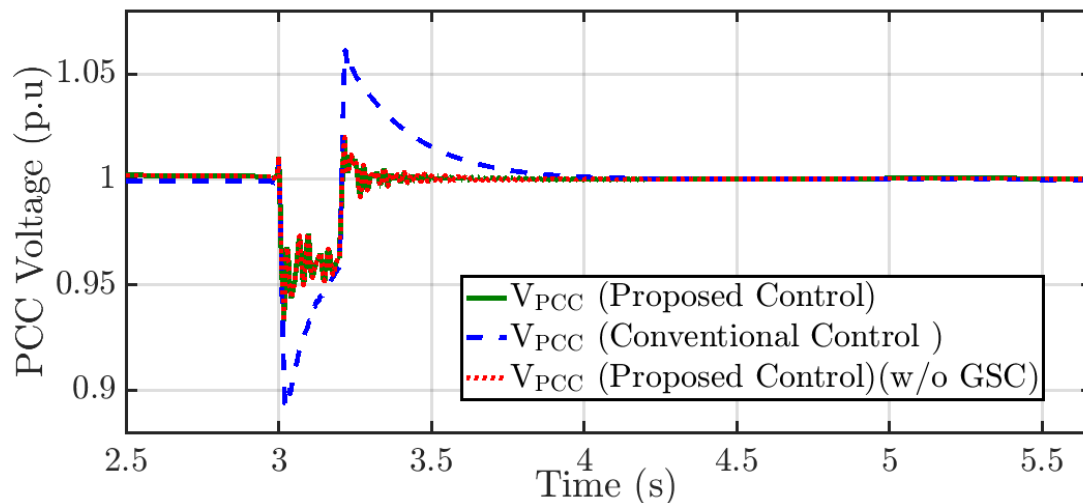


Figure 6.12: PCC Voltage During Voltage Sag.

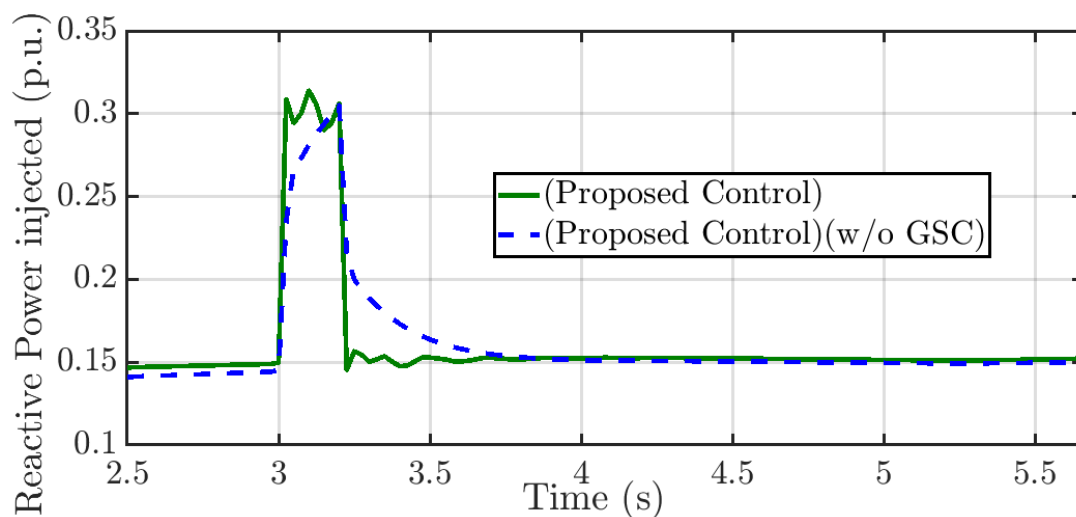


Figure 6.13: Reactive Power Support Using Proposed Technique During Voltage Sag.

6.1.5.4 Test on IEEE 68 bus Power Grid

For evaluating the performance of the controllers connected as a part of the grid, IEEE 68 bus, 16-machine, 5-area system is considered [3]. In this study, all the conventional generators are provided with PSS and exciters, for improved damping of local modes of oscillation and stabilize otherwise unstable open-loop system. The overall system is modified with one aggregated wind farm, where bus 13 is the slack bus (see Figure 6.14). The wind farm has 100 nos. of 1.5 MW wind turbines. The

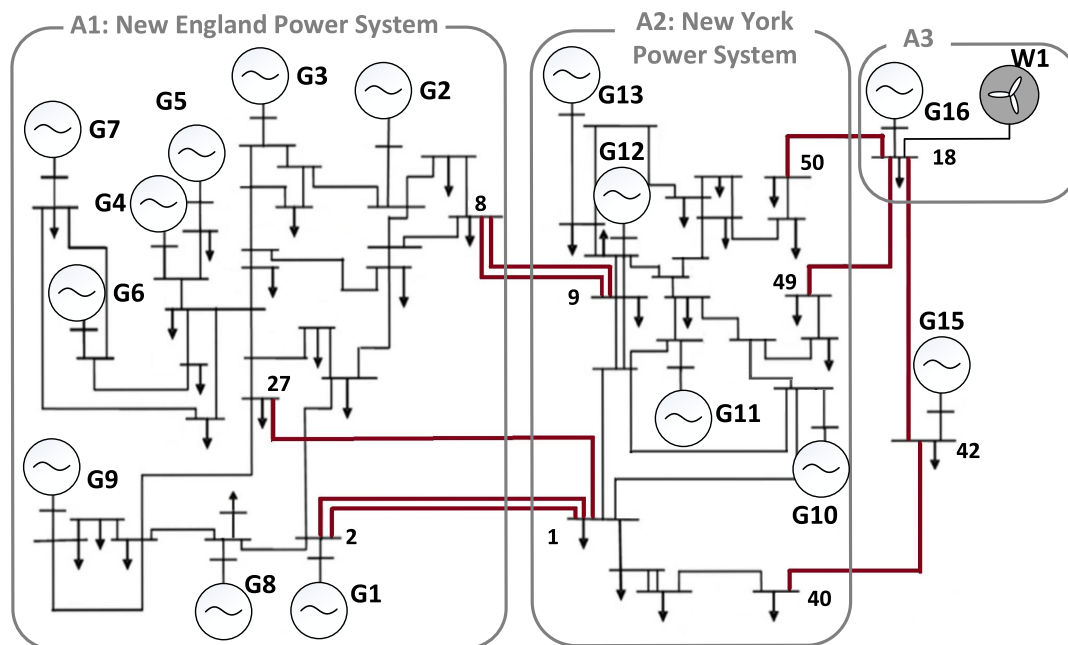


Figure 6.14: One Line Diagram of the 68 Bus System [3].

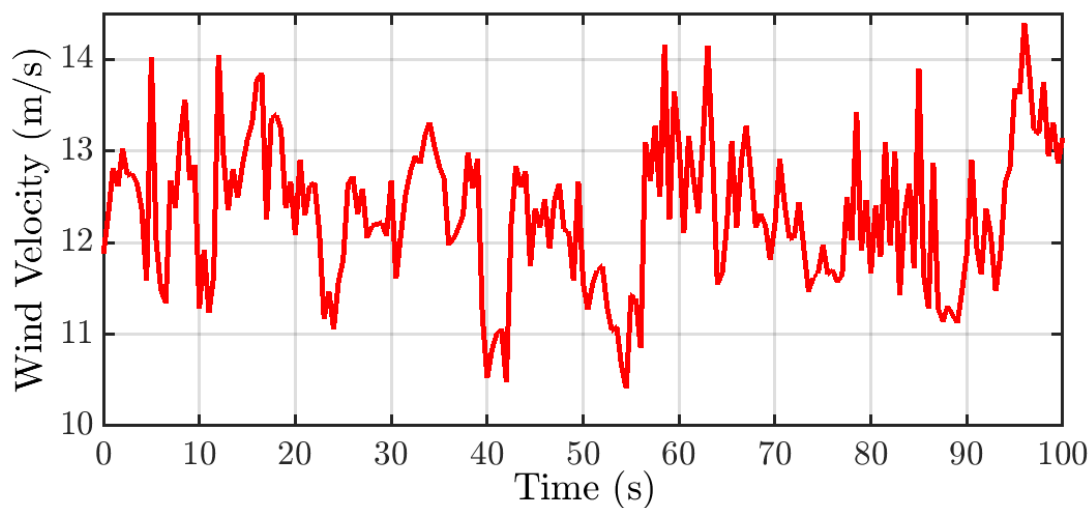


Figure 6.15: Wind Speed (v_w) used for the Case Study.

nonlinear dynamic models of the turbine including the converter dynamics is modeled using Dig-Silent Power Factory[®] [115]. The total wind farm output is thus 107.385 MW at bus 38 contributing to 0.6% penetration with base wind speed of 12m/s. In order to evaluate the performance of the wind farms, the existing exciters and PSS had been removed from generator 16. For balancing the system operation, an

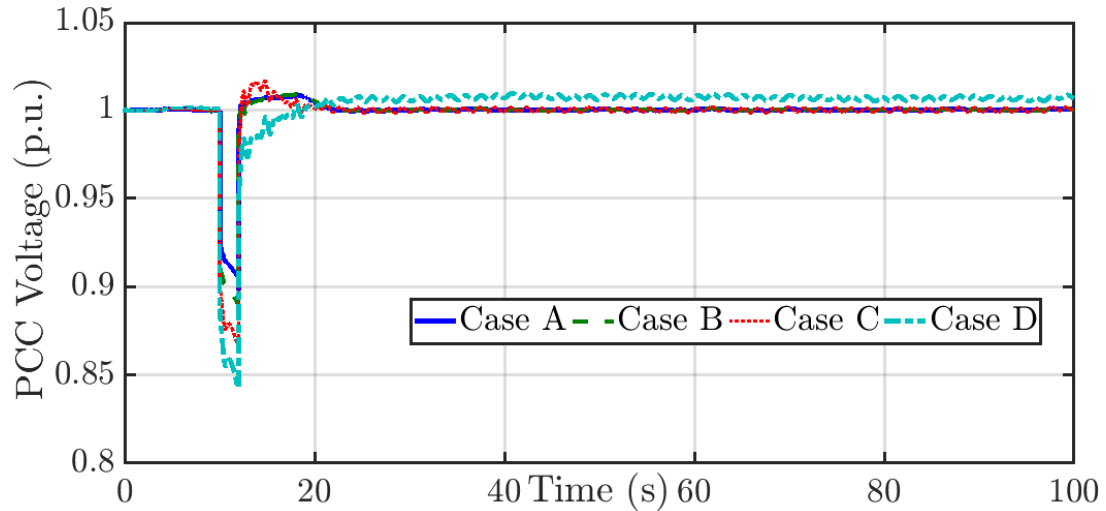


Figure 6.16: PCC Voltage Recovery on 68 Bus System through use of DFIG based Windfarm.

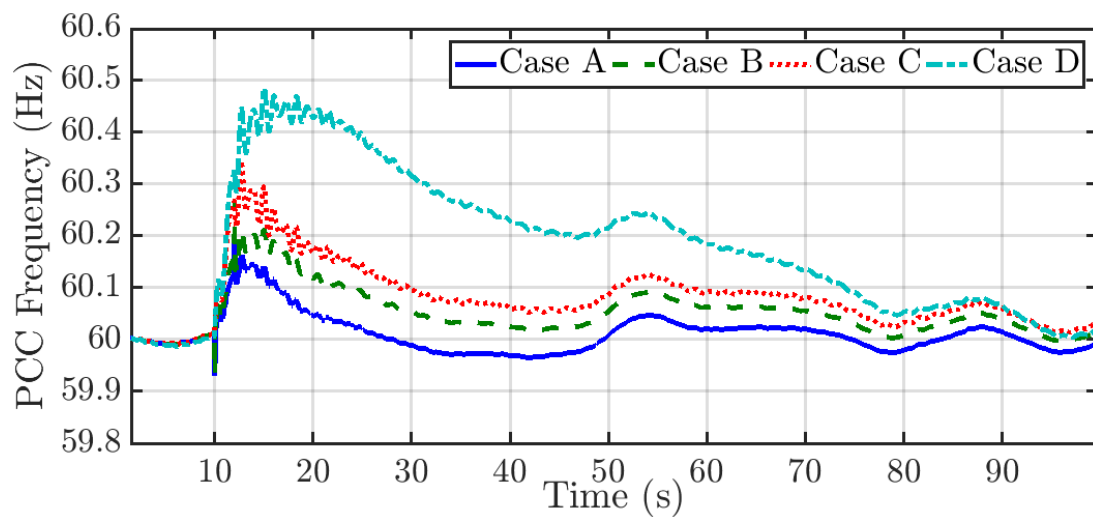


Figure 6.17: PCC Frequency on Windfarm bus.

Table 6.2: Wind Farm Interconnected Grid Details (MW)

	Synchronous Generator	Wind Farm	Load
Power	18408	107	17612

equivalent aggregated load of 107.385 MW has been added to the PCC. Table 6.2 shows the details of the interconnected grid. Table 6.3 shows the different control test comparisons for analysis. For the case studies, the real wind speed profile (v_w) [97] is used as shown in Figure 6.15.

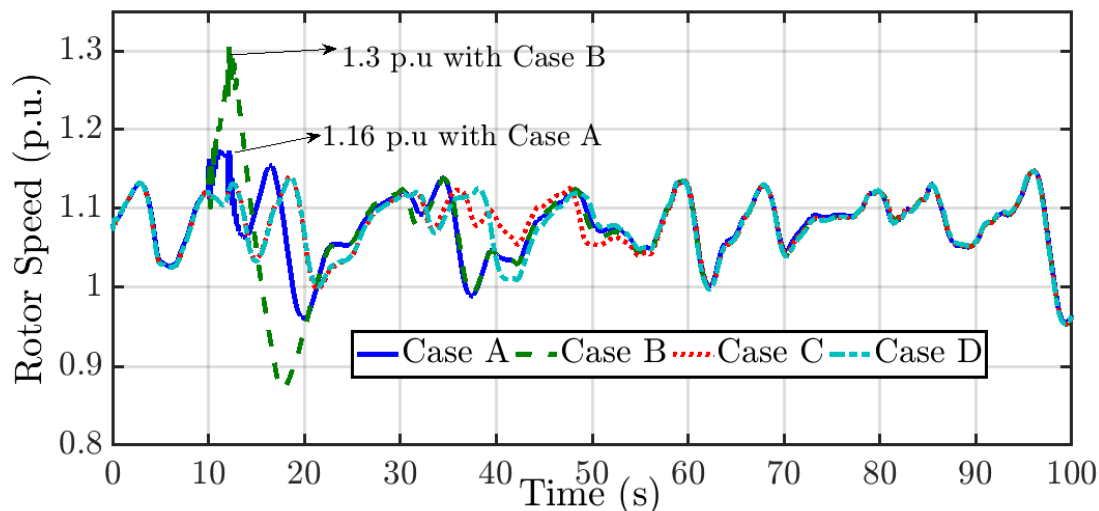


Figure 6.18: Rotor Speed of DFIG.

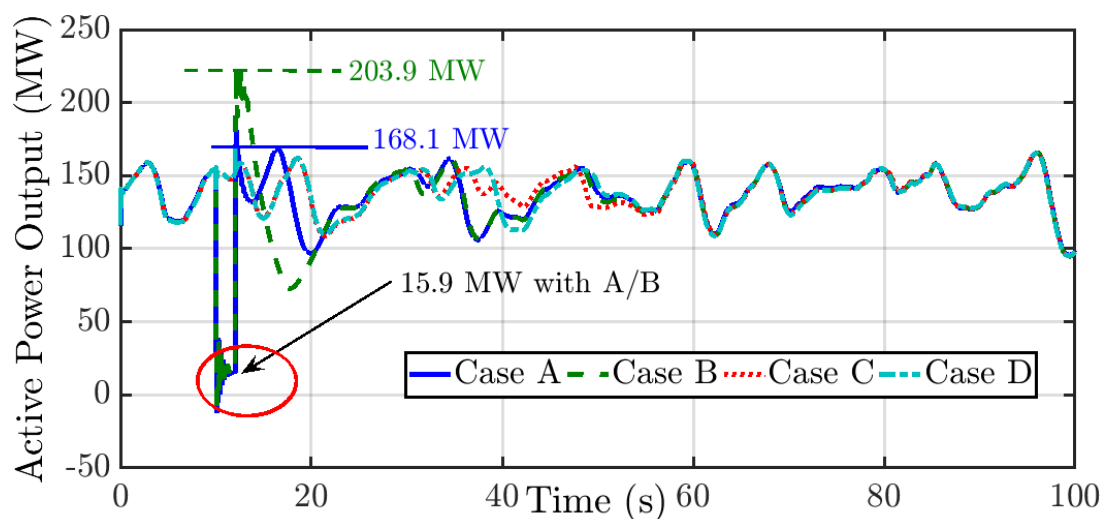


Figure 6.19: Active Power Support from DFIG.

Table 6.3: Different Control Cases Considered

Controller	Description
Case A	Proposed Controller: Full co-ordination ON
Case B	Proposed Controller: GSC and Pitch Control co-ordination OFF
Case C	Existing Voltage Controller
Case D	Existing power factor (pf) controller

6.1.5.5 Results and Discussion

To assess the performance of proposed controller with existing controller a low voltage condition was created at PCC at 10s, continuing up to 12 s by introducing

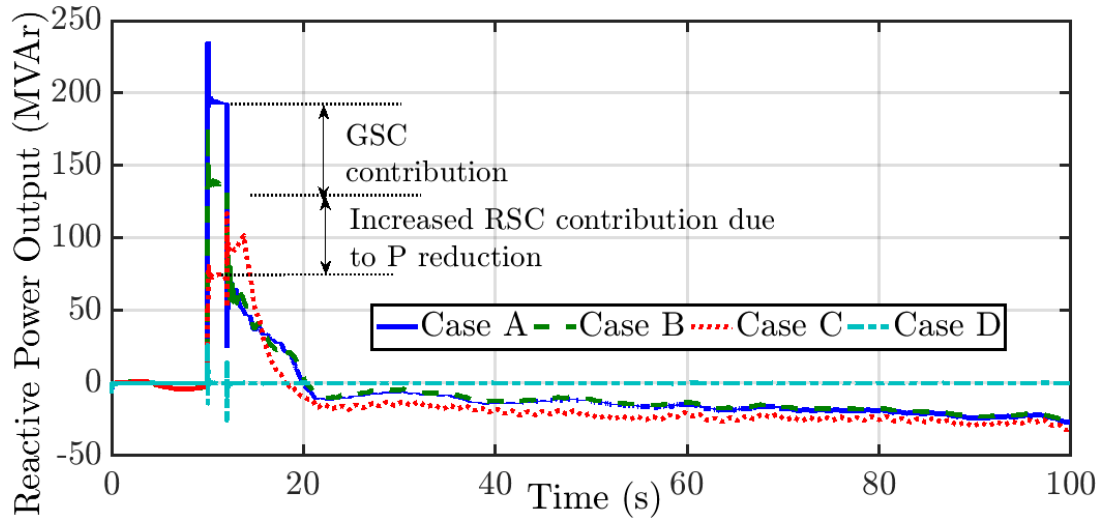


Figure 6.20: Reactive Power Support from DFIG.

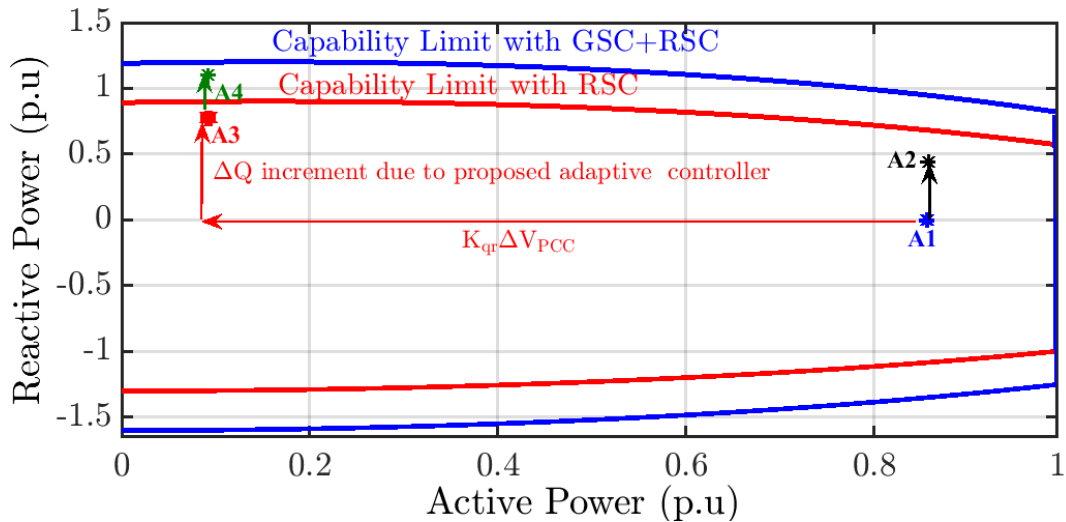


Figure 6.21: PQ plot of Individual WT of Windfarm for the above cases.

Table 6.4: Comparison of Performance of Proposed Control Technique with Conventional Voltage Control Technique.

Conditions	Conventional Control	Proposed Control
Voltage Sag (p.u.)	(10-20)% improvement	(35-45)% improvement
Frequency Deviation (Hz)	(25-35)% improvement	(60-70)% improvement

reactive sink at PCC bus. Figure 6.16 shows the overall contribution of proposed control for improvement of PCC bus voltage; whereas Figure 6.17 shows comparisons of frequency dynamics with the proposed control architectures. It can be seen that

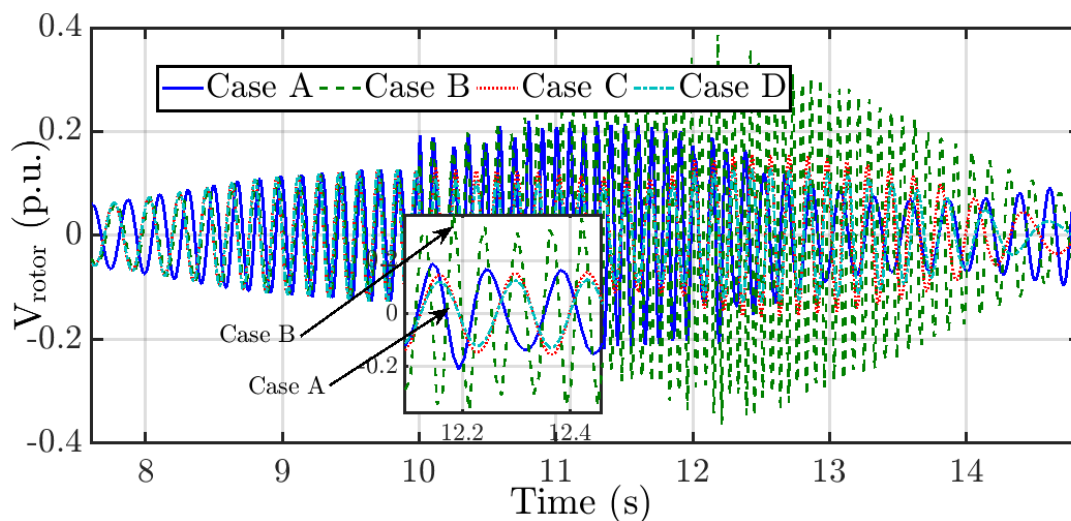


Figure 6.22: Rotor Voltage Dynamics.

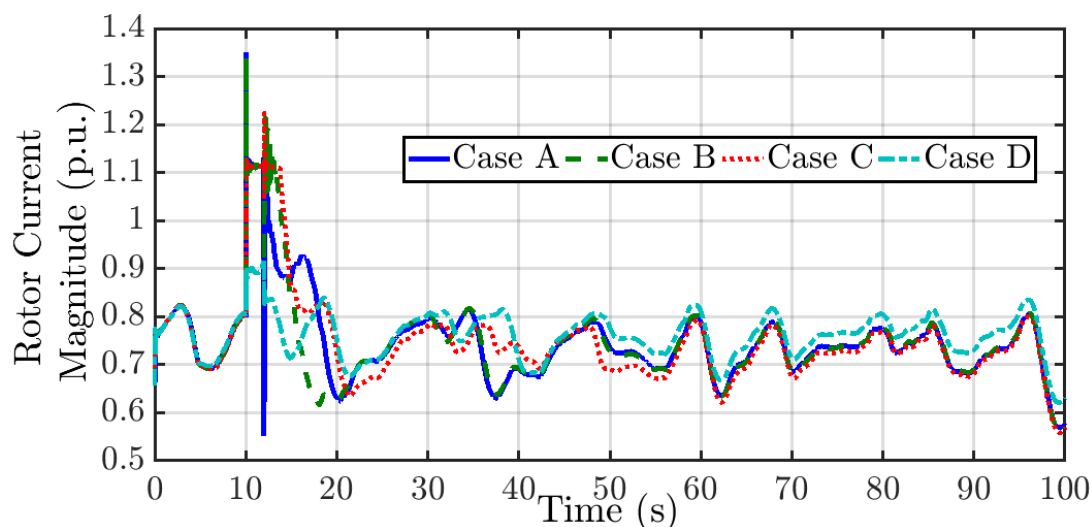


Figure 6.23: Rotor Current Dynamics.

with the proposed controller, the grid voltage recovery is better and the frequency deviation is less. Table 6.4 tabulates the performance of proposed control when compare to existing controller. Figure 6.18 illustrates rotor speed comparison. It can be seen that the proposed architecture controls the rotor speed to maintain the frequency response. The spike in rotor speed with case B is due to the reduction of active power without limiting the mechanical power. With the mechanical power controlled, the rotor speed spike is reduced (see case A). It can be noticed from

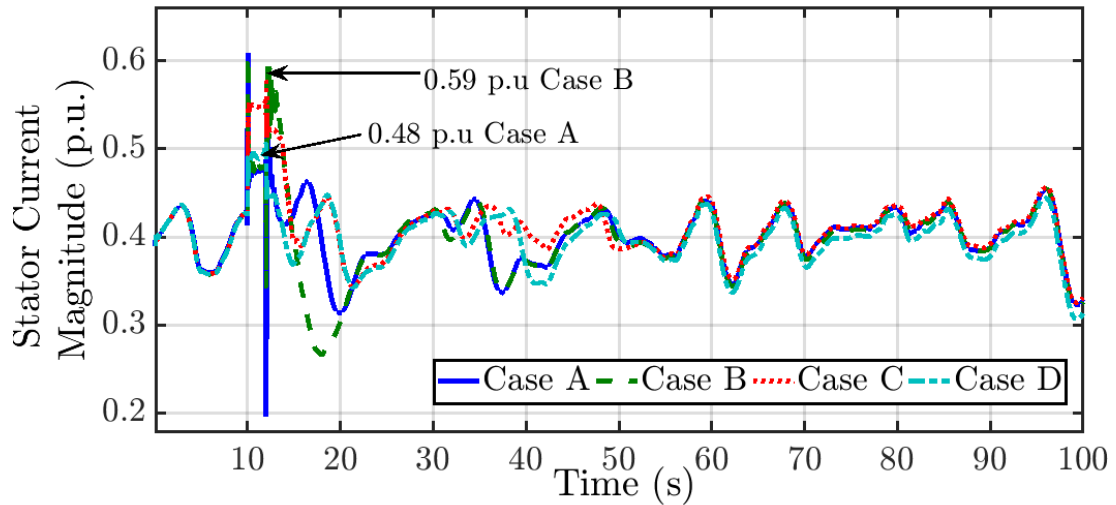


Figure 6.24: Stator Current Dynamics.

Figure 6.19 and 6.20 that the methodologies have provided effective control of active and reactive power so that the grid voltage profile is improved and the active power contribution is within the limit. The contribution of GSC and pitch coordination is also shown (case A compared to case B) where the active power limit is beyond the rated value (203.9 MW for a 150 MW WF capacity). Figure 6.21 shows the changes in machine operating points from the initial conditions for various controllers. Point ‘A1’ is the initial operating point, whereas point ‘A2’ shows the operating point for voltage control, point ‘A4’ shows the new operating point with proposed controller case A and point ‘A3’ shows the operating point if GSC control is shut down.

Further, Figure 6.22 illustrates how the proposed architecture limits rotor over-voltages. Figure 6.23 and Figure 6.24 show the rotor current and stator current dynamics respectively. It can be noted that the best performance is achieved with the proposed architecture in Case A. It is worth noting that the overall control performance can be maximized if GSC and mechanical power co-ordination is performed simultaneously.

6.2 Chapter Summary

In this chapter, a dynamic reactive power estimation based transient voltage control for grid integrated DFIG by coordinating RSC, GSC and pitch control is proposed. The proposed architecture calculates a reference reactive power and required active power using the designed adaptive controller and P-V droop controller respectively during transient voltage changes. Then a dynamic reactive power estimation algorithm evaluates the machine limits and operating conditions to ensure that maximum reactive power support is achieved. Based on this, the existing machine and pitch controllers are coordinated. The test results with professional grade nonlinear simulator considering practical GE 1.5 MW system parameters show that, when compared to the existing DFIG control methodologies, the approach provides at an average 20-30% improvement in voltage support and ensures maximum reactive power support without violating machine limits.

CHAPTER 7: CONTROL OF LARGE SCALE DFIG TO PROVIDE ACTIVE POWER SUPPORT TO BULK POWER GRID

In this chapter, the use of DFIG based wind farms to provide active power support to power grid and damp the system electromechanical oscillations is studied. Electromechanical oscillations often arise between areas in large inter-connected power grids due to dynamic interaction of large group of generators connected through relatively weak interconnections [123]. With the rise in the wind farm penetration level in power grid, it is essential to study and understand the effect of these newer generation sources on the system electromechanical modes of oscillation. The first section in this chapter deals about the study of low frequency electromechanical mode of a test system when the penetration of wind farm in the bulk power grid changes and when the system active power loading changes at different wind farm penetration. Once the impact of wind farm penetration on bulk power grid is studied, a system oscillation damping controller based on system identification is proposed in second section.

In the second section, a novel multi-channel RLS identification based adaptive WADC has been proposed for DER integrated bulk power grid. In this chapter, RLS technique is used for system identification, as opposed to the block processing algorithm [124], as RLS does not require fixed memory allocation making it more suitable for online applications. In this method, the MIMO transfer function model of the system is identified using autoregressive exogenous (ARX) model structure based on ring-down data obtained using measurements. Then a oscillation damping controller based on minimum variance control (MVC) architecture is designed using the transfer function model and is used to augment with the local controller (LC) of

the DER. The advantage of the MVC control is that it looks certain steps ahead in the future and regulates the system output as close as possible to the desired set-point with minimum variance which is dependent on identification error and process noise. The effectiveness of proposed method is demonstrated by case studies on a two area four machine system.

The major advantages of the proposed approach are:

- The controller is based on the online identification of the system dynamics which results in adjusting the controller output as the system operating condition changes.
- The controller is independent of the network topology and only requires WAMs for identification and control.
- The proposed controller can be augmented with the existing LC in the DER.
- The proposed controller adapts to variety operating condition and can consider the complete order of identified system model as opposed to considering the mode with highest residue which can lead to improper design of damping controller causing sustained oscillation in the system as shown in [4].

7.1 Impact Study of Wind Farm penetration on a test power grid

In this section, a small signal stability study of two-area four generator system is presented at different operating condition with different penetration level of the wind energy. The electromechanical modes were computed over a range of operating conditions using both the linearized models and detailed time domain simulation models. The linearized models were studied using small signal stability analysis toolbox (SSAT) of DSA Tools and the time domain simulation was performed using PSCAD EMTP software, which validates the result obtained from modal analysis. The modal characteristics of the system, when the production from synchronous machine is reduced as the power output from wind farm increases is studied. The test system is

shown in Figure 7.1. This is a test system developed in [122] to demonstrate the modal characteristics in larger and complex power grids. The test system consists of Area 1 and Area 2 with each area consisting of two equivalent synchronous generators. The wind farm modeled by an equivalent DFIG wind turbine system is connected in either Area 1 or Area 2. The test system is suitable for preliminary analysis related to small signal stability behavior of a large scale power grid. The aggregated model of wind farm by a single turbine generator system provides a reasonable amount of accuracy as the impedance of a typical collector system is relatively small as compared to the impedance of the unit transformer [123].

The wind farm was scaled from 0% to 40% of total generation in one particular area. The synchronous machines are modeled using ‘GENROU’ model and is equipped with power system stabilizer ‘STAB1’, Governor model ‘TGOV1’ and excitation system ‘ESAC4A’. The wind farm is modeled using Turbine model ‘WT3T1’, pitch controller model ‘WT3P1’, generator model ‘WT3G2’ and converter control model ‘WT3E1’. The loads are modeled as constant impedance loads.

Penetration Level defined here is based on the total power generation from wind farm when compared to the total generation by the wind farm and the synchronous machine it is displacing. i.e.

$$\text{Penetration level} = \frac{\text{Wind Generation}}{\text{Wind Generation} + \text{Synchronous Machine Generation}} * 100\% \quad (7.1)$$

The test system was analyzed at different operating conditions as described below:

7.1.1 Case 1: Wind Generator in Area 1

It was assumed that the total generation capacity of wind farm in the system was 525 MW and the power output of the wind farm varies from 0 MW to the maximum of 525 MW. When the power from the wind farm, which is connected a bus 5 in area 1 is increased, the power output of the equivalent generator ‘G1’ is proportionally

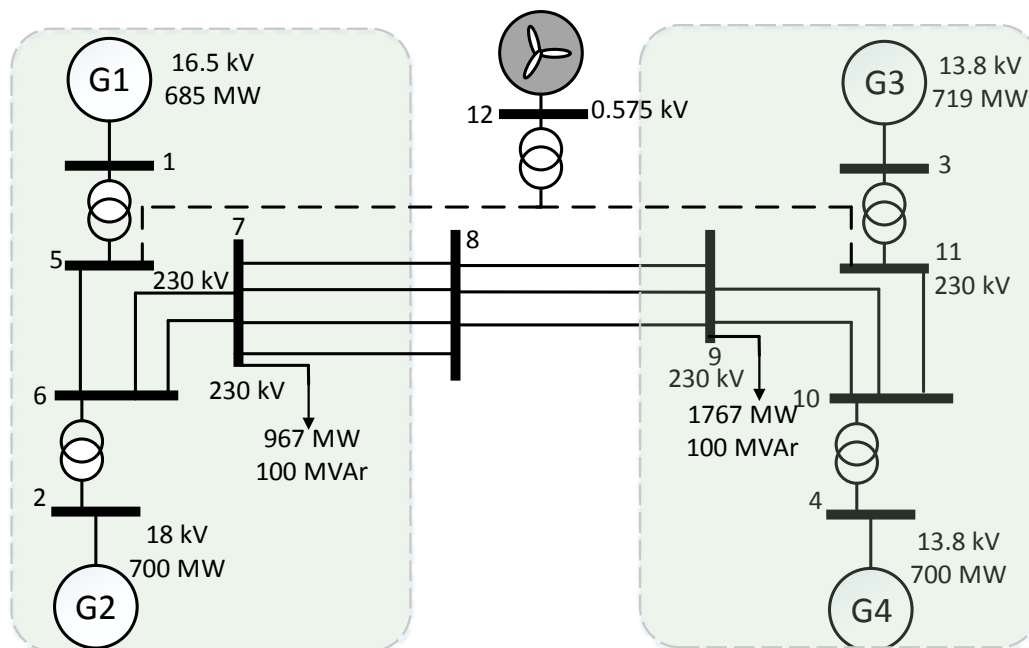


Figure 7.1: Five Generator Two Area Test System.

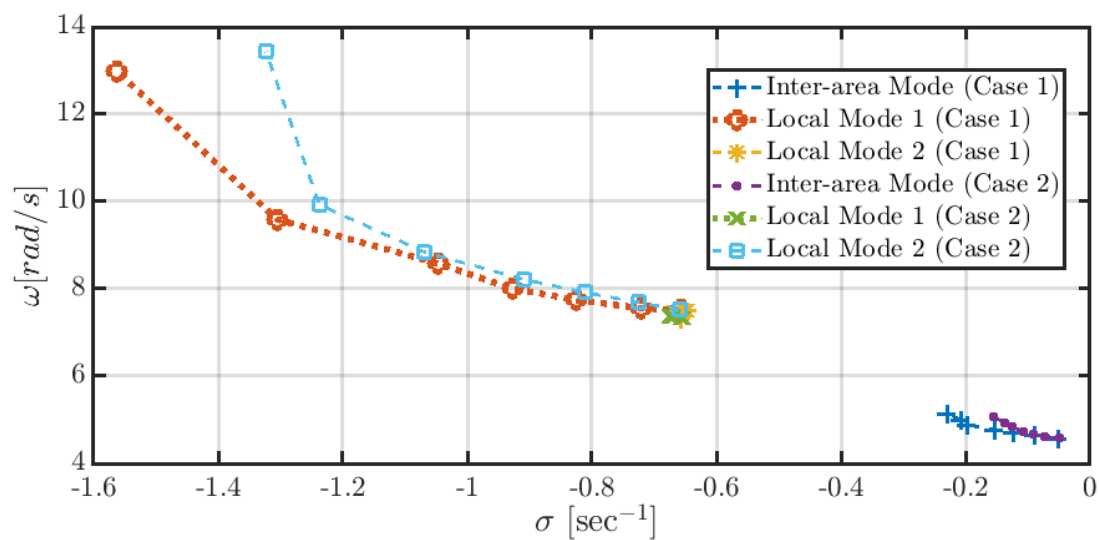


Figure 7.2: Locus of Inter-area mode and Local Mode at Different Penetration Level of Renewable Energy Resources.

decreased along with its equivalent inertia. This is done so as to make sure that the tie-line power flow does not change. The locus of the inter-area mode and the local mode is then traced at various power output of the wind farm.

Table 7.1: Inter-area Modes at different penetration level of Wind Farm

Penetration Level	Real Part	Imaginary Part	Frequency (Hz)	Damping (%)
Case 1				
0	-0.0520	4.5701	0.7274	1.13
10	-0.0896	4.6328	0.7373	1.93
20	-0.1234	4.6992	0.7479	2.62
30	-0.1524	4.7690	0.7590	3.19
45	-0.1855	4.8788	0.7765	3.80
60	-0.2076	4.9919	0.7945	4.15
80	-0.2284	5.1405	0.8181	4.43
Case 2				
0	-0.0500	4.5736	0.7279	1.09
10	-0.0723	4.6232	0.7358	1.56
20	-0.0911	4.6785	0.7446	1.94
30	-0.1070	4.7392	0.7543	2.25
45	-0.1242	4.8339	0.7693	2.56
60	-0.1364	4.9333	0.7852	2.76
80	-0.1551	5.0614	0.8055	3.06

Table 7.2: Local Mode 1 at different penetration level of Wind Farm

Penetration Level	Real Part	Imaginary Part	Frequency (Hz)	Damping (%)
Case 1				
0	-0.6563	7.5211	1.1970	8.70
10	-0.7206	7.5581	1.2029	9.50
20	-0.8249	7.7436	1.2324	10.60
30	-0.9270	8.0055	1.2741	11.50
45	-1.0479	8.5852	1.3664	12.11
60	-1.3052	9.5926	1.5267	13.48
80	-1.5622	12.9715	2.0645	11.96
Case 2				
0	-0.6555	7.3312	1.1668	8.90
10	-0.6704	7.3519	1.1701	9.08
20	-0.6726	7.3611	1.1716	9.10
30	-0.6728	7.3660	1.1723	9.09
45	-0.6729	7.3693	1.1729	9.09
60	-0.6730	7.3709	1.1731	9.09
80	-0.6732	7.3719	1.1733	9.09

7.1.2 Case 2: Wind Generator in Area 2

It was assumed that the total generation capacity of wind farm in the system was 525 MW and the power output of the wind farm varies from 0 MW to the maximum of 525 MW. When the power from the wind farm, which is connected a bus 11 in area 2 is increased, the power output of the equivalent generator 'G3' is proportionally decreased along with its equivalent inertia. This is done so as to make sure that the tie-line power flow does not change. The locus of the inter-area mode and the local mode is then traced at various power output of the wind farm.

The result for locus of inter-area mode and local mode for these two cases is shown in Figure 7.2. The results show that the inter-area mode becomes more stable as the penetration of wind generator in either area increases. Note that in both the cases the effect brought about by the increased penetration of wind generator is the reduction in inertia. Thus based on the observation made for the inter-area mode trajectory for two area system one can infer that the reduction in system inertia can help dampen the inter-area mode faster.

As far as the local mode of oscillation is considered, when the wind farm penetration in area 1 increases, it impacts the local mode of oscillation of area 1 only, it had negligible impact on the local mode of oscillation in area 2. Similarly, penetration of wind farm in area 2 had effect on the local mode of area 2 only. This is expected as the tie-line power flow is unchanged in this case. Thus the increased penetration of wind farm in one area only affects the local mode in that area when the tie-line power flow remains unchanged. The locus of local mode 1 and local mode 2

The details about the real part, imaginary part, frequency of oscillation, damping for the inter-area mode and local modes are listed in Table 7.1, 7.2 and 7.3 respectively.

Table 7.3: Local Mode 2 at different penetration level of Wind Farm

Penetration Level	Real Part	Imaginary Part	Frequency (Hz)	Damping (%)
Case 1				
0	-0.6569	7.3313	1.1668	8.92
10	-0.6670	7.4633	1.1878	8.90
20	-0.6495	7.4874	1.1917	8.64
30	-0.6473	7.4935	1.1926	8.60
45	-0.6504	7.4970	1.1932	8.64
60	-0.6474	7.4985	1.1934	8.60
80	-0.6479	7.4995	1.1936	8.60
Case 2				
0	-0.6599	7.5200	1.1968	8.74
10	-0.7253	7.6908	1.2240	9.39
20	-0.8118	7.9173	1.2601	10.2
30	-0.9085	8.2124	1.3070	11.00
45	-1.0694	8.8461	1.4079	12.00
60	-1.2376	9.9236	1.5794	12.37
80	-1.3234	13.4401	2.1391	9.80

7.1.3 Changes in the Operating Condition causing Change in Tie-line Power Flows

In this case, the test system was analyzed at five different operating condition for each of the penetration level. For each operating condition, the load at bus 9 is varied such that the tie-line power flow changes. Only the generation from the slack bus (bus 1) is changed to accommodate the load changes. The generation of generator G2, G3 and G4 were kept constant at 700 MW, 719 MW and 700 MW respectively. The load at bus 9 is varied from 1542 MW to 1842 MW at steps of 75 MW to cause the changes in system operating condition.

Table 7.4 lists the inter-area mode location at different loading condition and at different wind penetration corresponding to area 1. Table 7.5 lists the inter-area mode location at different loading condition and at different wind penetration corresponding to area 2. Figure 7.3 shows the locus of the inter-area mode corresponding to different

Table 7.4: Interarea Mode at different penetration level of Wind Farm on Area 1 and at different operating condition

Load at bus 9	Real Part	Imaginary Part	Frequency (Hz)	Damping (%)
10% Penetration				
1542	-0.2159	4.8081	0.7652	4.49
1617	-0.1818	4.7767	0.7602	3.80
1692	-0.1399	4.7205	0.7513	2.96
1767	-0.0896	4.6328	0.7373	1.93
1842	-0.0283	4.5053	0.7170	0.63
20% Penetration				
1542	-0.2291	4.8758	0.7760	4.69
1617	-0.2034	4.8438	0.7709	4.20
1692	-0.1682	4.7872	0.7619	3.51
1767	-0.1234	4.6992	0.7479	2.63
1842	-0.0664	4.5713	0.7276	1.45
30% Penetration				
1542	-0.2326	4.9479	0.7875	4.69
1617	-0.2170	4.9146	0.7822	4.41
1692	-0.1903	4.8573	0.7731	3.91
1767	-0.1524	4.7690	0.7590	3.19
1842	-0.1010	4.6408	0.7386	2.18
45% Penetration				
1542	-0.2221	5.0634	0.8059	4.38
1617	-0.2228	5.0267	0.8000	4.43
1692	-0.2107	4.9677	0.7906	4.24
1767	-0.1855	4.8788	0.7765	3.80
1842	-0.1448	4.7501	0.7560	3.05
60% Penetration				
1542	-0.2075	5.1834	0.8250	4.00
1617	-0.2192	5.1429	0.8185	4.26
1692	-0.2199	5.0814	0.8087	4.32
1767	-0.2076	4.9919	0.7945	4.16
1842	-0.1787	4.8630	0.7740	3.67
80% Penetration				
1542	-0.2125	5.3135	0.8457	4.00
1617	-0.2243	5.2726	0.8392	4.25
1692	-0.2323	5.2287	0.8322	4.44
1767	-0.2284	5.1405	0.8181	4.44
1842	-0.2097	5.0124	0.7978	4.18

Table 7.5: Interarea Mode at different penetration level of Wind Farm on Area 2 and at different operating condition

Load at bus 9	Real Part	Imaginary Part	Frequency (Hz)	Damping (%)
10% Penetration				
1542	-0.2334	4.8001	0.7640	4.86
1617	-0.1872	4.7692	0.7590	3.92
1692	-0.1337	4.7129	0.7501	2.84
1767	-0.0723	4.6232	0.7358	1.56
1842	-0.0005	4.4961	0.7156	0.01
20% Penetration				
1542	-0.2681	4.8604	0.7736	5.51
1617	-0.2171	4.8282	0.7684	4.49
1692	-0.1584	4.7703	0.7592	3.32
1767	-0.0911	4.6785	0.7446	1.95
1842	-0.0133	4.5487	0.7239	0.29
30% Penetration				
1542	-0.2978	4.9246	0.7838	6.04
1617	-0.2426	4.8911	0.7784	4.95
1692	-0.1792	4.8313	0.7689	3.71
1767	-0.1070	4.7392	0.7543	2.26
1842	-0.0233	4.6049	0.7329	0.51
45% Penetration				
1542	-0.3321	5.0274	0.8001	6.59
1617	-0.2716	4.9916	0.7944	5.43
1692	-0.2026	4.9291	0.7845	4.11
1767	-0.1242	4.8339	0.7693	2.57
1842	-0.0131	4.6957	0.7473	0.71
60% Penetration				
1542	-0.3553	5.1344	0.8172	6.90
1617	-0.2915	5.0963	0.8111	5.71
1692	-0.2190	5.0312	0.8007	4.35
1767	-0.1364	4.9333	0.7852	2.76
1842	-0.0403	4.7918	0.7626	0.84
80% Penetration				
1542	-0.3789	5.2737	0.8393	7.17
1617	-0.3140	5.2316	0.8326	5.99
1692	-0.2400	5.1627	0.8217	4.64
1767	-0.1551	5.0614	0.8056	3.064
1842	-0.0545	4.9142	0.7821	1.11

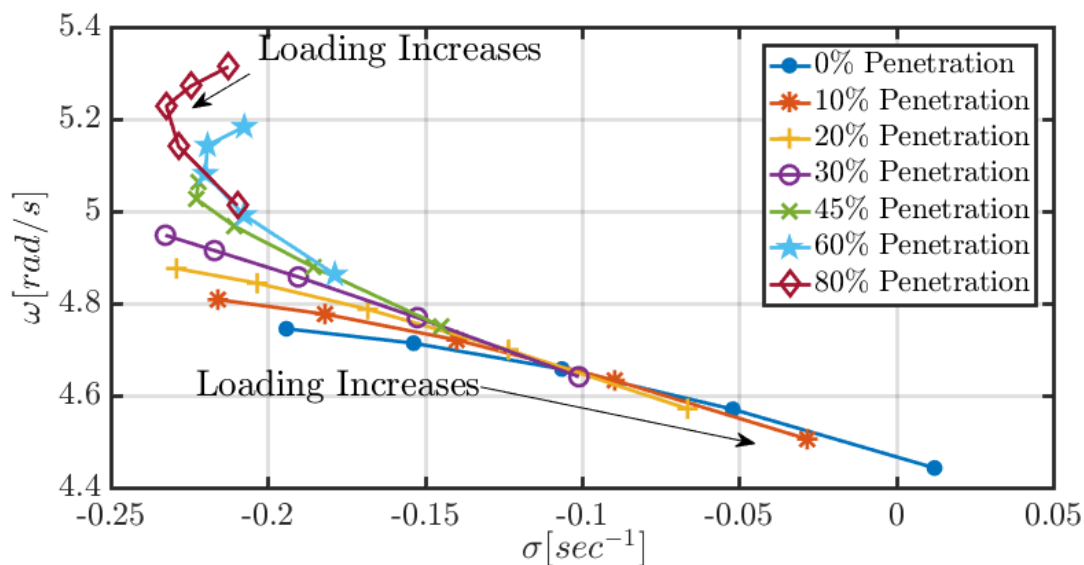


Figure 7.3: Locus of Inter-area Mode with Different Penetration Level of Renewable Energy Resources in Area 1 with Different Loading Condition.

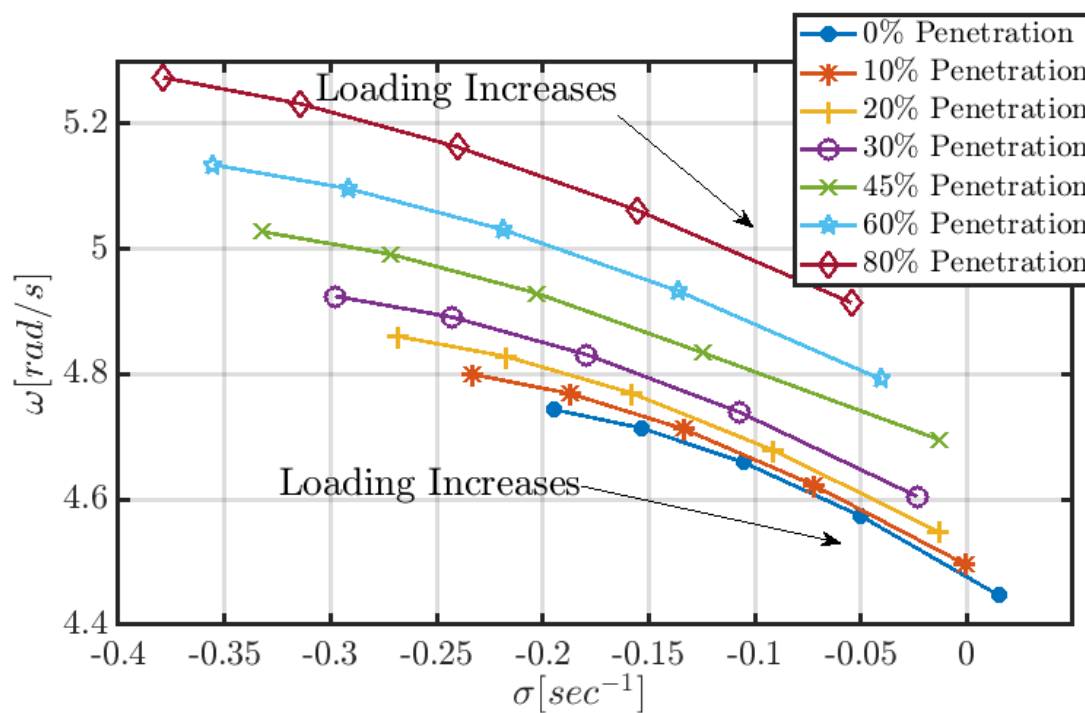


Figure 7.4: Locus of Inter-area Mode with Different Penetration Level of Renewable Energy Resources in Area 2 with Different Loading Condition.

penetration of wind farm in area 1 and at different loading condition. It can be observed from Figure 7.3 that at higher penetration of wind farm on area 1 which is the

power exporting area, the damping of inter-area mode increases for certain increment in load. This is particularly true as at higher penetration as the contribution of wind farm power output in overall tie-line power flow is higher, which means majority of tie-line power flow is not coupled with system frequency causing the system to have better damping. But, this deteriorates as the loading is further increased or renewable energy penetration is lowered as the majority of tie-line power flow then comes from synchronous machines.

Figure 7.4 shows the locus of the inter-area mode corresponding to different penetration of wind farm in area 2 and at different loading condition. It can be observed from Figure 7.4 that the inter-area mode damping increases when the wind farm penetration increases, but decreases as load in area 2 increases.

The difference in characteristic of locus of eigenvalues with synchronous machine and wind farm arises from the fact that the wind farm appears to the rest of the system as a voltage source behind an impedance and does not interface with the network through an internal angle as a synchronous machine[123].

Table 7.6 and Table 7.7 lists the location of local mode 1 and local mode 2 at different loading condition and at different wind penetration corresponding to area 1. Table 7.8 and Table 7.9 lists the location of local mode 1 and local mode 2 at different loading condition and at different wind penetration corresponding to area 2. Figure 7.5 shows the locus of local mode 1 with different penetration level of renewable energy resources in area 1 with different loading condition. It can be observed from Figure 7.5 that as loading in area 2 is increased for every penetration level of renewable energy resource, the local mode in area 1 move towards RHP. Figure 7.6 shows the locus of local mode 2 with different penetration level of renewable energy resources in area 1 with different loading condition. From Figure 7.6 it can be observed that local mode 2 first observes increasing in damping for a certain loading and then damping decreases beyond a further loading. Figure 7.7 shows the locus of local

Table 7.6: Local Mode 1 at different penetration level of Wind Farm on Area 1 and at different operating condition

Load at bus 9	Real Part	Imaginary Part	Frequency (Hz)	Damping (%)
10% Penetration				
1542	-0.9346	7.4363	1.1835	12.47
1617	-0.8626	7.4856	1.1914	11.45
1692	-0.7828	7.5208	1.1970	10.35
1767	-0.7206	7.5581	1.2029	9.49
1842	-0.6774	7.5466	1.2011	8.94
20% Penetration				
1542	-1.0350	7.6074	1.2108	13.48
1617	-0.9651	7.6745	1.2214	12.48
1692	-0.8953	7.7225	1.2291	11.52
1767	-0.8249	7.7436	1.2324	10.59
1842	-0.7494	7.7359	1.2312	9.64
30% Penetration				
1542	-1.1463	7.8397	1.2477	14.47
1617	-1.0792	7.9135	1.2595	13.51
1692	-1.0061	7.9720	1.2688	12.52
1767	-0.9270	8.0055	1.2741	11.50
1842	-0.8403	8.0101	1.2749	10.43
45% Penetration				
1542	-1.3083	8.9384	1.3366	15.39
1617	-1.2574	8.4623	1.3468	14.70
1692	-1.1874	8.5312	1.3578	13.79
1767	-1.1028	8.5852	1.3664	12.74
1842	-1.0054	8.6111	1.3705	11.60
60% Penetration				
1542	-1.4048	9.4604	1.5057	14.69
1617	-1.4135	9.4777	1.5084	14.75
1692	-1.3764	9.5309	1.5169	14.29
1767	-1.3052	9.5926	1.5267	13.48
1842	-1.2076	9.6355	1.5335	12.44
80% Penetration				
1542	-1.2348	12.7964	2.0366	9.61
1617	-1.4506	12.7765	2.0334	11.28
1692	-1.5437	12.9224	2.0567	11.86
1767	-1.5622	12.9715	2.0645	11.96
1842	-1.5029	13.0125	2.0710	11.47

Table 7.7: Local Mode 2 at different penetration level of Wind Farm on Area 1 and at different operating condition

Load at bus 9	Real Part	Imaginary Part	Frequency (Hz)	Damping (%)
10% Penetration				
1542	-0.6442	7.5827	1.2068	8.47
1617	-0.6557	7.5600	1.2032	8.64
1692	-0.6724	7.5262	1.1978	8.90
1767	-0.6670	7.4633	1.1878	8.90
1842	-0.6344	7.4239	1.1816	8.51
20% Penetration				
1542	-0.6462	7.5779	1.2061	8.50
1617	-0.6520	7.5513	1.2018	8.60
1692	-0.6532	7.5200	1.1969	8.65
1767	-0.6495	7.4874	1.1917	8.64
1842	-0.6420	7.4554	1.1866	8.58
30% Penetration				
1542	-0.6448	7.5744	1.2055	8.48
1617	-0.6477	7.5502	1.2016	8.55
1692	-0.6485	7.5231	1.1973	8.59
1767	-0.6473	7.4935	1.1926	8.61
1842	-0.6438	7.4622	1.1876	8.60
45% Penetration				
1542	-0.6423	7.5725	1.2052	8.45
1617	-0.6450	7.5507	1.2017	8.51
1692	-0.6467	7.5255	1.1977	8.56
1767	-0.6471	7.4970	1.1932	8.60
1842	-0.6451	7.4657	1.1882	8.61
60% Penetration				
1542	-0.6406	7.5721	1.2051	8.43
1617	-0.6440	7.5512	1.2018	8.50
1692	-0.6465	7.5266	1.1979	8.56
1767	-0.6474	7.4985	1.1934	8.60
1842	-0.6460	7.4671	1.1884	8.62
80% Penetration				
1542	-0.6395	7.5727	1.2052	8.41
1617	-0.6434	7.5519	1.2019	8.49
1692	-0.6464	7.5274	1.1980	8.56
1767	-0.6479	7.4995	1.1936	8.61
1842	-0.6469	7.4678	1.1885	8.63

Table 7.8: Local Mode 1 at different penetration level of Wind Farm on Area 2 and at different operating condition

Load at bus 9	Real Part	Imaginary Part	Frequency (Hz)	Damping (%)
10% Penetration				
1542	-0.8531	7.3229	1.1655	11.57
1617	-0.7942	7.3533	1.1703	10.74
1692	-0.7339	7.3632	1.1719	9.92
1767	-0.6704	7.3519	1.1701	9.08
1842	-0.6000	7.3235	1.1656	8.17
20% Penetration				
1542	-0.8499	7.3329	1.1671	11.51
1617	-0.7933	7.3632	1.1719	10.71
1692	-0.7349	7.3729	1.1734	9.92
1767	-0.6726	7.3611	1.1716	9.10
1842	-0.6031	7.3308	1.1667	8.20
30% Penetration				
1542	-0.8459	7.3377	1.1678	11.45
1617	-0.7911	7.3680	1.1727	10.68
1692	-0.7341	7.3776	1.1742	9.90
1767	-0.6728	7.3660	1.1723	9.10
1842	-0.6045	7.3344	1.1673	8.21
45% Penetration				
1542	-0.8418	7.3408	1.1683	11.39
1617	-0.7887	7.3713	1.1732	10.64
1692	-0.7331	7.3809	1.1747	9.88
1767	-0.6729	7.3693	1.1729	9.09
1842	-0.6055	7.3371	1.1677	8.22
60% Penetration				
1542	-0.8394	7.3419	1.1685	11.36
1617	-0.7873	7.3727	1.1734	10.62
1692	-0.7325	7.3825	1.1750	9.87
1767	-0.6730	7.3709	1.1731	9.09
1842	-0.6061	7.3384	1.1680	8.23
80% Penetration				
1542	-0.8376	7.3422	1.1686	11.33
1617	-0.7863	7.3735	1.1735	10.60
1692	-0.7320	7.3834	1.1751	9.87
1767	-0.6732	7.3719	1.1733	9.09
1842	-0.6066	7.3385	1.1680	8.24

Table 7.9: Local Mode 2 at different penetration level of Wind Farm on Area 2 and at different operating condition

Load at bus 9	Real Part	Imaginary Part	Frequency (Hz)	Damping (%)
10% Penetration				
1542	-0.7072	7.7589	1.2349	9.08
1617	-0.7136	7.7406	1.2319	9.18
1692	-0.7198	7.7182	1.2284	9.29
1767	-0.7253	7.6908	1.2240	9.39
1842	-0.7288	7.6594	1.2190	9.47
20% Penetration				
1542	-0.7906	7.9833	1.2706	9.85
1617	-0.7973	7.9658	1.2678	9.96
1692	-0.8044	7.9443	1.2644	10.07
1767	-0.8118	7.9173	1.2601	10.20
1842	-0.8174	7.8883	1.2555	10.31
30% Penetration				
1542	-0.8872	8.2740	1.3168	10.66
1617	-0.8938	8.2576	1.3142	10.76
1692	-0.9011	8.2372	1.3110	10.87
1767	-0.9085	8.2124	1.3070	11.00
1842	-0.9152	8.1831	1.3024	11.11
45% Penetration				
1542	-1.0539	8.9016	1.4167	11.76
1617	-1.0587	8.8875	1.4145	11.83
1692	-1.0640	8.8693	1.4116	11.91
1767	-1.0694	8.8461	1.4079	12.00
1842	-1.0740	8.8180	1.4034	12.09
60% Penetration				
1542	-1.2415	9.9686	1.5866	12.36
1617	-1.2405	9.9586	1.5850	12.36
1692	-1.2393	9.9439	1.5826	12.37
1767	-1.2376	9.9236	1.5794	12.38
1842	-1.2347	9.8975	1.5752	12.38
80% Penetration				
1542	-1.4155	13.4665	2.1433	10.45
1617	-1.3873	13.4634	2.1428	10.25
1692	-1.3567	13.4549	2.1414	10.03
1767	-1.3234	13.4401	2.1391	9.80
1842	-1.2867	13.4179	2.1355	9.55

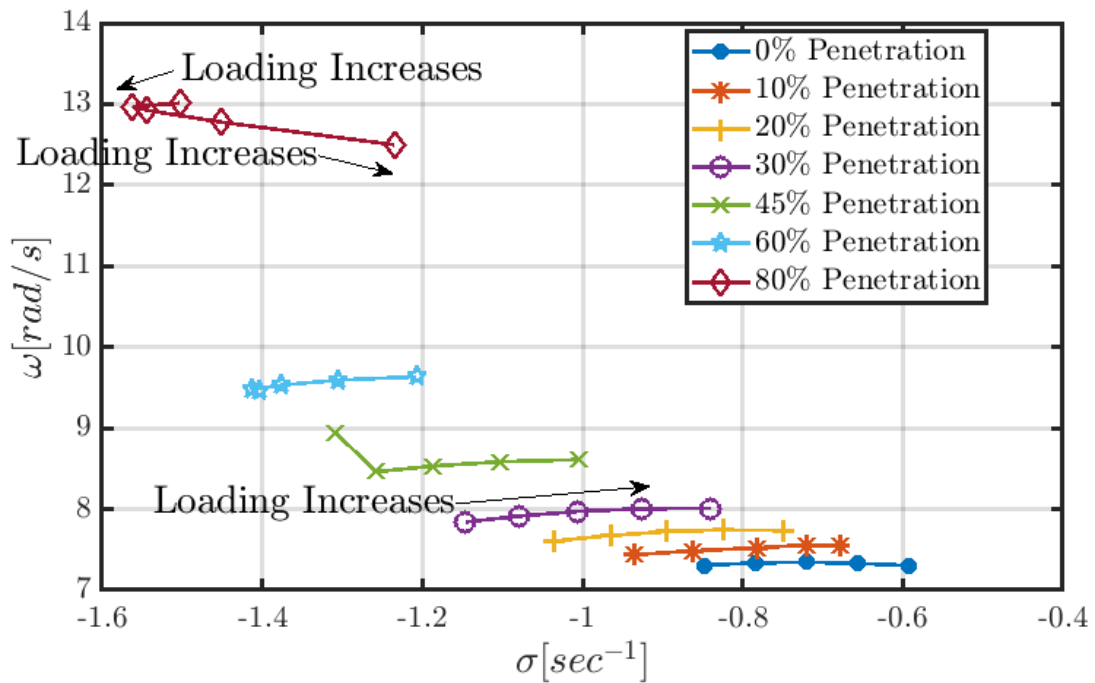


Figure 7.5: Locus of Local Mode 1 with Different Penetration Level of Renewable Energy Resources in Area 1 with Different Loading Condition.

mode 1 with different penetration level of renewable energy resources in area 1 with different loading condition. It can be observed from Figure 7.7 that the local mode 1 move towards RHP as the loading in area 2 increases irrespective of wind penetration level. Figure 7.8 shows the locus of local mode 2 with different penetration level of renewable energy resources in area 1 with different loading condition.

Figure 7.9 shows the inter-area speed oscillation following a three phase fault for a fixed operating point at different penetration of wind farm in the system. From Figure 7.9 it can be observed that the system damping increases for exactly similar type of faults for similar operating condition as the penetration of wind farm in power grid increases. However, a generic conclusion cannot be drawn as the system damping is affected by a lot of factors including the penetration level of the wind farm, location of the wind farm, operating condition of the wind farm, location of fault and so on. As the objective of the dissertation is not to quantify the effect of wind farm on the

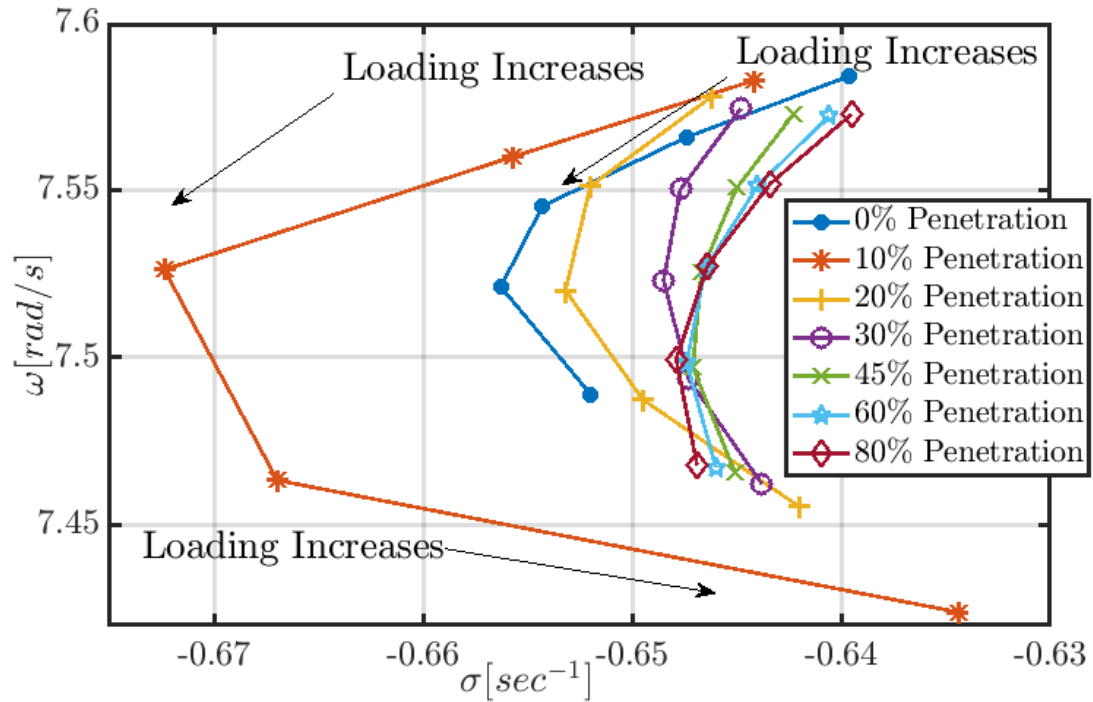


Figure 7.6: Locus of Local mode 2 with Different Penetration Level of Renewable Energy Resources in Area 1 with Different Loading Condition.

bulk power grid, detailed study on impact of wind farm on bulk power grid is not pursued. It has been considered in this dissertation that if any detrimental impact is caused on power grid by increased penetration of wind farm, such impact can be properly minimized by control of wind farms during grid fault conditions. In the following sections, DFIG based wind farm has been utilized to provide both active and reactive power support in order to enhance the stability of the bulk power grid.

7.2 System Modeling

The classical second order model of a synchronous machine is often used to study the transient stability of a power system during the period of time in which the system dynamics depend largely on the stored kinetic energy in the rotating masses [122].

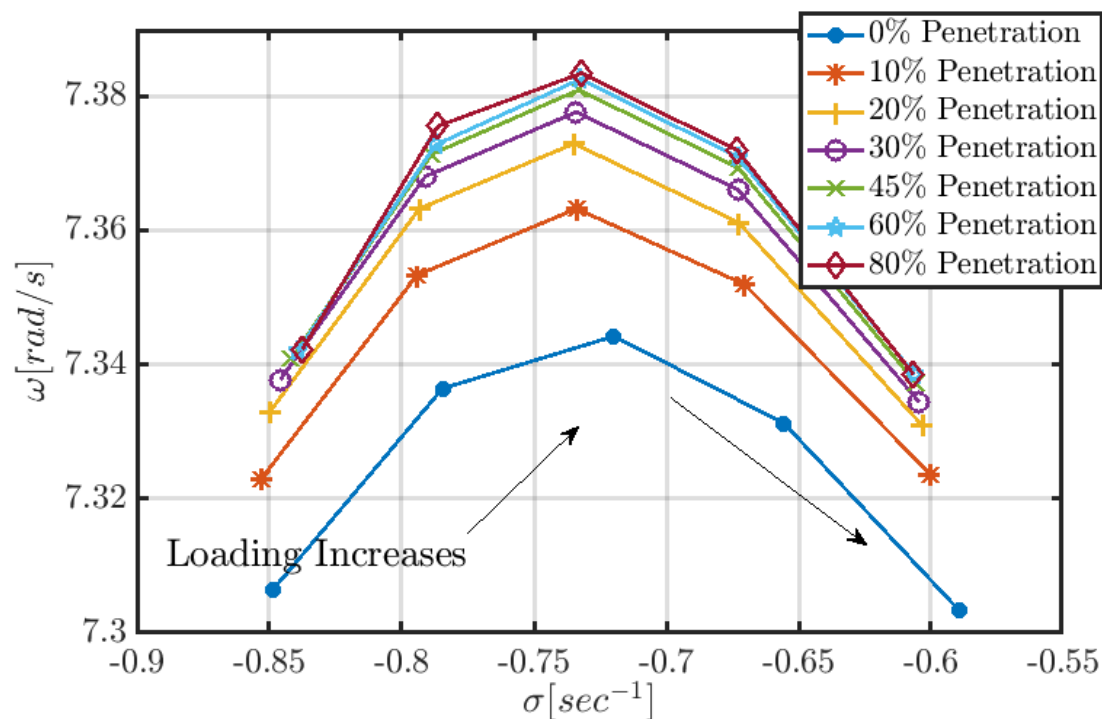


Figure 7.7: Locus of Local mode 1 with Different Penetration Level of Renewable Energy Resources in Area 2 with Different Loading Condition.

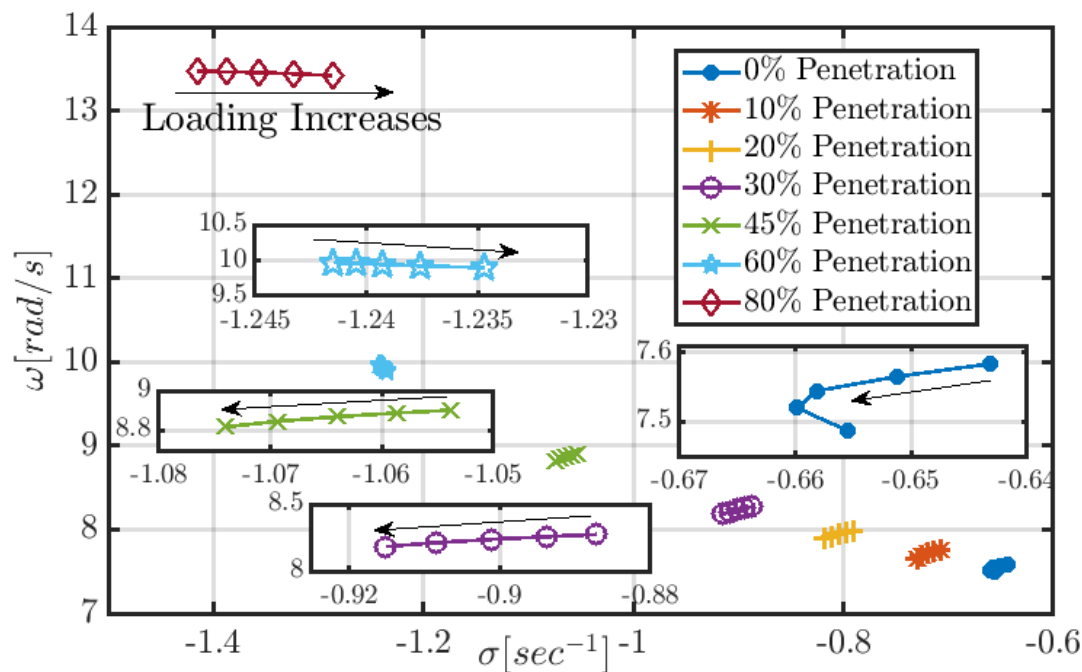


Figure 7.8: Locus of Local mode 2 with Different Penetration Level of Renewable Energy Resources in Area 2 with Different Loading Condition.

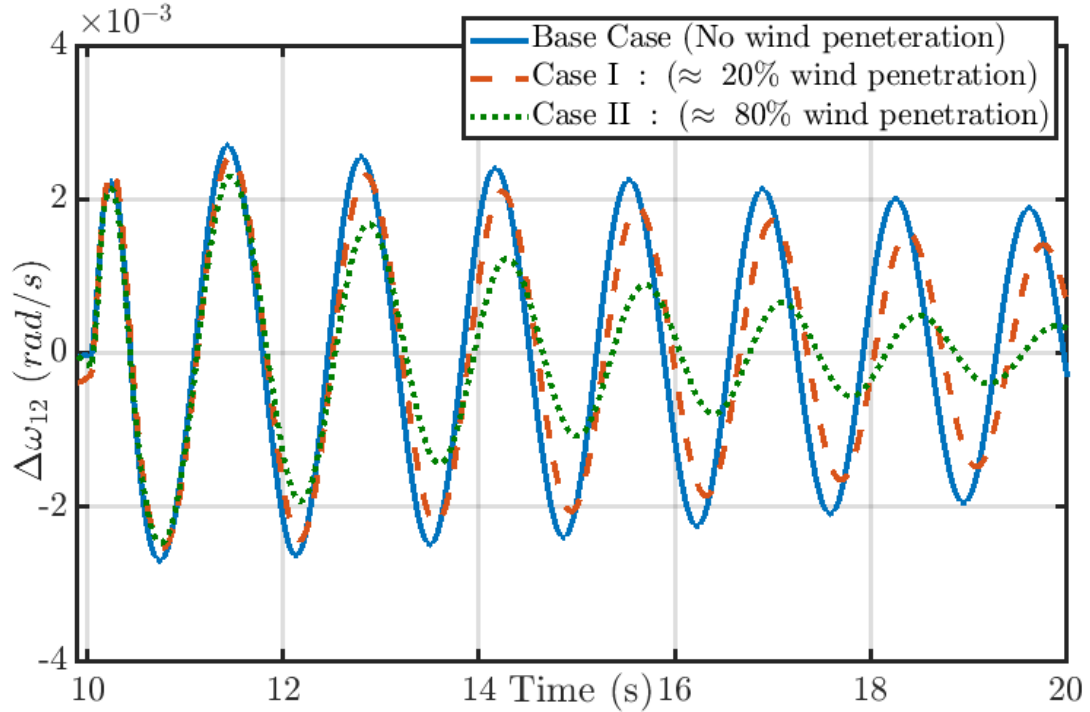


Figure 7.9: Inter-area Speed Oscillation for a Three Phase Fault for a Fixed Operating Point at Different Penetration of Wind Farm.

The equations of motion for a classical representation of power system are given by,

$$\begin{aligned} \dot{\omega}_i &= \frac{1}{M_i} \left(P_{m_i} - D_i \omega_i - E_i \sum_{j=1}^n E_j (B_{ij} \sin \delta_{ij} + G_{ij} \cos \delta_{ij}) \right) \\ \dot{\delta} &= \omega_i - \omega_s \quad i = 1, \dots, n \end{aligned} \quad (7.2)$$

where n is the number of synchronous machines, ω_s is the synchronous angular frequency, $\delta_{ij} = \delta_i - \delta_j$, $M_i = \frac{2H_i}{\omega_s}$, and H_i is the inertia constant in seconds and D_i is the damping coefficient of the machine i . B_{ij} and G_{ij} are the elements of the reduced admittance matrix Y at the internal nodes of the machine. The loads are modeled as constant impedances which are then absorbed into the admittance matrix.

The DER connected on the various buses modeled as a constant negative PQ load or a PV bus depending on the mode of control employed in the DER system.

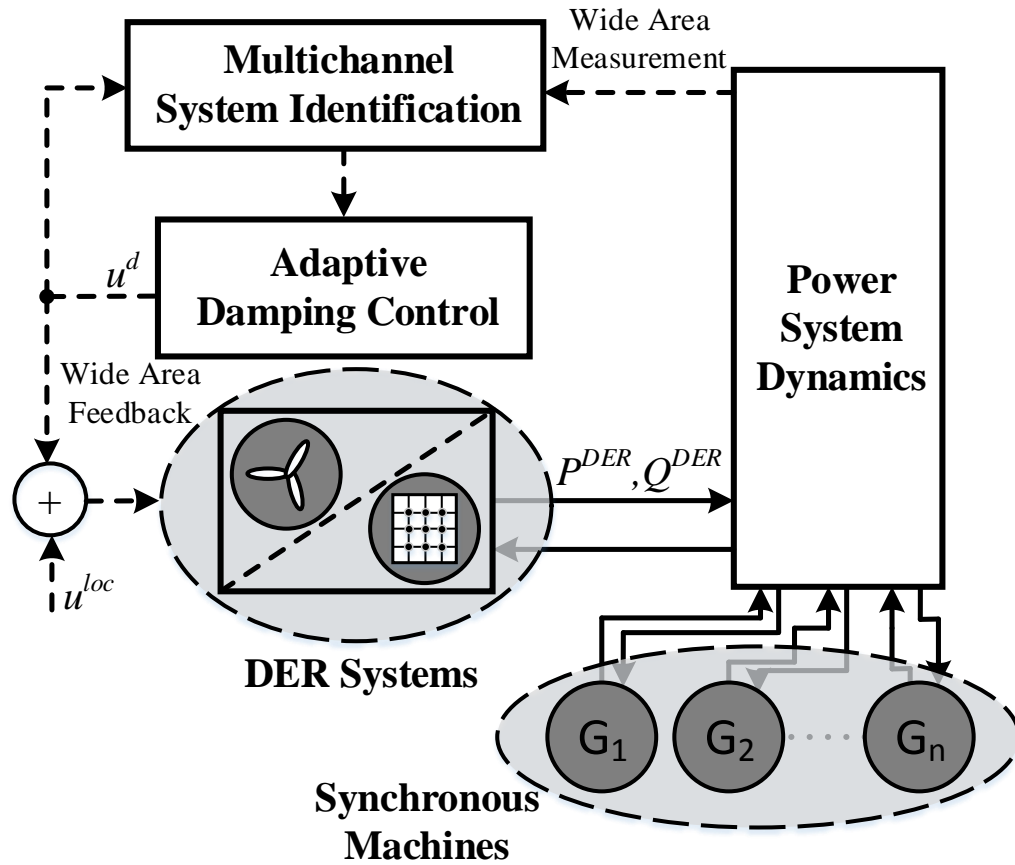


Figure 7.10: Proposed structure of damping controller based on system identification.

Considering DER as constant negative PQ load, (7.2) can be rewritten as,

$$\dot{\omega}_i = \frac{1}{M_i} \left(P_{m_i} - D_i \omega_i - \sum_{i=1}^n P_{ld_i} - \sum_{i=1}^m P_{ls_i} + \sum_{i=1}^o P_i^{DER} \right) \quad (7.3)$$

$$\dot{\delta} = \omega_i - \omega_s \quad i = 1, \dots, n$$

where m is the number of lines, and o is the number of DER in the network. P_{ld_i} represents the load connected at the i th bus, P_{ls_i} represents the line losses in the i th line and P_i^{DER} represents the active power injected by DER on i th bus.

The power injected by the DER on the i th bus is given by,

$$P_i^{DER} = \frac{P_i^{DER*}}{1 + sT_i^{DER}} \quad (7.4)$$

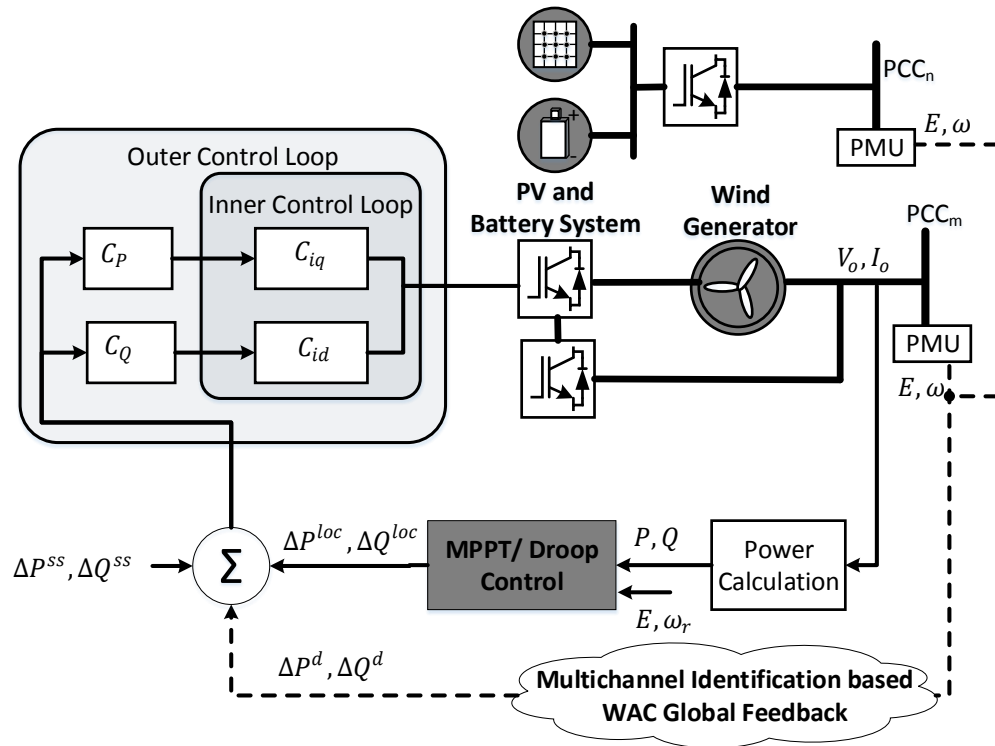


Figure 7.11: Augmentation of DER LC using Proposed WAC Signal.

where P_i^{DER*} power reference for i th DER system and T_i^{DER} is the DER system response time constant for i th DER.

From (7.3) and (7.4), it can be observed that the power output of DER can have an impact on system frequency dynamics even though DER themselves are operating in asynchronous mode.

7.3 Augmentation of DER Local Controller with Proposed WAC Technique

A general representation of the proposed system identification based adaptive controller applied to DER is shown in Figure 7.10. The controller action of DER with the proposed augmentation with WAC comprises of two parts as,

$$u(t) = u^d(t) + u^{loc}(t) \quad (7.5)$$

where u^d is the damping component of the control input provided by the damping controller designed using identified system parameters and u^{loc} is the component of control signal required to track the local reference input. For the system identification, inter-area speed deviation $\Delta\omega_{ij}$ is considered as the system output and the ΔP_{DER} is considered as the system input. The identified linearized model of the system is then utilized for the design of damping controller. The goal is to enhance the overall system stability while minimizing the inter-area speed deviation.

It is worth noting that in this work the focus is to utilize this architecture and augment DER LCs such that DER can take part in damping the system oscillations. For DER, the objective of LC is to track the reference set-point provided either by maximum power point tracking (MPPT) controller or by the DER operator. The goal of the WAC is to damp the system oscillations by appropriately modifying the active and reactive power output of DER system. The augmentation of the LC of DER to incorporate the damping functionality is shown in Figure 7.11. Overall, the active power set-point given to the DER system comprises of three terms: $(\Delta P^{loc}, \Delta Q^{loc})$ for load sharing or MPPT control as local reference, $(\Delta P^{ss}, \Delta Q^{ss})$ as a set-point provided by secondary/tertiary level controller from DER control center and $(\Delta P^d, \Delta Q^d)$ as a remote set-point signal provided by damping controller. Once the sum of these three different set-points is available, the tracking of these set-point is achieved through the conventional vector control techniques implemented in DER systems [125]. The outer loop controls (C_P, C_Q) the active and reactive power set-points and provides an equivalent current reference to the inner loop control (C_{id}, C_{iq}) which track the current flowing out of the DER system.

By controlling the active and reactive power output of the DER system, the speed oscillation brought about by local and wide area disturbances could be mitigated. Thus, the goal of the multichannel identification based WADC is to monitor and identify the local and inter-area oscillations and send proper damping signals to DER

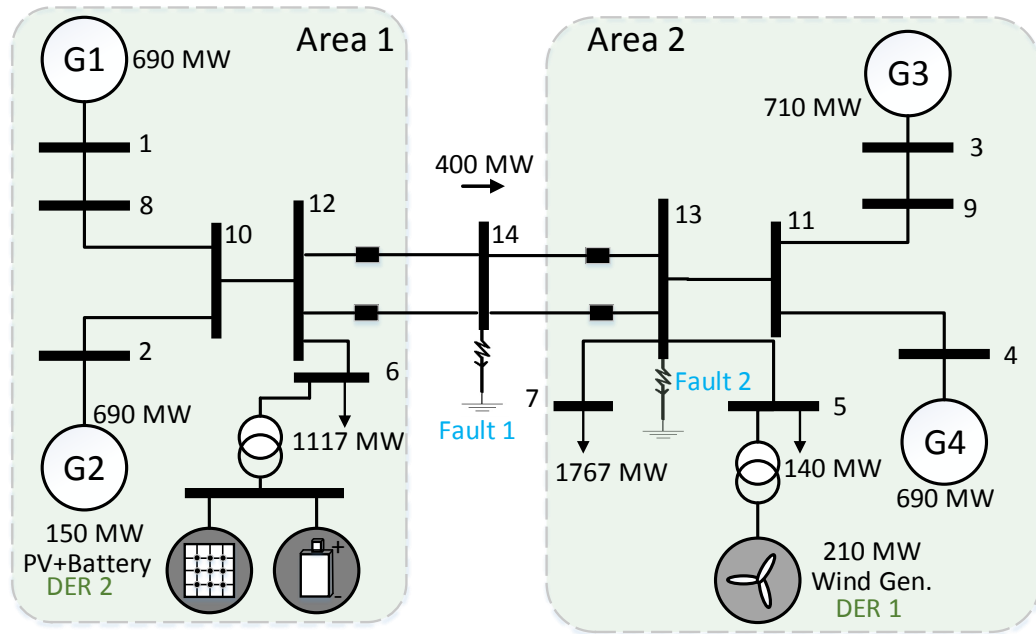


Figure 7.12: Modified Classical Two-area Four-machine System with Integrated DER.

systems in order to dampen the system oscillation.

7.3.1 System Identification based Damping Controller Design

The damping controller designed for this work is based on MVC architecture used in polynomial methods [126] which solves the optimal control problem of minimizing the output variance of the ARMAX system identified k steps ahead of time. Polynomial method is chosen in this work as opposed to state space form [127] due to easier and simpler implementation and application for practical purposes. The controller designed in this work is based on the second order identification of the system and the controller takes in the following form [126]:

$$u_1(k) = \frac{a^1 y_1(k) + a^2 y_1(k-1) - b_{12}^1 u_1(k-1)}{b_{11}^1} \quad (7.6)$$

for a step ahead prediction error minimization.

7.4 Simulation Results and Discussion

Figure 7.12 shows the test system that has been utilized to assess the performance of the proposed system identification based damping controller with respect to conventional PSS that has been implemented in the synchronous machine. The test system is a modified version of classic two area four machine system [122]. The test system has been implemented in MATLAB-Simulink. The model consists of two areas connected through a tie-line. Area 1 has two synchronous generators each generating 690 MW power and area 2 also has two synchronous generator each generating 710 MW and 690 MW respectively. In this section, the full-order model of the synchronous generators is used with LCs of governor, exciter, and PSS. On top of synchronous machine, each area consists of aggregated DER models. In area 1, a 100 MW PV farm coupled with a 50 MW storage unit is connected to bus 6 along with a 150 MW load and in area 2, a 210 MW wind farm is connected to bus 5 along with a 140 MW load. Two case studies are performed to test the performance of the proposed system identification based damping controller.

Figure 7.13 and Figure 7.14 shows the performance of the proposed multi-channel identification technique for properly capturing the system dynamics. At 10 seconds, when the fault is applied there is a large error but the parameters are updated recursively and they converge quickly to stable values.

7.4.1 Fault in Middle of Transmission Line

In this case, a bolted three phase fault for 6 cycles is applied to middle of the tie-line connecting Area-1 and Area-2. It is assumed that the fault is auto-cleared after 6 cycles and the circuit breakers on the either end of the line are not opened. This disturbance excites the interarea oscillation in the system.

The purpose of this study is first to show that if not explicitly asked to take part in mitigating the system oscillation, the DER systems basically continue to send

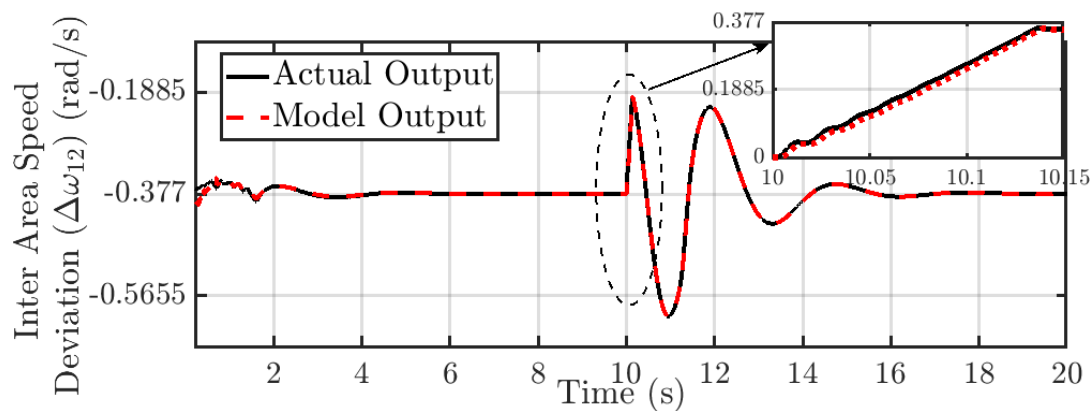


Figure 7.13: Comparison of Actual Inter-area Speed Deviation and Estimated Inter-area Speed Deviation.

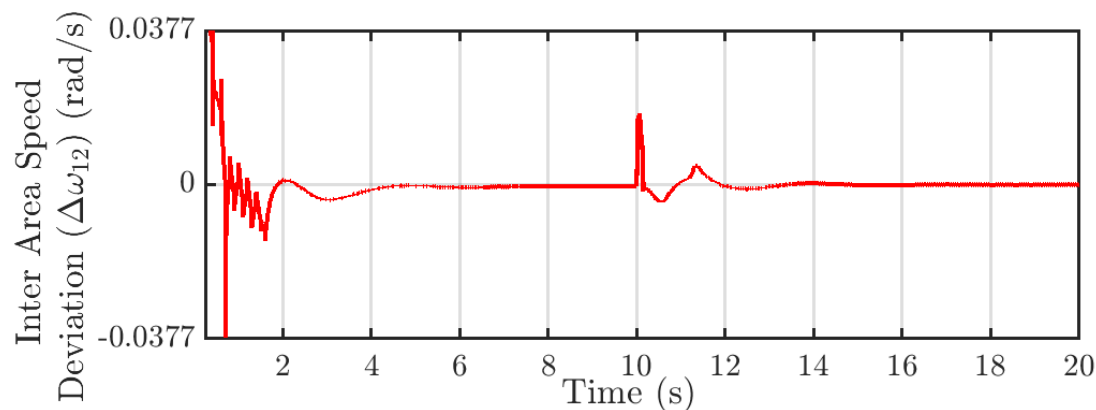


Figure 7.14: Estimation Error of the Recursive Least Square Multi-channel Identification Routine.

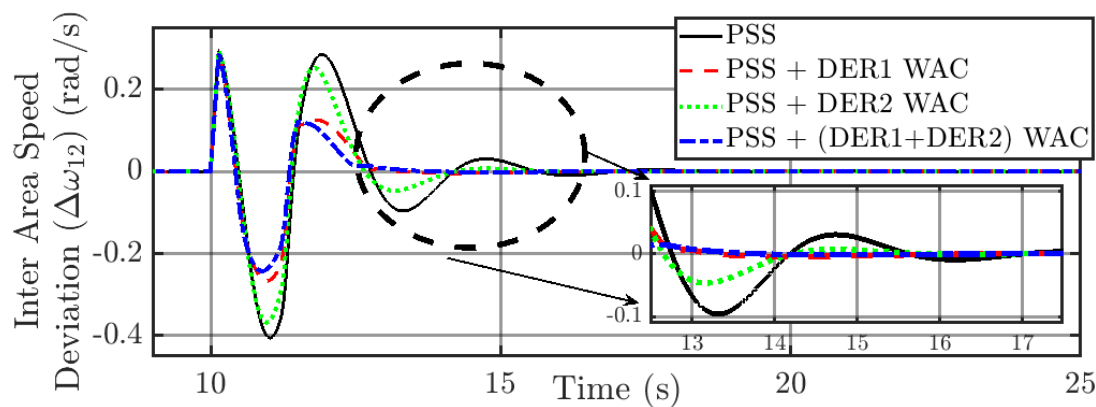


Figure 7.15: Inter-area Speed Deviation Comparison with PSS and Proposed Technique with Multiple Combination of DER.

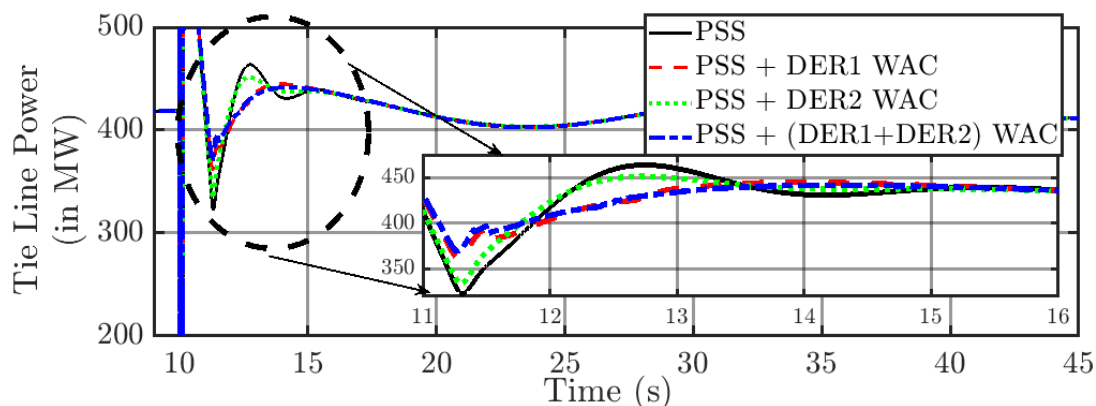


Figure 7.16: Tie-line Power Flow Transfer Comparison with PSS and Proposed Technique with Multiple Combination of DER.

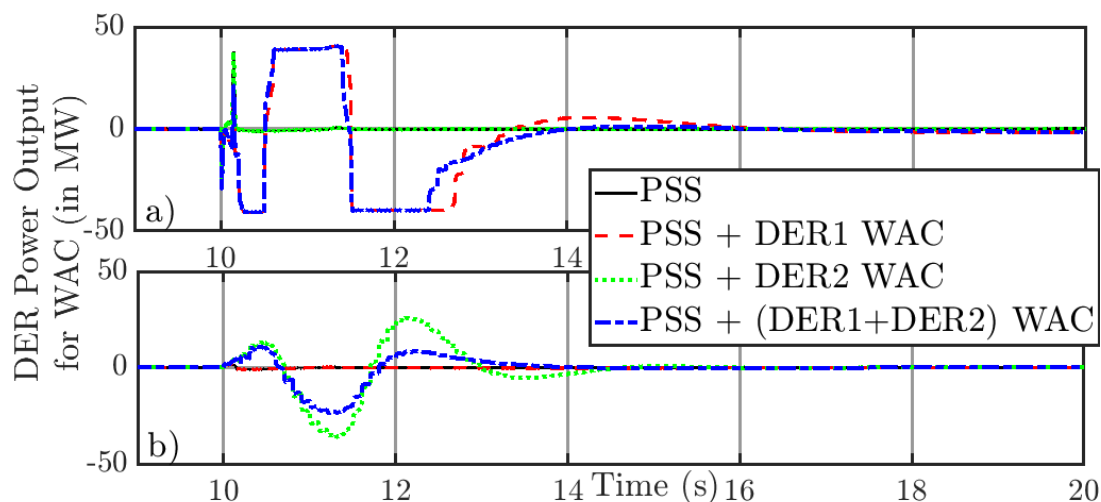


Figure 7.17: DER Power Output Deviation from its Local Setpoint for WAC Contribution a)DER1 b)DER2.

the same amount of power to the grid irrespective of the system oscillation. This primarily happens because of the asynchronous nature of operation of DER systems i.e. their power output naturally does not depend on system speed. Once that is demonstrated, next the capability of WAC augmented DER systems to dampen the system oscillation is shown and the performance is compared with the damping performance of PSS employed in synchronous machine.

Figure 7.15 shows the inter-area speed deviation for four different cases: a) PSS of synchronous machines are enabled and damping control in DERs are disabled b) PSS

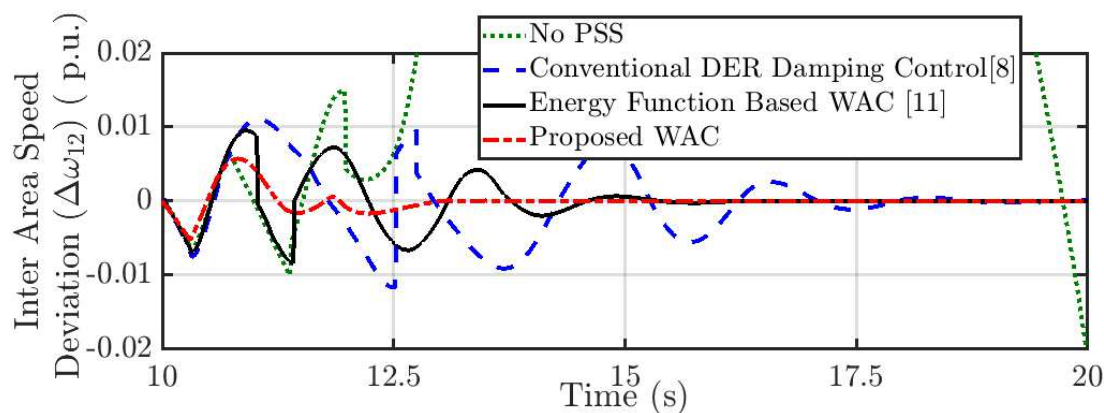


Figure 7.18: Inter-area Speed Oscillation Damping Comparison for Different WAC Schemes.

of synchronous machines are enabled along with damping controller in DER of area 1
 c) PSS of synchronous machines are enabled along with damping controller in DER of area 2
 d) PSS of synchronous machines are enabled along with damping controller in DER of both area 1 and area 2. It can be observed that with the proposed damping controller enabled, the dynamic response of system following the fault improves in terms of less overshoot and better damping. It can also be observed that better damping is obtained when DER in both area are utilized and also DER in sending end can provide more damping effect than the DER in area 2.

Figure 7.16 shows the tie-line power flow for the different cases studied. It can be observed that with the proposed WAC controller implemented on DER the tie-line power oscillations is minimized as well. Figure 7.17 shows the variation of DER power output in area 1 and area 2 from its local set-point in order to contribute for damping the inter-area mode. It can be observed that the DER only contributes to damping the system oscillation when the WAC signal is enforced. Without the WAC signal it can be observed that the DER strictly forces its power output to the reference level. Also, note that the DER power output variation on both area is limited to ± 45 MW to be utilized for WAC application which is low compared to the net system generation of 2800 MW.

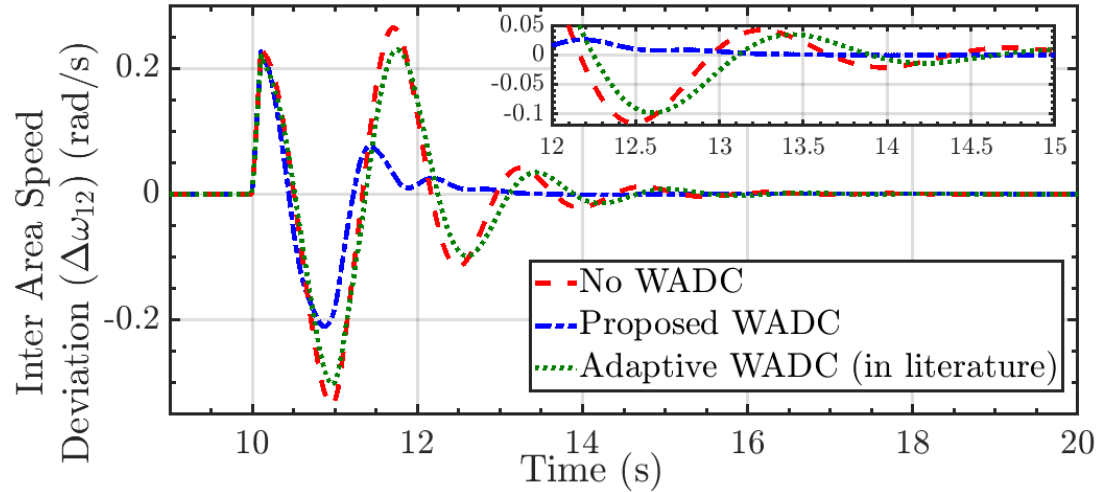


Figure 7.19: Inter-area Speed Oscillation Damping Comparison between Proposed Adaptive WADC and WADC proposed in [4].

7.4.2 Comparison with the Existing WADC architecture for DER

This test case presents the comparison of the proposed WAC with the existing WAC architecture for DER systems proposed in literature. The cases compared are a) No PSS and damping control implemented in DER systems b) with supplementary damping wind PSS designed as conventional WAC as in [128] c) Energy Function based direct intelligent WAC as in [129] and d) Proposed multichannel identification based WAC controller. A fault is applied at the middle of line as in section 7.4.1 at 10 secs for a 300 ms period and various WAC schemes are compared. The result shown in Figure 7.18 shows that the proposed WAC technique outperforms the other existing WAC schemes, the major advantage comes in from the fact that the proposed technique is not dependent on knowing the system parameters as the parameters are estimated online on the proposed control technique. Thus it can be seen that the proposed control technique can be a better alternative to the existing WAC scheme employed for DER systems.

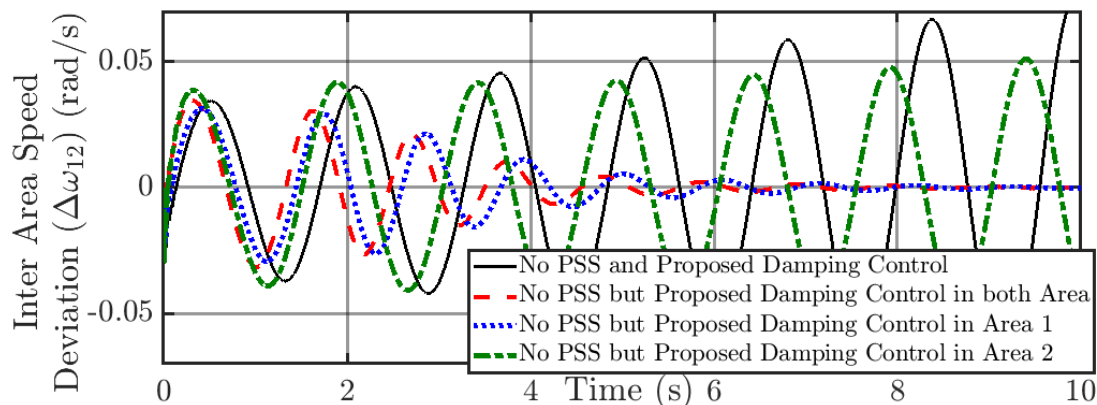


Figure 7.20: Inter-area Speed Oscillation Comparison without PSS but only with Proposed Damping Controller.

7.4.3 Comparison with the Existing system identification based Adaptive WADC architecture

This test case presents the comparison of the proposed adaptive WADC with the existing adaptive WADC architecture. The adaptive WADC proposed in [4] was implemented for DER and the performance comparison between technique in [4] and proposed technique was performed. Figure 7.19 shows the performance of the proposed damping controller and damping controller in [4] for fault conditions mentioned in Section 7.4.1. It can be observed that the proposed technique has a better response as compared to the technique presented in [4].

7.4.4 Performance of the Proposed DER damping controller on System without PSS

Figure 7.20 shows the performance of the proposed WAC without the presence of PSS in synchronous machine. As can be seen from Figure 7.20 without the PSS and no damping control in DER, the interarea speed deviation continues to grow overtime, however with the proposed DER based WAC implementation on both area and area 1 the inter area speed deviation settles down to zero. With the WAC implemented on area 2 DER it can be observed that the oscillation are contained.

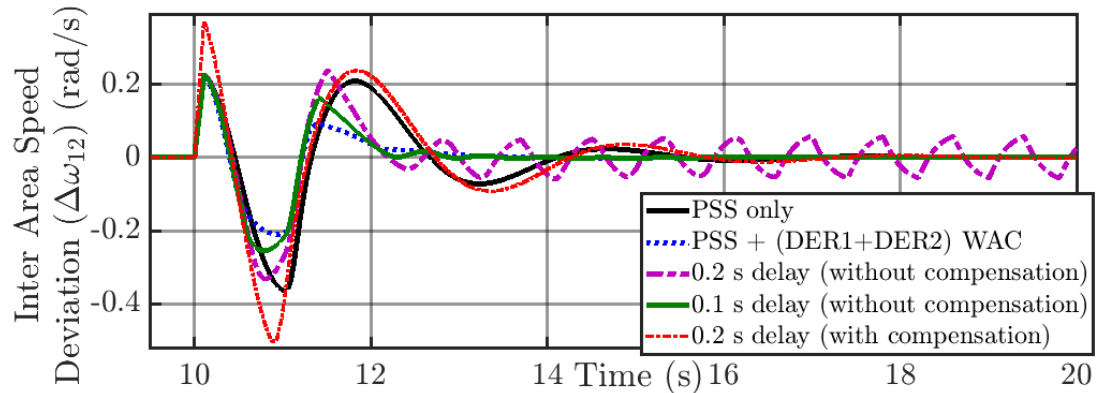


Figure 7.21: Inter-area Speed Oscillation Comparison with and without Delay Compensation for Proposed DER Damping Controller.

7.4.5 Effect of Time Delay on Proposed DER damping controller

The delay of the signals in the communication network for WAC implementation can have a detrimental impact on the performance of the WAC [113]. However utilizing the time stamp data from the WAC signal can help determine the delay that have occurred between dispatch and arrival of control signal. Once the delay is determined a local time delay compensator can be designed to ensure that the WAC based DER damping controller still performs well. Figure 7.21 shows the inter-area speed oscillation damping performance of the proposed controller at different time delays and with and without delay compensation. It can be observed that at larger time delays the proposed damping controller can damp the first swing however because of larger time delay a sustained oscillation is introduced in the system. It can also be observed that with proper compensation the inter-area oscillations can be damped even with presence of significant time delay.

7.5 Chapter Summary

In this chapter, the small signal impact of large scale wind farm penetration on a test power grid is studied and an adaptive WADC for DER integrated power grid is proposed in order to damp the system speed oscillations. Multichannel RLS estima-

tion technique has been utilized to identify the relation between the power system speed deviation as a system output and the power output of DER as a system input. The proposed approach augments the existing LC of DER to achieve the goal of damping the system speed oscillations. The results based on dynamic simulation of two area system in MATLAB Simulink shows better damping functionality of the proposed technique.

CHAPTER 8: CONCLUSIONS AND FUTURE WORKS

In this dissertation, an adaptive control framework for DFIG is designed and demonstrated. The main purpose is to increase the reliability, dispatchability and operational stability of renewable energy resources integrated power grid. The focus is mainly on measurement based approach for control of DFIG which can ensure the reliable operation of DFIG based wind farms. Detailed comparison of the proposed control technique has been performed with the existing control topologies reported in the literature. Also, the effect of renewable energy penetration on the power grid has been studied and DFIG based wind farm has been utilized to enhance the transient stability of the bulk power grid. For measurement based control, an online identification of the system was proposed. System identification based approach has the advantage that the system to be controlled can be treated as a black box and controller can be designed using the system model identified with input and output measurements. Such approach also eliminates the need to measure/estimate the system states thus increasing the reliability of operation of the closed loop system.

Further, system identification based adaptive control approach for speed sensorless control and rotor current sensorless control of DFIG has been discussed in depth. The performance analysis of the proposed technique was conducted using real time simulation platform as well as hardware in the loop simulation platform in order to validate the merit of the proposed control technique. The system identification based approach was also utilized to provide active and reactive power support to the bulk power grid through DFIG based wind farm. Considering the grid states as system output and DFIG power output as system input a reduced order model of the DFIG integrated power grid was identified, based on which the system oscillations were

damped or the voltage recovery was improved.

The work proposed in this dissertation leads to a number of future research plans for developing appropriate analytical tools for in-depth information extraction from power system networks and, thereafter, to build control methods for ensuring system wide stability and performance. For example,

- In this dissertation, the system identification and control has been performed considering a single input single output (SISO) system. A better controller can be designed for an overall DFIG system considering a multiple input multiple output (MIMO) system. This can lead to better response of the proposed control technique when both the active and reactive power support from DFIG is required at the same time.
- Regarding the use of wind farms and RERs for enhancing the power system stability, a sensitivity based approach can be implemented on large scale power grid to assign only some specific wind farms to act, when a certain frequency oscillation occurs in the power grid. This will lead to proper utilization of RERs and help solve the system oscillation problem without creating unwanted power flow changes in the power grid which is one of the way RERs impact stability of power grid.

LIST OF PUBLICATIONS

Peer Reviewed Journal Publications

[J1]. **R. Bhattarai**, N. Gurung and S. Kamalasan, "Dual Mode Control of Three Phase Inverter using Minimum Variance Adaptive Architecture" in IEEE Transactions on Industry Applications, vol. PP, no. 99, pp. 1-1.

[J2]. **R. Bhattarai**, N. Gurung, A. Thakallapelli and S. Kamalasan, "Reduced Order State Observer Based Feedback Control Methodologies for Doubly Fed Induction Machine," in IEEE Transactions on Industry Applications, vol. PP, no. 99, pp. 1-1.

[J3]. R. Yousefian, **R. Bhattarai**, S. Kamalasan, "Transient Stability Enhancement of Power Grid with Integrated Wide-Area Control of Wind Farms and Synchronous Generators," in IEEE Transactions on Power Systems, vol. PP, no.99, pp.1-1.

Peer Reviewed Conferences

[C1]. S. J. Hossain, **R. Bhattarai**, R. Yousefian, and S. Kamalasan, "Adaptive Wide-Area Damping Controller for Distributed Energy Resources Integrated Power Grid", accepted for publication in proceedings of PES GM 2018.

[C2]. **R. Bhattarai**, S. J. Hossain, J. Qi, J. Wang and S. Kamalasan, "Sustained System Oscillation by Malicious Cyber Attacks on Distributed Energy Resources", accepted for publication in proceedings of PES GM 2018.

[C3]. R. Bisht, S. Subramaniam, **R. Bhattarai** and S. Kamalasan, "Active and Reactive Power Control of Single Phase Inverter with Seamless Transfer Between Grid-connected and Islanded Mode", accepted for publication in proceedings of Power and Energy Conference at Illinois (PECI), 2018.

[C4]. S. Ghosh, **R. Bhattarai**, and S. Kamalasan, "Reactive Power Estimation Based Adaptive Voltage Control for Improved Grid Voltage Restoration using Doubly

Fed Induction Generators", 2nd IEEE International Conference on Transportation Electrification-India (ITEC-India) 2017.

[C5]. **R. Bhattarai**, N. Gurung, S. Ghosh, and S. Kamalasadán, "Parametrically robust dynamic speed estimation based control for doubly fed induction generator," 2017 IEEE Industry Applications Society Annual Meeting, Cincinnati, OH, 2017, pp. 1-8.

[C6]. S. J. Hossain, **R. Bhattarai**, M. Ahmed, S. Abdelrazek and S. Kamalasadán, "Operational cost value assessment and value-based stacked energy storage management for active power distribution systems," 2017 IEEE Industry Applications Society Annual Meeting, Cincinnati, OH, 2017, pp. 1-8.

[C7]. M. Ahmed, **R. Bhattarai**, S. J. Hossain, S. Abdelrazek and S. Kamalasadán, "Coordinated voltage control strategy for voltage regulators and voltage source converters integrated distribution system," 2017 IEEE Industry Applications Society Annual Meeting, Cincinnati, OH, 2017, pp. 1-8.

[C8]. N. Gurung, **R. Bhattarai**, and S. Kamalasadán, "Optimal Linear-Quadratic-Integral Controller Design for Doubly-Fed Induction Generator," 2017 IEEE Power and Energy Society General Meeting (PESGM), Chicago, IL, 2017, pp. 1-5.

[C9]. **R. Bhattarai**, N. Gurung and S. Kamalasadán, "Discrete real-time state observer based feedback control methodology for Doubly Fed Induction machine," 2016 IEEE International Conference on Power Electronics, Drives and Energy Systems (PEDES), Trivandrum, 2016, pp. 1-6.

[C10]. **R. Bhattarai**, N. Gurung and S. Kamalasadán, "Control of grid-connected inverters using minimum variance adaptive architecture," 2016 IEEE International Conference on Power Electronics, Drives and Energy Systems (PEDES), Trivandrum, 2016, pp. 1-6.

[C11]. **R. Bhattarai**, N. Gurung, and S. Kamalasadán, "Reduced order state observer based feedback control methodologies for doubly fed induction generator

(DFIG)," 2016 IEEE Industry Applications Society Annual Meeting, Portland, OR, 2016, pp. 1-8.

[C12]. **R. Bhattarai**, N. Gurung, and S. Kamalasadana, "Minimum variance controller based adaptive control for doubly fed induction generator," 2016 North American Power Symposium (NAPS), Denver, CO, 2016, pp. 1-6.

[C13]. **R. Bhattarai**, N. Gurung and S. Kamalasadana, "Reduced order model based state feedback control of Doubly Fed Induction Generators," 2016 IEEE Power and Energy Society General Meeting (PESGM), Boston, MA, 2016, pp. 1-5.

[C14]. R. Yousefian, **R. Bhattarai** and S. Kamalasadana, "Direct intelligent wide-area damping controller for wind integrated power system," 2016 IEEE Power and Energy Society General Meeting (PESGM), Boston, MA, 2016, pp. 1-5.

[C15]. **R. Bhattarai**, N. Gurung and S. Kamalasadana, "Minimum variance adaptive speed estimation technique for vector control of Doubly Fed Induction Generator," 2015 North American Power Symposium (NAPS), Charlotte, NC, 2015, pp. 1-6.

REFERENCES

- [1] Global Wind Energy Council, “Global wind statistics 2016,” October 2017.
- [2] M. G. Molina and J. G. Alvarez, “Technical and regulatory exigencies for grid connection of wind generation,” in *Wind Farm - Technical Regulations, Potential Estimation and Siting Assessment* (G. O. Suvire, ed.), ch. 01, Rijeka: InTech, 2011.
- [3] B. C. Pal and A. K. Singh, “Ieee pes task force on benchmark systems for stability controls report on the 68-bus 16-machine 5-area system,” *Version 2.0*, 2013.
- [4] F. Bai, L. Zhu, Y. Liu, X. Wang, K. Sun, Y. Ma, M. Patel, E. Farantatos, and N. Bhatt, “Design and implementation of a measurement-based adaptive wide-area damping controller considering time delays,” *Electric Power Systems Research*, vol. 130, pp. 1 – 9, 2016.
- [5] Department of Energy, “Wind vision: A new era for wind power in the united states,” 2016.
- [6] F. Mei, “Small-signal modelling and analysis of doubly-fed induction generators in wind power applications,” 2008.
- [7] F. Blaabjerg, F. Iov, R. Teodorescu, and Z. Chen, “Power electronics in renewable energy systems,” in *2006 12th International Power Electronics and Motion Control Conference*, pp. 1–17, Aug 2006.
- [8] S. Heier, *Grid Integration of Wind Energy: Onshore and Offshore Conversion Systems*. Wiley, 2014.
- [9] X. Yu and H. Qu, “Wind power in china: Opportunity goes with challenge,” *Renewable and Sustainable Energy Reviews*, vol. 14, no. 8, pp. 2232–2237, 2010.
- [10] G. Boyle, *Renewable Energy: Power for a Sustainable Future*. OUP Oxford, 2012.
- [11] M. O. Hansen, *Aerodynamics of wind turbines*. Routledge, 2015.
- [12] J. Manwell, J. McGowan, and A. Rogers, *Wind Energy Explained: Theory, Design and Application*. Wiley, 2010.
- [13] E. Muljadi, C. Butterfield, A. Ellis, J. Mechenbier, J. Hochheimer, R. Young, N. Miller, R. Delmerico, R. Zavadil, and J. Smith, “Equivalencing the collector system of a large wind power plant,” in *Power Engineering Society General Meeting, 2006. IEEE*, pp. 9–pp, IEEE, 2006.
- [14] B. Wu, Y. Lang, N. Zargari, and S. Kouro, *Power Conversion and Control of Wind Energy Systems*. I E E Power Engineering Series, Wiley, 2011.

- [15] M. R. Islam, Y. Guo, and J. Zhu, "A transformer-less compact and light wind turbine generating system for offshore wind farms," in *2012 IEEE International Conference on Power and Energy (PECon)*, pp. 605–610, Dec 2012.
- [16] R. Cardenas, R. Pena, S. Alepuz, and G. Asher, "Overview of control systems for the operation of dfigs in wind energy applications," *IEEE Trans. on Ind. Electron.*, vol. 60, pp. 2776–2798, Jul. 2013.
- [17] V. Vittal and R. Ayyanar, *Grid Integration and Dynamic Impact of Wind Energy*. Power Electronics and Power Systems, Springer New York, 2012.
- [18] M. Reder, E. Gonzalez, and J. J. Melero, "Wind turbine failures-tackling current problems in failure data analysis," in *Journal of Physics: Conference Series*, vol. 753, p. 072027, IOP Publishing, 2016.
- [19] F. Blaabjerg and K. Ma, "Future on power electronics for wind turbine systems," *Emerging and Selected Topics in Power Electronics, IEEE Journal of*, vol. 1, pp. 139–152, Sept 2013.
- [20] F. Blaabjerg and Z. Chen, "Power electronics for modern wind turbines," *Synthesis Lectures on Power Electronics*, vol. 1, no. 1, pp. 1–68, 2006.
- [21] R. Datta and V. T. Ranganathan, "Variable-speed wind power generation using doubly fed wound rotor induction machine-a comparison with alternative schemes," *IEEE Transactions on Energy Conversion*, vol. 17, pp. 414–421, Sep 2002.
- [22] G. Abad, J. López, M. Rodríguez, L. Marroyo, and G. Iwanski, *Doubly Fed Induction Machine: Modeling and Control for Wind Energy Generation*. IEEE Press Series on Power Engineering, Wiley, 2011.
- [23] B. Bose, *Modern Power Electronics and AC Drives*. Eastern Economy Edition, Prentice Hall PTR, 2002.
- [24] W. Leonhard, *Control of Electrical Drives*. Power Systems, Springer Berlin Heidelberg, 2001.
- [25] R. Pena, J. C. Clare, and G. M. Asher, "Doubly fed induction generator using back-to-back pwm converters and its application to variable-speed wind-energy generation," *IEE Proceedings - Electric Power Applications*, vol. 143, pp. 231–241, May 1996.
- [26] P. Krause, O. Wasynczuk, S. Sudhoff, and S. Pekarek, *Analysis of Electric Machinery and Drive Systems*. IEEE Press Series on Power Engineering, Wiley, 2013.
- [27] R. Pena, R. Cardenas, J. Proboste, G. Asher, and J. Clare, "Sensorless control of doubly-fed induction generators using a rotor-current-based mras observer," *Ind. Electron., IEEE Trans. on*, vol. 55, pp. 330–339, Jan. 2008.

- [28] J. Arbi, M. J. B. Ghorbal, I. Slama-Belkhodja, and L. Charaabi, "Direct virtual torque control for doubly fed induction generator grid connection," *IEEE Transactions on Industrial Electronics*, vol. 56, pp. 4163–4173, Oct 2009.
- [29] B. B. Pimple, V. Y. Vekhande, and B. G. Fernandes, "A new direct torque control of doubly-fed induction generator under unbalanced grid voltage," in *Applied Power Electronics Conference and Exposition (APEC), 2011 Twenty-Sixth Annual IEEE*, pp. 1576–1581, March 2011.
- [30] L. Qizhong, Y. Lan, and W. Guoxiang, "Comparison of control strategy for double-fed induction generator (dfg)," in *2011 Third International Conference on Measuring Technology and Mechatronics Automation*, vol. 1, pp. 741–744, Jan 2011.
- [31] E. Tremblay, S. Atayde, and A. Chandra, "Comparative study of control strategies for the doubly fed induction generator in wind energy conversion systems: A dsp-based implementation approach," *IEEE Transactions on Sustainable Energy*, vol. 2, pp. 288–299, July 2011.
- [32] F. BonnetFrancois, P. E. Vidal, and M. Pietrzak-David, "Dual direct torque control of doubly fed induction machine," *IEEE Transactions on Industrial Electronics*, vol. 54, pp. 2482–2490, Oct 2007.
- [33] G. Abad, M. A. RodrÁguez, J. Poza, and J. M. Canales, "Direct torque control for doubly fed induction machine-based wind turbines under voltage dips and without crowbar protection," *IEEE Transactions on Energy Conversion*, vol. 25, pp. 586–588, June 2010.
- [34] G. Abad, M. . Rodriguez, and J. Poza, "Two-level vsc based predictive direct torque control of the doubly fed induction machine with reduced torque and flux ripples at low constant switching frequency," *IEEE Transactions on Power Electronics*, vol. 23, pp. 1050–1061, May 2008.
- [35] H. Malik and S. Mishra, "Application of gene expression programming (gep) in power transformers fault diagnosis using dga," *IEEE Transactions on Industry Applications*, vol. 52, pp. 4556–4565, Nov 2016.
- [36] G. Abad, M. . RodrÁguez, G. Iwanski, and J. Poza, "Direct power control of doubly-fed-induction-generator-based wind turbines under unbalanced grid voltage," *IEEE Transactions on Power Electronics*, vol. 25, pp. 442–452, Feb 2010.
- [37] D. Santos-Martin, J. L. Rodriguez-Amenedo, and S. Arnalte, "Direct power control applied to doubly fed induction generator under unbalanced grid voltage conditions," *IEEE Transactions on Power Electronics*, vol. 23, pp. 2328–2336, Sept 2008.

- [38] L. Xu and P. Cartwright, "Direct active and reactive power control of dfig for wind energy generation," *IEEE Trans. on Energy Conv.*, vol. 21, pp. 750–758, Sep. 2006.
- [39] R. Datta and V. T. Ranganathan, "Direct power control of grid-connected wound rotor induction machine without rotor position sensors," *IEEE Transactions on Power Electronics*, vol. 16, pp. 390–399, May 2001.
- [40] N. Amiri, S. M. Madani, T. A. Lipo, and H. A. Zarchi, "An improved direct decoupled power control of doubly fed induction machine without rotor position sensor and with robustness to parameter variation," *IEEE Transactions on Energy Conversion*, vol. 27, pp. 873–884, Dec 2012.
- [41] O. Anaya-Lara, F. M. Hughes, N. Jenkins, and G. Strbac, "Rotor flux magnitude and angle control strategy for doubly fed induction generators," *Wind Energy*, vol. 9, no. 5, pp. 479–495, 2006.
- [42] S. Q. Bu, W. Du, H. F. Wang, and S. Gao, "Power angle control of grid-connected doubly fed induction generator wind turbines for fault ride-through," *IET Renewable Power Generation*, vol. 7, pp. 18–27, February 2013.
- [43] L. Fan, Z. Miao, S. Yuvarajan, and J. Glower, "A comparison of slip control, fma control and vector control in dfig converter," in *Industrial Electronics, 2008. IECON 2008. 34th Annual Conference of IEEE*, pp. 2075–2081, Nov 2008.
- [44] D. J. Burnham, S. Santoso, and E. Muljadi, "Variable rotor-resistance control of wind turbine generators," in *2009 IEEE Power Energy Society General Meeting*, pp. 1–6, July 2009.
- [45] M. S. Marhaba, S. Farhangi, and M. A. Paymani, "Comparison of power fluctuation between optislip and dfig controlled wind turbines," in *Power Electronics and Drive Systems Technology (PEDSTC), 2012 3rd*, pp. 290–295, Feb 2012.
- [46] M. R. Khadraoui and M. Elleuch, "Comparison between optislip and fixed speed wind energy conversion systems," in *Systems, Signals and Devices, 2008. IEEE SSD 2008. 5th International Multi-Conference on*, pp. 1–6, July 2008.
- [47] L. Lin, F. Sun, Y. Yang, and Q. Li, "Comparison of reactive power compensation strategy of wind farm based on optislip wind turbines," in *2009 International Conference on Sustainable Power Generation and Supply*, pp. 1–6, April 2009.
- [48] F. Taveiros, L. Barros, and F. Costa, "Back-to-back converter state-feedback control of {DFIG} (doubly-fed induction generator)-based wind turbines," *Energy*, vol. 89, pp. 896 – 906, 2015.
- [49] R. Bhattarai, N. Gurung, and S. Kamalasan, "Reduced order model based state feedback control of doubly fed induction generators," in *Power and Energy Society General Meeting (PES GM), 2016*, Jul. 2016.

- [50] A. Tapia, G. Tapia, J. X. Ostolaza, and J. R. Saenz, "Modeling and control of a wind turbine driven doubly fed induction generator," *IEEE Transactions on Energy Conversion*, vol. 18, pp. 194–204, June 2003.
- [51] T. Noguchi, H. Tomiki, S. Kondo, and I. Takahashi, "Direct power control of pwm converter without power-source voltage sensors," *IEEE Transactions on Industry Applications*, vol. 34, pp. 473–479, May 1998.
- [52] G. Escobar, A. M. Stankovic, J. M. Carrasco, E. Galvan, and R. Ortega, "Analysis and design of direct power control (dpc) for a three phase synchronous rectifier via output regulation subspaces," *IEEE Transactions on Power Electronics*, vol. 18, pp. 823–830, May 2003.
- [53] M. Malinowski, M. P. Kazmierkowski, S. Hansen, F. Blaabjerg, and G. D. Marques, "Virtual-flux-based direct power control of three-phase pwm rectifiers," *IEEE Transactions on Industry Applications*, vol. 37, pp. 1019–1027, Jul 2001.
- [54] P. Rodriguez, J. Pou, J. Bergas, J. I. Candela, R. P. Burgos, and D. Boroyevich, "Decoupled double synchronous reference frame pll for power converters control," *IEEE Transactions on Power Electronics*, vol. 22, pp. 584–592, March 2007.
- [55] R. Teodorescu, F. Blaabjerg, M. Liserre, and P. C. Loh, "Proportional-resonant controllers and filters for grid-connected voltage-source converters," *IEE Proceedings - Electric Power Applications*, vol. 153, pp. 750–762, September 2006.
- [56] D. N. Zmood and D. G. Holmes, "Stationary frame current regulation of pwm inverters with zero steady state error," in *Power Electronics Specialists Conference, 1999. PESC 99. 30th Annual IEEE*, vol. 2, pp. 1185–1190 vol.2, 1999.
- [57] F. Blaabjerg and J. M. Guerrero, "Smart grid and renewable energy systems," in *2011 International Conference on Electrical Machines and Systems*, pp. 1–10, Aug 2011.
- [58] A. Sato and T. Noguchi, "Voltage-source pwm rectifier inverter based on direct power control and its operation characteristics," *IEEE Transactions on Power Electronics*, vol. 26, pp. 1559–1567, May 2011.
- [59] R. Teodorescu, M. Liserre, and P. Rodriguez, *Grid converters for photovoltaic and wind power systems*, vol. 29. John Wiley & Sons, 2011.
- [60] J. Han, "From pid to active disturbance rejection control," *IEEE Transactions on Industrial Electronics*, vol. 56, pp. 900–906, March 2009.
- [61] H. Cai, W. Wei, Y. Peng, and H. Hu, "Fuzzy proportional-resonant control strategy for three-phase inverters in islanded micro-grid with nonlinear loads," in *2014 IEEE International Conference on Fuzzy Systems (FUZZ-IEEE)*, pp. 707–712, July 2014.

- [62] R. S. R. Chilipi, N. A. Sayari, K. H. A. Hosani, and A. R. Beig, "Adaptive notch filter-based multipurpose control scheme for grid-interfaced three-phase four-wire dg inverter," *IEEE Transactions on Industry Applications*, vol. 53, pp. 4015–4027, July 2017.
- [63] E. Muljadi and C. P. Butterfield, "Pitch-controlled variable-speed wind turbine generation," in *Industry Applications Conference, 1999. Thirty-Fourth IAS Annual Meeting. Conference Record of the 1999 IEEE*, vol. 1, pp. 323–330 vol.1, 1999.
- [64] M. Abdullah, A. Yatim, C. Tan, and R. Saidur, "A review of maximum power point tracking algorithms for wind energy systems," *Renewable and Sustainable Energy Reviews*, vol. 16, no. 5, pp. 3220 – 3227, 2012.
- [65] Y. Xia, K. H. Ahmed, and B. W. Williams, "Wind turbine power coefficient analysis of a new maximum power point tracking technique," *IEEE Transactions on Industrial Electronics*, vol. 60, pp. 1122–1132, March 2013.
- [66] A. Mirecki, X. Roboam, and F. Richardeau, "Comparative study of maximum power strategy in wind turbines," in *Industrial Electronics, 2004 IEEE International Symposium on*, vol. 2, pp. 993–998 vol. 2, May 2004.
- [67] H. Camblong, I. M. de Alegria, M. Rodriguez, and G. Abad, "Experimental evaluation of wind turbines maximum power point tracking controllers," *Energy Conversion and Management*, vol. 47, pp. 2846 – 2858, 2006.
- [68] M. A. Abdullah, A. H. M. Yatim, and C. W. Tan, "A study of maximum power point tracking algorithms for wind energy system," in *Clean Energy and Technology (CET), 2011 IEEE First Conference on*, pp. 321–326, June 2011.
- [69] R. Cardenas, R. Pena, J. Proboste, G. Asher, and J. Clare, "Mras observer for sensorless control of standalone doubly fed induction generators," *Ener. Conv., IEEE Trans. on*, vol. 20, pp. 710–718, Dec. 2005.
- [70] B. Shen, B. Mwinyiwiwa, Y. Zhang, and B.-T. Ooi, "Sensorless maximum power point tracking of wind by dfig using rotor position phase lock loop (pll)," *Power Electron., IEEE Trans. on*, vol. 24, pp. 942–951, Apr. 2009.
- [71] M. Abolhassani, P. Niazi, H. Toliyat, and P. Enjeti, "A sensorless integrated doubly-fed electric alternator/active filter (idea) for variable speed wind energy system," in *Industry Applications Conference, 2003. 38th IAS Annual Meeting. Conference Record of the*, vol. 1, pp. 507–514 vol.1, Oct. 2003.
- [72] R. Datta and V. Ranganathan, "Direct power control of grid-connected wound rotor induction machine without rotor position sensors," *Power Electron., IEEE Trans. on*, vol. 16, pp. 390–399, May 2001.

- [73] B. Hopfensperger, D. Atkinson, and R. Lakin, "Stator-flux-oriented control of a doubly-fed induction machine with and without position encoder," *Elec. Power Appl., IEE Proc.*, vol. 147, pp. 241–250, Jul. 2000.
- [74] Z. Krzeminski, "Sensorless multiscalar control of double fed machine for wind power generators," in *Power Conv. Conf., 2002. PCC-Osaka 2002. Proc. of the*, vol. 1, pp. 334–339 vol.1, 2002.
- [75] R. Cardenas, R. Pena, J. Proboste, G. Asher, J. Clare, and P. Wheeler, "Mras observers for sensorless control of doubly-fed induction generators," in *Power Electron., Machines and Drives, 2008. PEMD 2008. 4th IET Conf. on*, pp. 568–572, Apr. 2008.
- [76] Y. Guofeng, L. Yongdong, C. Jianyun, and J. Xinjian, "A novel position sensor-less control scheme of doubly fed induction wind generator based on mras method," in *Power Electron. Specialists Conf., 2008. PESC 2008. IEEE*, pp. 2723–2727, Jun. 2008.
- [77] G. Iwanski, M. Szypulski, T. Luszczuk, and P. Pura, "Cross and dot product based mras observer of the rotor position of doubly fed induction machine," in *Ecological Vehicles and Renewable Energies (EVER), 2014 Ninth Int. Conf. on*, pp. 1–5, Mar. 2014.
- [78] B. Mwinyiwiwa, Y. Zhang, B. Shen, and B.-T. Ooi, "Rotor position phase-locked loop for decoupled p-q control of dfig for wind power generation," *Energy Conv., IEEE Trans. on*, vol. 24, pp. 758–765, Sep. 2009.
- [79] G. Marques, V. Pires, S. Sousa, and D. Sousa, "A dfig sensorless rotor-position detector based on a hysteresis controller," *Energy Conv., IEEE Trans. on*, vol. 26, pp. 9–17, Mar. 2011.
- [80] S. Yang and V. Ajjarapu, "A speed-adaptive reduced-order observer for sensorless vector control of doubly fed induction generator-based variable-speed wind turbines," *IEEE Trans. on Energy Conv.*, vol. 25, pp. 891–900, Sep. 2010.
- [81] A. B. Ataji, Y. Miura, T. Ise, and H. Tanaka, "A rotor-current-based slip angle estimator for grid-connected doubly fed induction generator requiring the stator inductance only," *IEEE Trans. on Power Electron.*, vol. 32, pp. 4827–4838, Jun. 2017.
- [82] L. Y. Lu, N. Avila, C. C. Chu, and T. W. Yeh, "Model reference adaptive back-electromotive-force estimators for sensorless control of grid-connected dfigs," *IEEE Trans. on Ind. Appl.*, vol. PP, no. 99, pp. 1–1, 2017.
- [83] N. Amiri, S. M. Madani, T. A. Lipo, and H. A. Zarchi, "An improved direct decoupled power control of doubly fed induction machine without rotor position sensor and with robustness to parameter variation," *IEEE Transactions on Energy Conversion*, vol. 27, pp. 873–884, Dec. 2012.

- [84] R. Maharjan and S. Kamalasan, "A novel online adaptive sensorless identification and control of doubly fed induction generator," in *PES Gen. Meeting / Conf. Expo., 2014 IEEE*, pp. 1–5, Jul. 2014.
- [85] R. Bhattarai, N. Gurung, and S. Kamalasan, "Minimum variance adaptive speed estimation technique for vector control of doubly fed induction generator," in *North American Power Symp. (NAPS), 2015*, pp. 1–6, Oct. 2015.
- [86] C. Chen, *Linear System Theory and Design*. Linear System Theory and Design, Oxford University Press, 1999.
- [87] J. Kautsky, N. K. Nichols, and P. V. Dooren, "Robust pole assignment in linear state feedback," *International Journal of Control*, vol. 41, no. 5, pp. 1129–1155, 1985.
- [88] P. Ledesma and J. Usaola, "Effect of neglecting stator transients in doubly fed induction generators models," *Energy Conversion, IEEE Transactions on*, vol. 19, pp. 459–461, June 2004.
- [89] R. Dorf and R. Bishop, *Modern Control Systems*. Pearson Education, 2016.
- [90] M. Singh and S. Santoso, "Dynamic models for wind turbines and wind power plants," *NREL Tech Report*, October 2011.
- [91] M. Singh, *Dynamic models for wind power plants*. PhD thesis, 2011.
- [92] C.-T. Chen, *Linear System Theory and Design*. New York, NY, USA: Oxford University Press, Inc., 3rd ed., 1998.
- [93] D. Luenberger, "Observers for multivariable systems," *IEEE Trans. on Autom. Control*, vol. 11, pp. 190–197, Apr. 1966.
- [94] D. Luenberger, "An introduction to observers," *IEEE Trans. on Autom. Control*, vol. 16, pp. 596–602, Dec. 1971.
- [95] S. Peresada, V. Blagodir, and M. Zhelinskyi, "Output feedback control of stand-alone doubly-fed induction generator," in *Intelli. Energy and Pow. Syst. (IEPS), 2016 2nd Int. Conf. on*, pp. 1–6, IEEE, 2016.
- [96] V. Radisavljevic-Gajic, "Linear observers design and implementation," in *Proc. of the 2014 Zone 1 Conf. of the Amer. Soc. for Eng. Edu.*, pp. 1–6, Apr. 2014.
- [97] "Wind speed profile."
- [98] P. Gayen, D. Chatterjee, and S. Goswami, "Stator side active and reactive power control with improved rotor position and speed estimator of a grid connected dfig (doubly-fed induction generator)," *Energy*, vol. 89, pp. 461 – 472, 2015.

- [99] D. D. Reigosa, J. M. Guerrero, A. B. Diez, and F. Briz, "Rotor temperature estimation in doubly-fed induction machines using rotating high-frequency signal injection," *IEEE Trans. on Ind. Appl.*, vol. 53, pp. 3652–3662, Jul. 2017.
- [100] K. Åström and B. Wittenmark, *Adaptive Control*. Addison-Wesley series in electrical engineering : control engineering, Addison-Wesley, 1995.
- [101] E. Tremblay, S. Atayde, and A. Chandra, "Comparative study of control strategies for the doubly fed induction generator in wind energy conversion systems: A dsp-based implementation approach," *IEEE Trans. on Sust. Energy*, vol. 2, pp. 288–299, Jul. 2011.
- [102] R. Bhattarai, N. Gurung, and S. Kamalasan, "Minimum variance controller based adaptive control for doubly fed induction generator," in *2016 North Amer. Power Symp. (NAPS)*, pp. 1–6, Sep. 2016.
- [103] M. Davari and Y. A. R. I. Mohamed, "Robust vector control of a very weak-grid-connected voltage-source converter considering the phase-locked loop dynamics," *IEEE Transactions on Power Electronics*, vol. 32, pp. 977–994, Feb 2017.
- [104] A. A. Rockhill, M. Liserre, R. Teodorescu, and P. Rodriguez, "Grid-filter design for a multimegawatt medium-voltage voltage-source inverter," *IEEE Transactions on Industrial Electronics*, vol. 58, pp. 1205–1217, April 2011.
- [105] L. Xu and P. Cartwright, "Direct active and reactive power control of dfig for wind energy generation," *IEEE Transactions on Energy Conversion*, vol. 21, pp. 750–758, Sep. 2006.
- [106] Y. Zhang, Z. Li, Z. Piao, W. Xie, X. Wei, and W. Xu, "A novel three-vectors-based predictive direct power control of doubly fed induction generator for wind energy applications," in *2012 IEEE Energy Conversion Congress and Exposition (ECCE)*, pp. 793–800, Sep. 2012.
- [107] B. Lu, Y. Li, X. Wu, and Z. Yang, "A review of recent advances in wind turbine condition monitoring and fault diagnosis," in *2009 IEEE Power Electronics and Machines in Wind Applications*, pp. 1–7, June 2009.
- [108] R. Bhattarai, N. Gurung, A. Thakallapelli, and S. Kamalasan, "Reduced order state observer based feedback control methodologies for doubly fed induction machine," *IEEE Transactions on Industry Applications*, vol. PP, no. 99, pp. 1–1, 2018.
- [109] K. Rothenhagen and F. W. Fuchs, "Current sensor fault detection and reconfiguration for a doubly fed induction generator," in *2007 IEEE Power Electronics Specialists Conference*, pp. 2732–2738, June 2007.

- [110] H. Jadhav and R. Roy, "A comprehensive review on the grid integration of doubly fed induction generator," *International Journal of Electrical Power & Energy Systems*, vol. 49, pp. 8 – 18, 2013.
- [111] R. Zavadil, N. Miller, A. Ellis, and E. Muljadi, "Making connections [wind generation facilities]," *IEEE Power and Energy Magazine*, vol. 3, pp. 26–37, Nov 2005.
- [112] A. Ellis, R. Walling, B. Zavadil, D. Jacobson, and R. Piwko, "Interconnection requirements for variable generation," *Special Assessment*, 2012.
- [113] R. Yousefian, R. Bhattarai, and S. Kamalasan, "Transient stability enhancement of power grid with integrated wide area control of wind farms and synchronous generators," *IEEE Transactions on Power Systems*, vol. 32, pp. 4818–4831, Nov 2017.
- [114] W. Du, J. Bi, J. Cao, and H. F. Wang, "A method to examine the impact of grid connection of the dfigs on power system electromechanical oscillation modes," *IEEE Transactions on Power Systems*, vol. 31, pp. 3775–3784, Sept 2016.
- [115] D. PowerFactory, "Version 14.0," *DIgSILENT International, Germany*, 2010.
- [116] M. Kayikci and J. V. Milanovic, "Reactive power control strategies for dfig-based plants," *IEEE Transactions on Energy Conversion*, vol. 22, pp. 389–396, June 2007.
- [117] A. A. Ghandakly and A. M. Farhoud, "A parametrically optimized self-tuning regulator for power system stabilizers," *IEEE Transactions on Power Systems*, vol. 7, pp. 1245–1250, Aug 1992.
- [118] S. Kamalasan and A. Hande, "A pid controller for real-time dc motor speed control using the c505c microcontroller.," in *CAINE*, pp. 34–39, 2004.
- [119] R. Maharjan and S. Kamalasan, "A novel online adaptive sensorless identification and control of doubly fed induction generator," in *2014 IEEE PES General Meeting / Conference Exposition*, pp. 1–5, July 2014.
- [120] S. Ghosh, S. Kamalasan, N. Senroy, and J. Enslin, "Doubly fed induction generator (dfig)-based wind farm control framework for primary frequency and inertial response application," *IEEE Transactions on Power Systems*, vol. 31, pp. 1861–1871, May 2016.
- [121] S. Ghosh and N. Senroy, "Electromechanical dynamics of controlled variable-speed wind turbines," *IEEE Systems Journal*, vol. 9, pp. 639–646, June 2015.
- [122] P. Kundur, N. J. Balu, and M. G. Lauby, *Power system stability and control*, vol. 7. McGraw-hill New York, 1994.

- [123] J. J. Sanchez-Gasca, N. W. Miller, and W. W. Price, "A modal analysis of a two-area system with significant wind power penetration," in *IEEE PES Power Systems Conference and Exposition, 2004.*, pp. 1148–1152 vol.2, Oct 2004.
- [124] H. Liu, L. Zhu, Z. Pan, F. Bai, Y. Liu, Y. Liu, M. Patel, E. Farantatos, and N. Bhatt, "Armax-based transfer function model identification using wide-area measurement for adaptive and coordinated damping control," *IEEE Transactions on Smart Grid*, vol. 8, pp. 1105–1115, May 2017.
- [125] R. Pena, J. Clare, and G. Asher, "Doubly fed induction generator using back-to-back pwm converters and its application to variable-speed wind-energy generation," *IEE Proceedings-Electric Power Applications*, vol. 143, no. 3, pp. 231–241, 1996.
- [126] R. Bhattarai, N. Gurung, and S. Kamalasan, "Minimum variance controller based adaptive control for doubly fed induction generator," in *2016 North American Power Symposium (NAPS)*, pp. 1–6, Sept 2016.
- [127] R. Trentini, R. Kutzner, and L. Hofmann, "State-space generalized minimum variance controller based pss for damping of interarea modes," in *2016 18th Mediterranean Electrotechnical Conference (MELECON)*, pp. 1–6, April 2016.
- [128] Z. Miao, L. Fan, D. Osborn, and S. Yuvarajan, "Control of dfig-based wind generation to improve interarea oscillation damping," *IEEE Transactions on Energy Conversion*, vol. 24, pp. 415–422, June 2009.
- [129] R. Yousefian, S. Kamalasan, and R. Bhattarai, "Direct intelligent wide-area damping controller for wind integrated power system," in *2016 IEEE Power and Energy Society General Meeting (PESGM)*, pp. 1–5, July 2016.
- [130] K. Åström and B. Wittenmark, *Adaptive Control: Second Edition*. Dover Books on Electrical Engineering, Dover Publications, 2013.
- [131] N. Gurung, R. Bhattarai, and S. Kamalasan, "Optimal linear-quadratic-integral controller design for doubly-fed induction generator," in *IEEE PES Gen. Meeting, 2017*, Jul. 2017.
- [132] "Pole placement design." www.mathworks.com/help/control/ref/place.html. Accessed: 2017-09-02.

APPENDIX A: MATHEMATICAL MODELING OF DOUBLY FED INDUCTION
MACHINE

The dynamic equations modeling the DFIM in per unit based on a synchronously rotating reference frame considering generator convention is given by [26]:

$$\begin{aligned} v_{dqs} &= -R_s i_{dqs} + j \frac{\omega_s}{\omega_b} \Psi_{dqs} + p \frac{\Psi_{dqs}}{\omega_b} \\ v'_{dqr} &= R'_r i'_{dqr} + j \left(\frac{\omega_s - \omega_r}{\omega_b} \right) \Psi'_{dqr} + p \frac{\Psi'_{dqr}}{\omega_b} \end{aligned} \quad (\text{A.1})$$

where v_{qs} , v_{ds} , i_{qs} , i_{ds} and ψ_{qs} , ψ_{ds} are the quadrature and direct axis components of stator terminal voltages, stator currents and stator flux respectively. Likewise, v'_{qr} , v'_{dr} , i'_{qr} , i'_{dr} and ψ'_{qr} , ψ'_{dr} are the quadrature and direct axis components of rotor terminal voltages, rotor currents and rotor flux respectively. ω_s , ω_r and ω_b are the angular speeds of synchronously rotating reference frame, DFIM rotor and the base angular speed for DFIM rotor respectively and p is the derivative operator.

Also, the flux linkage equations are given by,

$$\begin{aligned} \Psi_{dqs} &= -L_{ls} i_{dqs} + L_m (-i_{dqs} + i'_{dqr}) \\ \Psi'_{dqr} &= L'_{lr} i'_{dqr} + L_m (-i_{dqs} + i'_{dqr}) \end{aligned} \quad (\text{A.2})$$

Note: $L_s = L_{ls} + L_m$ and $L'_r = L'_{lr} + L_m$.

Likewise, the instantaneous active (P_{st}) and reactive power (Q_{st}) from the stator in synchronously rotating $d - q$ axis based reference frame is given by,

$$\begin{aligned} P_{st} &= v_{qs} i_{qs} + v_{ds} i_{ds} \\ Q_{st} &= v_{qs} i_{ds} - v_{ds} i_{qs} \end{aligned} \quad (\text{A.3})$$

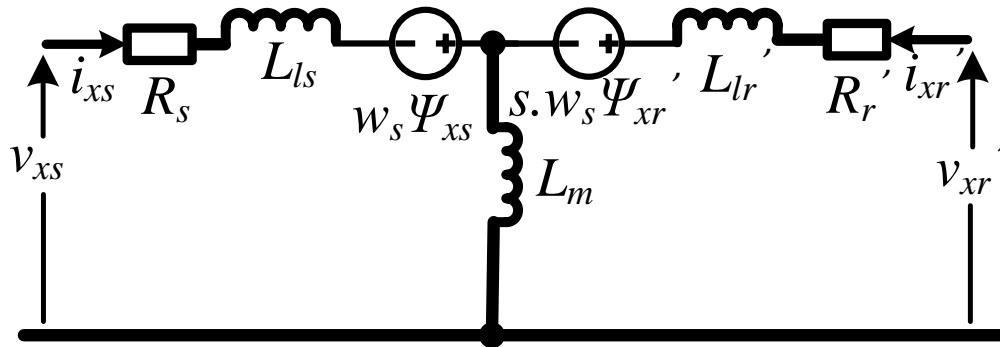


Figure A.1: Dynamic Electric Circuit Model of DFIM

The electromagnetic torque developed by machine in per unit is expressed as,

$$T_e = \Psi_{ds} i_{qs} - \Psi_{qs} i_{ds} \quad (\text{A.4})$$

$$T_e = \Psi_{qr}' i_{dr}' - \Psi_{dr}' i_{qr}'$$

Figure A.1 represents a dynamic equivalent electrical model of DFIM. Figure A.1 is a representation of DFIM in motor convention with both the stator and rotor current entering into the circuit considered as positive. In generator convention, however, the current coming out of stator is considered as positive.

APPENDIX B: MATHEMATICAL MODELING OF A GRID CONNECTED
INVERTER

A detailed representation of a GCI is shown in Figure B.1 from which a mathematical model of GCI can be obtained.

From Figure B.1, the voltage balance across the inductor and resistor can be written as

$$\begin{bmatrix} V_{ai} \\ V_{bi} \\ V_{ci} \end{bmatrix} = R \begin{bmatrix} I_a \\ I_b \\ I_c \end{bmatrix} + L \frac{d}{dt} \begin{bmatrix} I_a \\ I_b \\ I_c \end{bmatrix} + \begin{bmatrix} V_a \\ V_b \\ V_c \end{bmatrix} \quad (\text{B.1})$$

where R and L are the line inductance and resistance, respectively and V_{xi} , V_x and I_x are inverter output voltage, grid voltage and inverter output current respectively with $x = [a \ b \ c]$. Using the abc to $d - q$ transformation, (B.1) is transformed into a synchronously rotating $d - q$ reference frame rotating at ω_e rad/s:

$$\begin{aligned} v_{di} &= Ri_d + L \frac{di_d}{dt} - \omega_e Li_q + v_d \\ v_{qi} &= Ri_q + L \frac{di_q}{dt} + \omega_e Li_d + v_q \end{aligned} \quad (\text{B.2})$$

where, ω_e is the angular frequency of the grid voltage, i_d and i_q is the d -axis and q -axis current from inverter respectively, v_d and v_q is the d -axis and q -axis grid voltage respectively and v_{di} and v_{qi} is the d -axis and q -axis output voltage of the inverter.

The instantaneous active and reactive power output of GCI is given by

$$\begin{aligned} P_{GSC} &= v_d i_d + v_q i_q \\ Q_{GSC} &= v_d i_q + v_q i_d \end{aligned} \quad (\text{B.3})$$

The angular position of the grid voltage is determined as

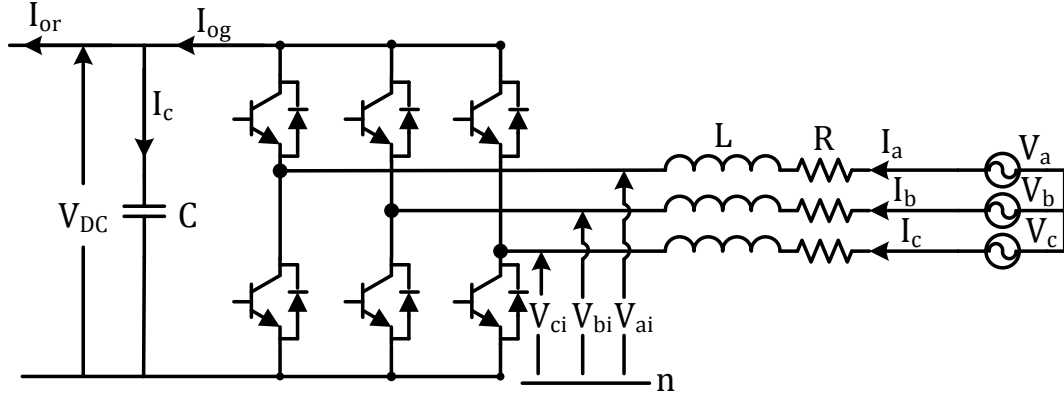


Figure B.1: Arrangement of a bidirectional GCI.

$$\theta_e = \int \omega_e dt = \tan^{-1} \left(\frac{v_\beta}{v_\alpha} \right) \quad (\text{B.4})$$

where v_α and v_β are the $\alpha - \beta$ components of grid voltage.

If the d -axis of the synchronously rotating reference frame is aligned with the grid voltage position given by (B.4), v_q is zero, and considering constant amplitude of the grid voltage v_d can be assumed constant.

Also, neglecting any harmonics due to the inverter switching and switching losses in general, it can be observed from Figure B.1 that

$$\begin{aligned} v_d i_d &= V_{DC} I_{og} \\ C \frac{dE}{dt} &= I_{or} - I_{og} \\ v_d &= m_i V_{DC} \\ I_{og} &= m_i i_d \end{aligned} \quad (\text{B.5})$$

From (B.5) it can be seen that the DC-link voltage can be regulated through i_d .

APPENDIX C: RECURSIVE LEAST SQUARES BASED SYSTEM
IDENTIFICATION

The RLS technique is a computational algorithm that minimizes weighted linear cost function which is a squared error between the measured and estimated output for a particular input signal [130]. In this technique, a transfer function representation of a system relating the desired input and output signal is first hypothesized and then the parameters of the transfer function are estimated online so as to minimize the error between the estimated output and the actual output of the system. The parameters of a z -domain transfer function, that models the process, are identified every sample period using the system input and output at every discrete sampling time.

If model output is in close approximation to the actual system output, then the z -domain transfer function model is assumed to be a good approximation of the actual system. Once the approximate model of the system is achieved, any model based controller can be designed.

C.1 Autoregressive Exogenous Model

Consider a ARX system represented by a monic n^{th} order z -domain transfer function of the following form.

$$\frac{y(k)}{u(k)} = \frac{b_0z^{-1} + b_1z^{-2} + \dots + b_{n-1}z^{-n}}{1 + a_1z^{-1} + a_2z^{-2} + \dots + a_nz^{-n}} = \frac{B(z^{-1})}{A(z^{-1})} \quad (C.1)$$

which in turn can be represented by a difference equation form for sample ' k ' as,

$$y(k) = -a_1y(k-1) - a_2y(k-2) - \dots - a_ny(k-n) + b_0u(k-1) + b_1u(k-2) + \dots + b_{n-1}u(k-n)$$

For a previous sample ' $k - 1$ ', it can be observed that

$$y(k - 1) = -a_1y(k - 2) - a_2y(k - 3) - \dots - a_ny(k - 1 - n) + \\ b_0u(k - 2) + b_1u(k - 3) + \dots + b_{n-1}u(k - 1 - n)$$

Similarly for sample ' $k - N + 1$ '

$$y(k - N + 1) = -a_1y(k - N) - a_2y(k - N - 1) - \dots - a_ny(k - N + 1 - n) + \\ b_0u(k - N) + \dots + b_{n-1}u(k - N + 1 - n)$$

where ' N ' is the observation length. The above group of difference equations can be written in the matrix form as:

$$\underbrace{\begin{bmatrix} y(k) \\ y(k - 1) \\ \cdot \\ \cdot \\ y(k - N + 1) \end{bmatrix}}_{\Phi_{model}} = \underbrace{\begin{bmatrix} a_1 \\ \cdot \\ \cdot \\ a_n \\ b_0 \\ \cdot \\ \cdot \\ b_{n-1} \end{bmatrix}}_{\Theta} \quad (C.2)$$

where, X is,

$$\begin{bmatrix} -y(k-1) & \cdots & -y(k-n) & u(k-1) & \cdots & u(k-n) \\ -y(k-2) & \cdots & -y(k-n-1) & u(k-2) & \cdots & u(k-1-n) \\ \vdots & \cdots & \vdots & \vdots & \cdots & \vdots \\ \vdots & \cdots & \vdots & \vdots & \cdots & \vdots \\ -y(k-N) & \cdots & -y(k-N+1-n) & u(k-N) & \cdots & u(k-N+1-n) \end{bmatrix}$$

Let ' ϵ ' be the error between the output of the actual system and estimated model,

$$\epsilon = \Phi_{system} - \Phi_{model} \quad (C.3)$$

From (C.2), $\Phi_{model} = X.\Theta$, which can be substituted in (C.3) to get,

$$\epsilon = \Phi_{system} - X.\Theta \quad (C.4)$$

The basis of the least squares identification is to minimize the square of the error ' ϵ ' for which a criterion ' J ' is defined as,

$$J = \epsilon^t \epsilon = \sum_{i=k}^{k+N} \epsilon^2 \quad (C.5)$$

On minimizing, the criterion ' J ', the system parameters ' Θ ' representing the parameter vector is solved and the following form of equation for ' Θ ' is obtained.

$$\Theta(k) = \Theta(k-1) + K(k) [\Phi(k) - X^t(k)\Theta(k-1)] \quad (C.6)$$

where,

$$K(k) = \frac{P(k-1)X(k)}{\gamma + X^t(k)P(k-1)X(k)} \quad (C.7)$$

and,

$$P(k) = \frac{[I - K(k)X^t(k)] P(k-1)}{\gamma} \quad (\text{C.8})$$

where, $K(k)$ is the Kalman filter gain, $P(k)$ is the co-variance matrix of the error during the estimation of parameter vector Θ and has size of $2n \times 2n$, I is the identity matrix of size $2n \times 2n$ and γ is the forgetting factor.

Once Θ is solved using (C.6), the parameters $a_1, a_2, \dots, a_n, b_0, b_1, \dots, b_{n-1}$ defining the n^{th} order transfer function model of the system is obtained. Once, the system parameters are obtained, the controller is then designed using the identified system parameters.

C.2 Autoregressive Moving Average Exogenous Model

For ARMAX the system represented by a monic n^{th} order z -domain transfer function of the following form.

$$\begin{aligned} y(k) &= \frac{b_0 z^{-1} + b_1 z^{-2} + \dots + b_{n-1} z^{-n}}{1 + a_1 z^{-1} + a_2 z^{-2} + \dots + a_n z^{-n}} u(k) + \frac{c_0 z^{-1} + c_1 z^{-2} + \dots + c_{n-1} z^{-n}}{1 + a_1 z^{-1} + a_2 z^{-2} + \dots + a_n z^{-n}} \varrho(k) \\ &= \frac{B(z^{-1})}{A(z^{-1})} u(k) + \frac{C(z^{-1})}{A(z^{-1})} \varrho(k) \quad (\text{C.9}) \end{aligned}$$

APPENDIX D: MACHINE PARAMETERS

D.1 General Electric 1.5 MW DFIG parameters

DFIG parameters: $R_s = r_s = 0.0071$ pu, $L_{ls} = 0.1714$ pu, $R_r = r_r = 0.005$ pu, $L_{lr} = 0.1563$ pu, $L_m = 2.9$ pu, no. of pole pairs = 3, Turbine Inertia $H_t = 4.5$ s, Generator Inertia $G_t = 0.5$ s

D.2 Single Phase Inverter Parameters

VA rating of SPI = 1.5 kVA, Rated Voltage = 230 Volts, $R_f = 10^{-3} \Omega$, $L_f = 10^{-3}$ H; $R_c = 10^{-4} \Omega$, $C = 6.6 \mu\text{F}$, $L_g = 10^{-2}$ H; $R_g = 0.033 \Omega$, DC Link Voltage = 400 Volts, Grid nominal frequency = 60 Hz, Inverter Switching Frequency = 25 kHz

APPENDIX E: GAIN COMPUTATION FOR SFC

E.1 Computation Sample for Feedback and Observer Gains

STEP 1: For a particular operating condition, say $s = 0$, system A , B , C and E matrices can be calculated for the DFIG with parameters represented in D, using (3.23) and (3.24). The obtained matrices are $A = \begin{bmatrix} -5.9250 & 0 \\ 0 & -5.9250 \end{bmatrix}$, $B =$

$$\begin{bmatrix} 1185 & 0 \\ 0 & 1185 \end{bmatrix}, C = \begin{bmatrix} 0.9442 & 0 \\ 0 & 0.9442 \end{bmatrix}, E = \begin{bmatrix} 0 \\ 0 \end{bmatrix}.$$

STEP 2: Once the controllability and observability has been tested of the system by checking the rank of controllability and observability matrix, the optimal closed loop eigenvalue provided by the optimal gain computation technique in [131] is considered as optimal location of eigenvalues. For this case, the closed loop eigenvalues are obtained to be at (-10, -20) based on objective function minimization considering (3.9).

STEP 3: The feedback gain matrix can then be computed using pole placement technique. For example, using pole place function defined in [132], the gain matrix $K = \begin{bmatrix} 0.0034 & 0 \\ 0 & 0.0119 \end{bmatrix}$.

STEP 4: Utilizing (3.31) and (3.24), considering at steady state the error is close to zero and controller goal is to drive system output close to reference input, the gain matrix G is computed as $G = -[C(A - B.K)^{-1}B]^{-1}$ [49]. The computed gain matrix G for the machine in Appendix A is $G = \begin{bmatrix} 0.0089 & 0 \\ 0 & 0.0179 \end{bmatrix}$.

STEP 5: For the observer gain, the eigenvalues are placed at least 10 times

farther than the closed loop eigenvalues. In this case to place the closed loop observer eigenvalues at $(-200,-400)$, the observer gain matrix is computed as $L =$

$$\begin{bmatrix} 0.1638 & 0 \\ 0 & 0.3326 \end{bmatrix}.$$

APPENDIX F: SIMULATION MODELS AND SOURCE CODES

The simulation models and source code of the controller designed in this dissertation is the property of Power, Energy and Intelligent Systems Lab (PEISL), Department of Electrical and Computer Engineering, University of North Carolina at Charlotte. Please contact Dr. Sukumar Kamalasan or the author for further information about the models and source codes.

VITA

Rojan Bhattarai was born in Bardaghat, Nawalparasi, Nepal on the 30th of October, 1991, the son of Chudamani Bhattarai and Bhumkala K.C. (Bhattarai). He received his B.E. in electrical engineering from Institute of Engineering, Pulchowk Campus, Tribhuvan University, Nepal in November 2012. He is currently a Ph.D. candidate at University of North Carolina at Charlotte under the supervision of Dr. Sukumar Kamalasan and started Fall 2014. His current research interests include distributed energy systems integration, modeling and control, stability studies of renewables integrated bulk power grid and use of distributed energy resources for supporting stability of power grid. He will be joining the Argonne National Laboratory in Lemont, IL as a postdoctoral research associate in June 2018 under the supervision of Dr. Ning Kang.